

ABSTRACT

Title of dissertation: MAGNETIC & ELECTRIC FIELD SENSING
AND APPLICATIONS
BASED ON COHERENT EFFECTS
IN NEUTRAL ATOMS

David Henry Meyer
Doctor of Philosophy, 2018

Dissertation directed by: Dr. Steve Rolston
Department of Physics

This work encompasses two projects employing coherent probing of neutral rubidium atom vapors for sensing applications: 1) observing and characterizing new “twists” within Nonlinear Magneto-Optical Rotation (NMOR) signals in laser-cooled atoms. Using these features an in-situ, multi-directional characterization of magnetic fields and gradients at the sub-mG (and mG/mm) level in a compact cold-atom system is demonstrated; 2) high-bandwidth, phase-sensitive electrometry via Electromagnetically Induced Transparency (EIT) with a warm vapor of Rydberg atoms is employed as a digital communication receiver of free-space, modulated RF carrier electric fields. Channel capacities in excess of 10 Mbit/s are measured. Performance limitations due to EIT probing and fundamental quantum noise are explored in detail.

MAGNETIC & ELECTRIC FIELD SENSING AND
APPLICATIONS BASED ON COHERENT EFFECTS IN
NEUTRAL ATOMS

by

David Henry Meyer

Dissertation submitted to the Faculty of the Graduate School of the
University of Maryland, College Park in partial fulfillment
of the requirements for the degree of
Doctor of Philosophy
2018

Advisory Committee:
Professor Steve Rolston, Chair
Dr. Fredrik Fatemi, Advisor
Professor Frederick Wellstood
Professor Trey Porto
Professor Edo Waks

© Copyright by
David Henry Meyer
2018

Acknowledgments

I am grateful to all who have contributed to making this dissertation a reality. Without the help, support, and encouragement of others, this milestone would have never been crossed.

I must first thank my advisor, Dr. Fredrik Fatemi, for his many hours of dedicated work at the U.S. Army Research Laboratory (ARL). Without his efforts, the funding and creative space necessary to finish this dissertation would not have been. Fredrik is also an infinite well of optics tricks, knowledge and experience which have proven invaluable. More importantly, despite his incredibly busy schedule he always made time for in-depth discussions of physics and our progress in the lab, where his true passion lies. Without people like Fredrik, explorative basic research would not be possible.

I must also express my extreme gratitude to Dr. Paul Kunz for his many years of informal advising. We started work at ARL at nearly the same time 5 years ago and have since learned together, often from scratch, the atomic physics covered in this work. Paul has a deep, intuitive knowledge of atomic physics; I owe much of my understanding to his insights. Paul has also been an indispensable bulwark against the negative aspects of doing research at ARL. I doubt I would still be at ARL without his support, and would have missed out on the many exciting questions and opportunities we are now having.

Another indispensable advisor has been Professor Steve Rolston. Steve officially advises a great many students on top of his already tremendous workload,

and I am grateful he also advised me. He has always been very understanding and timely with my paperwork needs and concerns.

The Neutral Atom Group at ARL is a very young group and I owe a lot to the other members thereof whom I have had the pleasure to work with. In particular I would like to thank Dr. Kevin Cox who has boundless energy for exciting and impactful physics. It has been a privilege to learn cavity QED and the many finer subtleties of quantum noise from him as we have worked together on many projects in the lab. I would also like to thank Zac Castillo, my replacement in the lab. It is a pleasure to pass on what knowledge I have and relearn from him the knowledge I've forgotten from my early coursework.

I would also like to thank all of the other members of the Quantum Sciences Branch at ARL. We have had many riveting discussions of both physics and not-so-physics at the lunch table and in the halls that have broadened my understanding. I especially would like to express my gratitude to Neal Solmeyer, Mike Foss-Feig, Joe Britton, Elizabeth Goldschmidt, and James Siverns.

This work would have been little more than a wishful thought without the various support staff of ARL. Jamie Eller and Teresa Kipp in particular have been extremely helpful in navigating the minefield of government paperwork, regulations, and general inefficiency laid by others. Art Harrison, the electronics shop master at ARL, has provided significant help debugging the many electronic circuits I've brought him over the years and was always polite when informing me when damaged circuits were my own fault.

I thank my family and friends who have supported me throughout my long

academic career. Special thanks go to my parents for raising me well and instilling a continuous desire to learn; my brother-in-law Mark who initially steered me away from chemistry to physics; and my beloved wife, Lauren, who's infinite compassion and love have supported me through the long hours of physics research.

I would like to acknowledge financial support from ARL, Oak Ridge Associated Universities (ORAU), Oak Ridge Institute for Science and Education (ORISE), and the Office of the Secretary of Defense's (OSD) Quantum Science and Engineering Program (QSEP).

To any I may have overlooked, I apologize for the oversight.

Finally, I express gratitude to my God for seeing me through to this point in life. I eagerly await what the next adventure He has in mind for me.

Research was sponsored by the Army Research Laboratory and was accomplished under Cooperative Agreement Number **W911NF-17-2-0015**. The views and conclusions contained in this document are those of the authors and should not be interpreted as representing the official policies, either expressed or implied, of the Army Research Laboratory or the U.S. Government. The U.S. Government is authorized to reproduce and distribute reprints for Government purposes notwithstanding any copyright notation herein.

Contents

| | |
|--|------|
| Acknowledgements | ii |
| List of Tables | viii |
| List of Figures | ix |
| List of Abbreviations | xi |
| 1 Dissertation Outline | 1 |
| 1.1 Contributions | 3 |
| 2 Twists in Nonlinear Magneto-Optical Rotation | 4 |
| 2.1 Introduction | 8 |
| 2.1.1 Observing NMOR | 10 |
| 2.1.2 Relation to EIT & EIA | 15 |
| 2.2 Formalism Primer | 20 |
| 2.2.1 The Density Matrix | 22 |
| 2.2.2 Defining the Hamiltonian | 25 |
| 2.2.3 Dephasing Mechanisms | 30 |
| 2.2.4 The Lindblad Equation | 33 |
| 2.2.5 Observables Derivation | 35 |
| 2.2.6 The Polarization Moments Basis | 40 |
| 2.2.6.1 Changing Bases | 40 |
| 2.2.6.2 Orientation vs. Alignment | 42 |
| 2.2.7 Frame Rotations | 47 |
| 2.3 NMOR Models | 51 |
| 2.3.1 Single-Axis Models | 51 |
| 2.3.1.1 Low Probe Intensity – Linear Polarizer Model | 51 |
| 2.3.1.2 High Probe Intensity – AOC Model | 54 |
| 2.3.2 Multi-Axis Perturbation Model | 56 |
| 2.3.2.1 2-Axis Solution | 59 |
| 2.3.2.2 3-Axis Solution | 71 |
| 2.4 Experimental Characterization of the “Twist” | 79 |
| 2.4.1 Experimental Configuration | 79 |
| 2.4.1.1 Magnetic Coil Calibration | 81 |
| 2.4.1.2 NMOR Measurement | 86 |

| | | |
|---------|---|-----|
| 2.4.1.3 | Experiment –Numerical Simulation Correspondence | 88 |
| 2.4.2 | “Twist” Dependence on Magnetic Fields | 89 |
| 2.4.2.1 | Magnitude | 89 |
| 2.4.2.2 | Orientation | 91 |
| 2.4.3 | “Twist” Dependence on Probe Field | 92 |
| 2.4.3.1 | Ellipticity | 93 |
| 2.4.3.2 | Optical Intensity | 94 |
| 2.4.4 | Measuring Magnetic Gradients with the “Twist” | 96 |
| 2.5 | Conclusion | 100 |
| 3 | Rydberg Electrometry for Digital Communication | 102 |
| 3.1 | Introduction | 105 |
| 3.1.1 | Rydberg Electromagnetically Induced Transparency | 106 |
| 3.1.1.1 | Doppler-Averaging | 113 |
| 3.1.1.2 | Transit Dephasing | 118 |
| 3.1.1.3 | Black-Body Radiation Induced Dephasing | 119 |
| 3.1.2 | Rydberg Electrometry | 121 |
| 3.1.2.1 | Derivation of scaling factor D | 124 |
| 3.1.3 | Electrometry of Far Off-Resonant RF Fields | 126 |
| 3.1.4 | Classical Antennas & Communication Basics | 126 |
| 3.1.4.1 | Carrier Modulation & Channel Capacity | 127 |
| 3.1.4.2 | Antennas & the Chu Limit | 131 |
| 3.1.4.3 | Noise Background | 133 |
| 3.2 | Digital Communication with a Rydberg Receiver | 136 |
| 3.2.1 | Experimental Configuration | 137 |
| 3.2.2 | Demodulated Signal | 140 |
| 3.2.2.1 | Demodulated Signal Dependence on Ω_μ | 140 |
| 3.2.3 | Phase Shift Keying Demonstration | 144 |
| 3.2.4 | EIT Detection Bandwidth Limitations | 145 |
| 3.2.4.1 | Derivation of τ_f Limit for a Transit-Broadened Medium | 148 |
| 3.2.5 | Measuring Channel Capacity | 152 |
| 3.2.6 | Contrast with Classical Receivers | 155 |
| 3.3 | Digital Communication in the Electrically Small Regime | 160 |
| 3.3.1 | Far Off-Resonant Configuration | 161 |
| 3.3.2 | Measuring Channel Capacity | 164 |
| 3.3.3 | Comparison with the Chu Limit | 166 |
| 3.4 | The Standard Quantum Limit for Digital Communication | 169 |
| 3.4.1 | The Standard Quantum Limit | 169 |
| 3.4.2 | The Standard Quantum Limit for Channel Capacity | 171 |
| 3.4.3 | EIT, Photon Shot Noise, and the Standard Quantum Limit | 172 |
| 3.4.4 | Quantum Limits for Resonant Electrometry | 178 |
| 3.5 | Sensitivity of the Rydberg Receiver | 180 |
| 3.5.1 | Resonant Rydberg Electrometer/Receiver Sensitivity & SNR | 180 |
| 3.5.2 | Converting to Power Sensitivity | 182 |
| 3.5.3 | Improving the Sensitivity of the Rydberg Receiver | 185 |

| | | |
|---------|--|-----|
| 3.5.3.1 | Increasing Sensing Volume | 188 |
| 3.5.3.2 | High QE Probing | 190 |
| 3.5.3.3 | Doppler-Broadening | 191 |
| 3.5.3.4 | Estimated Improvement to Rydberg Electrometer Sensitivity | 192 |
| 3.6 | Conclusions | 194 |
| A | <code>labscript</code> Experimental Control | 196 |
| A.1 | Adoption | 198 |
| A.2 | Hardware Augmentation | 198 |
| A.2.1 | AC-Line Trigger Box | 199 |
| A.2.2 | Novatech Synchronous Trigger Conversion | 200 |
| A.3 | Software Augmentation | 201 |
| A.3.1 | VISA Devices– <code>VISA.py</code> | 202 |
| A.3.1.1 | Tektronix Oscilloscopes– <code>TekScope.py</code> | 203 |
| A.3.1.2 | Keysight Oscilloscopes– <code>KeysightXXXXScope.py</code> | 204 |
| A.3.1.3 | Signal Generators | 205 |
| A.3.1.4 | Stanford Research SR865 Lock-In Amplifier– <code>SR865.py</code> | 207 |
| A.3.2 | Novatech 409B Series Boards | 207 |
| A.3.3 | Camera Servers | 208 |
| A.3.3.1 | Basler Pylon SDK | 208 |
| A.3.3.2 | Princeton Instruments Pcam SDK | 210 |
| A.3.3.3 | Andor 3 SDK | 210 |
| B | Computational Packages & Example Source Code | 212 |
| B.1 | Atomic Density Matrix Package | 212 |
| B.1.1 | NMOR Numerical Simulations | 213 |
| B.1.2 | Perturbation Model Calculation | 220 |
| B.2 | Alkali Rydberg Calculator | 229 |
| B.3 | Rydberg EIT with <i>Mathematica</i> | 236 |
| | Bibliography | 242 |

List of Tables

| | | |
|-----|---|-----|
| 2.1 | Summary of Figure 2.16 | 75 |
| 3.1 | Doppler-Averaging Parameters and EIT Conditions | 117 |

List of Figures

| | | |
|------|---|-----|
| 2.1 | NMOR Example Trace | 5 |
| 2.2 | NMOR Example Trace with “Twist” | 9 |
| 2.3 | NMOR Level Diagrams | 11 |
| 2.4 | Linear Faraday Effect | 14 |
| 2.5 | Example EIA | 18 |
| 2.6 | Example Polarization Moments | 45 |
| 2.7 | Linear Polarizer Model for NMOR | 52 |
| 2.8 | AOC Model for NMOR | 55 |
| 2.9 | 5-Step AOC Model for NMOR | 58 |
| 2.10 | Axes in Perturbation Models | 60 |
| 2.11 | Orientation due to Alignment in Lab Units | 68 |
| 2.12 | Orientation due to Alignment along and perpendicular to \vec{B}_{tot} | 69 |
| 2.13 | “Twist” Polarization Moments | 70 |
| 2.14 | 5-Step Model with Arbitrary Transverse Field | 72 |
| 2.15 | NMOR simulation versus linear polarization angle | 73 |
| 2.16 | Shift of “Twist” versus Transverse Field Orientation | 74 |
| 2.17 | Shift of “Twist” versus Stark Shift | 77 |
| 2.18 | NMOR Experimental Setup | 80 |
| 2.19 | Example Free-Induction-Decays | 81 |
| 2.20 | Example of FID Calibration Fits | 83 |
| 2.21 | FID Measurement of 60 Hz noise | 85 |
| 2.22 | FID Measurement in the presence of Gradients | 86 |
| 2.23 | “Twist” versus Transverse Field Magnitude | 90 |
| 2.24 | “Twist” Dependence on Light Polarization Angle | 91 |
| 2.25 | “Twist” Dependence on Light Ellipticity | 93 |
| 2.26 | “Twist” Dependence on Probe Power | 95 |
| 2.27 | Example CCD Polarimeter Image | 97 |
| 2.28 | NMOR Measurements in Atomic Cloud | 98 |
| 3.1 | ^{85}Rb States Manifold | 107 |
| 3.2 | ^{85}Rb $ nD_{5/2}\rangle$ Natural Lifetimes | 109 |
| 3.3 | Example Rydberg EIT on Doppler Background | 112 |
| 3.4 | Doppler-Averaged Linewidths | 116 |
| 3.5 | Transit Time versus Beam Waist | 119 |
| 3.6 | Black-Body Photon Density versus Frequency at Room Temperature | 120 |

| | | |
|------|--|-----|
| 3.7 | $^{85}\text{Rb } nD_{5/2}\rangle$ Rydberg State Decay Rates Including Black-Body Ra- diation | 121 |
| 3.8 | $^{85}\text{Rb } nD_{5/2}\rangle \rightarrow (n+1)P_{3/2}\rangle$ Transitions | 123 |
| 3.9 | Structure of PSK Communication Signal | 129 |
| 3.10 | Terrestrial Atmospheric Noise Temperatures | 134 |
| 3.11 | Resonant Digital Communications Setup | 138 |
| 3.12 | Rydberg EIT, AT, & Modulated Signal Comparison | 141 |
| 3.13 | Signal Dependence on Ω_μ | 142 |
| 3.14 | PSK Demonstration | 144 |
| 3.15 | Example Timetrace | 145 |
| 3.16 | Probe Transmission Rise & Fall Times | 147 |
| 3.17 | Fall Time Models Comparison | 151 |
| 3.18 | Channel Capacity of Resonant Electrometer | 153 |
| 3.19 | Rydberg-Classical Receiver Comparison | 156 |
| 3.20 | Off-Resonant Electrometry Configuration | 162 |
| 3.21 | Example DC Stark Splitting | 163 |
| 3.22 | Example DC Electrometry Timetrace & SNR Measurement | 165 |
| 3.23 | Measured Channel Capacity in the Electrically Small Regime | 166 |
| 3.24 | Capacity Comparison to Chu-limited Antenna | 168 |
| 3.25 | Quantum Limited Data Communication | 170 |
| 3.26 | Shot Noise in EIT | 174 |
| 3.27 | Off-Resonant Receiver Quantum Limited Performance | 175 |
| 3.28 | Resonant Receiver Quantum Limited Performance | 179 |
| A.1 | AC-Trigger Wiring Diagram | 200 |

List of Abbreviations

| | |
|-------|---|
| AC | Alternating Current |
| ADM | Atomic Density Matrix |
| AMPS | Angular Momentum Probability Surface |
| AOC | Alignment-to-Orientation Conversion |
| ARL | Army Research Laboratory |
| CCD | Charge-Coupled Device |
| DAQ | Digital Acquisition |
| DC | Direct Current |
| DDS | Direct Digital Synthesis |
| EIA | Electromagnetically Induced Absorption |
| EIT | Electromagnetically Induced Transparency |
| ESA | Electrically Small Antenna(s) |
| FID | Free Induction Decay |
| MOT | Magneto-Optical Trap |
| MW | Microwave |
| NMOR | Non-linear Magneto-Optical Rotation |
| ORAU | Oak Ridge Associated Universities |
| ORISE | Oak Ridge Institute for Science and Education |
| OSD | Office of the Secretary of Defense |
| PSK | Phase Shift Keying |
| PSN | Photon Shot Noise |
| QSEP | Quantum Science and Engineering Program |
| RF | Radio Frequency |
| SDK | Software Development Kit |
| SQL | Standard Quantum Limit |
| VISA | Virtual Instrument Software Architecture |

Chapter 1: Dissertation Outline

This dissertation covers two separate projects that employ neutral rubidium atom vapors as sensors of electro-magnetic fields. Since neutral atom ensembles are constituted of identical atoms, these vapors provide a platform of many identical quantum systems that behave as identical detectors of external fields. Both projects employ probing techniques that excite coherent states in the atomic ensembles that are uniquely sensitive to the externally applied fields while also providing optical readout. One chapter is dedicated to each project, with both chapters being self-contained works.

In Chapter 2, I describe the observation of new “twists” in Nonlinear Magneto-Optical Rotation (NMOR) signals. NMOR is a well-known technique often used in single-axis atomic magnetometers. It employs coherences between ground states of alkali atoms to create atomic polarizations that can be extremely sensitive to perturbations from magnetic fields. Typically great care is taken to ensure magnetic fields transverse to the magnetometer axis are minimized to avoid complications from mis-alignment of the quantization axis relative to the sensing axis. However, in systems where both optical access and complete magnetic control is difficult to achieve, these complicating fields must be considered. Here I explore “twists” in the

typical NMOR signal due to transverse fields as a method to characterize transverse field orientation, strengths, and gradients within an operating, compact cold-atom system. I also present numerical and analytical models to ascertain the underlying physical phenomenon responsible for these “twists.”

In Chapter 3, I introduce the Rydberg receiver, an atom-based receiver of classical, digital information. This receiver is based on Rydberg atoms in a warm vapor cell which has been previously shown to be a precision sensor of electric fields. In particular, Rydberg states have very strong sensitivity to RF electric fields ranging from quasi-DC to 1 THz. Using Electromagnetically Induced Transparency (EIT), coherences between the Rydberg state and a probing ground state allows for record sensitivity when measuring RF electric field amplitudes. In this work I apply this exquisite electric field sensor to the realm of digital communication as a receiver, where information is communicated using modulated RF carriers. I demonstrate phase-sensitive detection of the modulation on the carrier and characterize the Rydberg receiver bandwidth and sensitivity. I also derive the Standard Quantum Limit (SQL) for channel capacity, or max potential data rate, and demonstrate that the receiver performance scales with this limit for an effective atom number of $N_{eff} \approx 60$.

Also included are two appendices. Appendix A describes my implementation of the open-source `labscript` experiment control system. In particular it highlights custom code I wrote to control hardware unique to the lab in which I worked. Appendix B includes example source code used for some of the calculations I undertook. This code is included so that these calculations might be easier to reproduce by the interested reader.

1.1 Contributions

The work described in this dissertation was not performed in isolation; I was part of a group of researchers that included Fredrik Fatemi, Paul Kunz, Kevin Cox, and (more recently) Zachary Castillo. Throughout this dissertation I will occasionally use the pronoun “we” to reflect this reality, where appropriate.

While I was involved in all aspects of the presented work, I was the primary contributor to the following aspects.

In Chapter 2: data collection and analysis of the NMOR data, the numerical modeling of the NMOR data, and the extension of the perturbation model (outlined for us initially by Dr. Simon Rochester of Rochester Scientific, LLC) to arbitrary magnetic field angles.

In Chapter 3: building the Rydberg apparatus from scratch, initiating the idea of using a Rydberg electrometer to receive digital communication, data collection and most of the subsequent analysis, as well as the modeling (excluding the quantum noise model which Kevin derived).

I was also responsible for programming-related tasks, including standing up the `labscript` experiment control system for all experiments in the neutral atom lab.

Portions of this dissertation are drawn from previously published works of which I am a co-author. [1–3] I have also co-authored two related works, [4, 5] which are not directly covered in this dissertation.

Chapter 2: Twists in Nonlinear Magneto-Optical Rotation

Nonlinear magneto-optic rotation (NMOR) has been extensively studied, particularly as a tool for sensitive magnetometry. [6, 7] In typical NMOR experiments such as that shown in Fig. 2.1, a linearly polarized optical beam simultaneously pumps and probes atoms as a magnetic field (collinear to the beam propagation axis) is swept through zero. The polarization of the transmitted optical beam follows a dispersive-shaped resonance centered on the magnetic zero. For sufficiently small fields, the amount of polarization rotation is proportional to the magnetic field magnitude. This resonance can always be used to determine the field zero accurately and the linear slope can be used to accurately measure small fields as well. The sensitivity of this measurement depends on the slope of the resonance which depends on the signal-to-noise ratio of the polarization measurement and the resonance width. In general, these resonances can be much narrower (≤ 1 Hz [8]) than typical optical atomic resonances as they rely on the spin-coherence lifetime of the atoms' ground state, which is long-lived.

If magnetic fields transverse to the optical beam path are present, the typical

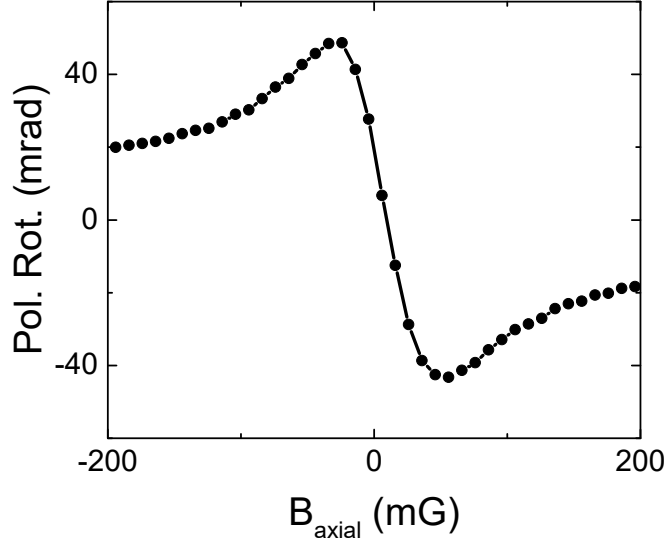


Figure 2.1: Example NMOR data showing the dispersive-resonance of the polarization rotation as a function of axial magnetic field magnitude.

dispersive shape of the NMOR signal can be greatly distorted. These distortions include both broadening and even sub-features, both of which limit the sensitivity. As a result, most NMOR-based magnetometers are used in highly shielded environments to limit these corrupting fields.

In this chapter I will discuss the application of NMOR magnetometry in an un-shielded environment where these transverse fields cannot be ignored. In particular I discuss our observation of a particular sub-feature due to transverse fields that has been dubbed the “twist” in the literature where it was not extensively studied. I demonstrate that this “twist” can be used to accurately determine the transverse magnetic field amplitude and direction. Specifically, I show that the width of the “twist” is proportional to the transverse field amplitude. I also show that standard numerical models accurately predict this behavior. I also develop an analytical model that describes the underlying physics of this phenomenon and

confirms the observed linear relationship. Taken together, the “twist” allows for an NMOR magnetometer that can accurately characterize magnetic fields with arbitrary orientation. Finally I demonstrate that a simple modification of the polarization measurement can lead to simultaneous sensitivity to transverse magnetic gradients.

The experimental portions of this chapter are based on a previously published work. [\[1\]](#)

Chapter Contents

| | | |
|---------|--|-----|
| 2.1 | Introduction | 8 |
| 2.1.1 | Observing NMOR | 10 |
| 2.1.2 | Relation to EIT & EIA | 15 |
| 2.2 | Formalism Primer | 20 |
| 2.2.1 | The Density Matrix | 22 |
| 2.2.2 | Defining the Hamiltonian | 25 |
| 2.2.3 | Dephasing Mechanisms | 30 |
| 2.2.4 | The Lindblad Equation | 33 |
| 2.2.5 | Observables Derivation | 35 |
| 2.2.6 | The Polarization Moments Basis | 40 |
| 2.2.6.1 | Changing Bases | 40 |
| 2.2.6.2 | Orientation vs. Alignment | 42 |
| 2.2.7 | Frame Rotations | 47 |
| 2.3 | NMOR Models | 51 |
| 2.3.1 | Single-Axis Models | 51 |
| 2.3.1.1 | Low Probe Intensity – Linear Polarizer Model | 51 |
| 2.3.1.2 | High Probe Intensity – AOC Model | 54 |
| 2.3.2 | Multi-Axis Perturbation Model | 56 |
| 2.3.2.1 | 2-Axis Solution | 59 |
| | Step 1 | 62 |
| | Step 2 | 64 |
| | Step 3 | 65 |
| | Step 4 | 66 |
| | Step 5 | 66 |
| 2.3.2.2 | 3-Axis Solution | 71 |
| 2.4 | Experimental Characterization of the “Twist” | 79 |
| 2.4.1 | Experimental Configuration | 79 |
| 2.4.1.1 | Magnetic Coil Calibration | 81 |
| 2.4.1.2 | NMOR Measurement | 86 |
| 2.4.1.3 | Experiment – Numerical Simulation Correspondence | 88 |
| 2.4.2 | “Twist” Dependence on Magnetic Fields | 89 |
| 2.4.2.1 | Magnitude | 89 |
| 2.4.2.2 | Orientation | 91 |
| 2.4.3 | “Twist” Dependence on Probe Field | 92 |
| 2.4.3.1 | Ellipticity | 93 |
| 2.4.3.2 | Optical Intensity | 94 |
| 2.4.4 | Measuring Magnetic Gradients with the “Twist” | 96 |
| 2.5 | Conclusion | 100 |

2.1 Introduction

An example NMOR trace showing the sub-feature that will be extensively studied is shown in Fig. 2.2. The sub-feature takes a similar dispersive form to the overall NMOR resonance, though with opposite slope. A similar nested coherence was observed in warm vapor, [8] where it was termed a “twist.” It appears when a transverse magnetic field, parallel to the probing optical beam’s linear polarization, is present with a magnitude comparable to the width of the NMOR feature. In this prior work it was ascribed to couplings among multiple hyperfine levels, which are unresolved due to Doppler broadening in the warm vapor, causing multiple atomic polarization subsystems. These subsystems derive from independent velocity classes of atoms that were optically pumped to different magnetic sublevels depending on the excited hyperfine state that Doppler-shifted into resonance with the light. These polarization subsystems can be orthogonal to each other resulting in optical polarization rotation towards opposite directions depending on which subsystem dominates.

Another similar “twist” feature in warm vapor was reported in double-resonance magneto-optic experiments, [9–11] where a combination of resonant optical and radio-frequency (RF) fields were used. Zigdon *et al.* thoroughly explained the mechanism behind their “twist” through the evolution of the atomic *alignment* tensor (the rank-*two* tensor components in the polarization moment series expansion [12]). They described how the atomic alignment transforms between two distinct polariza-

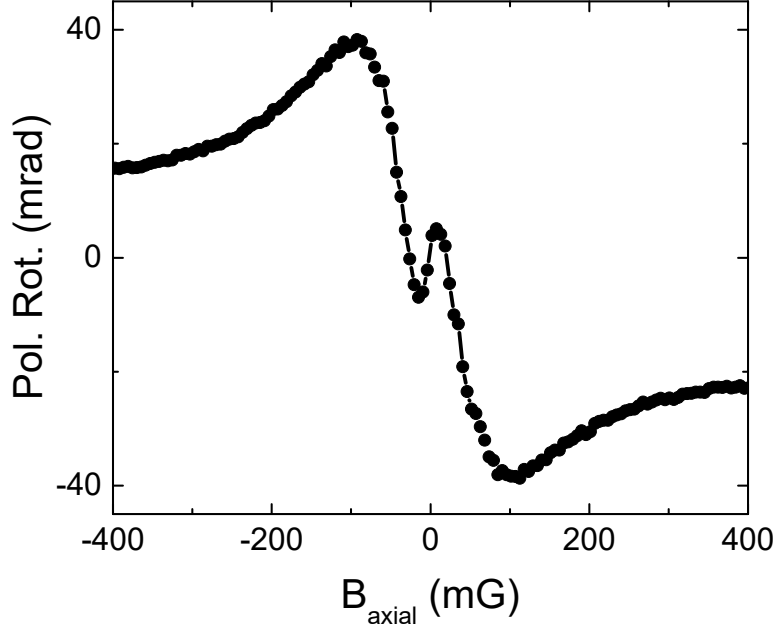


Figure 2.2: Typical NMOR data showing a “twist” as the axial magnetic field is swept through zero. This data was taken with a $10.6\mu\text{W}$ probe beam of 1 mm diameter that is detuned 27 MHz from the zero-field atomic resonance. A static transverse field of 55 mG is applied parallel to the polarization vector.

tion moments in the series expansion, which have perpendicular axes of symmetry, due to the averaging effect of the off-axis magnetic field. These two different axes of symmetry rotate the light’s polarization in opposite directions resulting in their observed “twist.”

Here, I discuss cold atoms in which the excited hyperfine levels are well resolved and individually addressable, which suppresses the complication of multiple excited state hyperfine levels. This excludes the “twist” mechanism described in [8], where competition among excited hyperfine levels was responsible. The mechanism behind the “twist” in our system is also distinct from that of the double-resonance experiments in that, aside from the lack of RF fields, ours is dominated by atomic *orientation* (the rank-*one* tensor components in the polarization moment series ex-

pansion). Acting alone, linearly polarized light can only induce *alignment* because the electric field has a preferred axis but not a preferred direction or orientation. In other words, averaged over a wavelength the light’s electric field points equally in opposite directions along its polarization axis, thus no orientation. But when a magnetic field is present and directed at some non-perpendicular angle to the optical polarization, then alignment-to-orientation conversion (AOC) occurs [13]. The AOC mechanism relies on AC Stark shifts from the probe light, and rotation due to AOC will dominate over that of alignment when the Stark shifts ($\sim \Omega_R^2/\Delta_p$) exceed the optical pumping rate ($\sim \Gamma\Omega_R^2/\Delta_p^2$). Using a detuned probe with optical intensities near saturation ensures the system is in the AOC-dominated regime.

In this chapter I outline the experimental conditions necessary to observe the NMOR resonances discussed, the theoretical formalism used for modeling the systems presented, simplified models to describe the underlying physical mechanisms, and finally the experimental characterization of the “twist.”

2.1.1 Observing NMOR

NMOR itself is the result of coherent interactions between an optical probing field and the atomic sublevels of the hyperfine transition being probed. An intuitive way to picture this interaction is to consider NMOR as the result of a coherent interaction of an atom with multiple, linearly-polarized probe photons. For concreteness I will consider a $F = 1 \rightarrow F' = 0$ hyperfine transition, as shown in Fig. 2.3(b). The atom is initially un-polarized (*i.e.* has equal probability for being in any of

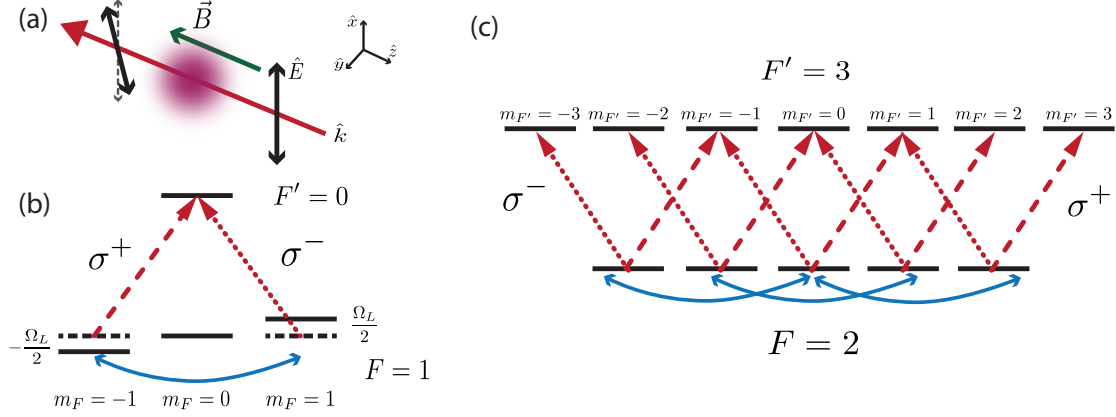


Figure 2.3: (a) Basic Configuration for NMOR. Light propagating along \hat{z} with linear polarization along \hat{x} transmits through an atomic ensemble. An axial magnetic field \vec{B} causes polarization rotation. (b) $F = 1 \rightarrow F' = 0$ transition used in examples and theory models. Linearly polarized light, broken into circular components, couples $|m_F - m_{F'}| = 1$ sublevels. Coherence between the $m_F = 1$ and $m_F = -1$ sublevels polarizes the atom. These same levels are Zeeman shifted by $\Omega_L/2$, causing rotation of the atomic polarization. (c) $F = 2 \rightarrow F' = 3$ transition used in full numeric models and experimental measurements. The circular components allow for multiple coherences in the ground state that all contribute to the NMOR signal.

the ground states) when the atom absorbs a linearly-polarized probe photon. This polarizes the atom parallel to the linear polarization of the light. The atomic polarization precesses when an axial magnetic field is present, rotating the polarization axis which acts as a polarizer for a second probe photon, effectively rotating the transmitted light polarization (see Fig. 2.3(a)).

The tools necessary to observe NMOR are fairly simple. I first require an atomic sample with magnetically sensitive hyperfine sublevels. This work employs ^{87}Rb atoms that have been laser-cooled using a Magneto-Optical Trap (MOT) to a temperature of $\sim 100 \mu\text{K}$. Rubidium has a multitude of optical hyperfine transitions within its first excited state, but the focus is on the $F = 2 \rightarrow F' = 3$ cooling transition, see Fig. 2.3(c). Since this transition is closed,¹ it gives high signal relative

¹*i.e.* by electric dipole transition selection rules, atoms that decay from $F' = 3$ return to the

to the other potential transitions when performing the optical measurement. This transition has 12 magnetic sublevels. As a result, theoretical modeling quickly becomes cumbersome. In this work I use numerical modeling of the $F = 2 \rightarrow F' = 3$ system to match measured data to theory and use a simpler $F = 1 \rightarrow F' = 0$ transition for analytical models. Qualitatively the two systems are similar enough that intuition derived from the simpler system can translate to the real experimental system.

I also require an axis of optical access that allows one to measure transmitted light through the atomic sample. The optical field should to be linearly polarized and have an intensity on par with saturation for the atomic transition to be interrogated. In a cold atom system, one should also detune from atomic resonance in order to avoid heating/pushing of the cooled atoms via scattering events with the probing light.

Finally, I require a magnetic environment where the applied fields cause Zeeman shifts on order with the natural linewidth of the probing transition. Since NMOR is a coherent effect between the magnetic sublevels of the hyperfine levels being probed, stray magnetic fields that split these levels beyond the natural linewidth prevent any such coherent effects. While this makes NMOR a highly sensitive method for finding magnetic field zeros, it also proves a fairly stringent requirement limiting maximum allowed magnetic fields strengths to the sub-Gauss level. Even Earth's magnetic field of 500 mG can be significant enough to make

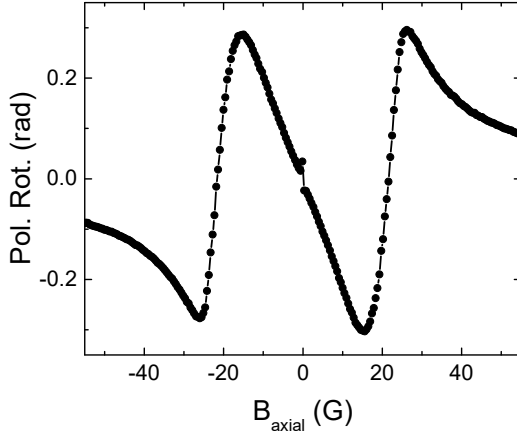
$F = 2$ ground state which keeps them within the system. In reality a weak quadrupole transition also exists so a small fraction decay to $F = 1$, which is why the MOT itself requires some repump light to return these atoms to the cycling transition.

observation of NMOR difficult, necessitating shielding or active field cancellation.

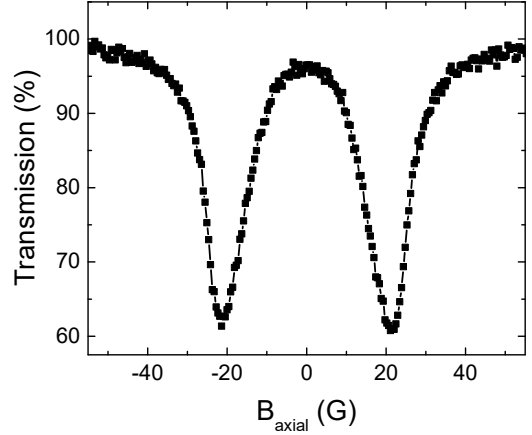
Furthermore, the cold atom system used to demonstrate the following results requires significantly stronger magnetic fields in order to initially trap the cooled atoms and is designed to be compact. As a result, complete, arbitrary control of the magnetic field across the entire sample is difficult and even complete cancellation of the background fields below the measurement resolution was not possible. In fact, it was the characterization of these non-ideal magnetic field conditions that originally motivated this work.

Efficient cooling and capture of a large number of atoms in a MOT generally requires minimized stray magnetic fields and accurate control of the applied trapping fields, often derived from nearby Helmholtz coils. NMOR allows for highly accurate measurement of field zeros and even some coil calibration, but only if the magnetic field is small enough to allow for NMOR to be present. This is typically not the case for a new, uncharacterized system, so other less sensitive measures of magnetic field are required when initially setting up a system.

One such method that requires no modification of the NMOR experiment is to measure the linear Faraday effect, as shown in Fig. 2.4(a). The linear Faraday effect is the lowest order magneto-optical rotation signal and is the result of circular birefringence (*i.e.* left and right circular polarizations of light have different interactions). When light is resonant with a hyperfine transition, a single dispersion resonance is observed in the polarization rotation versus axial magnetic field strength as the shifting magnetic levels absorb either left or right circularly polarized light more strongly. When performing this measurement with cold atoms,



(a) Circular Birefringence causes the linear Faraday effect near the two resonances. At each resonance, one circular component of the linear light field interacts causing an overall rotation of the light polarization angle.



(b) When one of the circular components is resonant, the overall absorption of the light field is increased, resulting in reduced transmission at each resonance. Data is normalized to the total probe transmission.

Figure 2.4: Linear polarization rotation and absorption from the $F = 2 \rightarrow F' = 3$ hyperfine transition in ^{87}Rb . Here the probe light is detuned from the atomic resonance by $\sim 5\Gamma$. Linear resonances occur when the axial magnetic field causes the $|F = 2, m_F = \pm 2\rangle \rightarrow |F' = 3, m_{F'} = \pm 3\rangle$ transitions to be resonant. Note the visible NMOR near zero magnetic field. There is also EIA present in the transmission spectrum, though with significantly reduced contrast.

the probing field must be detuned significantly from resonance to avoid scattering events that heat the atoms. The result is two resonances symmetrically split from atomic resonance, shifted from zero by the detuning. These resonances occur when the axial magnetic field shifts a pair of sublevels into resonance with the detuned light. These levels will only be able to absorb left or right circularly polarized light, leading to effective rotation of the linear polarization axis as well as significant absorption. This can be seen in the corresponding transmission, shown in Fig. 2.4(b). If the optical detuning is well known, this splitting of resonances provides a reliable initial calibration of the axial field strength since the Zeeman shifts are accurately known.

Figure 2.4(a) also shows NMOR relative to this linear effect. It is centered at zero axial field and has a significantly smaller contrast. This trace was taken without any transverse field applied; applying a transverse field reduces the contrast and eliminates NMOR entirely when the field is strong enough. Again, this highlights the need for some initial level of magnetic field control in order to see NMOR which allows the techniques outlined below to enact very precise control and calibration of magnetic fields.

2.1.2 Relation to EIT & EIA

Systems that exhibit NMOR also exhibit non-linear absorptive effects in much the same way systems that exhibit linear polarization rotation like the linear Faraday effect also exhibit absorptive effects (see Fig. 2.4(b)). Nonlinear absorptive ef-

fects can be divided into two sub-classes: Electromagnetically Induced Transparency (EIT) and Electromagnetically Induced Absorption (EIA).

EIT occurs when the generated atomic coherence responsible for NMOR forms an optical dark state. This occurs when the atomic polarization of the ground state takes the form of a superposition state that is not coupled to the optical transition. This results in a transparency window where the material absorbs less light. This can be seen by inspecting the eigenstates of the $F = 1 \rightarrow F' = 0$ Hamiltonian, the derivation of which is explained in more detail below.

A simplified version of the Hamiltonian in the Zeeman basis is

$$\mathcal{H} = \hbar \begin{pmatrix} -\Omega_L & 0 & 0 & \Omega_p \\ 0 & 0 & 0 & 0 \\ 0 & 0 & \Omega_L & -\Omega_p \\ \Omega_p & 0 & -\Omega_p & 0 \end{pmatrix} \quad (2.1)$$

where Ω_L is the Larmor frequency of an axial magnetic field and Ω_p is the Rabi frequency of the resonant probing light. Assuming $\Omega_L \ll \Omega_p$, the eigenstates of this Hamiltonian are

$$\vec{e}_1 = (0, 1, 0, 0) \quad (2.2)$$

$$\vec{e}_2 = (1, 0, 1, \Omega_L/\Omega_p) \quad (2.3)$$

$$\vec{e}_3 = \left(1/\sqrt{2} + \Omega_L/2\Omega_p, 0, -1/\sqrt{2} + \Omega_L/2\Omega_p, 1 \right) \quad (2.4)$$

$$\vec{e}_4 = \left(1/\sqrt{2} - \Omega_L/2\Omega_p, 0, -1/\sqrt{2} - \Omega_L/2\Omega_p, 1 \right) \quad (2.5)$$

to first order in Ω_L .

The first state \vec{e}_1 is the $|F = 1, m_F = 0\rangle$ incoherent dark state which is not coupled to the circular components of the probing light. The second state \vec{e}_2 also does not couple to the excited state when the magnetic field is zero, yet has population in both $|F = 1, m_F = \pm 1\rangle$ stretch states that would nominally be coupled to the light field. This state is the coherent dark state where optical pumping results in a coherent superposition of ground states. Atoms optically pumped into this state are polarized and sensitive to the magnetic field (leading to NMOR) while also having increased transparency to the probe field overall.

The final two states \vec{e}_3 and \vec{e}_4 are also superposition states, but these are strongly coupled to the excited state for all magnetic fields making them bright coherent states. If F_g and F_e are non-zero it is possible to optically pump into such bright states. [14] The process involves creating atomic coherences in the excited state and having those coherences spontaneously decay to the ground state. [15] In general, NMOR systems with $F_{g,e} \neq 0$ can, in principle, exhibit both EIT and EIA as both optical pumping processes are possible. EIA is the dominant factor when $F_e > F_g$, [16] assuming the excited state coherence lifetime is not significantly reduced by a secondary dephasing process. [14] Furthermore, the optical pumping rate for the EIA coherence tends to be smaller than that for EIT, resulting in absorptive resonances with smaller contrast in comparison.

Since the experimental system uses the $F = 2 \rightarrow F' = 3$ hyperfine transition, EIA is expected. Figure 2.5 shows the near-zero axial magnetic field portion of the transmission trace from Fig. 2.4(b). Near zero magnetic field there appears to be

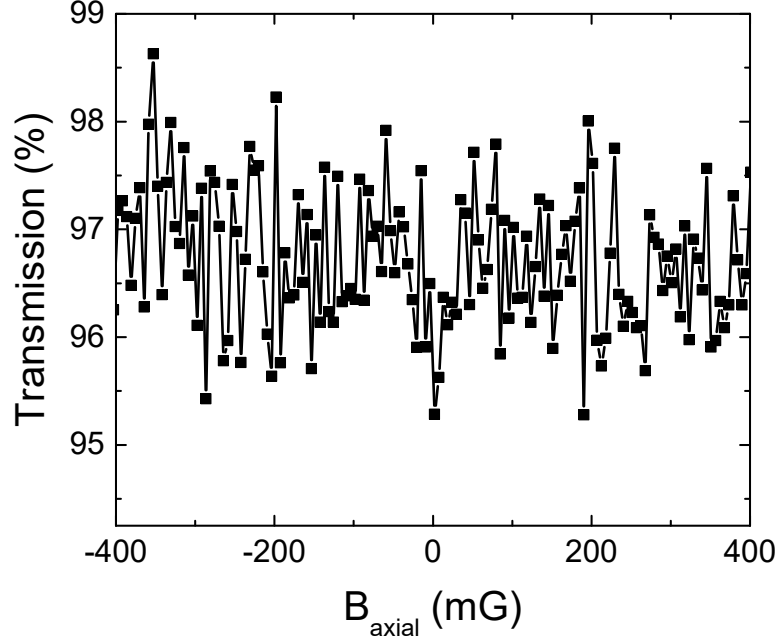


Figure 2.5: Probe transmission data corresponding to Fig. 2.1. The lines simply connect the data points in order to guide the eye. Noisy, low-contrast EIA is observed near $B_{axial} = 0$.

decreased transmission (increased absorption) that could correspond to EIA. It is difficult to be certain since the dip in transmission is on the order of the noise. A significant portion of this noise is due to amplitude drifts in the probe from shot-to-shot, as described in Section 2.4. In any case, I am confident that this signal represents EIA as it has the correct signatures, including small contrast.

While this chapter focuses on NMOR, being aware of these other coherent effects can be beneficial. A number of underlying physical processes that lead to NMOR are simpler to visualize in terms of the absorptive effects. Conversion between NMOR and EIT/EIA signals can be done via Kramers-Krönigs relations due to the underlying dependence of both absorptive and refractive effects on the same complex quantity, the susceptibility tensor. [17] While not generally true for higher-

order non-linear interactions, the Kramers-Krönigs relations often reduce to a simple derivative relationship (*i.e.* one is proportional to the derivative of the other). By considering both manifestations of the non-linear interaction, deeper understanding of the underlying physical mechanism in the interaction is available.

Finally, it is interesting to note that the EIA shown in Fig. 2.5 is the absorptive resonance that corresponds to the NMOR of Fig. 2.1 (both plots derive from the same measurements). While the absorptive effect is small with low signal-to-noise ratio, the refractive effect has a much larger signal-to-noise ratio. This is partly due to the typical signal reduction of EIA described above. However there is also common-mode noise reduction for polarization measurements since two photo-detector signals are subtracted, effectively normalizing the measurement to the total power. This significantly reduces amplitude noise allowing for much more precise measurements of the atomic coherence.

2.2 Formalism Primer

In order to better understand the experimental observations and determine the physical origin of the “twist,” I must model the atomic system. In this work I will pursue two models based on the density matrix formalism: (1) a full numerical model of the $F = 2 \rightarrow F' = 3$ transition in order to capture the complete dynamics of the experimental system and attempt extraction of unknown experimental parameters for characterization purposes; (2) an analytical model derived using perturbative solutions of the simpler $F = 1 \rightarrow F' = 0$ transition to establish the physical origin of the “twist.”

In this section I will briefly outline the density matrix formalism and use it to answer some basic questions about the physical phenomena of interest. This treatment closely follows that developed by Simon Rochester *et.al.* to model NMOR in warm vapors. [12, 18–20] The goal of this section is not to re-derive the formalism but rather familiarize the reader with the symbols, terms, and the results thereof.

I begin with the standard equation of nonlinear optics that relates the average atomic polarization to the applied electric field via a constant known as the susceptibility tensor $\overleftrightarrow{\chi}$:

$$\vec{P} = \epsilon_0 \overleftrightarrow{\chi} \cdot \vec{E}. \quad (2.6)$$

This tensor can be approximated to arbitrary order by performing a Taylor expan-

sion in the electric field to produce

$$\vec{P} = \epsilon_0 \overleftrightarrow{\chi} \cdot \vec{E} \simeq \epsilon_0 \left(\overleftrightarrow{\chi}^{(1)} \cdot \vec{E} + \overleftrightarrow{\chi}^{(2)} \cdot \vec{E}^2 + \overleftrightarrow{\chi}^{(3)} \cdot \vec{E}^3 + \dots \right), \quad (2.7)$$

where the successive susceptibility tensors correspond to nonlinear processes of increasing order in the electric field. Within this framework different nonlinear interactions can be categorized and solved independently; *e.g.* $\overleftrightarrow{\chi}^{(1)}$ dictates the processes of linear refraction and absorption, $\overleftrightarrow{\chi}^{(2)}$ the second-order effects such as second harmonic and sum/difference frequency generation, and $\overleftrightarrow{\chi}^{(3)}$ the third-order effects such as two-photon absorption, four-wave mixing, and stimulated Raman scattering. [17, 21]

Following the typical nonlinear optics formalism I could, in principle, try to use the expansion in Eq. 2.7 to write down a set of coupled differential equations for the slowly varying electric field amplitudes that would allow me to solve for changes in the electric fields due to the nonlinear material. For nonlinear magneto-optics this approach is less desirable since it works best far off-resonance, which limits the utility; and assumes that the susceptibility is fixed and known, which is not always the case for atomic vapor ensembles.

Instead a more direct approach is to use Eq. 2.6 and allow the susceptibility to depend on the electric and magnetic fields. The average atomic polarization \vec{P} can be determined via the density matrix formalism as a function of the probe light and magnetic field which can then be related to the initial probe field using the wave

equation for polarizable media:

$$\left(k^2 + \frac{d^2}{dz^2}\right) \vec{E} = -4\pi k^2 \vec{P}. \quad (2.8)$$

It is this process that will be outlined in the following sections.

Note that much of this section is pedagogical in nature and covers common theoretical elements in atomic physics. As such, much of it can be skipped by an experienced atomic physicist. The exception is Section 2.2.6 which covers the polarization moment basis for representing polarized atomic states. This basis is not as commonly known to the general atomic physicist and is critical to the perturbative models I developed for describing the origins of the “twist.” It is suggested this particular subsection be read in its entirety.

2.2.1 The Density Matrix

The description of a pure state of a quantum system is given by its state vector, known as a *ket*. This vector spans the Hilbert space of possible quantum states of the system. The density matrix of any quantum mechanical state $|\psi\rangle$ can be written

$$\rho = |\psi\rangle \langle\psi| \quad (2.9)$$

which produces a matrix of probabilities and couplings that describes the state. The diagonal elements represent probabilities for measuring each basis state of the Hilbert space. The off-diagonal elements represent coherences between these basis

states.

As an example, consider an atomic system with two hyperfine levels $F = 1$ and $F' = 0$. The general density matrix is written as

$$\rho = \begin{pmatrix} \rho_{(1,1),(1,1)} & \rho_{(1,1),(1,0)} & \rho_{(1,1),(1,-1)} & \rho_{(1,1),(2,0)} \\ \rho_{(1,0),(1,1)} & \rho_{(1,0),(1,0)} & \rho_{(1,0),(1,-1)} & \rho_{(1,0),(2,0)} \\ \rho_{(1,-1),(1,1)} & \rho_{(1,-1),(1,0)} & \rho_{(1,-1),(1,-1)} & \rho_{(1,-1),(2,0)} \\ \rho_{(2,0),(1,1)} & \rho_{(2,0),(1,0)} & \rho_{(2,0),(1,-1)} & \rho_{(2,0),(2,0)} \end{pmatrix} \quad (2.10)$$

where each diagonal element represents a state population and each off-diagonal element $\rho_{(F_1, m_{F_1}), (F_2, m_{F_2})}$ represents a coherence between the $|F_1, m_{F_1}\rangle$ and $|F_2, m_{F_2}\rangle$ states. This matrix can be interpreted to represent the state of a single atom or the average quantum mechanical state of an ensemble of atoms.

To simplify the discussion (which the interested reader can find in [22]), I provide three specific density matrices for some common ensemble states we will see in this work that illustrates how to interpret a density matrix.

First is an unpolarized ensemble of atoms in the ground state.

$$\rho = \frac{1}{3} \begin{pmatrix} 1 & 0 & 0 & 0 \\ 0 & 1 & 0 & 0 \\ 0 & 0 & 1 & 0 \\ 0 & 0 & 0 & 0 \end{pmatrix} \quad (2.11)$$

If you were to measure the state of an atom in this ensemble, you would find it to

be in any of the three ground states with equal probability of $1/3$.² By extension, if you were to measure the state of every atom in the ensemble, you would find $1/3$ of the total atom number in each state. Note that the trace of the density matrix must always be equal to 1 in order to preserve atom number in the system.

The next example describes a polarized atomic sample.

$$\rho = \frac{1}{2} \begin{pmatrix} 1 & 0 & 0 & 0 \\ 0 & 0 & 0 & 0 \\ 0 & 0 & 1 & 0 \\ 0 & 0 & 0 & 0 \end{pmatrix} \quad (2.12)$$

Here the atoms are all either in the $|F = 1, m_F = 1\rangle$ or $|F = 1, m_F = -1\rangle$ states. Measuring the states of individual atoms in this ensemble, you would find no atoms in the $m_F = 0$ ground state.

The final example shows an atomic ensemble that has a light field applied to excite atoms to the excited state $|0, 0\rangle$.

$$\rho = \frac{1}{6} \begin{pmatrix} 0 & 0 & 0 & 0.5 \\ 0 & 5 & 0 & 0 \\ 0 & 0 & 0 & -0.5 \\ 0.5 & 0 & -0.5 & 1 \end{pmatrix} \quad (2.13)$$

In this example, $1/6$ of the atoms have been excited with the remaining atoms in the $|0, 0\rangle$ ground state. Couplings between the other ground states and the

²Predicting measurements using the density matrix is discussed in Section [2.2.5](#)

excited state are also present in the form of off-diagonal elements. In the case of an optical transition, these matrix elements would be proportional to the absorption and refractive index of the atomic ensemble to the light field, which will be covered in more detail in Section [2.2.5](#).

2.2.2 Defining the Hamiltonian

While the density matrix defines the state of the atoms, the Hamiltonian defines the interactions of the atoms with their environment. In this section I will briefly review the external field interactions we are going to see when considering NMOR and how those fields are represented in the system Hamiltonian. I will build the Hamiltonian for the $F = 1 \rightarrow F' = 0$ hyperfine transition as a concrete example.

I begin by defining the bare Hamiltonian for an alkali hyperfine transition:

$$\mathcal{H}_0 = \sum_{m_F=-F}^F |F, m_F\rangle \langle F, m_F| + \sum_{m_{F'}=-F'}^{F'} \hbar\omega_0 |F', m_{F'}\rangle \langle F', m_{F'}|, \quad (2.14)$$

where $\hbar\omega_0$ is the optical transition energy separating the hyperfine transitions. This Hamiltonian has two multiply degenerate manifolds of magnetic sublevels. For the $F = 1 \rightarrow F' = 0$ transition this Hamiltonian is written as

$$\mathcal{H}_0 = \frac{\hbar}{2} \begin{pmatrix} 0 & 0 & 0 & 0 \\ 0 & 0 & 0 & 0 \\ 0 & 0 & 0 & 0 \\ 0 & 0 & 0 & 2\omega_0 \end{pmatrix}. \quad (2.15)$$

The addition of optical and magnetic fields will break the degeneracy of the ground state (adding to the diagonal elements) and induce couplings between levels (adding to the off-diagonal elements).

I next apply an optical field with amplitude E_0 and frequency $\omega_p = \omega_0 + \Delta_p$ that is nearly resonant with the optical transition. I will also take the polarization of the field to be along the x -axis and the propagation along the z -axis. The light interaction Hamiltonian is then written, with the aid of the optical dipole moment operator \vec{d} , as

$$\mathcal{H}_L = -\vec{E} \cdot \vec{d} = E_0 d_x \cos(\omega_p t), \quad (2.16)$$

where d_x is the x -component of the dipole operator. This operator can be reduced using the Wigner-Eckart theorem to a common reduced dipole matrix element, $d_0 = \langle F | er | F' \rangle$, that depends only on the radial overlap of the coupled states, and Clebsch-Gordon coefficients determined by the angular components that depend on m_F and $m_{F'}$. It is common to define a new parameter that describes the strength of the optical coupling known as the Rabi frequency $\Omega_R = E_0 d_0 / \hbar$. As its name suggests, this quantity is given in units of angular frequency and depends on the amplitude of the coupling field and the strength of the reduced dipole moment. In the case of a coherent drive of population between two states, the Rabi frequency is the rate at which the population cycles between the two coupled states.

Using the z -axis as the quantization axis, the linear light polarization can be broken into a sum of left and right circular components ($d_x \rightarrow (d_{\sigma+} - d_{\sigma-})/\sqrt{2}$). These circular components couple levels with $|m_F - m_{F'}| = \pm 1$. This allows me to

write the light interaction Hamiltonian for our example system as

$$\mathcal{H} = \mathcal{H}_0 + \mathcal{H}_L = \frac{\hbar}{2} \begin{pmatrix} 0 & 0 & 0 & \Omega_R \cos(\omega_p t)/\sqrt{6} \\ 0 & 0 & 0 & 0 \\ 0 & 0 & 0 & -\Omega_R \cos(\omega_p t)/\sqrt{6} \\ \Omega_R \cos(\omega_p t)/\sqrt{6} & 0 & -\Omega_R \cos(\omega_p t)/\sqrt{6} & 2\omega_0 \end{pmatrix}. \quad (2.17)$$

In order to remove the time dependence of the Hamiltonian, I will move into a rotating frame that oscillates at the optical frequency. This is accomplished by the unitary transformation

$$U = \begin{pmatrix} 1 & 0 & 0 & 0 \\ 0 & 1 & 0 & 0 \\ 0 & 0 & 1 & 0 \\ 0 & 0 & 0 & e^{-i\omega_0 t} \end{pmatrix}. \quad (2.18)$$

This will result in matrix elements that have a quasi-static component and a component that oscillates at $2\omega_0$. Assuming the optical frequency is large and there are no other relevant atomic levels at $2\omega_0$, I can safely ignore those components. This is known as the rotating wave approximation. The interaction Hamiltonian under the rotating wave approximation becomes

$$\mathcal{H}_{\text{rot}} = U^{-1} \cdot \mathcal{H} \cdot U \approx \frac{\hbar}{2} \begin{pmatrix} 0 & 0 & 0 & \Omega_R/2\sqrt{6} \\ 0 & 0 & 0 & 0 \\ 0 & 0 & 0 & -\Omega_R/2\sqrt{6} \\ \Omega_R/2\sqrt{6} & 0 & -\Omega_R/2\sqrt{6} & -2\Delta_p \end{pmatrix}. \quad (2.19)$$

I next allow for a magnetic field. The magnetic interaction Hamiltonian is due to the magnetic dipole moment $\vec{\mu}$.

$$\mathcal{H}_B = -\vec{\mu} \cdot \vec{B} = g_F \mu_B \vec{F} \cdot \vec{B} \quad (2.20)$$

In a similar manner to that of the optical coupling, the magnetic moment can be re-written as orthogonal operators $F_{x,y,z}$ that depend on the F of the state, a fixed moment due to the electron known as the Bohr magneton μ_B , and the Lande g-factor g_F . Equivalent with the Rabi frequency, the Larmor frequency is defined as $\Omega_L = \mu_B B / \hbar$.

In the case of a weak axial magnetic field (*i.e.* along the quantization axis z), the field breaks the degeneracy of the magnetic sublevels in what is known as the Zeeman effect. The Hamiltonian can be explicitly written as

$$\mathcal{H}_{\text{rot}} = \mathcal{H}_0 + \mathcal{H}_L + \mathcal{H}_B \approx \frac{\hbar}{2} \begin{pmatrix} -\Omega_L & 0 & 0 & \Omega_R/2\sqrt{6} \\ 0 & 0 & \Omega_L & 0 \\ 0 & 0 & 0 & -\Omega_R/2\sqrt{6} \\ \Omega_R/2\sqrt{6} & 0 & -\Omega_R/2\sqrt{6} & -2\Delta_p \end{pmatrix}. \quad (2.21)$$

Note that the magnitude of the level splitting depends not only on the magnetic field in Ω_L but also the value of m_F . For a particular F level, the magnetic sublevels then split symmetrically about the zero field energy, depending on the sign of m_F .

Transverse fields are more complicated, with their effect being to couple magnetic sublevels with $|\Delta m_F| = \pm 1$ in the same F manifold. A simple, though not

necessarily intuitive way to picture this is to apply the same Hamiltonian as the axial field case, then rotate the basis such that the applied field is now transverse to the quantization axis. This rotation will mix sublevels in the rotated basis, which takes the form of couplings between those levels. Larmor frequencies for these couplings can also be defined $\delta\omega_i = \mu_B B_i / \hbar$.

A final, total Hamiltonian showing all of these coupling for a $F = 1 \rightarrow F' = 0$ hyperfine transition, in the rotating frame, is

$$\mathcal{H}_{\text{tot}} = \frac{\hbar}{2} \begin{pmatrix} -\Omega_L & -(\delta\omega_x - i\delta\omega_y)/\sqrt{2} & 0 & \Omega_R/2\sqrt{6} \\ -(\delta\omega_x + i\delta\omega_y)/\sqrt{2} & 0 & -(\delta\omega_x - i\delta\omega_y)/\sqrt{2} & 0 \\ 0 & -(\delta\omega_x + i\delta\omega_y)/\sqrt{2} & \Omega_L & -\Omega_R/2\sqrt{6} \\ \Omega_R/2\sqrt{6} & 0 & -\Omega_R/2\sqrt{6} & -2\Delta_p \end{pmatrix}. \quad (2.22)$$

Hamiltonians for hyperfine transitions between levels with larger F numbers will look approximately the same, though the numerical prefactors will differ due to Clebsch-Gordon coefficients and m_F quantum numbers. The ADM *Mathematica* package developed by Simon Rochester is very effective at building these Hamiltonians for arbitrary system configurations. [23]

This Hamiltonian can be used with the time dependent Schrödinger equation to obtain equations of motion that would allow us to take atoms with a defined initial state and determine their state at any later time. Combining the Schrödinger equation with the density matrix formalism gives the Liouville equation that defines

these equations of motion in terms of the density matrix:

$$i\hbar \frac{d}{dt} \rho = [\mathcal{H}, \rho]. \quad (2.23)$$

2.2.3 Dephasing Mechanisms

The above equation of motion ignores one very important aspect of any quantum system: interactions with the environment. In order for the above to account for these interactions, the entire environment would need to be included in the Hamiltonian. Since this is wildly impractical, an alternative formalism is needed. I will use the Lindblad modification of the Liouville equation that treats dissipation as interactions with a thermal bath, which results in dephasing of populations and coherences produced under the action of the system Hamiltonian. This will be described in more detail in the next section, but first I need to define the dephasing mechanisms to be considered.

I first consider the natural lifetime of the excited state. When an isolated atom absorbs a photon and transitions to the excited state, it would remain there indefinitely. In reality the atom is coupled to the vacuum modes of free space. In time fields arising from quantum fluctuations in these modes will stimulate emission of the atom and it transitions to the ground state while emitting a photon. The average time for this to occur is the natural lifetime of the state. For the first excited state of the $D2$ transition in ^{87}Rb , the natural lifetime is 27 ns which corresponds to a dephasing rate of $2\pi \times 6.0666 \text{ MHz}$. Thus any excitation on this transition will relax,

on average, at this rate. Since the quantum vacuum fluctuations that stimulate this dephasing are not polarized or directed, the resulting photons emitted will not be polarized or directed. In other words, the photons are randomly distributed into free-space with random polarization relative to each other.

Excited state populations are not the only thing that can relax due to this spontaneous mechanism; coherences between excited states can also spontaneously dephase. A simple argument for this follows from allowing arbitrary rotations of the atomic basis. Any coherence between sublevels of the same transition can be converted into populations with the correct rotation of the basis states. Given this and the fact that the quantum vacuum fluctuations are un-polarized and omnidirectional, there is always potential for a population changing event that appears as a change in coherence in a different basis. What is perhaps more curious is that this relaxation can preserve at least some of the coherence of the excited state in the resulting ground state. This mechanism is crucial to observing EIA in transitions between hyperfine states, as demonstrated in [15, 16].

The second dephasing mechanism I will consider amounts to the lifetime of the atomic coherences themselves. The “natural” lifetime of coherences in the ground state can be on the order of seconds, which is effectively infinite compared with the excited state. Instead the primary limitation to the coherence time is instead the interaction time of the atoms with the light. In the context of warm atoms this time is known as the transit time and is due to the time it takes for thermal atoms to traverse the probing beam profile. The coherences responsible for NMOR, EIT, and EIA are created only when the light and the atomic ensemble interact. By

limiting the interaction time, the resonances become Fourier broadened. For room temperature rubidium with a 1 mm diameter probe beam the transit dephasing rate due to this time is on the order of a few hundred kilohertz.

There exist many experimental methods for increasing the coherence time in NMOR in warm atoms. These include using buffer gases to slow the mean-free path of the atoms, [24] using a hollow pump beam around a small probe to obtain a Ramsey interrogation, [25] or employing spin anti-relaxation coatings. [26] The final method has proven particularly effective. A simple coating of paraffin on the inner surface of the vapor cell mitigates the randomizing wall collisions, allowing up to thousands of collisions before coherence is lost. This results in an effective Ramsey measurement as the atoms are optically-pumped then precess in the field between many collisions and are ultimately probed again resulting in polarization rotation. With the proper coating and significant care taken to ensure a uniform field throughout the vapor cell, effective transit rates below 1 Hz have been observed leading to highly sensitive magnetometers. [8]

Performing NMOR measurements in cold atoms have a close analog to the transit rate of warm atoms. While the cold atoms typically do not move through the transverse beam profile, the light-atom interaction time is still limited. Even with detuned probing light, extended optical interrogation will eventually disperse the atomic cloud as absorption of the light will push the atoms. In the presented data the interrogation time is 1.5 ms, which is equivalent to a transit dephasing rate of $2\pi \times 100$ Hz. As expected, this rate is significantly smaller than in thermal atoms.

2.2.4 The Lindblad Equation

Modifying the Liouville equation (Eq. 2.23) to include dissipation mechanisms requires a few approximations. It revolves around approximating the environment the Hamiltonian system is coupled to as a large reservoir. Two specific approximations are necessary to decouple the internal dynamics of the reservoir with the internal dynamics of the atomic system. The first is known as the Born approximation, which assumes that the reservoir is large and weakly coupled to the system of interest. This results in the reservoir states being weakly perturbed by the system of interest making the two systems separable. The second is known as the Born-Markov approximation, which assumes the dynamics of the system do not depend on the past state of the system. This equates to a statement that the reservoir dynamics are fast relative to the dynamics of the system which prevents history of the system from being preserved and influencing the system dynamics at a later time.

In this work I use the definition of the Lindblad equation defined in [12]:

$$i\hbar \frac{d}{dt}\rho = [\mathcal{H}, \rho] - i\hbar \frac{1}{2}(X\rho + \rho X) + i\hbar \Lambda, \quad (2.24)$$

where X is a matrix that encapsulates relaxation mechanisms due to dephasing and Λ another matrix that accounts for repopulation mechanisms. The relaxation matrix X is diagonal with each term being the sum of total dephasing mechanisms

for each level. For the example $F = 1 \rightarrow F' = 0$ system the matrix X is

$$X = \begin{pmatrix} \gamma & 0 & 0 & 0 \\ 0 & \gamma & 0 & 0 \\ 0 & 0 & \gamma & 0 \\ 0 & 0 & 0 & \gamma + \Gamma \end{pmatrix}, \quad (2.25)$$

where γ is the transit dephasing that effects atoms in all levels and $1/\Gamma$ is the natural lifetime of the excited state.

The repopulation matrix Λ encapsulates which states the relaxing states decay to. In our example system this matrix is

$$\Lambda = \frac{1}{3} \begin{pmatrix} \gamma + \Gamma \rho_{(2,0),(2,0)} & 0 & 0 & 0 \\ 0 & \gamma + \Gamma \rho_{(2,0),(2,0)} & 0 & 0 \\ 0 & 0 & \gamma + \Gamma \rho_{(2,0),(2,0)} & 0 \\ 0 & 0 & 0 & 0 \end{pmatrix}. \quad (2.26)$$

Off-diagonal elements are possible, representing the potential for spontaneous decay of coherence as well as population. This matrix also enforces proper normalization of the atomic population in the ensemble.

Taken together, the relaxation and repopulation matrices account for the dephasing mechanisms present in the system. The natural lifetime of the excited state relaxes atoms in the excited state at a rate of Γ into the individual ground states at a rate of $\Gamma/3$ since the excited state decays to any of the ground states with equal

probability. The transit dephasing mechanism dephases all populations and coherences at a rate of γ as atoms leave the probing field. Atoms enter the probe field unexcited at a rate $\gamma/3$ and are assumed to be de-polarized (*i.e.* equally populating the ground states).

The Lindblad equation gives $(2(F + F' + 1))^2$ coupled differential equations of motion for the atomic ensemble known as Optical Bloch Equations (OBEs). If I assume the measurement time is long compared with the internal system dynamics our measurements will actually reflect the steady-state solution. One can find the solution for the steady-state density matrix by setting the time derivatives to zero and solving the coupled system of linear equations. This solution can be found numerically using any number of computational packages. However, complex Hamiltonians or systems with large numbers of sublevels increase the complexity, and therefore the solving time, significantly.

2.2.5 Observables Derivation

With the steady-state solution of the light-atom system in hand, I now need to derive the effects of the atomic polarization on the probe light in terms of an observable quantity. For any physically observable quantity one can find the expected outcome for a given atomic state using

$$\mathcal{O} = Tr \left(\hat{\rho} \cdot \hat{O} \right), \quad (2.27)$$

where \mathcal{O} is the observable outcome, $\hat{\mathcal{O}}$ is the operator that corresponds to that observable, and $Tr()$ represents the trace operation. For the average atomic polarization observable this equation becomes, in direct correspondence to Eq. 2.6,

$$\vec{P} = Tr(\hat{p} \cdot \hat{\wp}) \quad (2.28)$$

where $\hat{\wp}$ is the electric dipole operator. This relation gives the average atomic polarization in terms of the steady-state density matrix elements which can be obtained using the Lindblad equation as described above.

To see how incident probe light is modified by the atomic polarization, one solves for the differential changes in the four parameters using the standard wave equation for a polarizable medium:

$$\left(k^2 + \frac{d^2}{dz^2}\right) \vec{E} = -4\pi k^2 \vec{P}. \quad (2.29)$$

I will parameterize \vec{E} & \vec{P} in terms of field amplitude, phase, linear polarization angle and polarization ellipticity; being careful to divide each into orthogonal polarizations. Without loss of generality I will take the propagation direction to be along the \hat{z} axis while the polarization angle α is measured relative to the \hat{x} axis. The magnitude of the electric field and overall phase are \mathcal{E} and φ respectively. The ellipticity, ϵ , is the arctangent of the ratio of the minor to major axes of the polarization ellipse. The important values of ϵ are $0, \pm\pi/4$ corresponding to linear and

σ^\pm circular polarization of light, respectively.

$$\begin{aligned}\vec{E}(z, t) = & \frac{1}{2} \left(-\frac{\mathcal{E}_0}{\sqrt{2}} e^{i(\varphi+\alpha)} e^{i(kz-\omega t)} (\cos \epsilon - \sin \epsilon) + c.c. \right) \hat{\sigma}^+ \\ & + \frac{1}{2} \left(\frac{\mathcal{E}_0}{\sqrt{2}} e^{i(\varphi-\alpha)} e^{i(kz-\omega t)} (\cos \epsilon + \sin \epsilon) + c.c. \right) \hat{\sigma}^- \end{aligned} \quad (2.30)$$

$$\vec{P}(z, t) = \frac{1}{2} \left(\tilde{P}_{\sigma^+} e^{i(kz-\omega t)} + c.c. \right) \hat{\sigma}^+ + \frac{1}{2} \left(\tilde{P}_{\sigma^-} e^{i(kz-\omega t)} + c.c. \right) \hat{\sigma}^- \quad (2.31)$$

Substituting Equations 2.30 & 2.31 into Eq. 2.29 and assuming a slowly varying wave approximation to discard all second-order derivatives I obtain the following complex equations for the two circular polarizations.

$$\begin{aligned}4\pi k \tilde{P}_{\sigma^+} = & \sqrt{2} [i\mathcal{E}_0(z)\epsilon'(z)(\sin(\epsilon(z)) + \cos(\epsilon(z))) \\ & - (\cos(\epsilon(z)) - \sin(\epsilon(z))) (i\mathcal{E}_0'(z) - \mathcal{E}_0(z)(\varphi'(z) + \alpha'(z)))] e^{i(\varphi(z)+\alpha(z))} \end{aligned} \quad (2.32)$$

$$\begin{aligned}4\pi k \tilde{P}_{\sigma^-} = & -\sqrt{2} [i\mathcal{E}_0(z)\epsilon'(z)(\sin(\epsilon(z)) - \cos(\epsilon(z))) \\ & + (\cos(\epsilon(z)) + \sin(\epsilon(z))) (i\mathcal{E}_0'(z) - \mathcal{E}_0(z)(\varphi'(z) - \alpha'(z)))] e^{i(\varphi(z)-\alpha(z))} \end{aligned} \quad (2.33)$$

Splitting these equations into real and imaginary components, I obtain a set of four coupled equations. It is then a simple matter of solving the system for the differential changes in electric field amplitude, optical phase, linear polarization angle, and ellipticity. It is important to note these results only apply in the case of an optically-thin medium where observables do not change appreciably through the medium and can thus be approximated to their initial values ($\mathcal{O}(z) \simeq \mathcal{O}(0) \equiv \mathcal{O}$).

I then find

$$\begin{aligned} \frac{1}{\mathcal{E}_0} \frac{d\mathcal{E}_0}{dz} = \frac{-\sqrt{2}\pi k}{\mathcal{E}_0} & \left[\left(\text{Im} \left(\tilde{P}_{\sigma+} \right) \cos(\alpha + \varphi) - \text{Re} \left(\tilde{P}_{\sigma+} \right) \sin(\alpha + \varphi) \right) (\cos(\epsilon) - \sin(\epsilon)) \right. \\ & \left. + \left(\text{Im} \left(\tilde{P}_{\sigma-} \right) \cos(\alpha - \varphi) + \text{Re} \left(\tilde{P}_{\sigma-} \right) \sin(\alpha - \varphi) \right) (\cos(\epsilon) + \sin(\epsilon)) \right] \end{aligned} \quad (2.34)$$

$$\begin{aligned} \frac{d\varphi}{dz} = \frac{\sqrt{2}\pi k}{\mathcal{E}_0} & \left[\left(-\text{Im} \left(\tilde{P}_{\sigma-} \right) \sin(\alpha - \varphi) + \text{Re} \left(\tilde{P}_{\sigma-} \right) \cos(\alpha - \varphi) \right) (\cos(\epsilon) - \sin(\epsilon)) \right. \\ & \left. + \left(\text{Im} \left(\tilde{P}_{\sigma+} \right) \sin(\alpha + \varphi) + \text{Re} \left(\tilde{P}_{\sigma+} \right) \cos(\alpha + \varphi) \right) (\cos(\epsilon) + \sin(\epsilon)) \right] \end{aligned} \quad (2.35)$$

$$\begin{aligned} \frac{d\alpha}{dz} = \frac{\sqrt{2}\pi k}{\mathcal{E}_0} & \left[\left(\text{Im} \left(\tilde{P}_{\sigma-} \right) \sin(\alpha - \varphi) - \text{Re} \left(\tilde{P}_{\sigma-} \right) \cos(\alpha - \varphi) \right) (\cos(\epsilon) - \sin(\epsilon)) \right. \\ & \left. + \left(\text{Im} \left(\tilde{P}_{\sigma+} \right) \sin(\alpha + \varphi) + \text{Re} \left(\tilde{P}_{\sigma+} \right) \cos(\alpha + \varphi) \right) (\cos(\epsilon) + \sin(\epsilon)) \right] \end{aligned} \quad (2.36)$$

$$\begin{aligned} \frac{d\epsilon}{dz} = \frac{-\sqrt{2}\pi k}{\mathcal{E}_0} & \left[\left(\text{Im} \left(\tilde{P}_{\sigma-} \right) \cos(\alpha - \varphi) + \text{Re} \left(\tilde{P}_{\sigma-} \right) \sin(\alpha - \varphi) \right) (\cos(\epsilon) - \sin(\epsilon)) \right. \\ & \left. + \left(-\text{Im} \left(\tilde{P}_{\sigma+} \right) \cos(\alpha + \varphi) + \text{Re} \left(\tilde{P}_{\sigma+} \right) \sin(\alpha + \varphi) \right) (\cos(\epsilon) + \sin(\epsilon)) \right] \end{aligned} \quad (2.37)$$

With the optically-thin approximation, the total change is the integration of these equations over the length of the medium. It is convenient to express these differential changes in terms of an experimental length. I choose to use the unsaturated absorption length ℓ_0 of the sample, defined as the distance light must travel through a uniform sample to have its intensity reduced by a factor of $\frac{1}{e}$. The unsaturated

absorption length for a given transition within this framework is defined as

$$\ell_0 \equiv (n\sigma_{abs})^{-1} = \lim_{\Omega_R, \gamma \rightarrow 0} \left[\frac{-2}{\mathcal{E}_0} \frac{d\mathcal{E}_0}{dz} \right]_{\vec{B}, \Delta=0}^{-1} \quad (2.38)$$

where n is the atomic number density and σ_{abs} is the absorption cross section of the transition.

To demonstrate the utility of developing these equations in the circular basis, consider Eq. 2.36 for a typical experimental configuration with an \hat{x} -linearly polarized probe, chosen to have $\varphi(0) = 0$. In this case, the differential polarization rotation due to the interaction with the polarized atomic system reduces to

$$\frac{d\alpha}{dz} = \frac{\sqrt{2}\pi k}{\mathcal{E}_0} \left[\text{Re} \left(\tilde{P}_{\sigma+} \right) - \text{Re} \left(\tilde{P}_{\sigma-} \right) \right]. \quad (2.39)$$

If I further assume the medium is lossless (which it generally is not), I can rewrite Eq. 2.6 to be $\tilde{P}_{\sigma\pm} = \epsilon_0 \chi_{\pm} \cdot \tilde{E}_{\sigma\pm} = \epsilon_0 (n_{\pm} - 1) \cdot \tilde{E}_{\sigma\pm}$. Substituting into Eq. 2.39 and noting that $\text{Re} \left(\tilde{E}_{\sigma+} \right) = \text{Re} \left(\tilde{E}_{\sigma-} \right) = \mathcal{E}_0/\sqrt{2}$ for linearly polarized light I obtain

$$\frac{d\alpha}{dz} = \pi k (n_+ - n_-). \quad (2.40)$$

Thus the polarization rotation is proportional to the difference in refractive indexes for the left and right circular polarizations of the probe light, which is classified as circular birefringence.

2.2.6 The Polarization Moments Basis

Atomic physics problems using the density matrix formalism are often written in the Zeeman basis, *i.e.* using the Zeeman sublevels as the basis for representation. Due to symmetries in the problems considered in this work, another basis known as the polarization moment basis has proven useful and will be briefly outlined here. [27] This section draws from the treatment found in Ref. [12] and the reader is directed there for the more rigorous treatment.

2.2.6.1 Changing Bases

The density matrix can be thought of as a decomposition of a general density operator into a complete basis set of operators. The basis operators used above are the projection operators for the various magnetic sublevels present in the system, which summed together produce the identity operator. Considering the example of an atomic state with angular momentum F , the density operator is decomposed as

$$\hat{\rho} = \sum_{mm'} \rho_{mm'} |m\rangle \langle m'|, \quad (2.41)$$

where $\rho_{mm'}$ represents the density matrix element corresponding to the $|m\rangle \langle m'|$ projection. While this is the common decomposition, the density operator can be decomposed using any complete basis set.

One basis set of particular interest, considering the symmetries that often arise when analyzing nonlinear optical interactions, is the polarization operator basis.

This basis corresponds to the spherical harmonics $Y_l^m(\theta, \phi)$ and are defined using irreducible spherical tensor operators $T^{\kappa q}$, where κ defines the rank of the tensor. Using this basis, the density matrix can be written

$$\hat{\rho} = \sum_{\kappa=0}^{2F} \sum_{q=-\kappa}^{\kappa} \rho_q^{\kappa} T^{\kappa q}, \quad (2.42)$$

where ρ_q^{κ} is known as a polarization moment. The polarization moments are related to the density matrix elements of Eq. 2.41 by

$$\rho_q^{\kappa} = \sum_{mm'} (-1)^{F-m'} \langle F, m, F, -m' | \kappa q \rangle \rho_{m'm}, \quad (2.43)$$

where $\langle F, m, F, -m' | \kappa q \rangle$ is a Clebsch-Gordon coefficient. The inverse statement defining the density matrix elements in terms of the polarization moments is

$$\rho_{m'm} = \sum_{\kappa q} (-1)^{F-m'} \langle F, m, F, -m' | \kappa q \rangle \rho_q^{\kappa}. \quad (2.44)$$

Some general properties of the polarization moments can be inferred from these relationships. Considering the Clebsch-Gordon coefficients, one can see that $\rho_q^{\kappa} \neq 0$ only when $m' - m = q$ is satisfied. When applied to Eq. 2.43, polarization moments with $q = 0$ can only depend on matrix elements with $m = m'$, *i.e.* the populations ρ_{mm} . As a result, these polarization moments only describe polarization aligned with the quantization axis of the Zeeman basis states. Considering polarization moments with $q \neq 0$, the Clebsch-Gordon coefficients imply that only matrix elements corresponding to coherences between neighboring sublevels with $|\Delta m| = |q|$

are present. As a result, $|\Delta m| = 2$ coherences responsible for NMOR, as described above, generate polarization moments that are transverse to the quantization axis.

From these considerations, one can see that q governs only the spatial directions of a given atomic polarization of rank κ . The rank of polarization gives the type of polarization involved and is often given a name corresponding to the rank of expansion of a static electric field into multipole moments. For example ρ^0 is known as the monopole moment, ρ^1 the dipole moment, ρ^2 the quadrupole moment, and so forth.

2.2.6.2 Orientation vs. Alignment

While a given atomic state supports polarization moments up to rank $\kappa = 2F$, the nonlinear effects considered in this work can be described using only the three lowest rank moments, known as the isotropic moment, orientation, and alignment corresponding to $\kappa = 0, 1, 2$ respectively. These terms derive from the physical interpretation of the atomic polarization they describe and can be visualized using spherical harmonics.

Note that being able to restrict our attention to the three lowest rank moments is an important simplification when considering hyperfine transitions with $F > 1$. In effect, it implies these transitions can be mapped to the simplest system that supports these three moments, $F = 1 \rightarrow F' = 0$.

Spherical harmonics, scaled by the polarization moments of the atomic state, allow the average atomic polarization to be visualized using what is known as an

Angular Momentum Probability Surface (AMPS). [27] The AMPS for an atomic state is defined as

$$\rho_{FF}(\theta, \phi) = \sqrt{\frac{4\pi}{2F+1}} \sum_{\kappa=0}^{2F} \sum_{q=-\kappa}^{\kappa} \langle F, F, \kappa, 0 | FF \rangle \rho_q^{\kappa} Y_{\kappa}^q(\theta, \phi), \quad (2.45)$$

where $\langle F, F, \kappa, 0 | FF \rangle$ is a Clebsch-Gordon coefficient. Plotting the real part of this equation in three dimensional space versus the angles θ and ϕ gives a surface of variable radial distance. The resulting AMPS is interpreted as the probability of finding the maximum projection of angular momentum along the (θ, ϕ) direction. These surfaces provide a quick way to identify symmetry axes and the different tensor components of the atomic polarization. I illustrate this by showing a few examples of AMPS and their corresponding density matrices in the Zeeman basis for an $F = 1$ atomic state.

The simplest example is that of an isotropic polarization moment. An isotropically polarized $F = 1$ atomic state has a density matrix of the form

$$\hat{\rho}^0 = \frac{1}{3} \begin{pmatrix} 1 & 0 & 0 \\ 0 & 1 & 0 \\ 0 & 0 & 1 \end{pmatrix}. \quad (2.46)$$

In the polarization moment basis only $\rho_0^0 = 1/\sqrt{2F+1}$ is non-zero. Applying Eq. 2.45, the AMPS is determined to be $\rho_{FF}(\theta, \phi) = 1/3$. The corresponding AMPS is plotted in Fig. 2.6a. As expected, an isotropically polarized atomic state is represented by a sphere centered at the origin.

An example of atomic orientation along the z -axis is given as

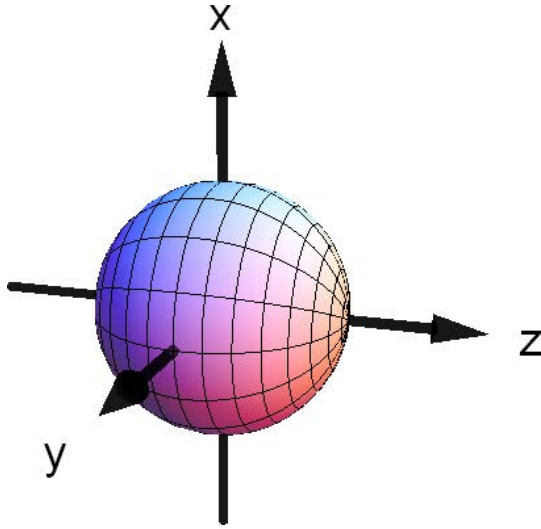
$$\hat{\rho}^1 = \begin{pmatrix} 1 & 0 & 0 \\ 0 & 0 & 0 \\ 0 & 0 & 0 \end{pmatrix} \quad (2.47)$$

in the Zeeman basis. The AMPS for this state takes the form of $\rho_{FF}(\theta, \phi) = \cos(\theta/2)^4$ and is plotted in Fig. 2.6b. This state is also a sphere, though it is oriented along the $+z$ direction. It is for this reason the rank-1 polarization moment is known as orientation—an oriented atomic polarization has polarization along a preferred direction.

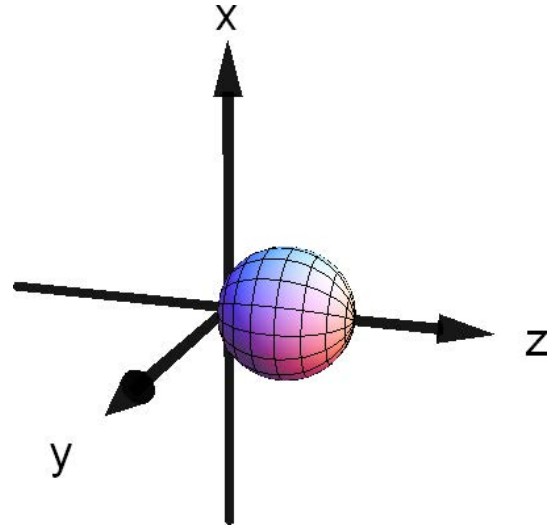
An example of atomic alignment along the z -axis is given as

$$\hat{\rho}^2 = \frac{1}{2} \begin{pmatrix} 1 & 0 & 0 \\ 0 & 0 & 0 \\ 0 & 0 & 1 \end{pmatrix} \quad (2.48)$$

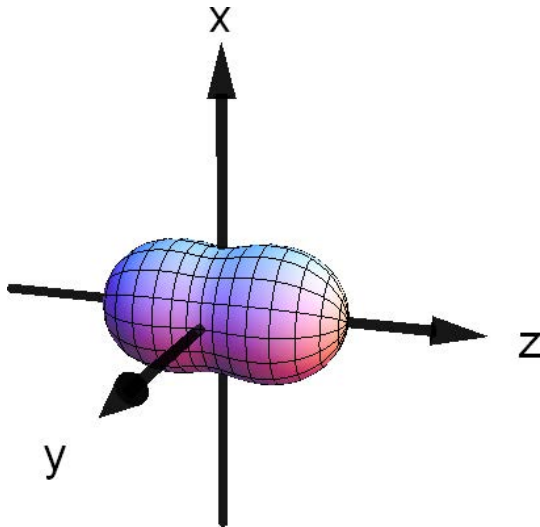
in the Zeeman basis. The AMPS for this state takes the form of $\rho_{FF}(\theta, \phi) = (3 + \cos(2\theta))/8$ and is plotted in Fig. 2.6c. This state has a more complicated shape resembling a dumbbell or peanut, aligned with the z -axis. This alignment along an axis is the reason the rank-2 polarization moment is known as alignment. In contrast with orientation, an aligned atomic polarization does not have a preferred direction, but rather a preferred axis.



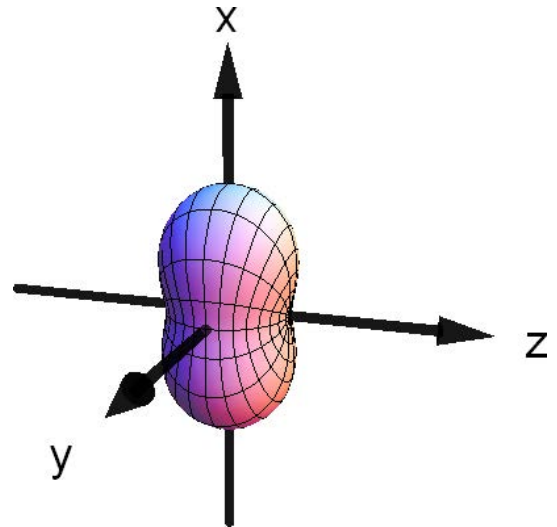
(a) The rank-0 polarization moment represents the isotropic portion of the atomic polarization.



(b) The rank-1 polarization moment represents oriented atomic polarization—polarization with a preferred direction.



(c) The rank-2 polarization moment represents aligned atomic polarization—polarization that has a preferred axis.



(d) This AMPS represents an optically-pumped state that is the sum of rank-0 and rank-2 polarization moments. This state arises from \hat{x} -polarized light aligning the atomic polarization with the applied electric field.

Figure 2.6: Example Polarization Moments visualized using their corresponding AMPS.

As a final example consider the following density matrix,

$$\hat{\rho}_{EIT} = \frac{1}{4} \begin{pmatrix} 1 & 0 & 1 \\ 0 & 2 & 0 \\ 1 & 0 & 1 \end{pmatrix}. \quad (2.49)$$

This density matrix arises when considering the ground state in the case of perfect optical pumping in an $F = 1 \rightarrow F' = 0$ system with linearly polarized light. While not obvious at first glance, this state is clearly seen to be aligned with the x -axis when converted to the polarization moment basis. In that basis, only the constant isotropic term ($\rho_0^0 = 1/\sqrt{3}$) and the rank-2 terms $\rho_0^2 = -1/2\sqrt{6}$, $\rho_{\pm 2}^2 = 1/4$ are non-zero. The corresponding AMPS is plotted in Fig. 2.6d.

The physical basis for both the EIT and NMOR observed in this system are simple to visualize when considering the atomic polarization acts analogously to a linear polarizer. When a magnetic field is applied along the light propagation axis (z -axis), the atomic polarization will precess. The transmitted light polarization then follows the precession in much the same way it would follow a rotating polarizer, leading to rotation of the transmitted polarization. Considering the light transmission, maximum transmission obviously corresponds to no precession or zero magnetic field, leading to a transparency window or EIT.

2.2.7 Frame Rotations

Proper analysis of the models developed in Section 2.3 requires the ability to rotate between arbitrary reference frames. This is accomplished using rotation operators constructed from Wigner-D functions. In a contracted form, the operator for a rotation θ about the axis \hat{n} is given by $\hat{D} = e^{-i\vec{J}\cdot\hat{n}\theta}$ where $\vec{J} = (J_x, J_y, J_z)$ is the angular momentum operator. Using this construction an arbitrary rotation is easily written using the Euler angles α, β, γ such that

$$\hat{D}(\gamma, \alpha, \beta) = e^{-iJ_z\gamma}e^{-iJ_y\alpha}e^{-iJ_z\beta}. \quad (2.50)$$

This particular parameterization follows that implemented in the ADM Mathematica package and can be thought of as a rotation of β about the z -axis, then a rotation of α about the rotated y' axis, and finally a rotation of γ about the doubly rotated z'' axis. This provides a general framework of rotations to change between reference frames to facilitate understanding of the atomic polarizations present in the systems studied. I will provide two examples of frame rotations that are commonly used throughout this work.

I will first demonstrate that the density matrix of Eq. 2.49 represents a pure atomic alignment polarization directed along the x -axis; something not directly obvious from the density matrix in the Zeeman basis itself but is a natural result of optically pumping an atomic sample with linearly polarized light. To see this I rotate frames such that the quantization axis will be along the x -axis or light

polarization direction. This is done using Eq. 2.50 with $\beta = \gamma = 0$ and $\alpha = \pi/2$ giving a 90° rotation about the y -axis. With a total angular momentum $J = 1$ the resulting rotation operator and rotated density matrix produce

$$\hat{\rho}_{EIT}^{(x)} = \hat{D}(0, \pi/2, 0) \cdot \hat{\rho}_{EIT}^{(z)} = \frac{1}{2} \begin{pmatrix} 1 & -\sqrt{2} & 1 \\ \sqrt{2} & 0 & -\sqrt{2} \\ 1 & \sqrt{2} & 1 \end{pmatrix} \cdot \frac{1}{4} \begin{pmatrix} 1 & 0 & 1 \\ 0 & 2 & 0 \\ 1 & 0 & 1 \end{pmatrix} = \frac{1}{2} \begin{pmatrix} 1 & 0 & 0 \\ 0 & 0 & 0 \\ 0 & 0 & 1 \end{pmatrix}. \quad (2.51)$$

This is exactly equal to the aligned density matrix example given above in Eq. 2.48 demonstrating that optically-pumped state is in fact an aligned polarization moment.

The next example involves the more complicated scenario of changing frames between the light propagation axis \vec{k} and the total magnetic field or quantization axis in an NMOR experiment. In a standard NMOR experiment these two axes are co-linear with only the magnitude and sign of the magnetic field changing during an experiment. In this work I must include the effect of constant transverse field as well—the total magnetic field direction can take on arbitrary direction relative to the light propagation direction. I begin by defining the total magnetic field components in the lab frame as

$$\vec{B} = \{B_x, B_y, B_z\}. \quad (2.52)$$

I then take the z -axis as the light propagation direction and the x -axis as the light polarization direction. In terms of these directions I will often refer to the magnetic field component B_z as the axial magnetic field and B_x, B_y as the transverse magnetic

fields.

In a typical NMOR experiment, the change in direction can be completely specified using the Euler angles α and β . I define them such that $-\pi/2 \leq \alpha \leq \pi/2$ as the axial field is swept through zero and β is the angle of the transverse field relative to the y -axis as follows:

$$\tan(\alpha) = \frac{B_z}{\sqrt{B_x^2 + B_y^2}}, \quad \tan(\beta) = \frac{B_y}{B_x}. \quad (2.53)$$

This parameterization assumes that the transverse field along the x -axis is always present and best represents the experimental work presented below. Using these angles the total magnetic field may be written as

$$\vec{B} = \|\vec{B}\| \{ \cos(\alpha) \cos(\beta), -\cos(\alpha) \sin(\beta), \sin(\alpha) \}. \quad (2.54)$$

Considering the same $J = 1$ system above the rotation operator becomes

$$\hat{D}(0, \alpha - \pi/2, \beta) = \frac{1}{2} \begin{pmatrix} e^{-i\beta} (\sin(\alpha) + 1) & \sqrt{2} \cos(\alpha) & e^{i\beta} (\sin(\alpha) - 1) \\ \sqrt{2} e^{-i\beta} \cos(\alpha) & 2 \sin(\alpha) & \sqrt{2} e^{i\beta} \cos(\alpha) \\ e^{-i\beta} (\sin(\alpha) - 1) & -\sqrt{2} \cos(\alpha) & e^{i\beta} (\sin(\alpha) + 1) \end{pmatrix}. \quad (2.55)$$

By applying this rotation operator I can move the reference frame to follow the total magnetic field quantization axis for an NMOR experiment as the axial magnetic field is swept through zero. Taking the specific, optically-pumped scenario of Eq. 2.49, ignoring B_y oriented transverse fields by letting $\beta = 0$, and further letting $\alpha = \pi/4$

corresponding to a point in the NMOR experiment when the axial field is equal in magnitude to the transverse field I can find the resulting density matrix of the optically-pumped state in the quantization axis reference frame:

$$\hat{\rho}_{EIT}^{(\alpha=\pi/2)} = \frac{1}{8} \begin{pmatrix} 3 & \sqrt{2} & 1 \\ \sqrt{2} & 2 & -\sqrt{2} \\ 1 & -\sqrt{2} & 3 \end{pmatrix}. \quad (2.56)$$

As expected, the optically-pumped aligned state is not purely along the quantization axis (as indicated by the non-zero off-diagonal elements). While certainly an obvious conclusion, the result is important to note since, as I will demonstrate in the next section, alignment parallel to the magnetic field has a different effect on NMOR than that of alignment perpendicular to the magnetic field; the typical condition considered in the literature.

2.3 NMOR Models

I will now apply the above formalism to the problem of Nonlinear Magneto-Optical Rotation. In the vernacular of nonlinear optics, NMOR is a $\chi^{(3)}$ nonlinearity, intensity-dependent process where a linearly-polarized probe beam experiences refraction upon interacting with the atomic medium and an external magnetic field. The $\chi^{(3)}$ nonlinearity is the result of optically-pumped, long-lived atomic coherences in the ground state. The interaction of these coherences with the external magnetic field and the probe light ultimately give rise to NMOR. In this section I present a number of theoretical models in order of increasing complexity as I generalize to account for greater probe intensity and arbitrary external magnetic field orientation.

2.3.1 Single-Axis Models

2.3.1.1 Low Probe Intensity – Linear Polarizer Model

The linear polarizer model was first proposed by Karnorsky *et. al.* [28] and is the simplest model of NMOR. In this model the simultaneous and continuous processes of NMOR are broken into three distinct steps. (1) The isotropic atomic vapor is optically pumped by the probe light; the optical pumping resulting in a polarized atomic system. (2) The polarized atomic system is then allowed to precess by interaction with the magnetic field. (3) The precessed atomic polarization then interacts with the probe light, causing rotation of the light polarization. The visual power of this model becomes apparent when I note that the optically-pumped

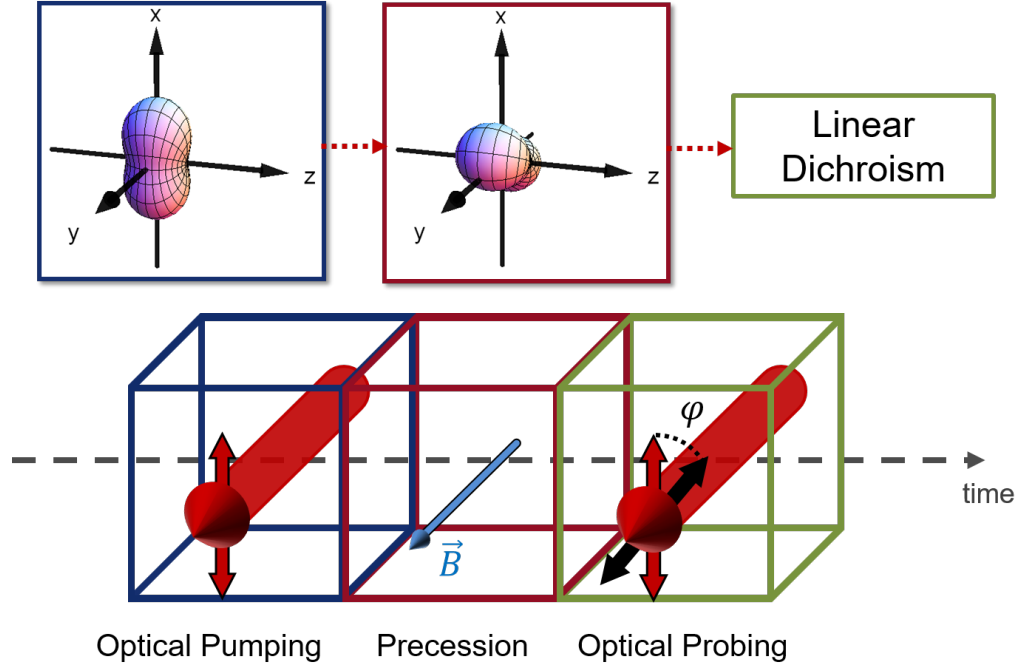


Figure 2.7: The linear polarizer model for low probe intensity NMOR. The light polarizes the atoms via optical pumping (blue region), this polarization precesses in the axial magnetic field (red region), the precessed atomic polarization acts as a linear polarizer, rotating the light polarization via linear dichroism (green region).

atomic polarization from step (1) is an aligned state like that shown in Fig. 2.6d. This polarization behaves as a linear polarizer with a transmission axis parallel to the axis of alignment. As the polarizer precesses about the axial magnetic field, the transmission axis also precesses leading to an observed rotation of the probe polarization axis (see Fig. 2.7).

This model provides simple intuition about the NMOR process. Most importantly it predicts a linear relationship between the observed polarization rotation and the applied axial field near the magnetic field zero. This linear relationship is limited due to two physical realities not included in the model: the simultaneous and continuous nature of the probing. Since the three steps of the model are in actuality occurring simultaneously a fundamental limit to the maximum observable rotation

is met as precessed polarization states become re-pumped to the initial polarization state over time. Since the steps of the model are continuously being excited, the observed polarization rotation is in fact a steady-state in the light-atomic system. In steady-state the width of the observed resonance is limited by the inverse of the coherence time for the optically-pumped atomic polarization. For many experimental realizations of NMOR (including the one I am presenting here) the coherence time is limited by the interaction time of the light with an average atom in the atomic system. Both of these considerations result in the damping of the linear relationship as the axial magnetic field strength is increased leading to the typical dispersion resonance of NMOR.

The final limitation is in the assumption that the atomic polarization acts as a linear polarizer. As will be discussed below this is not true for higher probe powers. More specifically, this model should only hold when the probe light is well below saturation of the NMOR transition: $\Omega_R^2/\gamma\Gamma \ll 1$, where Ω_R is the probe Rabi frequency, Γ the excited state decay rate, and γ the ground state coherence decay rate (aka transit rate). Since the ground state coherence time tends to far exceed the excited state lifetime, saturation of the NMOR transition occurs with much lower power than the bare excited state transition.

Beyond the narrow context of this model it is important to consider the limitations of the simultaneous and continuous damping effects on the typical application of NMOR: magnetometry. While limitations to maximum polarization rotation can be largely mitigated using high-quality detectors and a low-noise amplifier, the resonance width ultimately limits the attainable slope of the linear response to magnetic

field which in turn limits the sensitivity of the measurement. As a result methods for increasing the coherence time in NMOR have been of prominent importance within the field.

2.3.1.2 High Probe Intensity – AOC Model

When the NMOR transition nears saturation ($\Omega_R^2/\gamma\Gamma \simeq 1$) the three-step model described above requires modification as the linear polarizer assumption breaks down. As described by Budker *et. al.*, the electric field of a higher power probe must be accounted for in the precession stage of the three-step model which results in a phenomenon known as Alignment-to-Orientation Conversion (AOC). [13] This oriented atomic polarization also produces polarization rotation, though via circular birefringence in contrast with the linear dichroism of aligned polarization. The polarization rotation due to these mechanisms differs in the response to probe detuning. All other things being equal, linear dichroism has a symmetric lorentzian response versus detuning while circular birefringence has an anti-symmetric dispersion response.

The modification is done by including a DC electric field in the precession stage such that the resulting DC Stark shift of the model is equal to the AC Stark shifts due to the interaction of the atoms with the probe's electric field. Considering an $F = 1$ ground state in the semi-classical limit for small fields relative to the ground state coherence rate the AOC process is reasonably approximated as

$$\hat{\rho}^1 \propto \vec{d}_{ind} \times \vec{E} \propto \left[\left(\vec{B} \times \overleftrightarrow{Q} \right) \cdot \vec{E} \right] \times \vec{E}, \quad (2.57)$$

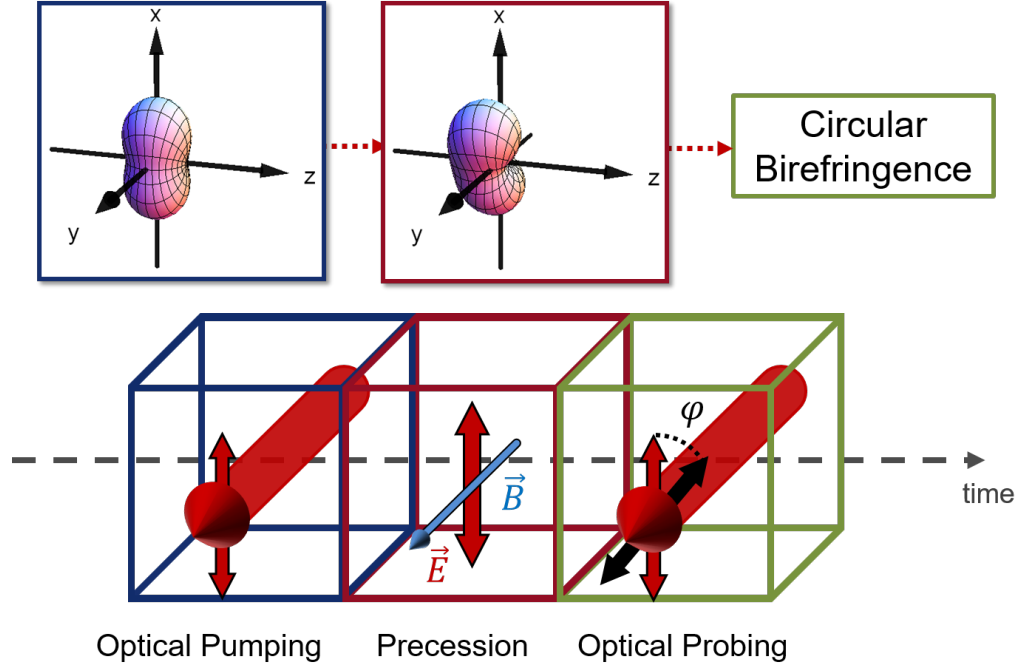


Figure 2.8: AOC model for high intensity NMOR. This uses the same three regions as the linear polarizer model, but the precession region includes the Stark shifts from the probe field. These Stark shifts cause a torque on the precessing alignment that generates orientation. The resulting atomic alignment then contains both alignment and orientation that can cause polarization rotation due to dichroism and circular birefringence, respectively.

where $\vec{d}_{ind} \propto (\vec{B} \times \overleftrightarrow{Q}) \cdot \vec{E}$ is the induced atomic dipole, \overleftrightarrow{Q} is the ground state quadrupole moment resulting from optical pumping, and $\hat{\rho}^1$ the generated orientation from the initially aligned atomic state. [29,30] In short, the electric field induces an electric dipole moment that then experiences a torque from the same electric field to produce orientation from an aligned polarization state.

Analyzing some simple cases will build intuition regarding the AOC mechanism. I begin by considering the standard NMOR geometry where the magnetic field is perpendicular to the electric field of the probe light. The resulting \overleftrightarrow{Q} due to optical pumping is then an aligned state that can be described as the sum of a rank-0 isotropic polarization moment and a rank-2 aligned polarization moment

that is parallel to the optical pumping electric field. If there is no magnetic field, the induced dipole is then parallel to the electric field. The resulting torque from the electric field is then zero by definition. As the magnetic field is increased the atomic alignment is rotated around the magnetic field which in turn generates an induced dipole that is no longer parallel to the electric field. This induced dipole can then experience the torque to produce orientation along the light propagation direction.

It is important to note that the AOC process is rarely 100% efficient. Therefore as the probe intensity is increased both alignment and orientation will be generated with polarization rotation resulting from both. In warm atoms this interplay can be rather complex and is described in depth in Ref. [13]. In cold atoms the interplay is greatly simplified since optimal signal is achieved when the probe is detuned from resonance to avoid resonant heating of the atoms. Detunings larger than the natural linewidth significantly suppress the polarization rotation due to linear dichroism. As a result, observed polarization rotation is due solely to the circular birefringent effect made possible by AOC. Since this work is in cold atoms, the effects of atomic alignment can be ignored moving forward.

2.3.2 Multi-Axis Perturbation Model

The above three step models can be used to obtain algebraic solutions for NMOR systems by perturbatively solving the optical Bloch equations (OBEs) in the optical Rabi frequency for each step. For the AOC model, one takes an isotropic,

un-polarized atomic system and solves the OBEs to 2nd order in the probe Rabi frequency without the magnetic field. This results in an aligned polarization in the atomic system. This alignment is then allowed to experience the AOC effect and Larmor precession by solving the OBEs again to 2_{nd} order with magnetic field and equivalent stark shifts applied. The resulting orientation is then probed by solving the OBEs to 1st order.

The reason full perturbative solutions to the OBEs were not used in the AOC model above is because they can be simplified to the closed-form approximation outlined in Eq. 2.57. This approximation relies on two assumptions: (1) the magnetic quantization axis and the light propagation axis are parallel; (2) the magnetic and electric fields that produce AOC are perpendicular. Obviously, when transverse magnetic fields are present these assumptions are no longer valid and the method of accounting for AOC above does not work. As a result, I first attempted using full perturbative solutions of the OBEs to obtain algebraic solutions. Thanks to Dr. Simon Rochester, our theorist on retainer, this method was successful but it also required significant computational resources for even the simplest transitions. It also did not provide much intuition to the underlying physical process since all the heavy lifting was done internally to the 2nd order perturbative solve for the AOC step.

With some more time, Dr. Rochester devised a simpler method that works for most NMOR transitions and does not require explicit perturbative solutions to the OBEs. I say explicit because the method uses known, closed-form results from the perturbation calculations. The basic principle is that the AOC step can be further

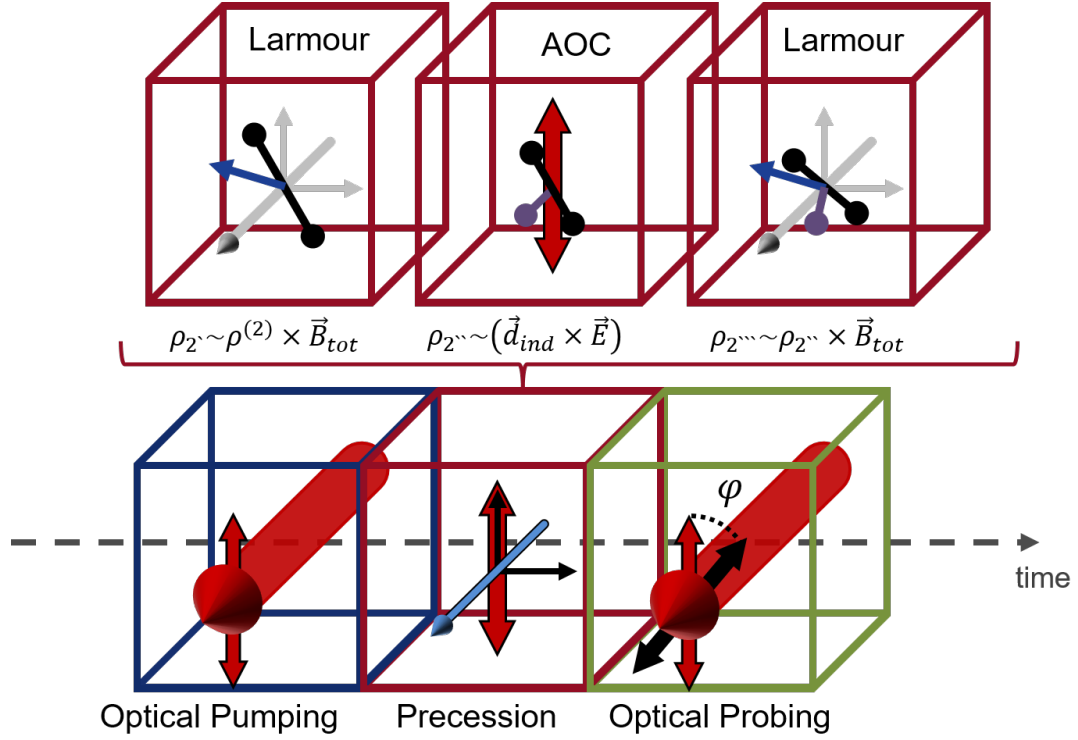


Figure 2.9: 5-Step AOC Model for NMOR. This model generalizes the AOC model by breaking the precession region into three steps. The first step allows for Larmour precession of the optically-pumped atomic polarization. The next region applies the Stark shifts from the probe field that gives AOC, the final step then precesses the remaining alignment and the generated orientation in the magnetic field. The resulting atomic polarization is again probed in the final stage.

broken down into three distinct steps: Larmor precession, alignment-to-orientation conversion, then another Larmor precession (see Fig. 2.9). Each of these steps have simple, known, closed-form solutions, resulting in an overall model that is much easier and faster to calculate. Furthermore, it is easy to break down the alignment and orientation tensors into components and determine their contribution to the end signal which allows for significant physical intuition.

In the next two sections I will describe this simple 5-step model when the transverse field is parallel to the light polarization axis and then for arbitrary transverse fields.

2.3.2.1 2-Axis Solution

In this section I discuss the 5-step model when a transverse magnetic field is present and parallel to the light polarization axis while an axial magnetic field is swept through zero. A diagram of the relevant axes and directions is shown in Fig. 2.10. There are two coordinate systems of interest. The first is the lab coordinate system where the light propagation direction is the z -axis and the light polarization direction is the x -axis. The second is the primed coordinate system aligned to the total magnetic field quantization axis, $\hat{z}' \parallel \vec{B}_{\text{tot}}$. As the axial magnetic field is swept through zero, this coordinate system will rotate about the y -axis. I define the angle $\tan(\alpha) = B_{\text{axial}}/B_{\text{trans}}$ to parameterize this rotation, where B_{axial} is the magnetic field along the z -axis and B_{trans} is the magnitude of the transverse magnetic field (restricted to the x -axis in this section).

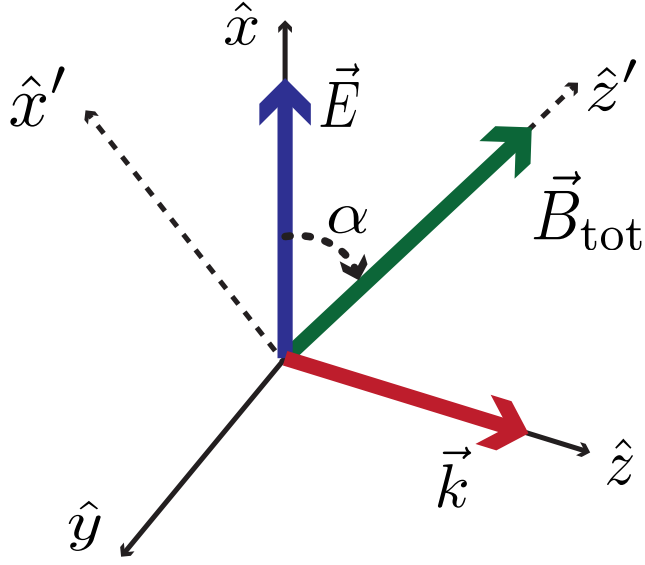


Figure 2.10: Axes definitions for the 5-Step Model. The un-primed axes are the lab frame with light propagation along the z -axis and the light polarization along the x -axis while the primed axes are the rotated coordinates such that $\hat{z}' \parallel \vec{B}_{\text{tot}}$. The angle α is between the light polarization axis and the total magnetic field direction in the $\hat{x} - \hat{z}$ plane.

Before I get into the details of the model, I need to discuss the various magneto-optical effects that could be present and justify my focus on only one of them. I do this by analyzing perturbative solutions of the OBEs in the probe Rabi frequency for the $F = 1 \rightarrow F' = 0$ transition.

At zeroth order in the Rabi frequency is the linear Faraday effect that depends on magnetic field being present in the probing stage. This optical rotation is given by

$$\ell_0 \frac{d\phi}{d\ell} = \frac{\Omega_L \Gamma (\Gamma^2 - 4\Delta_p^2) \sin(\alpha)}{4(\Gamma^2 + 4\Delta_p^2)^2} \propto \frac{\Omega_L \Gamma}{\Delta_p^2} \quad (2.58)$$

where ℓ represents the path length through the sample. The factor ℓ_0 is the unsaturated absorption length. This resonance does not depend on the light power and has a width of Γ . The scaling for large detunings, $\Delta_p \gg \Gamma, \Omega_L, \gamma$, is also shown.

Over the narrower NMOR region, which has width on the scale of γ this term is largely constant.

The next order effect is second order in the Rabi frequency and is due to orientation that results from optical pumping in the presence of a magnetic field. The Zeeman shifts of the ground state sublevels result in local detunings that differentially pump on $m_F \rightarrow m_{F'} = m_F \pm 1$ transitions resulting in circular birefringence.

$$\ell_0 \frac{d\phi}{d\ell} = \frac{\Omega_R^2 \Omega_L \Gamma^2 \Delta_p^2 \sin(\alpha)}{12\gamma(\Gamma^2 + 4\Delta_p^2)^3} \propto \frac{\Omega_L}{\gamma} \frac{\Omega_R^2 \Gamma^2}{\Delta_p^4} \quad (2.59)$$

This resonance also has a width of Γ and so is not overly important to the features in the NMOR resonance region.

There is another second order effect that corresponds to the low probe intensity NMOR described earlier: optical pumping generates alignment, which precesses in the field and is probed resulting in linear dichroism. The polarization rotation due to this effect is

$$\ell_0 \frac{d\phi}{d\ell} = -\frac{\Omega_R^2 \Gamma^3 (3 \cos(2\alpha) + 5) \sin(\alpha)}{192 \Omega_L (\Gamma^2 + 4\Delta_p^2)^2} \propto -\frac{\Gamma}{\Omega_L} \frac{\Omega_R^2 \Gamma^2}{\Delta_p^4}. \quad (2.60)$$

This resonance has width of γ and so could contribute to the NMOR region. However, at large detunings the scaling with Γ/Ω_L is not favorable and leads to small signals.

A more favorable scaling is found with the next higher order effect: that due to alignment-to-orientation conversion. As will be derived in more detail next, this

signal takes the form of

$$\ell_0 \frac{d\phi}{d\ell} = \frac{\Omega_R^4 \Gamma^2 \Delta_p^2 (9 \cos(4\alpha) + 20 \cos(2\alpha) + 3) \sin(\alpha)}{4608 \gamma \Omega_L (\Gamma^2 + 4 \Delta_p^2)^3} \propto \frac{\Gamma^2}{\gamma \Omega_L} \frac{\Omega_R^4}{\Delta_p^4}. \quad (2.61)$$

This resonance has the same large detuning scaling ($1/\Delta_p^4$) as the last two effects. It ends up dominating over both because it has width γ relative to the second order orientation effect and is amplified by a factor of Γ/γ relative to the second order alignment effect.

The validity of the perturbative approach depends on being below saturation for the coherent atomic effects studied here. Usually this saturation parameter would be $\Omega_R^2/\Gamma\gamma$, which is essentially a statement of how quickly coherences can be generated relative to the dephasing of the excited and ground states. However, when far detuned from resonance and using relatively strong magnetic fields, $\Gamma \rightarrow \Delta_p$ and $\gamma \rightarrow \Omega_L$. This gives an alternate saturation parameter more relevant to this work of $\Omega_R^2/\Delta_p\Omega_L$.

I will now outline the steps of the perturbative model, restricted to the terms that result in the AOC mechanism.

Step 1 I begin in step one by taking an unpolarized atomic sample and allowing the probe field to optically pump it, thereby polarizing the sample. This step is done only with the light interaction portion of the Hamiltonian; the magnetic fields and Stark shifts are ignored. As a result, this step can actually be performed by solving the OBEs without approximation for even more complicated transitions. However,

for the sake of simplicity I will apply some *a priori* knowledge about the system. Namely, only the alignment of the atomic polarization is relevant since the light is detuned sufficiently from resonance in the experiment. Further, I know that the alignment axis will be either parallel or perpendicular to the light polarization axis, depending on whether the transition exhibits EIT or EIA, respectively. Since I am considering the simpler $F = 1 \rightarrow F' = 0$ transition at the moment, I will take an EIT polarization.

This is most simply done by defining pure axial alignment in a frame aligned with the polarization axis. This reduces the alignment tensor to a single non-zero component: $\rho^{(2)} \propto (0, 0, 1, 0, 0)$. I then rotate from this frame to the primed frame, which is done by rotating about the y -axis with an angle $\alpha - \pi/2$. The initial optically-pumped alignment in the primed frame is then:

$$\rho'^{(2)} \propto \sqrt{\frac{3}{2}} \begin{pmatrix} \sin^2(\alpha)/2 \\ -\cos(\alpha)\sin(\alpha) \\ (3\cos(2\alpha) + 1)/2\sqrt{6} \\ \cos(\alpha)\sin(\alpha) \\ \sin^2(\alpha)/2 \end{pmatrix} \quad (2.62)$$

Note that the *a priori* assumption (that only alignment is relevant) restricts us to the case off-resonant probing as well as ground states that can support alignment, which is $F \geq 1$. The model is readily expanded beyond these limitations by applying the same steps to the other relevant tensors, usually the orientation tensor.

Step 2 This step begins the generalized treatment of the alignment-to-orientation conversion process. Here I account for Larmor precession of the alignment from step 1 as well as dephasing of that alignment. In the primed frame, the Larmor precession acts as a time-dependent phase shift on each alignment component: $e^{iq\Omega_L t}$, where q is the component number (ranging from -2 to 2) and Ω_L is the Larmor frequency corresponding to the total magnetic field. The dephasing for each component takes the form of $e^{-\gamma t}$, where γ is the ground state dephasing rate. In this experiment, this rate is predominantly due to finite light-atom interaction time. I assume that the alignment from step 1 is continuously pumped, leading to an average accumulated phase term for each alignment component of

$$\gamma \int_{-\infty}^t e^{-\gamma(t-t')} e^{iq\Omega_L(t-t')} dt' = \frac{\gamma}{\gamma - iq\Omega_L} = \frac{i\xi}{q + i\xi} \quad (2.63)$$

In this result I have defined a new parameter $\xi = \gamma/\Omega_L$ that represents the attenuation factor for the atomic coherences under Larmor precession. Note that when $q = 0$, corresponding to alignment parallel with the z' -axis, there is no phase shift. Applying these shifts to the alignment of step 1 gives the Larmor precessed result.

$$\rho''^{(2)} \propto \sqrt{\frac{3}{2}} \begin{pmatrix} i\xi \sin^2(\alpha)/4 \\ -i\xi \cos(\alpha) \sin(\alpha) \\ (3 \cos(2\alpha) + 1)/2\sqrt{6} \\ -i\xi \cos(\alpha) \sin(\alpha) \\ -i\xi \sin^2(\alpha)/4 \end{pmatrix} \quad (2.64)$$

Step 3 This step performs the actual alignment-to-orientation conversion, as discussed above in Section 2.3.1.2. As a reminder, AOC is due to Stark shifts from the probe field interacting with the precessed atomic polarization. The general effect can be thought of as the electric field inducing a dipole moment from the atomic alignment that then experiences a torque from the electric field to produce orientation. Here I use the same approximation from Eq. 2.57, but written in terms of spherical tensor products: [31]

$$\rho^{(1)} \propto i \left\{ \left\{ \rho^{(2)} \otimes E^{(1)} \right\}^{(1)} \otimes E^{(1)} \right\}^{(1)}, \quad (2.65)$$

where \otimes is the spherical tensor product and the superscripts say which tensor component each term is. To use this equation I need to define the electric field from the probe light in the spherical basis of the primed frame:

$$E^{(1)} \propto \begin{pmatrix} -\sin(\alpha)/\sqrt{2} \\ \cos(\alpha) \\ \sin(\alpha)/\sqrt{2} \end{pmatrix} \quad (2.66)$$

I substitute this field into Eq. 2.65 along with the precessed alignment from step 2 to obtain the following (expressed in cartesian coordinates of the primed frame for simplicity):

$$\rho_{\text{cart}}^{(1)} \propto \frac{3}{16\sqrt{5}} \begin{pmatrix} \xi \cos(\alpha)(7 \sin(\alpha) + 3 \sin(3\alpha))/2 \\ \sin(2\alpha)(3 \cos(2\alpha) + 1) \\ \xi \sin^2(\alpha)(3 \cos(2\alpha) + 5) \end{pmatrix} \quad (2.67)$$

Again, because the probe is detuned I know that the AOC mechanism is the dominant factor for polarization rotation. As a result, I will only track this generated orientation from this point forward.

Step 4 I now need to allow the generated orientation from the AOC process to precess in the magnetic field. This is done in exactly the same way as step 2. The resulting precessed orientation, again expressed in cartesian coordinates of the primed frame, is then:

$$\rho_{\text{cart}}^{'''(1)} \propto \frac{3}{16\sqrt{5}} \begin{pmatrix} -\xi \sin(2\alpha)(3 \cos(2\alpha) + 1) \\ 0 \\ \xi \sin^2(\alpha)(3 \cos(2\alpha) + 5) \end{pmatrix} \quad (2.68)$$

Here I have ignored any terms that are second order in ξ . This is justified under the assumption that the dephasing rate is small compared with the Larmor frequency of the total magnetic field for all values of the total magnetic field. Put more simply, the Larmor frequency of the static transverse field is larger than the dephasing rate.

Step 5 Finally, the generated and precessed orientation is probed. To first order in the optical Rabi frequency the polarization rotation due to atomic polarization is proportional to

$$\phi \sim \sqrt{2}\Delta_p \text{Re}(\rho_0^1) + \Gamma \text{Im}(\rho_2^2) \quad (2.69)$$

where ρ_0^1 and ρ_2^2 are the tensor components of the atomic polarization in the lab frame. In the experimental system $\Delta_p \sim 5\Gamma$, which means the orientation is the dominant source of polarization rotation. In particular, it is the orientation along the lab z -axis that determines the polarization rotation.

I rotate the orientation from step 4 from the primed frame to the lab frame and find that the polarization rotation becomes

$$\phi \sim \sqrt{2}\Delta_p \text{Re}(\rho_{\text{lab-}z}^{\prime\prime\prime(1)}) \propto \frac{3\sqrt{2}\Delta_p \xi \sin(\alpha)(9 \cos(4\alpha) + 20 \cos(2\alpha) + 3)}{64\sqrt{5}} \quad (2.70)$$

Figure 2.11 shows this result versus axial magnetic field where a “twist” qualitatively similar to that of the experiment is observed. Most importantly, this equation can be solved for the polarization rotation zero crossings to find the width of the “twist” feature. Solving Eq. 2.70 I find that the “twist” zero crossings occur when $\alpha = \pm \arctan\left(\sqrt{\sqrt{13}-3}\right) \approx \pm 0.661$. In the experimental data it is easier to reliably identify the peaks of the “twist.” I can find the peak splitting of this model by converting to the cartesian lab magnetic fields, taking the derivative with respect to B_z , and solving for the zeros. Doing so gives the peak splitting $\Delta B_z = 0.661 B_x$. The identical value is a coincidence.

I can also break up the total orientation into two distinct contributions: (1) that due to the precessed alignment from step 2 that is parallel to the z' -axis; (2)

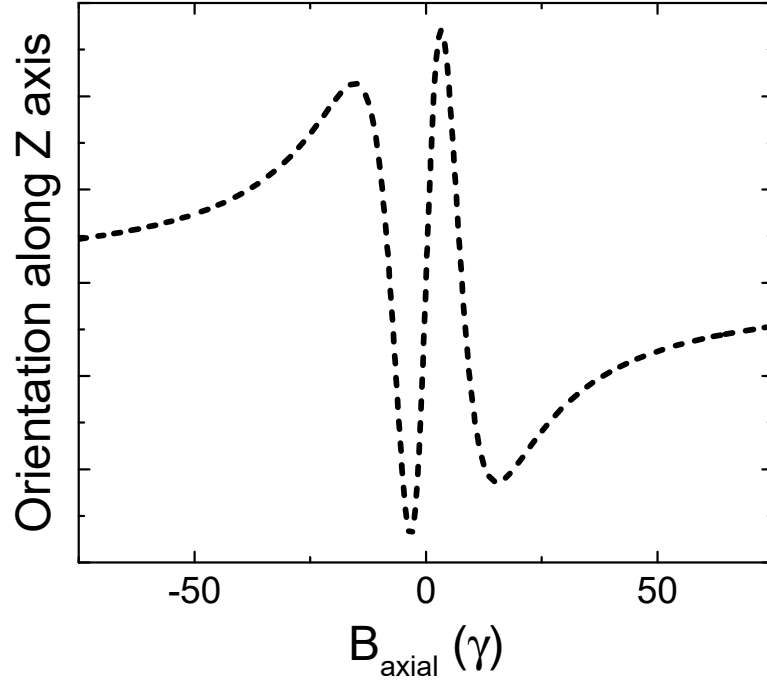


Figure 2.11: Total orientation along the z -axis from Fig. 2.12, plotted versus axial magnetic field instead of total magnetic field angle α . I have taken $B_{\text{trans}} = 10\gamma$.

that due to precessed alignment perpendicular to the z' -axis.

$$\begin{aligned}\phi &\sim \sqrt{2}\Delta_p \text{Re} \left(\rho_{\text{lab-z}}'''^{(1)} \right) = \sqrt{2}\Delta_p \text{Re} \left(\rho_{B\parallel}'''^{(1)} + \rho_{B\perp}'''^{(1)} \right) \\ &\propto \frac{3\sqrt{2}\Delta_p \xi}{16\sqrt{5}} \left(2\sin(\alpha)\cos^2(\alpha)(3\cos(2\alpha) + 1) - \sin^3(\alpha)(3\cos(2\alpha) + 5) \right) \quad (2.71)\end{aligned}$$

Figure 2.12 shows these two components as well as their total versus the angle α . It can be seen that the red trace showing orientation due to alignment parallel to z' exhibits a “twist” where the sign of polarization rotation is reversed near zero field. The orientation due to non-parallel alignment only serves to reduce the size of the “twist.” Note that it is the orientation from this non-parallel alignment that gives the NMOR signal for AOC without a transverse field present.

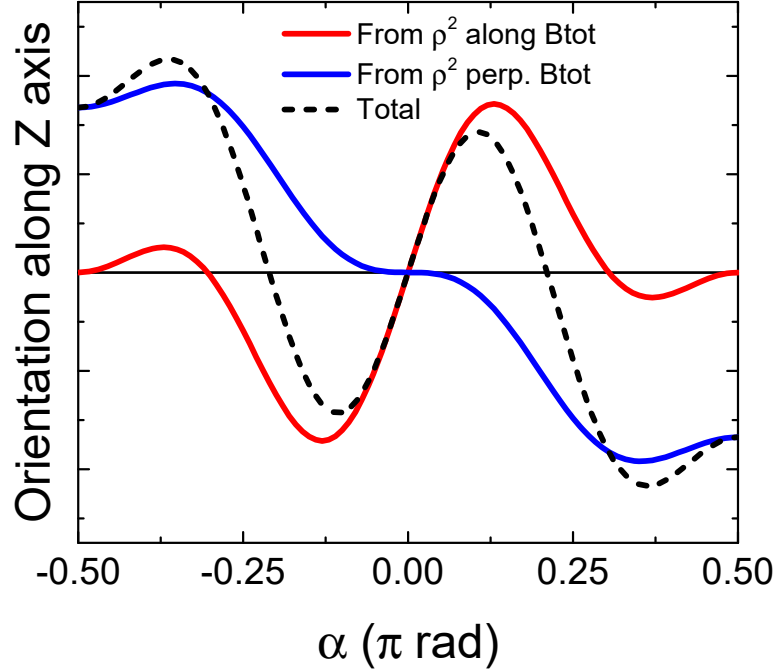


Figure 2.12: Plots of Orientation due to initial atomic alignment along and perpendicular to the total magnetic field direction as a function of magnetic field direction.

I can solve for the zero crossings of the red curve in Fig. 2.12 and find that they occur when $\alpha = \pm \arccos(1/\sqrt{3}) \approx 0.955$. The lab frame peak splittings of the “twist” for this angle gives $\Delta B_z = 0.80B_x$. This value is identical to that found in [11] where they observed a “twist” signal due to averaging effects from a coupled RF field. I can therefore claim that our “twist” is due to a similar mechanism where the Larmor precession of the aligned polarization in step 2 will average to net-zero alignment at a particular angle between the total magnetic field and the polarization axis. The only difference between their result and ours is that our “twist” mechanism must also compete with the typical NMOR-AOC mechanism, which reduces the angle at which to zero locations occur.

Ultimately, I expect the experimentally measured slope of the “twist” peak splitting to be between the two slopes derived here of 0.661 and 0.80.

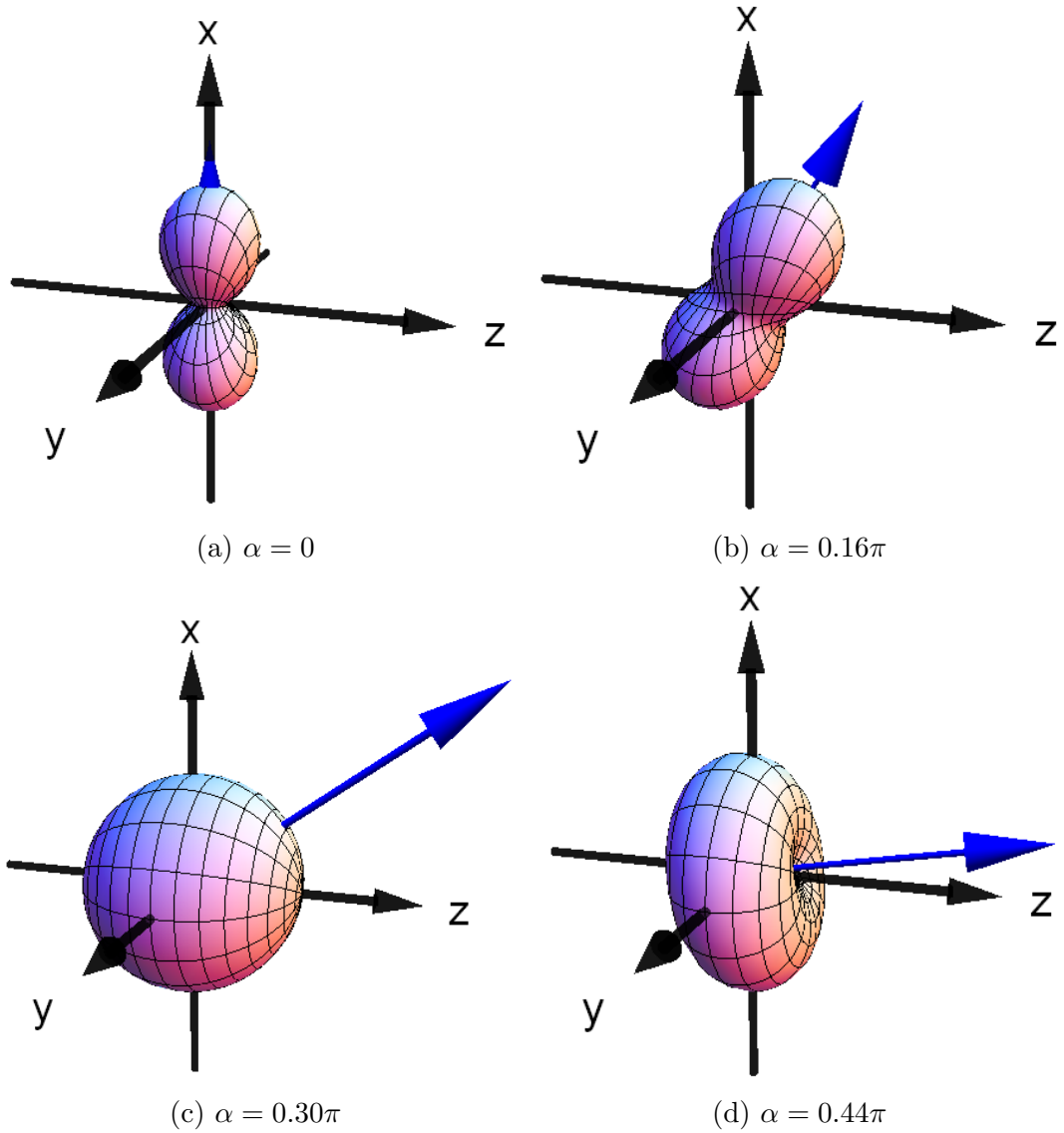


Figure 2.13: Progression of polarization moments showing the the precessed alignment parallel to the z' -axis. In order, the points shown show the central zero crossing, the peak polarization, the “twist” zero crossing, and the second peak location from the red trace of Fig. 2.12.

This averaging process is best visualized using polarization moments. In Fig. 2.13 I show the alignment after step 2 that is parallel to the z' -axis (the $\rho_0^{(2)}$ component in the primed frame). Parts (a-d) correspond to specific places of interest in the red trace of Fig. 2.12. Figure 2.13(a) shows the alignment at $\alpha = 0$. No polarization rotation results from this since the alignment axis is parallel to the electric field precluding the AOC mechanism. Figure 2.13(b) shows the alignment at $\alpha = 0.16\pi$. Here we see that the small total magnetic field has precessed some of the alignment to be parallel to the z' -axis, resulting in the peak positive polarization rotation. Figure 2.13(c) shows the alignment at $\alpha = 0.30\pi$. Here there is no polarization rotation because the alignment along \hat{z}' has been averaged to zero by the precession, leaving only an isotropic polarization. Figure 2.13(d) shows the alignment at $\alpha = 0.44\pi$. Here the peanut shaped alignment precesses about the magnetic field so quickly that an averaged donut shape is formed. The donut shape represents alignment with negative sign which can be thought of as taking a spherical, isotropic polarization moment and subtracting a peanut shaped alignment moment. This negative moment gives the peak negative polarization rotation.

2.3.2.2 3-Axis Solution

Generalizing the above treatment for arbitrary transverse field direction is relatively straight-forward. It only requires a more complex frame rotation to get into the \vec{B}_{tot} primed frame. This is most easily done by specifying a rotation about the z -axis by an angle $\tan(\beta) = B_y/B_x$, then a rotation about the new y axis by

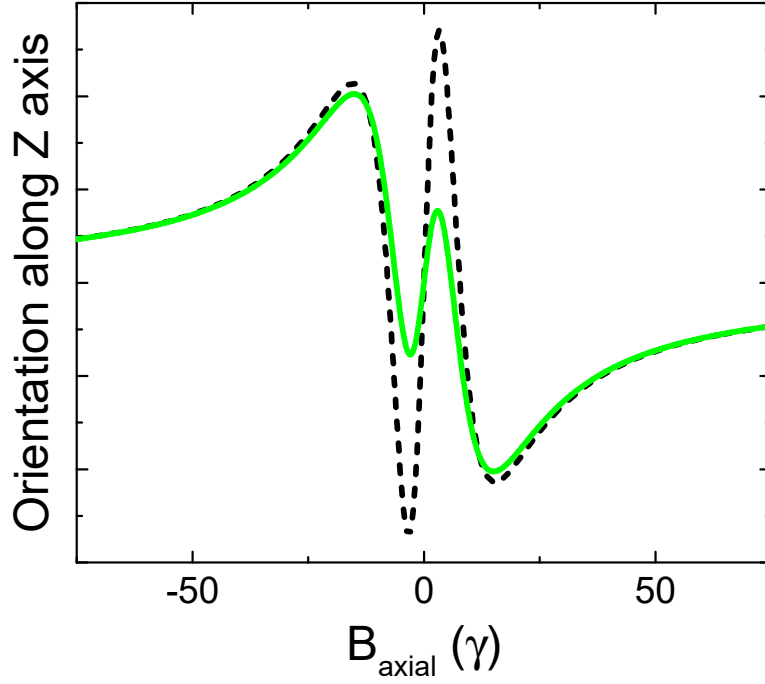


Figure 2.14: Total orientation along the z -axis. The black-dash trace has $B_x = 10\gamma$. The green trace includes a perpendicular transverse field $B_y = 5\gamma$.

the angle $\tan(\alpha) = B_{\text{axial}}/B_{\text{trans}}$, where $B_{\text{trans}} = \pm\sqrt{B_x^2 + B_y^2}$. Reversing these rotations will return to the lab frame. In this section I will often refer to the transverse magnetic field components by their relation to the light polarization axis: $B_x \rightarrow B_{\parallel}$ and $B_y \rightarrow B_{\perp}$.

The result of the 5-step model, including B_y , is quite complex so I do not include it here and instead direct the interested reader to Appendix B where the *Mathematica* code for the 5-Step model calculations can be found. Instead I show the result in the green trace of Fig. 2.14 in comparison with the result from the last section. The green trace includes a $B_{\perp} = 5\gamma$ perpendicular transverse field. Note that the primary, discernible effect is a reduction in the “twist” contrast and corresponding small changes to the “twist” zero locations. I will refrain from going

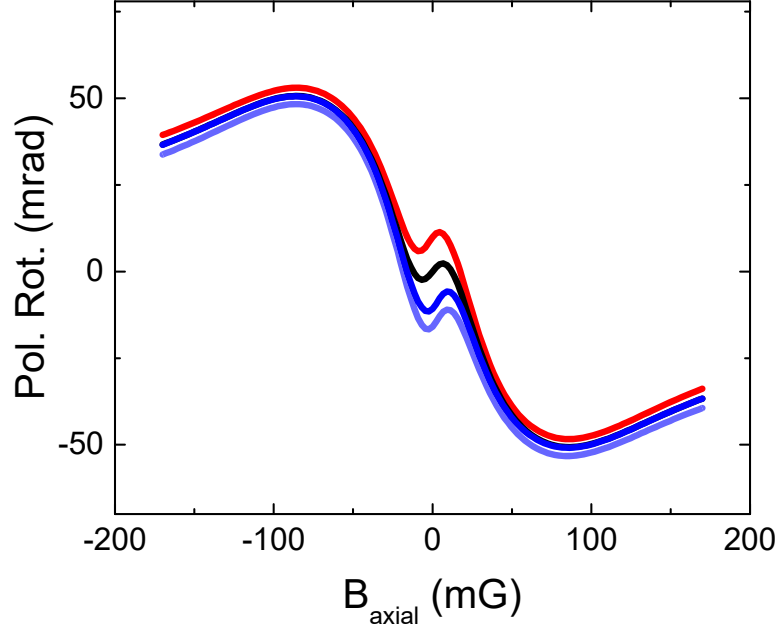


Figure 2.15: Simulations of NMOR for different linear polarization angles relative to a static B_x magnetic field. The linear polarization angles range from 4° , 0° , -4° , -7° ; from light red to light blue. The Rabi frequency is 9.26 MHz, the detuning 4.43Γ , and $B_x = 48$ mG. As the light polarization angle deviates from zero, some of the transverse field becomes perpendicular to the light E-field leading to a shift of the “twist” away from zero rotation.

into more detail on this model because it does not capture one very important feature of the “twist” dependence on B_\perp that is seen experimentally and in the full numerical model: the “twist” shifts relative to the polarization rotation zero.

In Fig. 2.15 I show numerical simulations of the NMOR signal from later in this chapter where the direction of linear polarization is rotated relative to a static transverse field. When the light polarization is not parallel to the transverse field the field is decomposed into parallel and perpendicular components. The perpendicular component then results in an offset of the “twist” away from zero rotation. This effect was observed in warm vapor NMOR [8, 32] and like the “twist” itself was attributed to interaction between the many optical pumping pathways between the

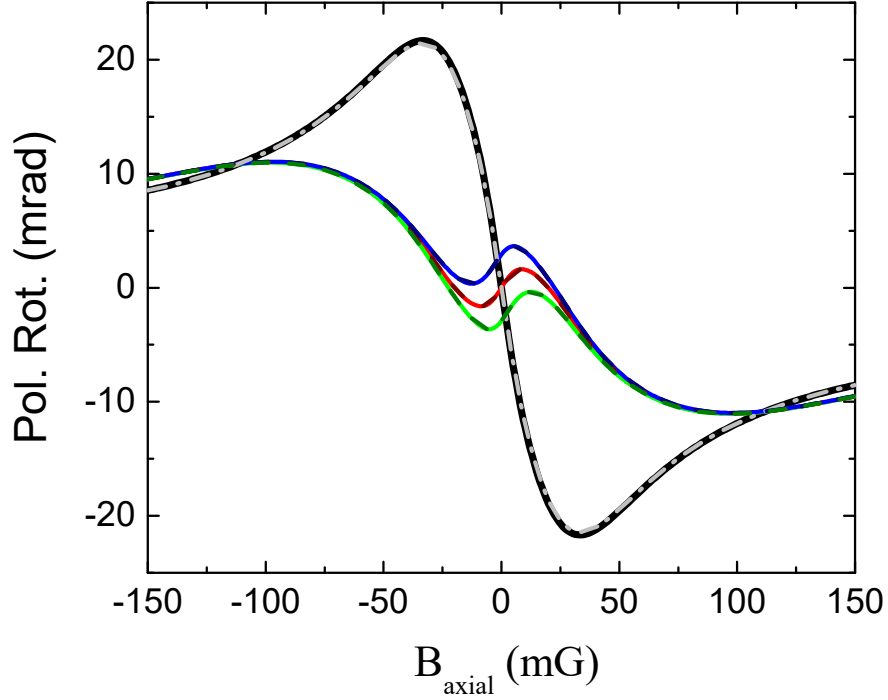


Figure 2.16: "Twist" shift vs transverse fields. The black trace is the typical NMOR with no transverse fields. The gray dash-dot trace is with $\pm\delta B_{\perp}$ fields. The red and dark red traces are with $\pm\delta B_{\parallel}$ fields. The green and dark green traces represent both transverse fields present with odd sign parity. The blue and dark blue traces have even sign parity. A fixed probe Rabi frequency of 9.26 MHz and a detuning of 4.43Γ is used. The transit rate is 2 kHz. The magnitudes of the transverse fields were $\delta B_{\parallel} = 55\text{ mG}$ & $\delta B_{\perp} = 5\text{ mG}$, when present.

Doppler-broadened hyperfine levels. This explanation is not applicable here as the simulation is ignorant of Doppler broadening and experimental data using cold atoms supports the Doppler-free simulation as will be shown below. Like the "twist" itself, a deeper explanation is required. Unfortunately the 5-Step model described above is not sufficient to describe this shifting behavior. Instead I will rely on full numerical simulations to gain insight into the parameters that govern this observed offset.

Figure 2.16 shows the "twist" offset for varying combinations of $B_{\parallel} = 0, \pm 55\text{ mG}$ and $B_{\perp} = 0, \pm 5\text{ mG}$. The opposite sign of a field represents the opposite orientation of the field along the same axis. In this figure there are four pairs of traces.

| δB_{\parallel} | δB_{\perp} | Twist |
|------------------------|--------------------|----------|
| 0 | 0 | None |
| 0 | \pm | None |
| + | 0 | Centered |
| - | 0 | Centered |
| + | + | Down |
| + | - | Up |
| - | + | Up |
| - | - | Down |

Table 2.1: **Summary of Fig. 2.16.** The parallel B-field magnitude is 55 mG. The perpendicular B-field magnitude is 5 mG.

The black trace is typical NMOR with no transverse fields present and is provided as a reference. The gray dash-dot trace (which nearly perfectly overlaps the black trace) is the resulting NMOR if the perpendicular transverse field $B_{\perp} = 5$ mG is present with either orientation along $\pm\hat{y}$. The overlapping red and dark red dashed traces show the typical “twist” when only the parallel transverse field $B_{\parallel} = 55$ mG is present, again in either orientation along $\pm\hat{x}$. The overlapping green and dark green dashed traces show an offset “twist” away from zero rotation when both the parallel and perpendicular transverse fields are present. In this case the fields are oriented such that they have opposite sign parity (*i.e.* $+/-$ and $-/+$). The overlapping blue and dark blue dashed traces are the same as the green traces, but with even sign parity (*i.e.* both signs positive or negative). These relations are summarized in Table 2.1. It is interesting that while the “twist” itself is agnostic to the sign of the transverse field, when an offset is present the direction of said offset away from zero rotation depends on the sign of both transverse field components. From this I infer that the offset is the result of some broken symmetry in the presence of a perpendicular transverse field.

The dependence of this shift is not isolated to the magnetic fields, as evidenced by the breakdown of the 5-Step model. Figure 2.17 shows the “twist” offset for varying Stark shifts with different probe Rabi frequencies and detunings. For the purposes of this discussion the Stark shift is defined as

$$\Omega_{AC} \propto \frac{\Delta_p \Omega_R^2}{\Gamma^2 + 4\Delta_p^2}. \quad (2.72)$$

The black trace shows the green trace from Fig. 2.16 while the blue and red traces have a detuning one natural linewidth smaller and larger, respectively, with $B_{\parallel} = 55$ mG and $B_{\perp} = 5$ mG. From this we see that the offset and qualitative shape of the “twist” itself depends on the detuning. The reduction in contrast of the “twist” as the detuning is reduced is due to the suppression of the AOC mechanism as described above. The offset shows proportional dependence on the detuning. The green trace has a detuning equal to that of the black trace, but with a higher Rabi frequency such that the AC Stark shift, as defined in Eq. 2.72, is equal to that of the blue trace. While the “twist” shape and offset are not identical, they are qualitatively similar hinting that the Stark shift plays a dominant role in the magnitude of the offset.

This dependence on the Stark shift is likely the reason the 5-Step model breaks down. That model relies on perturbative solutions to the OBEs in the probe Rabi frequency, implying that Ω_R is small relative to other rates in the problem. As discussed above, the saturation parameter that dictates validity for the perturbative model is $\Omega_R^2/\Omega_L\Delta_p$. For typical experimental parameters present here, this param-

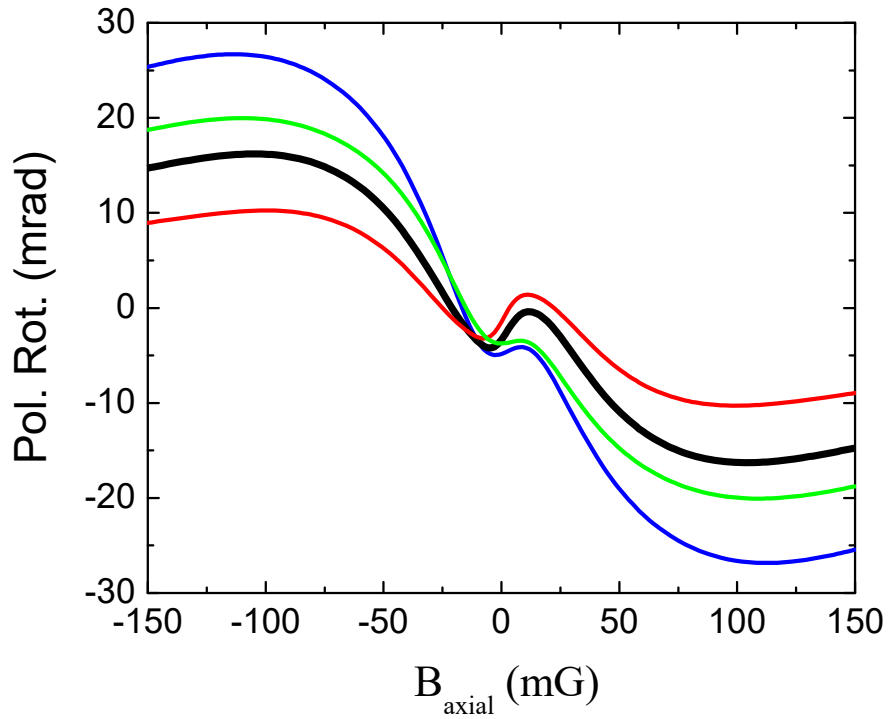


Figure 2.17: "Twist" shift vs Stark shift. The black trace has a detuning of 4.43Γ . The red trace a detuning of 5.43Γ . The blue trace a detuning of 3.43Γ . The green trace has a detuning of 4.43Γ and an increased Rabi frequency of 10.47 MHz . The blue and green traces have the same Stark shift as calculated from Eq. [2.72](#).

eter is on the order of 10. This constraint limits the validity of the model for large Stark shifts. Perhaps what is more interesting is that the perturbative model is successful at all when comparing to the experimental system, even at a qualitative level.

Moving away from the model, I can make a guess as to the functional dependence of the offset by trying to account for the observed dependencies. One such functional form that encapsulates the above behaviors is

$$shift \propto \frac{\Omega_{AC}\omega_{\perp}\omega_{\parallel}}{\Omega_{\text{tot}}^2}, \quad (2.73)$$

where ω_{\parallel} , ω_{\perp} , and Ω_{tot} are the Larmor frequencies of the parallel transverse, perpendicular transverse, and the total magnetic fields. Unfortunately the vacuum chamber of the experiment broke before significant data could be taken to confirm this guesstimate.

2.4 Experimental Characterization of the

“Twist”

In this section I present experimental measurements of the “twist” versus transverse magnetic field strength and orientation as well as probe power and polarization. I will compare this data with the full numerical model and show good quantitative agreement. I will also show how the “twist” can be used to measure transverse field gradients.

2.4.1 Experimental Configuration

The experimental setup is diagrammed in Fig. 2.18. The atomic sample comes from a cold cloud of roughly 10^7 ^{87}Rb atoms in a Magneto-Optical Trap (MOT), collected from background vapor in a 1 x 1 x 3 inch glass vacuum chamber, and further cooled in an optical molasses to approximately 50 μK . The magnetic field is applied using three perpendicular sets of Helmholtz coils (only 1 pair is shown in Fig. 2.18 for simplicity). The MOT light was produced by a pair of Distributed Bragg Reflector (DBR) laser diodes. One is locked to the $F = 1 \rightarrow F' = 2, 3$ crossover line in a spectroscopy cell via Saturated Absorption Spectroscopy (SAS). The pumping light in the spectroscopy setup was double-passed through an 80 MHz Acousto-Optic Modulator (AOM) to give a frequency shift of 160 MHz. [33] This shift results in a difference of 80 MHz between the SAS lock point and the master laser. This shift allows us to lock to the strongest transition of the repumping

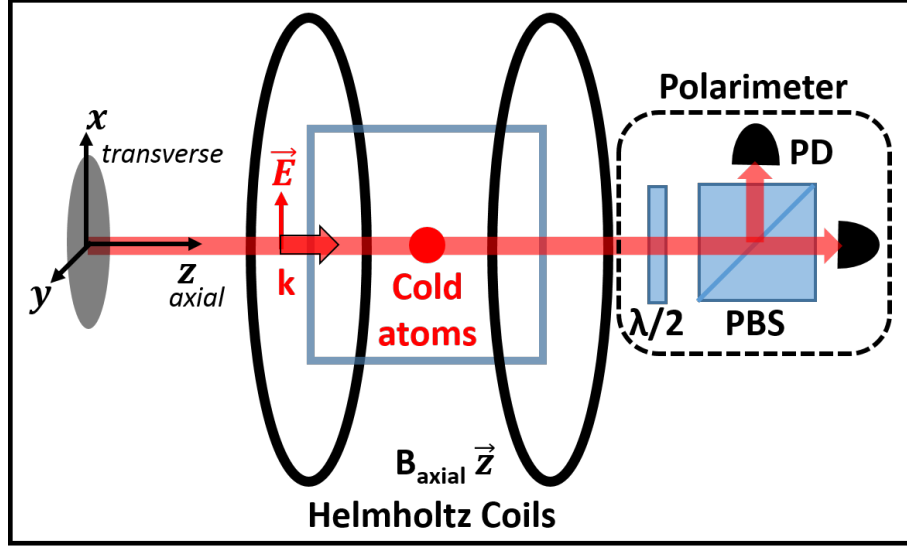


Figure 2.18: Experimental configuration. $\lambda/2$: half-wave plate, PBS: polarizing beam splitter, PD: photodetectors.

transition while still being able to use the main laser output as the repump laser for the MOT, which is resonant with the $F = 1 \rightarrow F' = 2$ repump transition. The second DBR is beat note locked to the repump light. This allows for fast, real-time control of the cooling light frequency during experimental shots. This laser is amplified using a tapered amplifier to produce the optical power necessary for the MOT cooling. All repump and cooling light has an AOM and physical shutter for fast, yet complete, shuttering of the MOT beams during the NMOR experiment.

The probe light comes from the cooling laser through an AOM and physical shutter. This light also has a fiber amplitude modulator that allows for power stabilization of the probe beam. Unless otherwise stated, the probe light is detuned 27 MHz to the red of the $F = 2 \rightarrow F' = 3$ transition of the $D2$ line with typical intensity of $11 \mu\text{W}/\text{mm}^2$. The beam size is chosen such that the size (the $1/e^2$ width) of the beam approximately matches that of the atomic cloud. The polarization is

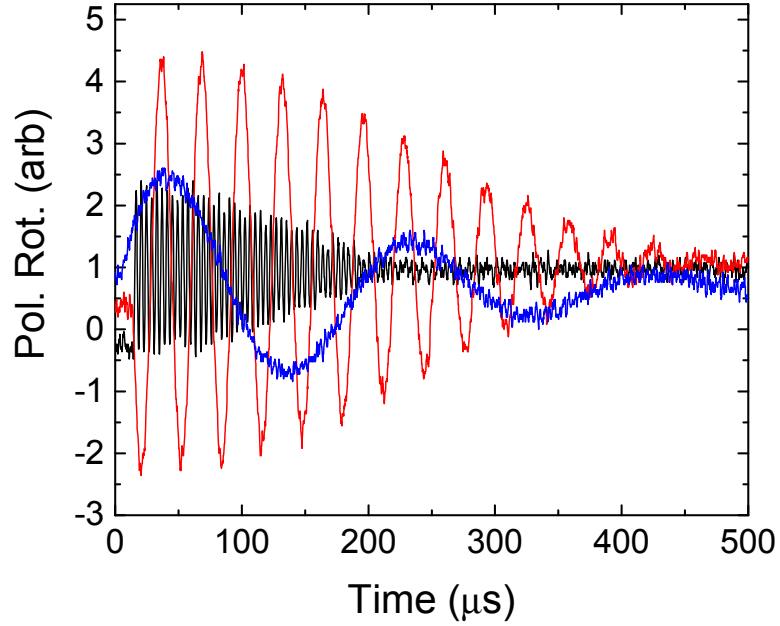


Figure 2.19: Example FID trace measurements. The total magnetic field at the atoms is reduced from black to red to blue traces. The frequency of the oscillation is proportional to the Larmor frequency while the decay time gives the approximate dephasing time for the optically pumped atomic polarization.

controlled with a Wollaston prism followed by a quarter-wave plate to compensate for induced ellipticity from the glass vacuum cell's birefringence. There is also a half-wave plate which allows arbitrary rotations of the probe polarization relative to the magnetic fields from the coils.

2.4.1.1 Magnetic Coil Calibration

In this experiment I took care to direct the beam coaxially with the relevant coil pair to better than one degree, as this keeps the magnetic field degrees of freedom relative to the light independent in the Helmholtz coils. These coils were calibrated using a Free-Induction Decay (FID) method. [34–36] This technique is a highly accurate method of measuring the total magnetic field experienced by the

atoms. It works by optically pumping the atoms into a maximally-oriented stretch state ($m_F = \pm F$) with a circularly-polarized light pulse resonant with the $F = 2 \rightarrow F' = 2$ transition and a non-zero magnetic field perpendicular to the pumping axis. One then measures the decay of oscillations in the polarization rotation of a subsequent probe pulse that is not co-linear with the pump. The frequency of oscillations is proportional to the total Larmor frequency of the magnetic field while the decay indicates the dephasing time. These oscillations take the form of

$$\phi(t) \propto \frac{G}{B^2} (B_z B_y (1 - \cos(g|B|t)e^{-t/T_2}) + B_x |B| \sin(g|B|t)e^{-t/T_2}) F_y(0) \quad (2.74)$$

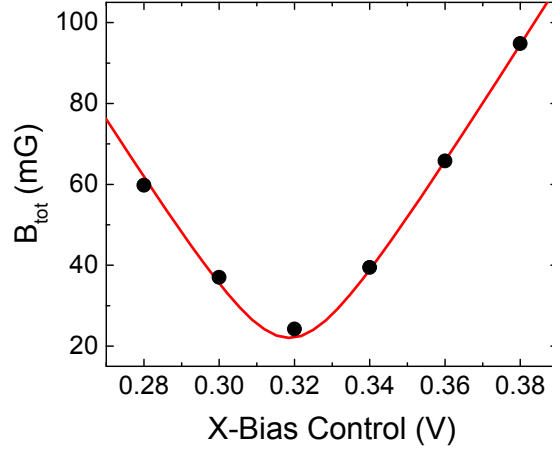
where G is an empirical coupling constant, $F_y(0)$ represents the initial atomic orientation along \hat{y} and perpendicular to the probing direction, $g = \mu_B g_F / \hbar$ is the gyromagnetic ratio, and T_2 is the coherence time. Example FID measurements for multiple magnetic fields are shown in Fig. 2.19.

Since this method is sensitive to the total Larmor frequency, complete calibration of the fields requires multiple steps:

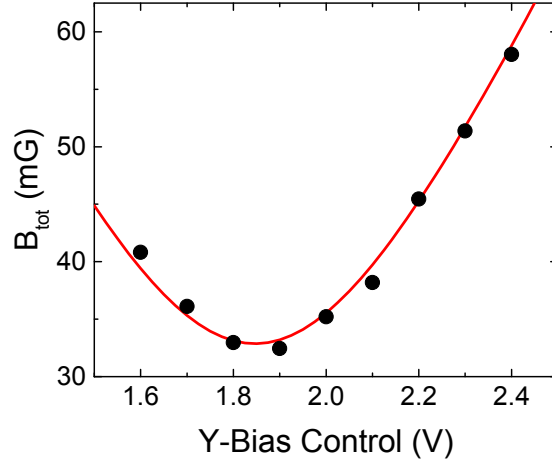
1. Null B_z , B_y by minimizing the total Larmor frequency with some $B_x \neq 0$ field.

This minimizes the cosine term in Eq. 2.74 simplifying the fits to experimental data. These fits are then performed for a range of B_x that traverses $B_z = 0$; the FID gives the total Larmor frequency for the total magnetic field from all three components.

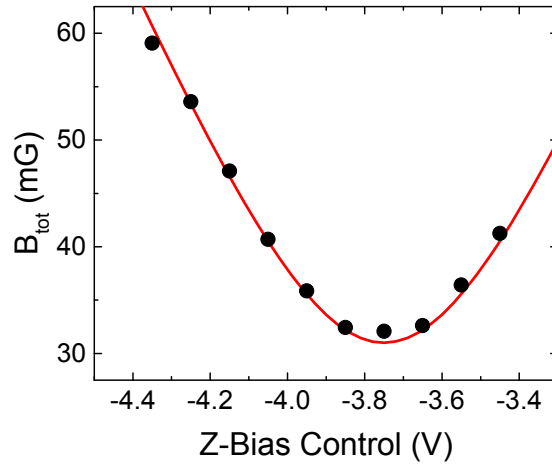
2. Apply a fixed $B_x \neq 0$ with B_z minimized such that the sine term is dominant



(a) B_{tot} extracted from FID measurements as the X-Coil control voltage is swept through $B_x = 0$ with $B_z \neq 0$.



(b) B_{tot} as the Y-Coil control voltage is swept through $B_y = 0$ with $B_z \neq 0$.



(c) B_{tot} as the Z-Coil control voltage is swept through $B_z = 0$ with B_x, B_y near zero.

Figure 2.20: The resulting data sets from following the calibration procedure in the text. I fit all data points simultaneously to Eq. 2.74 to obtain the coil calibration factors and field zeros. Statistical error bars from the fits are significantly smaller than the plotted data markers.

relative to the cosine in Eq. 2.74 and step B_y over a range of values traversing $B_y = 0$. Use FID to extract the total Larmor frequency.

3. Repeat the second step, varying B_z with B_y minimized.

The result of this process is three sets of measured Larmor frequencies versus the three perpendicular field directions, an example is shown in Fig. 2.20. I fit the entire data set to the equation

$$B_{\text{tot}} = \sqrt{G_x^2(V_x - V_{x0})^2 + G_y^2(V_y - V_{y0})^2 + G_z^2(V_z - V_{z0})^2} \quad (2.75)$$

shown as red lines in Figs. 2.20. The fit parameters V_{i0} give the control voltage for zero field along the i^{th} axis and G_i give the calibration factors that convert between control voltage and magnetic field. In general, the better B_z, B_y are nulled the better the FID fits will be, though exact cancellation is not required at any step for the overall calibration fit to converge.

Calibration of the coils using FID has a couple significant requirements that need to be considered. First is that two axes of optical access is required. Second is that the pumping light pulse needs to be relatively short (order 100 μs). Second, the magnetic fields need to be constant for the entire T_2 decay time in order to obtain an accurate fit of the Larmor oscillations. Our coil drivers were Kepco Bipolar current supplies that produce significant 60 Hz line noise magnetic fields. Using tuned 60 Hz magnetometers I estimated that the line noise field is on the order of 3 mG, which is more than enough to smear the FID signals. Ultimately it was necessary to trigger

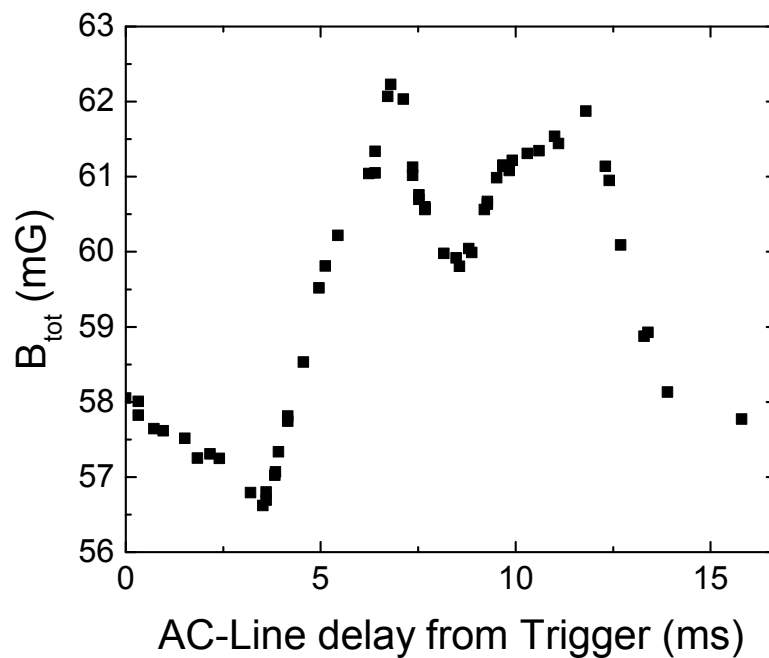


Figure 2.21: Ambient 60 Hz magnetic noise measured using FID by running the measurement many times and recording the offset of the FID pump pulse relative to the 60 Hz period. Significant structure is observed in the magnetic field experienced by the atoms. When the experiment is triggered on the line frequency, the time sensitive portions of the experiment are set to be during the relatively steady portion near 0 delay.

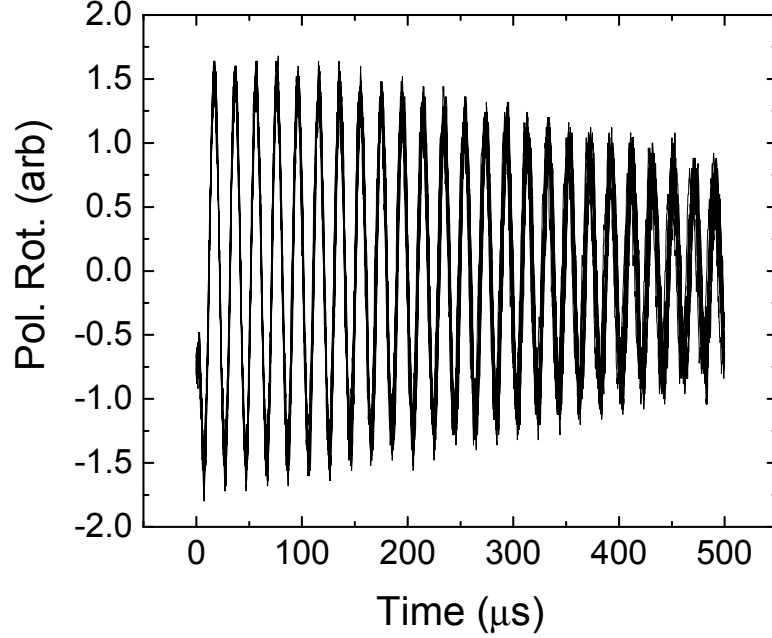


Figure 2.22: Multiple runs of the FID measurement with the same applied magnetic field and 60 Hz line triggering. Note that at longer times the small differences in frequency from shot to shot become more visible. This variation is due to residual ambient field fluctuations and the presence of magnetic gradients.

the experiment off the line frequency and map out the magnetic line noise to find a portion of the 60 Hz period with the smallest dynamic changes. Finally, magnetic gradients within the atomic sample also wash out the Larmor frequency measured and limit the T_2 time which ultimately limits the sensitivity.

2.4.1.2 NMOR Measurement

An NMOR experiment is performed by loading the atomic sample into the MOT for five seconds followed by brief cooling in the optical molasses with the MOT fields off. The optical molasses is released and probe light is shined through the atomic sample. The polarization rotation of the probe light, induced by interaction with the atoms, is measured with a balanced polarimeter as the coaxial

(*i.e.* $\hat{\mathbf{z}}$) magnetic field is swept through zero. The $\hat{\mathbf{x}}$ and $\hat{\mathbf{y}}$ magnetic fields in the perpendicular plane, which I call “transverse”, are held fixed.

The polarization rotation of the transmitted light is measured using a balanced polarimeter. This is made up of a half-wave plate, a polarizing beam splitter, and two photodiodes. The half-wave plate is rotated such that half of the probe light goes into each detector when no atoms are present. The polarization rotation angle is then related to the photodiode signals by

$$\phi = \frac{1}{2} \arcsin \left(\frac{S_1 - S_2}{S_1 + S_2} \right). \quad (2.76)$$

Note that this measurement is normalized to the total transmitted power, meaning that common-mode intensity noise is significantly reduced.

While the data can be collected with a continuous sweep of the axial magnetic field, our data are recorded using discrete steps. A continuous sweep complicates the analysis in three small but measurable ways. One is the atom loss during the course of the sweep, resulting in fewer atoms at the end of the sweep than at the beginning. The second is the induction of the coils causing a delay in achieving the magnetic field for a given current. Finally, the light-atom interaction time during the sweep is not constant. Stepping incrementally through the axial magnetic field values and reloading the MOT prior to each step eliminates these effects.

This experimental setup did not have the ability to actively stabilize the probe power during each shot. Instead the total transmitted power of the probe measured by the polarimeter was stabilized before each shot. This appears to have limited

probe power drifts during shots to less than 1%. In each discrete step, the polarization rotation signal is sampled after 1.5 ms of light-atom interaction time implying a ground state dephasing rate of at least $\gamma = 2\pi \times 100$ Hz.

2.4.1.3 *Experiment – Numerical Simulation Correspondence*

In order to relate experimental data to the full numerical simulations outlined in Section 2.2 I must estimate the probe Rabi frequency and the optical depth of the atomic sample.

The probe Rabi frequency can be estimated from the total measured power by

$$\Omega_R = \frac{d \cdot |E|}{\hbar} = \frac{d}{\hbar} \sqrt{\frac{2P}{c\epsilon_0\pi w^2}} \quad (2.77)$$

where d is the effective reduced dipole moment for the resonant transition, c is the speed of light, ϵ_0 is the vacuum permittivity, P is the probe power, and w is the $1/e^2$ waist. This formula is only approximate since it assumes the probe intensity is constant. Properly estimating the reduced dipole moment can also be tricky. Ultimately I tuned the Rabi frequency of the model to better match the data. The estimated Rabi frequency for the standard power used is $2\pi \times 9$ MHz.

The optical depth of the sample factors into the data as an overall multiplicative factor for the simulation. I estimated our optical depth using absorption imaging of the atomic cloud. I measured a typical depth of 1.25, though the depth of the atomic sample does vary from shot-to-shot, even more so over entire data sets. Again, the final optical depth for each data set was allowed some variation to

account for this.

2.4.2 “Twist” Dependence on Magnetic Fields

I begin by characterizing the “twist” versus static transverse magnetic fields. This characterization includes the dependence on transverse magnetic field magnitude as well as the angle of the transverse field relative to the probe polarization.

2.4.2.1 *Magnitude*

The raw data from typical B_{axial} scans where a transverse field parallel to the light polarization is applied is shown in Fig. 2.23(a). As expected, the width of the “twist” changes with the magnitude of B_{Tr} . The error bars represent the standard deviation statistical uncertainty. The results of my numerical simulation, using no free parameters, is plotted on top of the experimental data. We see that the numerical model accurately matches the data.

In Fig. 2.23(b) the black points show the measured “twist” width (*i.e.* the valley-to-peak width) as a function of B_{Tr} , and we see that it scales linearly as predicted by the perturbation model. This is a satisfying result as it shows the twist feature can be a useful measure of non-zero transverse field strength. The measured slope is 0.73, which falls between the predicted slopes from the perturbation model. We did observe that the measured slope depends on other experimental parameters, especially the probe power as discussed below. This means that the measured slope is not universal, but the relationship does appear to be consistently linear in the

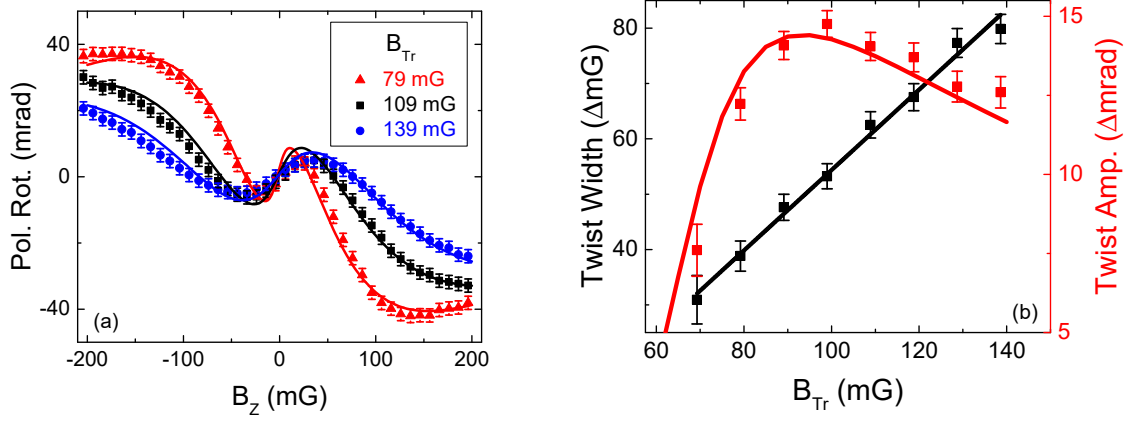


Figure 2.23: (a) Twist's dependence on the transverse magnetic field strength, lines are numerical simulation and points are experimental data. (b) Summary of twist widths & amplitudes versus the transverse field magnitude. In both cases the light is polarized along the direction of the transverse magnetic field with a fixed optical intensity of 1.03 mW/cm^2 .

transverse field magnitude.

The linear relationship seen in Fig. 2.23(b) holds for transverse magnetic field strengths whose Larmor frequencies (Ω_{L-Tr}) are on the order of the spin coherence lifetime ($1/\gamma$). If the transverse magnetic field is negligible ($\Omega_{L-Tr} \ll \gamma$) then the “twist” contrast is significantly reduced, as seen in the red points of Fig. 2.23(b). If the transverse magnetic field is too strong ($\Omega_{L-Tr} \gg \gamma$), such that the atoms precess many times within the decoherence time then the feature is essentially washed out.

Note that the lines of Fig. 2.23(b) also come from the numerical model, further showing the validity of the numerical model in predicting the experimental traces. The error bars on the data account for discrepancies between the numerical model and the experimental system.

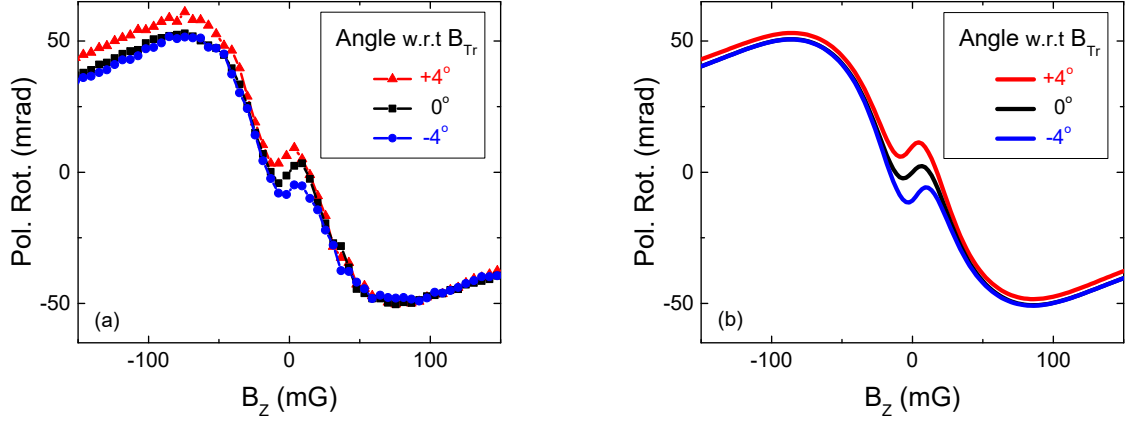


Figure 2.24: Impact of the angle between polarization and B_{Tr} (a) Points are Experimental data, while lines are guides for clarity; (b) Numerical simulation. Both have a fixed transverse field of $B_{Tr} = 48$ mG, and a Rabi frequency of 9 MHz.

2.4.2.2 Orientation

I next vary the orientation of the transverse field relative to the probe polarization axis. This is accomplished by rotating the plane of the linear polarization with a half-wave plate relative to a fixed transverse magnetic field. When the polarization is aligned with the transverse magnetic field, the “twist” is centered within the NMOR (both vertically and horizontally) and its contrast is maximized. Although not shown in these figures, I note that when the polarization is perpendicular to the transverse magnetic field the twist is not observed, rather the NMOR is simply broadened. In between the two extreme cases, *i.e.* when there is some intermediate angle between the optical polarization and transverse B-field, the “twist” is pulled vertically off-center relative to the NMOR feature. The “twist” feature itself remains centered horizontally as the polarization angle is changed; this is distinct from the effect of elliptical polarization described in the next section.

Figure 2.24 shows experimental (a) and simulated (b) data demonstrating the

dependence of the “twist” and NMOR features on the direction of the linear polarization vector relative to the transverse magnetic field direction. As described above, transverse magnetic field perpendicular to the light polarization angle causes the observed offset from zero polarization rotation. The direction of the perpendicular field dictates the sign of the offset relative to the overall NMOR. The numerical model gives good qualitative agreement. The quantitative overlap is not as good as in Fig. 2.23 because it was taken before I had configured the line frequency triggering of the experiment. As a result, the 3 mG 60 Hz magnetic field washes out the applied magnetic fields making the exact modeling difficult.

As described above, the magnitude of the offset depends on the magnitude of B_{\perp} as well as the Stark shift from the optical field. This effect could allow for some direct calibration of the B_{\perp} field magnitude. However, I note that the offset saturates when $B_{\perp} \sim B_{\parallel}$, which limits the dynamic range of any potential measurement.

2.4.3 “Twist” Dependence on Probe Field

I also measured the dependence of the “twist” on the ellipticity of the probe polarization and the probe power. These experimental parameters are not captured by the perturbative model but the numerical model appears to work well.

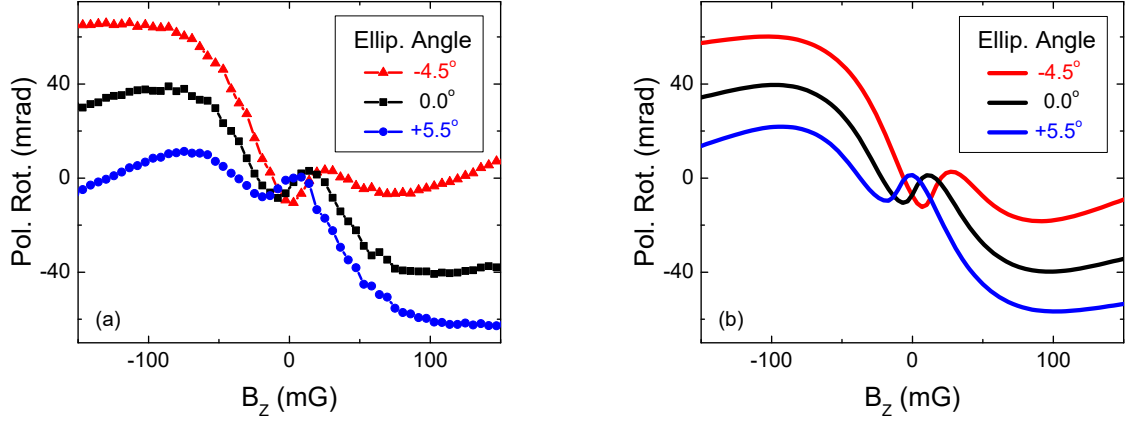


Figure 2.25: Impact of elliptical polarization. (a) Points are Experimental data, while lines are guides for clarity; (b) Numerical simulation. Both have $B_{\text{Tr}} = 55$ mG, and a Rabi frequency of 9 MHz.

2.4.3.1 Ellipticity

For elliptical polarization, the twist becomes asymmetric, as shown in Fig. 2.25.

I parameterize elliptical polarization using the angle of “ellipticity,” defined as the arctangent of the ratio of the minor to major axes of the polarization ellipse. As the degree of ellipticity is adjusted away from zero, we see that although the twist remains positioned about zero rotation (*i.e.* horizontal 0 mrad axis), it is not centered relative to the NMOR feature, and the central zero-crossing no longer occurs at $B_z = 0$. These effects are due to the vector component of the AC stark shift, associated with the circular polarization component of the light, which behaves as a fictitious magnetic field along the axial direction. [37] This breaks the symmetry of the real magnetic fields.

As I discussed above, to get pure linear polarization it was necessary to correct for the ellipticity induced by the birefringence of the glass vacuum cell by using a quarter-wave plate. The asymmetrically-shaped nature of the signal provided a

clear, qualitative indication of linear polarization, which made for simple optimization of this parameter.

2.4.3.2 *Optical Intensity*

Figure 2.26(a) shows the “twist” feature’s dependence on optical intensity. At intensities much lower than those used where the saturation parameter is small, $\Omega_R^2/\Gamma\gamma < 1$, the “twist” vanishes. Despite being detuned, intensities this small do not allow for significant AOC and therefore the rank-*two* polarization moment (alignment) dominates and does not result in the sign reversal behavior associated with the “twist.” As the intensity is increased, AOC becomes more prominent and orientation begins to dominate in the observed rotation signals, which allows the “twist” to become visible. As the intensity is increased further, the twist contrast saturates and ultimately diminishes until it is no longer visible. This occurs when $\Omega_R \gg \Gamma$.

The range of field strengths over which the “twist” is visible can be parameterized by a ratio of the $|\mathbf{E}|$ to $|\mathbf{B}|$ fields. I will use the ratio of the DC equivalent Stark shift, Ω_S , which is second order in the electric field, to the Larmor frequency, Ω_L . When the light is significantly detuned from resonance ($\Delta_p \gg \Gamma$), this Stark shift becomes $\Omega_S \simeq \Omega_R^2/\Delta_p$. In terms of the field ratio, Ω_S/Ω_L , the “twist” is visible over roughly two orders of magnitude from 0.01 to 1.0, revealing a wide range of applicability for these methods.

Note that at increased optical intensity the offset of the “twist” relative to

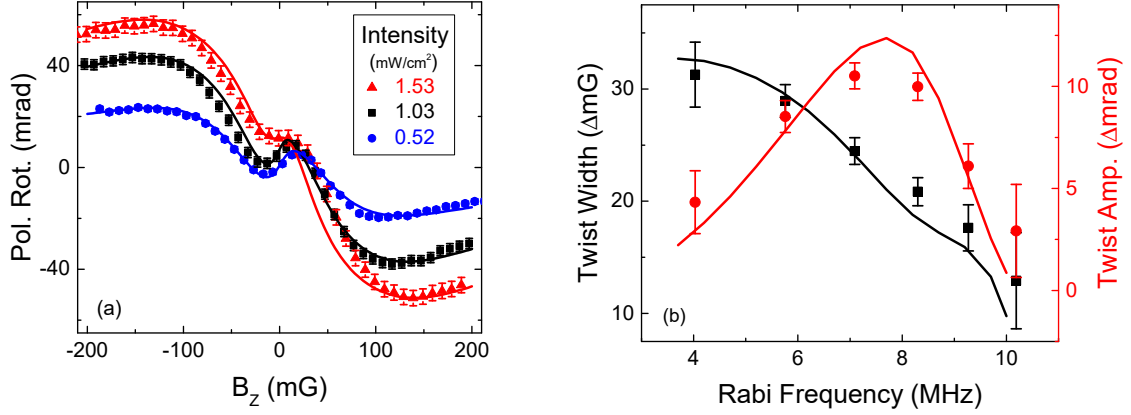


Figure 2.26: Experimental data (dots) of the twist’s dependence on optical power with numerical simulation (lines) overlaid. A fixed transverse field of 70 mG is applied parallel to the light polarization. (a) Raw data of axial field sweep at three different optical intensities. (b) The dependence of twist widths and amplitudes on the Rabi frequency.

0 mrad rotation increases despite the transverse field amplitude being fixed. This offset was not intentional, but is the result of the limited resolution in current settings for the B_{\perp} coils which limits our ability to null that field. This again supports the hypothesis that the offset is dependent on the optical power.

Figure 2.26(b) shows a summary of “twist” width (black) and contrast (red) versus the probe Rabi frequency. We see that there exists a peak contrast as can be expected. We also see that the width is reduced at higher Rabi frequency. Since the “twist” width is linearly related to the transverse field, the slope versus Rabi frequency can be found by dividing the measured “twist” width by the transverse field magnitude of 70 mG. Note that since there is some residual B_{\perp} , some of this reduction in slope is likely due to the shifting effect as well. However, the qualitative effect appears to be universal in numerical simulations. Once again, the lines come from the numerical model, showing good agreement with the experimental

measurements.

2.4.4 Measuring Magnetic Gradients with the “Twist”

Measuring magnetic gradients can be very important in characterizing the magnetic fields of working atomic systems. MOTs require significant gradients to trap, but many applications of cold atoms need gradient free environments. Accurate measurements of field gradients allows for accurate application and cancellation of these fields.

There is a natural extension of the NMOR “twist” measurement for static magnetic fields to measure the static field gradient transverse to the light propagation direction. This can be done simply by replacing the photodetectors in the above polarimeter with CCD cameras and imaging the probe light transmitted through the cloud. Calculation of the polarization rotation at each pixel then follows the same method as for photodetectors. Note that proper imaging of the atoms is necessary since the gradient measurement relies on accurate determination of the spacial dimensions. This configuration employed $4f$ imaging with no magnification, meaning the pixel dimensions can be directly used for the image dimensions.

In Fig. 2.27 I show an example polarization rotation image from the CCD polarimeter. A probe intensity of $700 \mu\text{W}/\text{mm}^2$ was used with an applied static transverse field of $B_{\parallel} = 40 \text{ mG}$ and an unknown gradient in the same direction. The axial field is $B_z = 50 \text{ mG}$. Quick inspection of the image shows significant structure in the polarization rotation image.

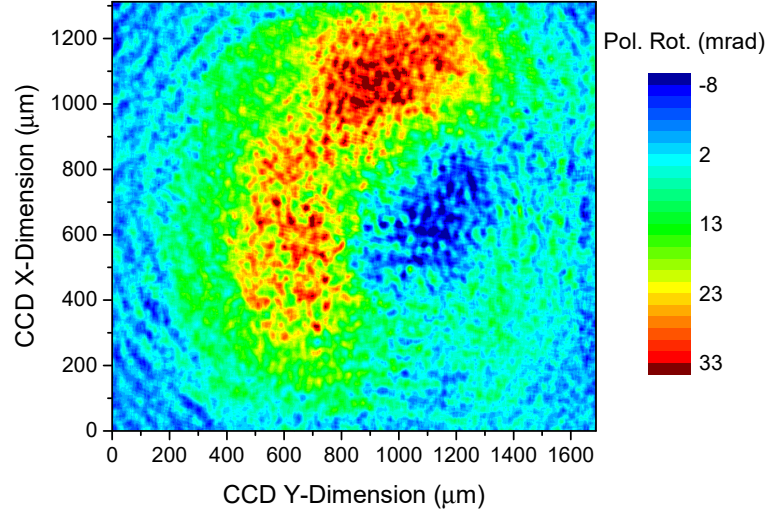
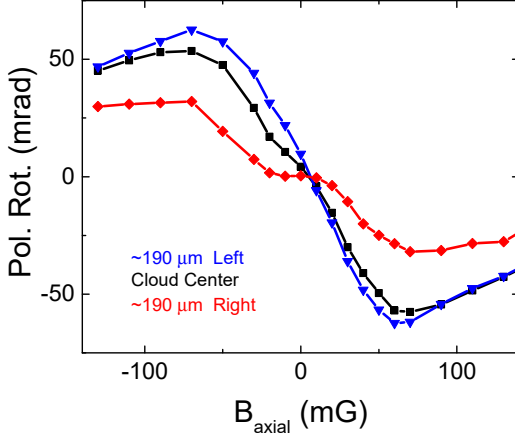
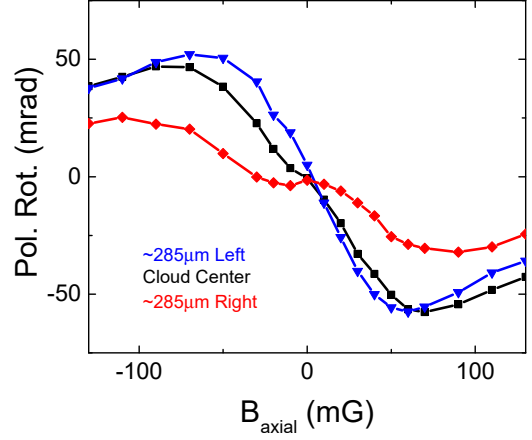


Figure 2.27: Image of the Polarization Rotation experienced by the light as it passes through the atomic cloud. The x,y axes mark the size of the CCD area sensor. This configuration employed $4f$ imaging to map the cloud dimensions to these dimensions one to one.

Before attempting to extract gradient information I need to note that the atomic density profile is approximately gaussian, as is the probe intensity profile. Both effect the observed polarization rotation. The reduced density at the edges will lower the overall contrast of the NMOR signals. The lower probe intensity at the edges is more complicated, as noted above, in that the “twist” width, contrast, and offset can depend on the exact probe power. If both gaussian profiles are centered with respect to each other, one can accurately find the gradient along any line through the center of the cloud by comparing symmetric points from the center. At any two equally-spaced points the probe power and atomic density should be the same. Note that this assumes the atomic motion during camera exposure is negligible. Using cold atoms ensures this assumption does not impose a significant limitation to the measurement.



(a) Measurement of NMOR at cloud center (black), 190 μm to the left, and 190 μm to the right. Note that the “twist” width changes significantly from zero to approximately 24 mG which is indicative of a gradient.



(b) Measurement of NMOR at cloud center (black), 285 μm to the left, and 285 μm to the right.

Figure 2.28: Data from the CCD Polarimeter

Figure 2.28 shows two examples of such comparisons where I have chosen points along a horizontal line through the cloud center separated by $2 \times 190 \mu\text{m}$ and $2 \times 285 \mu\text{m}$ in parts (a) and (b), respectively. By looking at the progression of the “twist” from left to right of the cloud we see that the transverse field goes through zero at approximately 190 μm left of cloud center by noting maximal NMOR contrast. As we move to the right we see an a “twist” of increasing width.

I can estimate the gradient by using the slope measured above to convert the “twist” width into a transverse magnetic field amplitude. The 190 μm right of center NMOR trace has a “twist” width of approximately 24 mG. This implies a transverse field of 33 mG. I approximate the zero field location to be near 190 μm left of the cloud center. Since they experience the same probe intensity, I can reasonably compare the NMOR directly. Taken together this implies a gradient along this axis

of 86 mG/cm.

The sensitivity of this method relies on how accurately the “twist” can be used to measure the transverse field and the spacial accuracy and extent of the atomic cloud. For this experiment I have an atomic cloud approximately 1 mm in diameter. Given the above results using the standard polarimeter, I can expect to be able to measure a minimum transverse field of 1 mG. Therefore the minimum gradient I can measure is approximately 10 mG/cm.

2.5 Conclusion

In this chapter I have investigated a sub-feature of NMOR signals known as a “twist” using laser-cooled atoms. I have shown that this “twist” has a width that depends on the strength of the transverse field parallel to the polarization of the probing light field and that this width scales linearly with the transverse field magnitude. I have also shown that the “twist” depends on the magnetic field perpendicular to the light polarization, the light ellipticity, and the probe intensity. I characterize these effects and describe how the “twist” can be used as an in-situ calibration of magnetic fields and probe polarization. I also describe a proof-of-principle measurement for imaging magnetic gradients using the “twist.”

I support these measurements with a full numerical model based on the optical Bloch equations that fits the data with a high degree of accuracy. I also develop a simplified perturbative model that reproduces many of the qualitative features of the “twist.” Most importantly, this model predicts the linear relationship of the “twist” width with the transverse magnetic field magnitude parallel to the light polarization.

For the presented measurements, the sensitivity to the transverse field is on the order of 1 mG (with corresponding 1 mG/cm gradient sensitivity). For the purpose of calibrating and nulling magnetic fields in cold-atom systems this sensitivity is often sufficient. However, should greater sensitivity be required, the fundamental limitations are atom number and coherence time. Improved trapping of the atoms

to either increase the optical depth and/or the light-atom interaction time could greatly improve the sensitivity of this technique.

Even at the current sensitivity, we have found these signals and associated techniques to be useful diagnostics for fields affecting our atomic experiments, and believe they could find use in a variety of other contexts, for example spinor BECs [38], spin-orbit coupled systems [39], and, more broadly, qubit systems that require stringent quantum control [40–42].

Chapter 3: Rydberg Electrometry for Digital Communication

Rydberg electrometry is the field of using atomic states with large principle quantum number n as sensors for electric fields. Rydberg states strongly resemble the classical Bohr model, resulting in relatively large atoms with characteristic radii many times the Bohr radius. As such, a Rydberg atom has many exaggerated properties compared with typical neutral atoms, including high sensitivity to external electric fields. This high sensitivity covers both static and oscillating electric fields ranging up to ~ 1 THz.

Modern digital communications rely heavily on RF electric fields to carry information between remote locations. In general, the RF field acts as a carrier which is modulated in some way with the desired information then broadcast, often over free-space. This broadcast is then received, mixed down to remove the carrier frequency, and demodulated to retrieve the information. Due to the wide variety of applications for remote communications many different carrier frequencies, modulation schemes, and broadcast/receiver systems are necessary. [43, 44]

In this chapter I will explore the application of Rydberg atoms as highly sensi-

tive electric field sensors to the problem of digital communication. I will characterize the channel capacity of such a device, assess bandwidth and sensitivity limitations, and determine the fundamental limit on the channel capacity due to quantum noise. I also provide some theoretical basis for comparing Rydberg atom sensors to their classical receiver counterparts.

Chapter Contents

| | | |
|---------|---|-----|
| 3.1 | Introduction | 105 |
| 3.1.1 | Rydberg Electromagnetically Induced Transparency | 106 |
| 3.1.1.1 | Doppler-Averaging | 113 |
| 3.1.1.2 | Transit Dephasing | 118 |
| 3.1.1.3 | Black-Body Radiation Induced Dephasing | 119 |
| 3.1.2 | Rydberg Electrometry | 121 |
| 3.1.2.1 | Derivation of scaling factor D | 124 |
| 3.1.3 | Electrometry of Far Off-Resonant RF Fields | 126 |
| 3.1.4 | Classical Antennas & Communication Basics | 126 |
| 3.1.4.1 | Carrier Modulation & Channel Capacity | 127 |
| 3.1.4.2 | Antennas & the Chu Limit | 131 |
| 3.1.4.3 | Noise Background | 133 |
| 3.2 | Digital Communication with a Rydberg Receiver | 136 |
| 3.2.1 | Experimental Configuration | 137 |
| 3.2.2 | Demodulated Signal | 140 |
| 3.2.2.1 | Demodulated Signal Dependence on Ω_μ | 140 |
| 3.2.3 | Phase Shift Keying Demonstration | 144 |
| 3.2.4 | EIT Detection Bandwidth Limitations | 145 |
| 3.2.4.1 | Derivation of τ_f Limit for a Transit-Broadened Medium | 148 |
| 3.2.5 | Measuring Channel Capacity | 152 |
| 3.2.6 | Contrast with Classical Receivers | 155 |
| 3.3 | Digital Communication in the Electrically Small Regime | 160 |
| 3.3.1 | Far Off-Resonant Configuration | 161 |
| 3.3.2 | Measuring Channel Capacity | 164 |
| 3.3.3 | Comparison with the Chu Limit | 166 |
| 3.4 | The Standard Quantum Limit for Digital Communication | 169 |
| 3.4.1 | The Standard Quantum Limit | 169 |
| 3.4.2 | The Standard Quantum Limit for Channel Capacity | 171 |
| 3.4.3 | EIT, Photon Shot Noise, and the Standard Quantum Limit | 172 |
| 3.4.4 | Quantum Limits for Resonant Electrometry | 178 |
| 3.5 | Sensitivity of the Rydberg Receiver | 180 |
| 3.5.1 | Resonant Rydberg Electrometer/Receiver Sensitivity & SNR | 180 |
| 3.5.2 | Converting to Power Sensitivity | 182 |
| 3.5.3 | Improving the Sensitivity of the Rydberg Receiver | 185 |
| 3.5.3.1 | Increasing Sensing Volume | 188 |
| 3.5.3.2 | High QE Probing | 190 |
| 3.5.3.3 | Doppler-Broadening | 191 |
| 3.5.3.4 | Estimated Improvement to Rydberg Electrometer Sensitivity | 192 |
| 3.6 | Conclusions | 194 |

3.1 Introduction

Large portions of this chapter follow from two of our published works, [2, 3], organized as follows. I first review Electromagnetically Induced Transparency (EIT) and extend it to probing Rydberg states of neutral alkali atoms. I then review the details of Rydberg electrometry for resonant and far off-resonant RF electric fields. I next review some basics of classical antenna theory to facilitate comparison of Rydberg atom sensors to classical receivers.

I will then introduce the concept of the Rydberg receiver, based on Rydberg electrometry, for the purpose of receiving classical, digital communication. I will present experimental measurements of the channel capacity and limitations thereof using a resonant RF transition. I next present measurements of channel capacity for a far off-resonant RF field, where the receiver is in the electrically small regime. I also show that the receiver performance scales with atom number, indicative of the standard quantum limit, and I will establish the fundamental limit to channel capacity for these systems. Finally, I discuss the current limitations to the sensitivity of Rydberg electrometry, and thereby the Rydberg receiver, as well as potential improvements that can be made.

Note that [2] only covers the initial demonstration and characterization of the Rydberg receiver using resonant RF transitions. As we moved to off-resonant detection in [3] our understanding of the quantum noise in the system improved. In this chapter I have striven to apply this improved understanding to the original

work.

3.1.1 Rydberg Electromagnetically Induced Transparency

The production of Rydberg states requires some special consideration. Ideally, one could use a direct optical transition between the ground state and the Rydberg state of choice. In practice this is difficult as it requires ultra-violet lasers which are difficult to produce and use. Instead, multiple excitation fields using multiple atomic levels are more convenient to achieve the excitation (see Fig. 3.1). In this work I focus on two-photon excitation: the first 780 nm photon excites through the standard ^{85}Rb $D2$ transition to the first excited state, the second 480 nm photon then excites to the Rydberg state of choice.

Which Rydberg states are accessible is then a question of how broadly tunable the 480 nm source is and within the last few years reasonable commercial products capable of the power output ($> 10\text{ mW}$) and tunability ($\sim 5\text{ nm}$) have become available. Another advantage of two-photon excitation is the possibility of coherent optical detection of Rydberg states via Electromagnetically Induced Transparency (EIT), largely due to the long natural lifetimes of Rydberg states.

These long lifetimes can be understood to be the result of two factors: weak overlap of the Rydberg state with the atomic ground state that limits direct decay, and reciprocal scaling with the transition frequency that limits cascading decays through nearby Rydberg states. Both factors can be easily seen by following the treatment in [45], where the natural lifetime, τ_n , can be modeled using the Einstein A

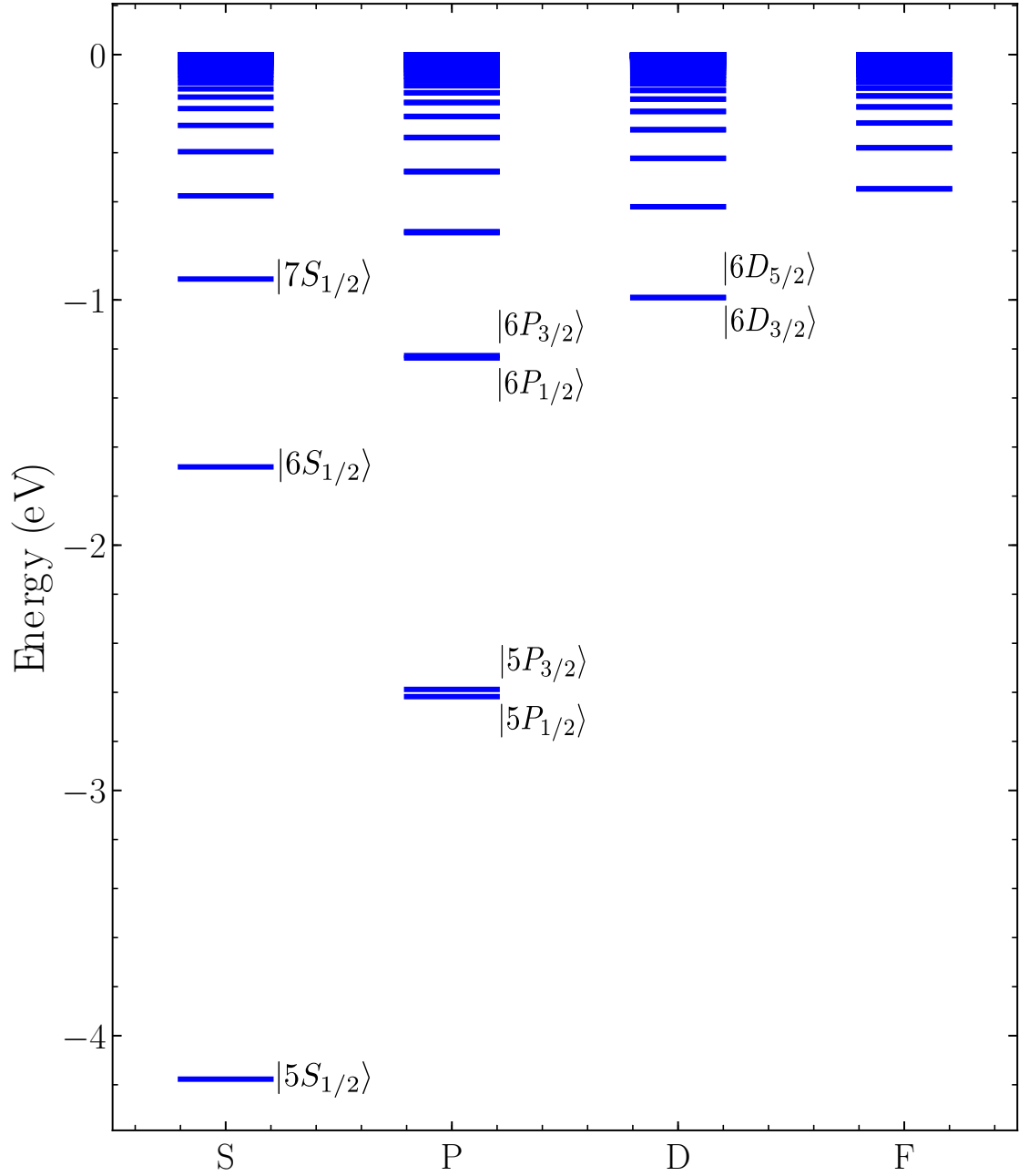


Figure 3.1: ^{85}Rb States Manifold. Includes states ranging from the ground state to $n = 100$ and angular momentum up to F . While any optically-allowed transition is possible, multi-photon excitation is usually necessary to excite to a Rydberg state ($n > 10$) in order to have sufficient energy. Also note that optically-allowed RF transitions between Rydberg states are also allowed. Due to the presence of so many levels, many resonant transitions covering the frequency spectrum are available.

coefficient between the Rydberg state and the various potential decay target states:

$$A = 1/\tau_n = \frac{\omega_0^3 |d|^2}{3\pi\epsilon_0 \hbar c^3}. \quad (3.1)$$

The A coefficient represents the natural decay rate between the two states, where ω_0 is the angular frequency and d is the dipole moment of the transition. The transition frequency to the ground state is approximated as

$$\omega_0 = \frac{Ryd}{\hbar} \left(\frac{1}{n^2} - 1 \right) \approx \frac{Ryd}{\hbar}. \quad (3.2)$$

The dipole moment between these states, specified in terms of the electron charge, e , and the Bohr radius, a_B , is found by taking the ground state dipole moment and normalizing it by the excited state.

$$|d| = \langle n, l | er | n', l + 1 \rangle \approx ea_B \sqrt{2/\pi n^3} \quad (3.3)$$

Putting these together and simplifying gives

$$A = 1/\tau_n \approx \frac{\alpha^4 c}{3\pi a_B} n^{-3}, \quad (3.4)$$

which gives the well-known $\tau_n \propto n^3$ scaling. This scaling has been measured experimentally and a more accurate empirical formula for rubidium D states is

$\tau_{nD} = (2.09 \text{ ns}) n^{2.85}$.¹ [45] For $n = 50$ this gives $\tau_{50D} = 145 \text{ ns}$. Exact numerical

¹Lifetimes will often be specified by their inverse, rate, throughout this work in units of Hz. A rate γ specified with frequency f and a lifetime τ are related by $\gamma = 2\pi \times f = 1/\tau$.

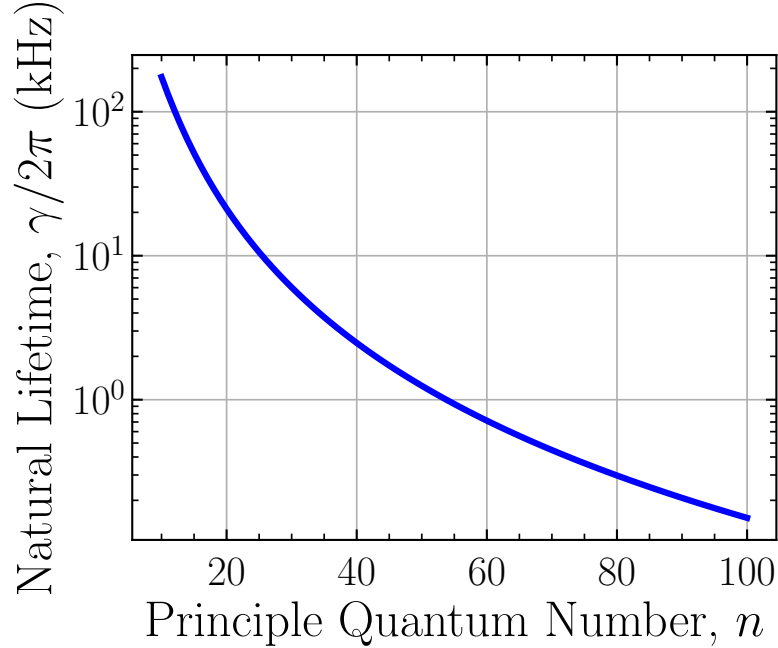


Figure 3.2: ^{85}Rb $|nD_{5/2}\rangle$ natural lifetimes. These times approximately follow a n^{-3} scaling law.

values for the lifetime are shown in Fig. 3.2. The deviation from the theoretical scaling is due to contributions from the case of cascading decay paths through nearby Rydberg states. These transitions have significantly stronger dipole moments, as will be discussed later, but the decay rate is strongly suppressed relative to optical transitions to the ground state since the transition frequencies are three orders of magnitude smaller.

As briefly discussed in Section 2.1.2, EIT is a nonlinear effect due to the interaction of at least a three atomic levels, often via optical fields, to produce dark coherent superposition states. Optically pumping atoms into this dark state produces an optical transparency that has subnatural linewidth and is readily detected through various optical methods. In that description the coherence is between two ground states with infinite lifetime. For two-photon excitation to Rydberg states,

this description must be generalized to include what are known as ladder, or cascade, systems.

It is relatively simple to generalize the Λ EIT system to a ladder EIT system. In the rotating frame the interaction Hamiltonian describing both systems is functionally identical. Ultimately, the primary difference is that the highest excited state has a finite lifetime, yet must be long compared with the intermediate state in order to maintain sufficient optical pumping into the dark state. Since Rydberg states generally have a small overlap integral with the ground state (see Eq. 3.4), the radiative lifetime is generally quite long, scaling with n^3 and on the order of 10's of μs (Rydberg state lifetimes for the $|nD_{5/2}\rangle$ states relevant to this work are shown in Fig. 3.2). In comparison, the intermediate state natural lifetime for the rubidium $D2$ transition is 27 ns, meaning the potential to observe EIT is still present.

To be more concrete, the conditions to observe EIT are outlined in [46]. As already discussed, the ground/Rydberg dephasing rate γ must be significantly smaller than the intermediate dephasing rate Γ to support dark coherent states. To lowest order the ratio Γ/γ of these dephasing rates governs the EIT contrast (size of transparency window relative to total probe absorption). The necessary coupling power needed can be reasoned using the dressed-atom picture, where the EIT dark state is due to the presence of a coupling field with Rabi frequency Ω_c that causes a common-mode splitting of the intermediate state. [47] When these split levels are within the probing linewidth a coherent, destructive interference between the two levels produces the transparency. The explicit condition encapsulating this picture is $\Omega_c^2/\Gamma\gamma \gg 1$ which enforces that the coupling Rabi frequency in EIT needs to be

larger than the geometric average of the dephasing rates. Finally, Autler-Townes (AT) splitting supplants EIT if $\Omega_c \gtrsim \Gamma/2$. When AT is present, an effective transparency window is still present, though it is no longer due to destructive interference but instead by producing an avoided crossing between the Stark shifted levels. The line between EIT and AT splitting is not firm and there exists a region of overlap between the two effects. Methods of differentiating the two signals exist and I invite interested readers to peruse the relevant literature. [48–50] From the practical experimentalist point of view, the difference is immaterial since both effects can result in a useful transparency window.

In this chapter I will describe excitation of Rydberg states in a thermal vapor cell. This greatly simplifies the experimental apparatus compared with the MOT system of the last chapter at the expense of more complicated modeling due to thermal averaging. While these complications are certainly significant and difficult to account for when attempting to observe Rydberg EIT, the advantage in simplicity and the crucial benefit of a metal-free sensing region that will not interfere with RF electric fields are worth the theoretical headaches. That said, the EIT mechanism is fairly robust and simple to observe in a vapor cell, as demonstrated first for high-lying Rydberg states by Mohapatra *et. al.* in [51].

The complications of using real atoms manifest as various dephasing mechanisms when observing EIT. These include: Doppler-averaging, transit dephasing, and Black-Body radiation induced dephasing. In thermal vapor cell experiments, Doppler-averaging and transit dephasing dominate the observed EIT signals. I will briefly discuss their origins and how to account for them.

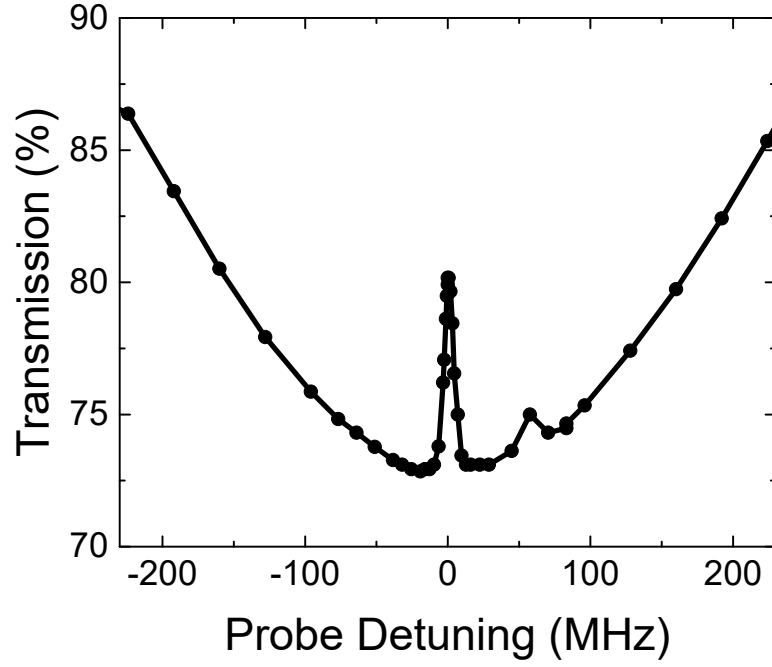


Figure 3.3: Typical Rydberg EIT transmission spectrum versus probe detuning, normalized to the off-resonant probe transmission, for the experimental system. The broad background is the $D2$ Doppler background which has a linewidth of ~ 500 MHz. The larger, narrow transmission peak corresponds to EIT using the $|50D_{5/2}\rangle$ Rydberg state. The smaller transmission peak is the $|50D_{3/2}\rangle$ Rydberg state.

3.1.1.1 Doppler-Averaging

Doppler averaging can be the source of much frustration when attempting to model Rydberg EIT signals in warm vapors. Assuming the beam sizes are not too small (see Section 3.1.1.2), residual Doppler broadening is the dominant effect, resulting in typical Rydberg EIT linewidths for two-photon excitation ranging from 2 to 20 MHz. These linewidths are obtained by counter-propagating the two beams. One might reasonably expect the partially canceled Doppler shifts experienced by the atoms produce the narrow Rydberg EIT linewidths observed. However, this is not the case. Instead the linewidth is due to velocity selection set by a combination of the natural linewidth of the intermediate state and the EIT two-photon resonance condition.

To demonstrate this, I will start by considering the well characterized Doppler linewidth of the $D2$ transition in rubidium. A simple expression to approximate this is: [19]

$$\Delta_{\text{FWHM}} = 2\sqrt{2\ln(2)}\frac{v_{1D\text{rms}}}{\lambda}, \quad (3.5)$$

where $v_{1D\text{rms}} = \sqrt{k_B T/m}$ is the single axis rms velocity of the atoms and λ is the resonant wavelength. For the $D2$ transition of rubidium 85 this comes out to be the expected 515 MHz. When considering partially canceled Doppler shifts like in Rydberg EIT, one replaces the wavelength with the residual wavelength of the two-photon transition $((1/780\text{ nm} - 1/480\text{ nm})^{-1} \approx 1900\text{ nm})$. This results in a $\Delta_{\text{FWHM}} = 320\text{ MHz}$, which is significantly larger than the observed EIT linewidth.

So what gives? Well, two-photon excitation is not a stringent enough condition in order to observe Rydberg EIT in a Doppler-broadened system. One must also stipulate single photon resonance for the probing leg of the excitation ladder. The reasoning is described in [46]. EIT measurements are by nature relative; one measures the extra transmitted photons due to the presence of the coupling field relative to the normal probe absorption. Therefore observing EIT requires not only being two-photon resonant with the dark state, but also that the probe photon is resonant and strongly absorbing. For a thermal ensemble, velocity classes that exhibit EIT are only those that are both single photon resonant with the probe and two-photon resonant with the EIT dark state. The probe photon resonance condition limits the potential velocity classes to those within the natural linewidth of the intermediate state where the probe is strongly absorbing ($2\pi \times 6$ MHz for the ^{85}Rb D2 probing transition). This can be seen in the contour plots of Fig. 3.4. When the probe detuning is greater than approximately the natural linewidth (corresponding to the absorption width shown in the plot), the velocity class of atoms that produces significant absorption is not the same velocity class of atoms that satisfies the two-photon EIT resonance condition. The result is that the effective rms velocity of the atoms that you can average over is significantly reduced.

This is not the only effect of Doppler-averaging on the Rydberg EIT linewidth. Due to the averaging of velocity classes, the coupling Rabi frequency Ω_c strongly influences the observed linewidth. This is because large Ω_c leads to AT splitting as described above, which has a similar transparency window to EIT that is both wider and with better contrast. When averaging over multiple velocity classes, this

larger window is not averaged out as easily as the sensitive EIT window. This dependence can be seen in the reported Rydberg EIT linewidths in thermal vapors in the literature that vary widely despite using similar atomic systems and excitation schemes.

To illustrate this point I show numerical solutions of the Optical Bloch Equations (OBEs) for a simple three-level system in Fig. 3.4 under EIT and AT conditions. For each set of parameters I show three plots of the probe absorption normalized to the peak, resonant absorption without the coupling light present: a contour plot of absorption versus atomic velocity class and probe detuning, a plot of the Doppler-averaged absorption (blue line), and the zero velocity class contribution, $\times 5$ (orange line). The Doppler-averaged trace is simply the sum of velocity classes at each detuning in the contour plot. The zero velocity class contribution is analogous to the corresponding Doppler-free signal.

Considering the contour plots, we can see the hallmarks of an avoided crossing, with the large, negative-sloped absorption line corresponding to the single photon resonance and the positive-sloped transmission line corresponding to the two-photon EIT resonance. In Figures 3.4(a & b) we are firmly in the EIT regime (see Table 3.1) and we can see that the EIT window is small relative to the single photon absorption line. Due to this, summing the velocity classes is likely to wash out the EIT resonance, as observed in the corresponding blue traces. Note that the Doppler-averaged EIT window is of similar depths and width despite having very different Rydberg dephasing rates (200 kHz or 1.2 MHz). While in the Doppler-free traces it is clear that this rate has the expected effect on EIT linewidth and contrast, those

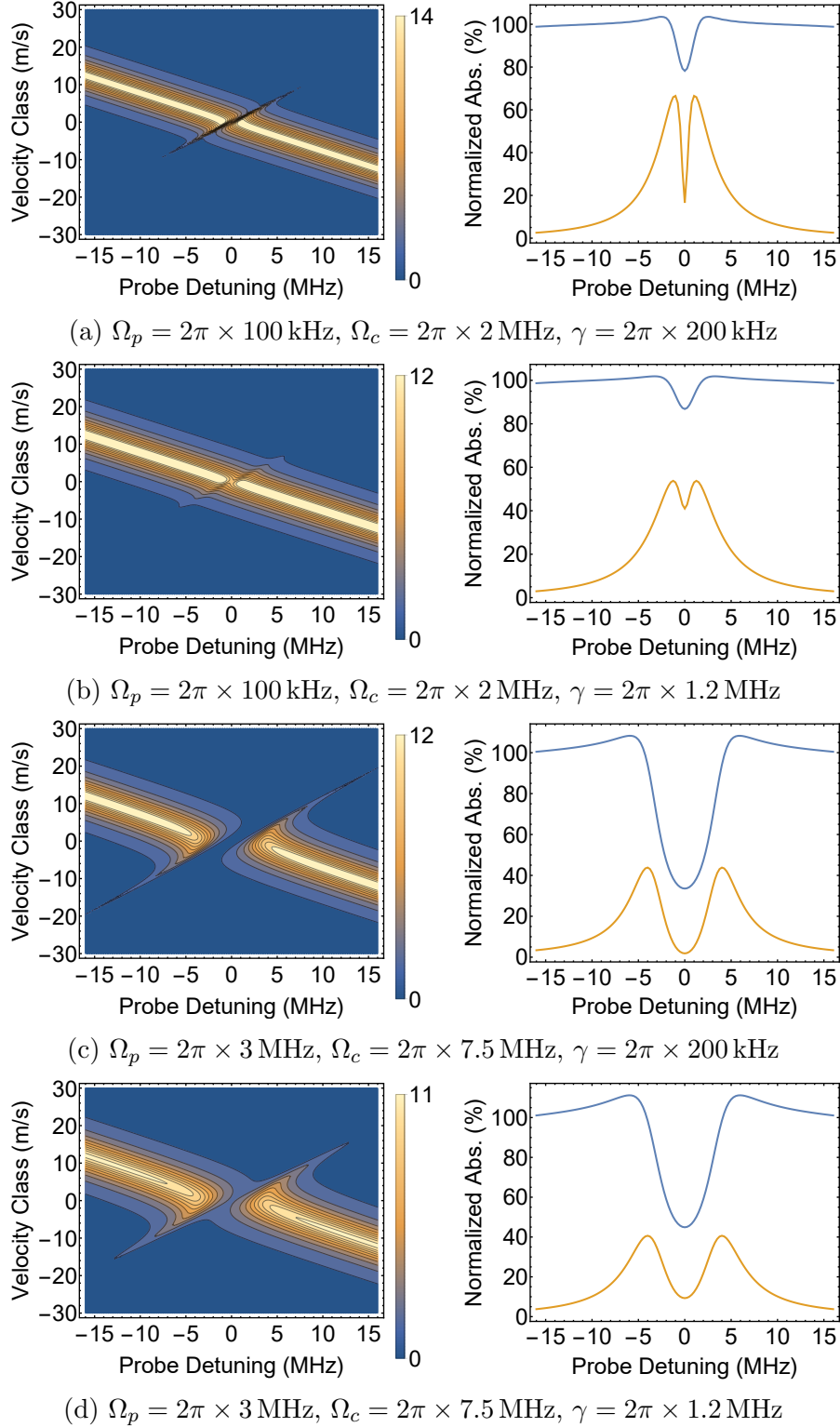


Figure 3.4: Numerical solutions of the OBEs for a three-level system with different probe/coupling Rabi frequencies and Rydberg dephasing rates. The left plots show normalized absorption versus atomic velocity class and probe detuning. The right plots show the averaged probe absorption (blue) and the contribution due to the zero velocity class (orange) times 5 for clarity. Natural linewidth is fixed at $\Gamma = 2\pi \times 6$ MHz.

| Panel | Ω_p | Ω_c | γ | EIT: $\Omega_c^2/\Gamma\gamma \gg 1$ | AT: $2\Omega_c/\Gamma \gtrsim 1$ | Contrast $\propto \Gamma/\gamma$ |
|-------|------------|------------|----------|--------------------------------------|----------------------------------|----------------------------------|
| (a) | 0.1 | 2.0 | 0.2 | 3.3 | 0.7 | 30 |
| (b) | 0.1 | 2.0 | 1.2 | 0.5 | 0.7 | 5 |
| (c) | 3.0 | 7.5 | 0.2 | 46 | 2.5 | 30 |
| (d) | 3.0 | 7.5 | 1.2 | 7.7 | 2.5 | 5 |

Table 3.1: Table of the simulation parameters in Fig. 3.4 and the corresponding EIT/AT condition indicators.

dependencies are greatly suppressed when Doppler-averaging is added.

In Figures 3.4(c & d) we are firmly in the AT regime (again see Table 3.1) and we see that the transparency window resulting from AT splitting is large, approaching the width of the single photon absorption linewidth. However, non-zero velocity classes result in AT peaks with asymmetric absorption and asymmetric splitting about atomic resonance. When averaging these velocity classes, only the central transparency remains approximately consistent while the distinct absorption peaks become washed out. This effect allows for significantly higher contrast windows with large linewidth, while also being relatively insensitive to the Rydberg dephasing rate. The linewidth itself is on the order of Ω_c , tending towards $\Omega_c - \Gamma$ in the limit of large AT splittings.

Many Rydberg Electrometry experiments operate in this AT dominated regime, including the experiments reported on in this chapter. I still choose to refer to the resulting Doppler-averaged signals as “Rydberg EIT” or “EIT” despite different underlying mechanism of the optical detection. I do this because accurately determining the underlying mechanism can be difficult as there is a smooth transition between them. More practically, the transparency windows in a Doppler background that I will show are induced by the presence of a second electromagnetic field, a defi-

dition that comfortably fits in with a concept known as Electromagnetically Induced Transparency.

3.1.1.2 *Transit Dephasing*

As discussed in the last chapter, transit dephasing is related to the amount of time an atom is in the light field. For thermal atoms, this corresponds to the transit time, or time it takes a thermal atom to cross the light field. While there are ways to circumvent typical transit dephasing for atomic magnetometers, those methods do not work with Rydberg EIT since they are not compatible with Rydberg atoms as they interfere with the Rydberg atoms directly.

For Rydberg EIT, transit broadening is often the dominant dephasing source. This is due to the small optical dipole moment for the final excitation to the Rydberg state being so small that significant focusing of that light is necessary to obtain optical intensities sufficient to see EIT. The common result is that the light field region is quite small, resulting in a correspondingly large Fourier broadening.

When estimating transit broadening, I use the method outlined in [52]. In that work the transit broadened linewidth was estimated to be

$$\gamma_t = (1.13 \pm 0.20) \frac{v_{2Drms}}{D_{FWHM}}, \quad (3.6)$$

where $v_{2Drms} = \sqrt{2k_B T/m}$ is the 2D rms velocity of the atoms and D_{FWHM} is the FWHM of a gaussian light intensity profile. Note that the result is in units of rad/s. Our beam profiler reports beam sizes in $1/e^2$ diameters so I can modify this equation

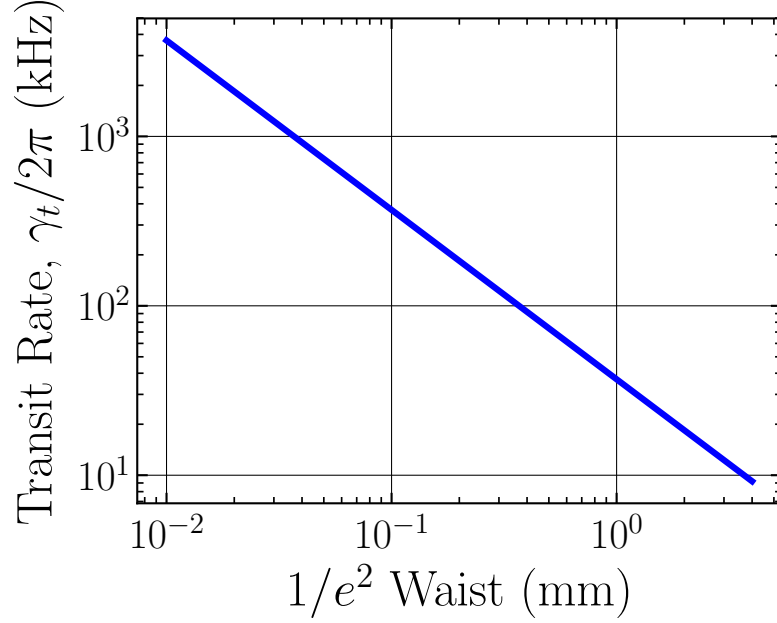


Figure 3.5: Plot showing transit rate versus beam waist at 24 °C.

to read

$$\gamma_t = \frac{(1.13 \pm 0.20)}{\sqrt{2 \ln 2}} \frac{v_{2Drms}}{w} \approx (0.959 \pm 0.17) \frac{v_{2Drms}}{w} \quad (3.7)$$

where w is the $1/e^2$ waist of the gaussian intensity profile. A couple example transit rates from this equation include: $2\pi \times 3.7$ MHz for a 10 μ m waist and $2\pi \times 37$ kHz for a 1 mm waist. Figure 3.5 shows the transit rate in units of hertz ($\gamma_t/2\pi$) versus beam waist at room temperature for rubidium 85.

3.1.1.3 Black-Body Radiation Induced Dephasing

Black-Body radiation due to the thermal temperature of the surrounding environment is the source of the next order dephasing. This is due to the spectral profile of the black-body radiation including frequencies that are resonant with transitions to nearby Rydberg states. These black-body induced transitions effectively de-

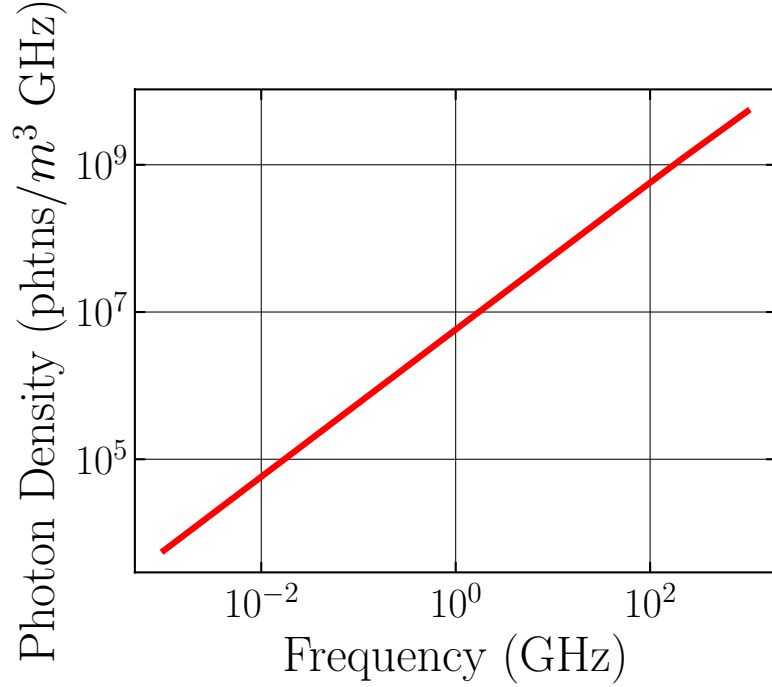


Figure 3.6: Photon Density versus photon frequency at 24°C. Note that these frequencies cover the range of resonant Rydberg transitions shown in Fig. 3.8a.

populate the targeted Rydberg state initially excited, resulting in dephasing of the EIT coherence.

The photon number spectral density is defined using Planck's Law as

$$B_{ph}(f, T) = \frac{8\pi}{c^3} \frac{f^2}{e^{hf/k_B T} - 1}. \quad (3.8)$$

Figure 3.6 plots this equation over the resonant frequency range for the various Rydberg transitions possible from each Rydberg state.

The influence on the Rydberg state lifetime can be calculated by convolving this spectrum with the manifold of resonant microwave transitions to nearby Rydberg states. Figure 3.7 compares the Rydberg state lifetimes including black-body radiation with the natural lifetime of the Rydberg states shown in Fig. 3.2. The

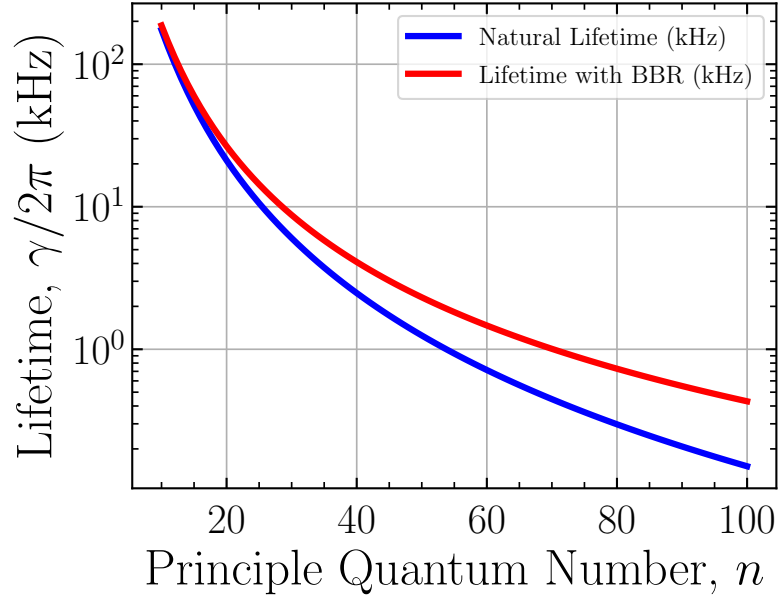


Figure 3.7: $^{85}\text{Rb } |nD_{5/2}\rangle$ Rydberg state relaxation rate without (blue) and including Black-Body Induced Dephasing (red). The thermal temperature for the red trace is 24 °C.

influence of black-body radiation on the lifetimes depends on the n level used, and is limited to less than one order of magnitude increase for room temperature.

3.1.2 Rydberg Electrometry

The idea of using Rydberg atoms to measure arbitrary, static electric fields was introduced by Osterwalder and Merkt in [53]. This method relies on the large atomic polarizability of Rydberg states that scales as n^7 which results in relatively large Stark shifts of the Rydberg state for small electric fields. [45] A related method to measure RF electric fields was introduced by Sedlacek *et. al.* in [54]. In this work they describe how RF transitions between nearby Rydberg levels could be used to precisely measure the amplitude of those RF fields with unprecedented accuracy. This is due to the Rydberg transition's dipole moment, d , which scales quadratically

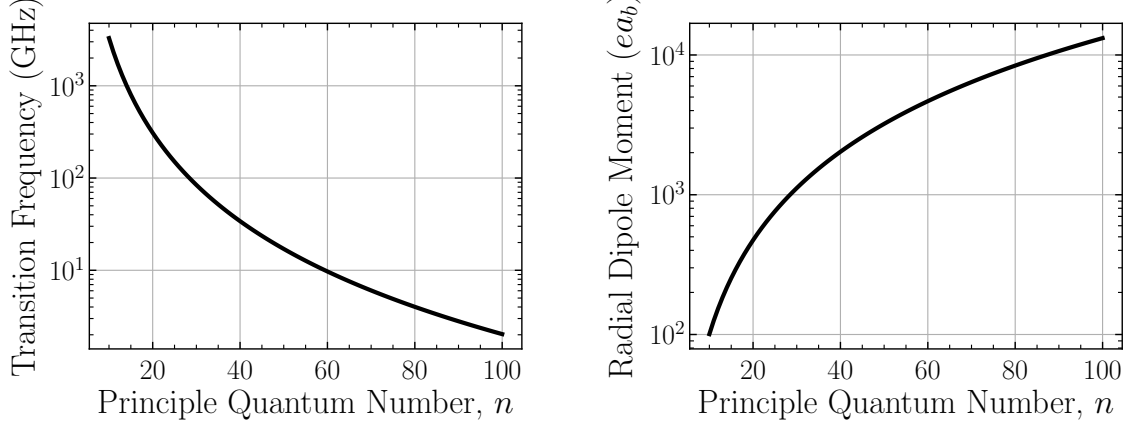
with the large, principal quantum number n , $d \sim ea_b n^2$, where a_b is the Bohr radius and e is the charge of the electron. [45] By probing many atoms at the standard quantum limit, [55] Rydberg sensors have the potential to reach many orders of magnitude higher sensitivity than traditional electrometers, [56] and have many other promising capabilities including high dynamic range, [54, 57] SI traceability and self-calibration, [58–60] and operation frequency spanning from MHz [61] to THz [62]. Furthermore, Rydberg atom ensembles are well suited to perform sub-wavelength imaging [62–64] and vector detection [65].

The basic premise for the resonant Rydberg electrometer is Autler-Townes splitting of RF transitions between nearby Rydberg transitions. When the Rabi frequency of the RF field, resonant with a Rydberg transition, is large compared with the linewidth the transition will split with a spacing proportional to the Rabi frequency. The Rabi frequency is then related to the electric field amplitude by the resonant dipole moment of the transition,

$$2\pi\Delta f_{\text{meas}} = D\Omega_\mu = D\frac{d|E_\mu|}{\hbar}. \quad (3.9)$$

The dipole moment, d , is readily calculable using quantum defect theory with high precision. [45]

I perform these calculations with the excellent Alkali Rydberg Calculator (ARC) written by Šibalić *et. al.* and I provide some example code using this package in Appendix B. [66] The factor D is a scaling factor due to Doppler-averaging and is described in greater detail in the next section. All other values are SI-defined



(a) Transition resonances versus principle quantum number n . These resonances follow a n^{-3} scaling law.

(b) Radial dipole moments versus principle quantum number n . These moments follow a n^2 scaling law.

Figure 3.8: ^{85}Rb $|nD_{5/2}\rangle \rightarrow |(n+1)P_{3/2}\rangle$ Transition resonant frequencies and radial dipole moments.

constants meaning that not only is this measurement highly accurate, but it provides an SI-traceable measure of RF electric field amplitudes which has not been possible before.

Because this method relies on resonant transitions, the nominal frequency coverage for the electrometer is discrete. However, there are many, allowed transitions. Figure 3.8a summarize a subset of these possible transitions versus principle quantum number n that considered in this work between states $|nD_{5/2}\rangle$ and $|(n+1)P_{3/2}\rangle$. I focus on these transitions since they tend to have larger radial dipole moments, as shown in Fig. 3.8b. Note that the total dipole moment is the matrix element $\langle nD_{5/2} | e\vec{r} | (n+1)P_{3/2} \rangle$ which can be broken down into two integrals: one with radial dependence and one with angular dependence. Figure 3.8b shows only the radial portion which depends on primarily on n . The angular portion is unit-less and depends on the l, j, m_j quantum numbers of the states as well as the polarization of

the RF electric field and typically takes a value of approximately 0.5.

Detection of the level shifts is done using the Rydberg EIT discussed above. As long as $\Omega_\mu \gg 2\Gamma_{\text{EIT}}$, where Γ_{EIT} is the Rydberg EIT linewidth, an accurate measure of the electric field using the AT technique is possible. [60] When $\Omega_\mu < 2\Gamma_{\text{EIT}}$, other methods must be used such as calibrating the EIT transmission window depth as done in [54, 67] or using the MW modulation technique I will describe in Section 3.2.2.1.

3.1.2.1 *Derivation of scaling factor D*

While always stated in Rydberg electrometry manuscripts, [54, 58, 60] the derivation of the scaling factor D in the electrometry context is not readily available in the literature. Here I provide the derivation, which is a specific application of the derivations used in the context of fine and hyperfine splitting measurements using ladder-EIT. [68, 69] This derivation was presented in the supplemental material of [2]. After finishing this dissertation I discovered the derivation could have been found in the un-titled appendix of Dr. Stephanie Miller. [70]

I begin by supposing a ladder-EIT measurement of an AT-split excited state like that shown in Fig. 3.12(a) in Section 3.2. In order to see the EIT transmission peaks the probe and coupling light must be two-photon resonant for some velocity class of the thermal atoms: $\Delta p(v) + \Delta c(v) = \pm \frac{\Omega_\mu}{2}$, where $\Delta i(v) = \delta_i + v/c(\omega_{0i} + \delta_i)$ is the detuning of the probe or coupling light seen by atoms with velocity v along the light propagation direction, ω_{0i} is the atomic resonance, and δ_i is the light detuning

from atomic resonance.

If Ω_μ is less than the Doppler linewidth of the probing state (~ 500 MHz for room temperature rubidium) the strongest observed resonance will always occur with atoms having a velocity such that the probe is resonant and the two-photon resonance condition is satisfied (see Section 3.1.1.1). This enforces that $\Delta p(v) = 0$ and $\Delta c(v) = \pm\Omega_\mu/2$. Using these relations to solve for the velocity class and light detuning that satisfies both equations gives the scaling factor D for when either the probe or coupling light is scanned over the AT splitting.

When the probe is scanned, the coupling light is kept resonant with the atomic transition, $\delta_c = 0$. Solving for the probe detuning that achieves resonance with the AT peaks gives $\delta_p^\pm = \left(\frac{\mp\Omega_\mu}{2} \frac{\omega_{0p}}{\omega_{0c}} \right) / \left(1 \mp \frac{\Omega_\mu}{2\omega_{0c}} \right)$. Since $\Omega_\mu \ll \omega_{0c}$ for all conceivable MW powers the denominator can be reduced, leading to a measured probe splitting due to the excited state AT splitting of $2\pi\Delta f = \Omega_\mu \omega_{0p}/\omega_{0c}$. This gives a scaling factor $D = \lambda_c/\lambda_p$.²

When the coupling light is scanned, the probe is kept resonant with the atomic transition, $\delta_p = 0$. The single-photon resonance condition stipulates that only the zero-velocity class atoms can interact. Solving for the coupling detunings that achieve resonance with the AT peaks gives $\delta_c^\pm = \pm\Omega_\mu/2$. This leads to a measured AT splitting of $2\pi\Delta f = \Omega_\mu$ and a scaling factor $D = 1$. Note that using cold atoms with a small rms velocity will give the same scaling factor.

²Note that this factor is often quoted in its reciprocal form in the literature.

3.1.3 Electrometry of Far Off-Resonant RF Fields

While resonant RF electrometry is what is typically considered in the literature, it is also possible to do off-resonant electrometry. If the RF field frequency detuning is on order with or less than the AT splitting, generalized resonant electrometry methods are possible. [71] In the case of far-off resonant RF fields, electrometry relies on single-sided Stark shifts in contrast with the Autler-Townes common mode splittings discussed above. In this case the relevant atomic property is known as the polarizability and strongly resembles measurement of static electric fields. The polarizability depends on the RF field frequency and the Rydberg state being probed and must be calculated using perturbation theory [72] or Floquet analysis [61].

When the RF frequency is both far from resonance and close to DC (*i.e.* less than ~ 100 MHz), the RF polarizability can sometimes be approximated with the DC polarizability which is readily calculated by diagonalizing the Hamiltonian describing the Rydberg state manifold for a range of DC electric fields and fitting the observed level shift. In fact, this type of calculation has been automated by the ARC package, which is what I use to estimate the polarizability in the low frequency communication receiver described in Section 3.3.

3.1.4 Classical Antennas & Communication Basics

As has already been demonstrated, Rydberg atoms are highly accurate and precise sensors of RF electric field amplitudes. This has important scientific implications which I will further explore by quantifying the sensing bandwidth. But

there is a large, existing field already dedicated to the accurate detection of RF electric fields: wireless communication. It is only natural to ask what this sensor can do in the realm of classical communication and that question is the primary focus of the rest of this chapter. In the course of conducting this research, I have discovered that direct comparisons to classical antennas/receiver systems can be difficult. Ensembles of Rydberg atoms are not the same as a dipole antenna. While their outputs in the presence of RF fields can be made very similar, their underlying principles of operation are very different, leading to subtleties when attempting to compare performance. In order to facilitate fair comparisons I include this section as a brief primer in classical communication basics for the atomic physicist. It largely draws from the standard textbooks by Hanzo *et. al.* [43], Stutzman *et. al.* [73], and Hansen [74].

3.1.4.1 *Carrier Modulation & Channel Capacity*

Modern classical communication of information relies on encoding information into modulations of a carrier RF field with frequency ω_μ . These modulations can be in amplitude, frequency, phase, or combinations thereof. The rate of this modulation is taken to be the bandwidth (BW) of the communication. A specific example of a modulated field RF field is: $E(t) = E_0 \cos(\omega_m t + \phi_m(t)) \sin(\omega_\mu t)$ shown in purple in Fig. 3.9. The base RF carrier field, $E_0 \sin(\omega_\mu t)$, shown in green in the figure. It is amplitude modulated by another sinusoidal field (shown in red) at a constant frequency ω_m with variable phase $\phi_m(t)$ (blue). Information is encoded into this

phase. If the information is encoded as digital symbols sent with a period τ_{sym} ,³ this scheme is known as Phase-Shift-Keying (PSK) which will be explicitly demonstrated in Section 3.2.

$$E(t) = E_0 \cos(\omega_m t + \phi_m(t)) \sin(\omega_\mu t) \quad (3.10)$$

A complete communications system includes a transmitter and a receiver. The transmitter produces a carrier frequency that is modulated to encode information and some sort of antenna for coupling the carrier+modulation into a free-space mode. The receiver performs the reverse of this operation. In many cases the transmitter and receiver are largely the same and can be formed into a single transceiver. However, in this work I focus on the receiver operation only and generally take transmission as *a priori*. Communication at a particular carrier frequency is called a communication channel.

One of the most important figures of merit for any receiver is the maximum channel capacity C for a single channel. This is given by the Shannon-Hartley Theorem in terms of the signal-to-noise ratio in standard deviation (SNR) and the channel bandwidth (BW), and can be used to determine the achievable communication rate for a channel given a symbol frequency f_{sym} , the measured signal \mathbb{S} in volts, and the voltage noise spectral density \mathbb{N} in volts per root hertz (assumed here

³In this case the bandwidth of communication is equivalent to $f_{\text{sym}} = 1/\tau_{\text{sym}}$.

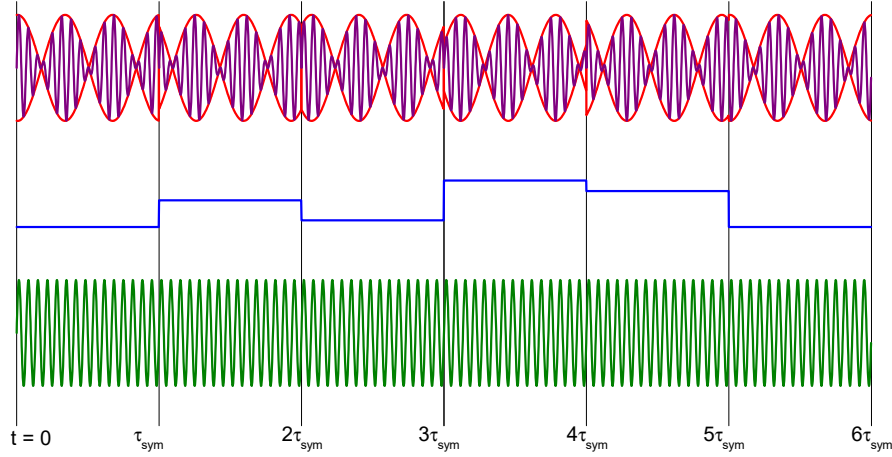


Figure 3.9: Components of an example PSK RF communication signal. The green trace shows the RF carrier signal at frequency ω_μ . The top trace shows the output modulated carrier in purple, overlaid with the amplitude modulation in red at frequency ω_m and varying phase ϕ_m . The blue trace shows the phase of the modulation signal ϕ_m that encodes the data. A new symbol is communicated every τ_{sym} .

to be random white noise): [43, 75]

$$C \text{ (bit/s)} = \text{BW} \log_2 (1 + \text{SNR}^2) = f_{\text{sym}} \log_2 \left(1 + \frac{S^2}{N^2 f_{\text{sym}}} \right). \quad (3.11)$$

The channel capacity is optimized when $\text{SNR} = 1$ and will, in principle, saturate with increasing f_{sym} beyond the optimal point. I will use the channel capacity as a figure of merit for comparing the Rydberg receiver to classical receiver systems.

The Shannon-Hartley theorem is a statement about the rate at which information can be transmitted over a noisy communications channel within a certain bandwidth, assuming an optimal encoding scheme. One can understand the Shannon-Hartley theorem as follows. The argument of the logarithm gives the number of accurately resolvable symbols in the transmitted signal given the noise. Typically the noise depends on the detection bandwidth, linearly in the case of white noise

shown here. The logarithm base-2 gives the number of digital bits that can be encoded per symbol. For example, $\text{SNR}^2 = 1$ implies only two resolvable states are possible, such as the presence and absence of signal, which can only encode 0 or 1. If $\text{SNR}^2 = 7$, there are eight resolvable states, where each symbol transmitted represents 3 bits of information (*i.e.* perturbations of 000 to 111). The bandwidth is then the rate at which symbols can be sent.

When optimizing channel capacity, it is always preferable to use a higher bandwidth until $\text{SNR} = 1$, as channel capacity scales linearly with symbol rate but only logarithmically with symbol number. Increasing the bandwidth beyond this point does not necessarily improve capacity since multiple symbol periods have to be averaged in order to accurately resolve the sent symbol from channel noise. However, in practical systems there is another consideration that limits operating bandwidth: spectral efficiency. The electro-magnetic spectrum is not infinite, particularly in frequency bands where atmospheric absorption is low. In order to leave room in the spectrum for multiple independent communication channels, the allowed bandwidth is artificially limited and more complicated encoding schemes are used to improve the data rate to match the lower channel capacity. Modulation schemes allowing for upwards of 1024 different symbols are commonly used. [43] I describe such an encoding scheme in Section 3.2.

3.1.4.2 *Antennas & the Chu Limit*

An important piece of the classical receiver system is the antenna. I take a classical antenna as a passive device that couples generated RF power into some free-space mode. Since it is passive by design, antennas are completely reversible, meaning they also couple free-space RF power from a particular mode into a transmission line coupled to the processing electronics. One important figure of merit for an antenna is its gain or directionality. These terms can often be used interchangeably since, as passive devices, antennas can only increase the RF power at a particular point by focusing the output radiation pattern. A common, though certainly not universal, measure of gain (and thereby directionality) is dBi, which is defined as the relative forward gain of the antenna to the same power radiating isotropically. While such a radiation pattern is difficult to achieve in practice, it is a useful benchmark. A second common benchmark that I will occasionally refer to is that of an ideal dipole. Note that the passive antenna typically does not effect the other operational parameters such as the bandwidth of the receiver system. I will describe such an instance where this is not the case later in this section.

A complementary way to characterize the gain or directionality of an antenna is to consider its cross-section or effective aperture. This cross-section corresponds to the effective area seen by an incident electro-magnetic wave that can capture power from the field. For antennas this effective aperture is found to be

$$Area = \frac{\lambda^2}{\Omega}, \tag{3.12}$$

where Ω is the acceptance solid angle of the antenna (maximum of 4π steradians) and λ the RF wavelength. [76] The total captured power for an incident RF field is then found by multiplying this cross-section by the field intensity. More directional antennas have smaller acceptance angles which increases the effective aperture and therefore the total captured power from an incident field.

Efficient antenna operation requires proper impedance matching of the antenna to both the transmission line and the free-space mode. Impedance matching is often straight-forward, involving simple elements like resistors, capacitors and inductors as well as clever antenna design. There is one case where impedance matching is a significant challenge: the electrically small regime. An antenna in the electrically small regime is an antenna with a physical size less than $\lambda/10$, where λ is the wavelength of the RF field being transmitted or received. In this regime the antenna's impedance can become vanishingly small, making proper impedance matching difficult. A simple method is to add losses, though this reduces the efficiency. In order to maintain a lossless, impedance-matched antenna, it can instead be made resonant which will reduce the functional bandwidth. This condition is encapsulated in what is known as the Chu limit.

What I call the Chu limit was pioneered by Wheeler, Chu, Harrington, McLean, as well as others and represents a fundamental limitation when using electrically small antennas. [74, 77–80] This limit assumes a lossless, passive device with a characteristic size much less than the wavelength λ of the electromagnetic field being received or transmitted. If one defines a sphere with radius a such that the device is completely enclosed, the quality factor Q must be greater than $Q_{\text{chu}} = \lambda^3/(2\pi a)^3$.

In the limit of large Q the antenna bandwidth is simply related such that $BW_{\text{chu}} \lesssim f_0/Q_{\text{chu}}$. In the never-ending quest for smaller communication devices, the Chu limit presents a fundamental challenge. I will address using the Rydberg receiver in the context of the Chu limit in Section 3.3.

3.1.4.3 Noise Background

Another fundamental challenge to classical communications is atmospheric noise. In receiver systems, the noise sources are often specified as a noise temperature which is defined as the temperature T that would produce the same noise power spectral density in a resistor due to Johnson noise, $P_N = k_B T$. [73] Specified this way, noise from different components can be easily summed by adding together their noise temperatures. This allows one to easily break up the receiver noise into internal and external sources of noise, $T_{\text{tot}} = T_{\text{int}} + T_{\text{ext}}$. The noise temperature of individual components is often specified as a noise figure, which is defined as the noise power relative to room temperature, $T = 290$ K. The noise figure of off-the-shelf amplifiers, which are typically the dominant internal noise source for a receiver system, have a noise figure of < 3 dB.

Atmospheric noise represents the limit to the external noise floor for terrestrial communications. It is a function of pointing angle of the antenna (*i.e.* pointing the antenna at the night sky will have a lower noise temperature than looking at the ground due to differences in black-body radiation) and the operating frequency of the system (*i.e.* non-black-body noise sources are typically not white and have frequency

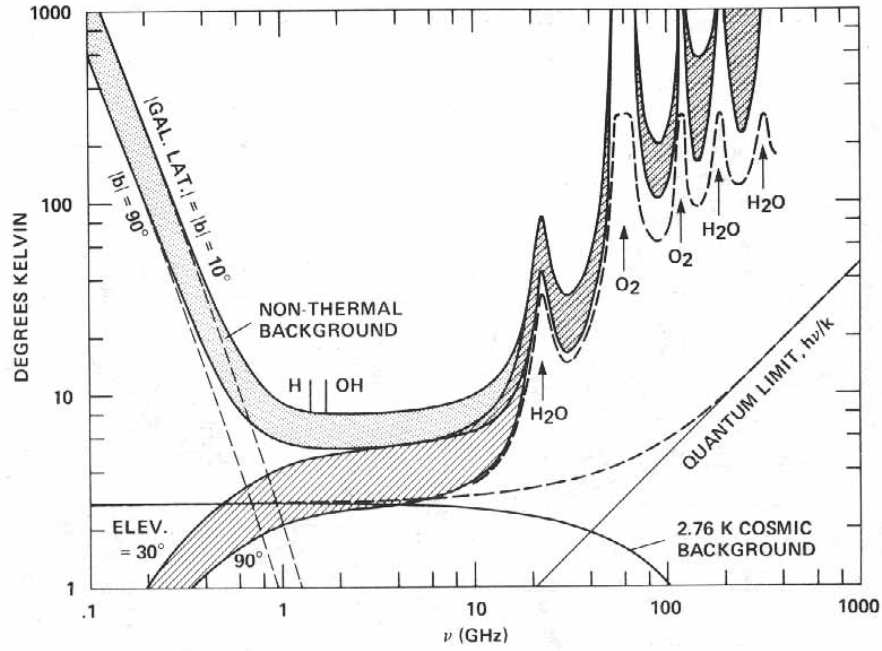


Figure 3.10: Atmospheric Noise Temperature versus frequency. These temperatures represent the minimum possible external noise temperature for any Earth-based communications receiver. Figure reproduced from [81].

dependence). A plot of typical atmospheric noise temperature as a function of frequency and pointing angle is shown in Fig. 3.10. Low frequencies are dominated by atmospheric events like lightning strikes and cosmic radiation. Higher frequencies contend with molecular absorption due to atmosphere composition. Between 1 and 10 GHz there is a window where the fundamental limitation is the cosmic microwave background. When considering receiver systems, if the external noise temperature is the dominant noise source, reducing the internal noise temperature of the receiver is of limited benefit. I will address Rydberg sensor's noise in Section 3.4.

Note that the fundamental noise limit for any receiver is ultimately quantum noise due to the discrete nature of the RF field. In principle, the absolute minimum detectable RF field is made of a single photon. The corresponding noise temperature,

$\hbar\omega_\mu/k_B\sqrt{N}$, where $N = 1$ is the minimum RF photon number, is also shown in Fig. 3.10. This noise is significantly lower than atmospheric noise and I will show in Section 3.4 that the quantum noise due to atom number is significantly larger than this quantum noise.

Ultimately, the goal of any quantum sensor is to reach the Standard Quantum Limit (SQL) for the system. Were this to be achieved with the Rydberg electrometer, quantum communication applications using RF photons would be possible in addition to the classical communication applications discussed here.

3.2 Digital Communication with a Rydberg

Receiver

Rydberg atoms offer several exciting possibilities to exceed what is possible with classical dipole antennas for classical digital communication. First, multiplexing communication using many transitions from 0.1 to 1000 GHz may lead to parallel, fast communication in multiple, widely disparate bands. Second, optically-interrogated Rydberg atoms avoid internal thermal noise that can limit classical antennas since the internal states of atoms can be optically pumped to effectively zero-temperature; [82] the readout noise is instead limited by the quantum projection noise. Rydberg atoms have already been shown to have record sensitivity in non-perturbative RF electrometry down to $0.3 \text{ mV}/(\text{m} \sqrt{\text{Hz}})$. [67] Finally, Rydberg atomic receivers could also, in principle, be used for sub-wavelength imaging [62–64] and vector detection [65]. Recent work has also shown cold Rydberg atoms can mediate direct, coherent electro-optical conversion of MW photons into the optical regime via six-wave mixing. [83, 84] Given these potential strengths I introduce Rydberg atoms as a new potential platform for digital communication worthy of in-depth study.

In this section, I show that room-temperature Rydberg atoms can be used to implement a microwave-frequency (MW) receiver “antenna” ⁴ for classical, digital communication. I demonstrate phase-sensitive conversion of amplitude-modulated

⁴This driven atomic sensor may not satisfy the definition of an antenna used in classical antenna theory since it breaks several common assumptions. See Section 3.2.6 for details.

MW signals into optical signals and perform a demonstration of 8-state phase-shift-keying (PSK), the canonical digital communication protocol. I also measure the bandwidth limit of the electromagnetically-induced-transparency (EIT) probing scheme and show near photon-shot-noise limited channel capacity of up to 8.2 Mbit/s for 395 mV/m microwaves at a 17 GHz carrier frequency.

3.2.1 Experimental Configuration

A schematic of the experimental apparatus is shown in Fig. 3.11(a), and the core elements are similar to those of other EIT-based Rydberg electrometry work [54, 58]. A MW horn addresses a 17.0415 GHz transition between the $|50D_{5/2}\rangle$ and $|51P_{3/2}\rangle$ states. The resonant MW field establishes an Autler-Townes splitting, proportional to the MW Rabi frequency Ω_μ , which is probed using EIT (level diagram in Fig. 3.11(b)). The 480 nm coupling beam counter-propagates with respect to the 780 nm probe to largely cancel Doppler-broadening of the room-temperature atoms. EIT is observed by either directly measuring the transmitted probe power (Fig. 3.11(c)) or performing heterodyne detection by interfering the probe with a 78.5 MHz-shifted local oscillator (LO).

The 780 nm probe light is generated by an external cavity diode laser, linewidth ~ 150 kHz, that is beat-note locked to a distributed Bragg reflector diode laser stabilized via saturated absorption spectroscopy to a separate reference vapor cell. The probe light power is actively stabilized using an acousto-optic modulator (AOM) and is focused to a $1/e^2$ radius of 100 μm at the center of a 75 mm long vapor cell. At

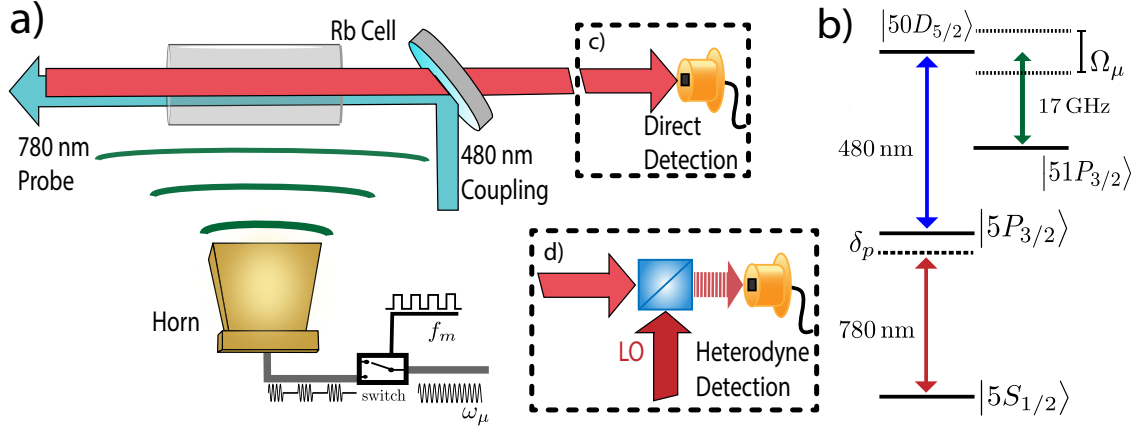


Figure 3.11: (a) Probe (red) and coupling (blue) light counter-propagate in a vapor cell of rubidium atoms, forming a ladder-EIT system (shown in (b)) that excites ground-state atoms to a Rydberg state. Microwaves (green) from a horn antenna couple the $|50D_{5/2}\rangle$ and $|51P_{3/2}\rangle$ states, and split the EIT peak. A switch modulates the microwaves, and thereby the EIT splitting, and this is detected as amplitude modulation of the probe laser intensity. (c) Probe intensity modulation can be measured directly with a fast photodetector (d) or measured using an optical heterodyne method, where a frequency-shifted local oscillator (LO) beam is mixed with the transmitted probe.

room-temperature, the measured optical depth is ~ 0.4 . The strong 480 nm coupling beam is also focused, to a $1/e^2$ radius of 50 μm , so as to have sufficient coupling to the Rydberg state and is generated by a commercial doubling system (Toptica SHG-Pro) that is stabilized to an ultra-low expansion (ULE) reference cavity. This stabilization reduces the linewidth to approximately 2 kHz. The probe and coupling light are overlapped using a dichroic mirror. These beams counter-propagate in a room temperature, natural abundance rubidium vapor cell with vertical linear polarizations. The (MW) field to be measured is also vertically polarized and propagates perpendicular to the light beams.

The MW field at the resonant 17.0415 GHz frequency is synthesized by a Rhode-Schwarz SMF100A signal generator and is applied to the vapor cell using

a WR51 waveguide horn antenna. The absolute generator power was calibrated using standard Autler-Townes measurements with MW field Rabi frequencies greater than the electromagnetically-induced-transparency full-width half-max linewidth ($\Gamma_{\text{FWHM}} \approx 4 \text{ MHz}$). The MW field modulation is done using an external MW switch (Hittite HMC-C019) on the output of the MW signal generator. The phase of the modulation is controlled via the phase of the TTL-control signal.

The probe intensity modulation due to the amplitude modulated MWs is measured by a fast photodetector (Thorlabs PDA10A) behind a 780 nm laser line filter in two configurations. The first configuration is direct detection (see Fig. 3.11(c)) with the signal analyzed using: a lock-in amplifier (Stanford Research SRS865) to demodulate the signal into I and Q quadratures, as done for the data of Figs. 3.12 & 3.14 (the modulation for 3.12(a) is on the coupling light, the modulation for 3.12(b) and 3.14 on the MWs); or a digital storage oscilloscope (Keysight DSOX1102G) to obtain the time-domain response, as done for the data of Figs. 3.15, 3.16, and 3.18. The second configuration is optical heterodyne detection, in which a strong ($\sim 4 \text{ mW}$) local oscillator derived from the probe laser, shifted 78.5 MHz, is interfered with the transmitted probe using a 50/50 fiber splitter. The resulting beat signal is measured using an identical fast photodetector with the output sent to a spectrum analyzer (Agilent N9020A), as done for the results shown in Fig. 3.18.

Overall experimental control and timing is implemented using the open-source labscript suite. [85] Further details about our lab specific implementation can be found in Appendix A.

3.2.2 Demodulated Signal

Figure 3.12(a) shows an example measurement of probe transmission, V_{trans} , normalized to the amplitude of the EIT peak V_0 , observing EIT with the microwaves on (green trace) and off (blue trace). To send digital information the MW field is amplitude modulated. The modulation phase φ_μ encodes 8 states, corresponding to all permutations of 3 bits ranging from 000 to 111. The possible states are shown in the I-Q plane in the inset of 3.12(b). The amplitude modulation is imposed, through EIT, onto the probe laser transmission, and the resulting oscillating probe transmission is then demodulated into an In-Phase voltage V_I and a Quadrature-Phase voltage V_Q using a lock-in amplifier.

Five distinct examples of the demodulated signal V_I are plotted versus probe detuning in Fig. 3.12(b). These V_I signals are proportional to the subtraction of two EIT signals V_{trans} , with microwaves on and off, such as those shown in Fig 3.12(a), which leads to features dependent on the MW Rabi frequency Ω_μ as described next.

3.2.2.1 Demodulated Signal Dependence on Ω_μ

In typical Rydberg electrometry measurements the MW field resonantly couples two nearby Rydberg states that are then probed using a ladder EIT scheme. The MW coupling results in Autler-Townes (AT) splitting of the EIT peak that is proportional to the MW Rabi frequency, by $\Omega_\mu = 2\pi D\Delta f$. This in turn provides a very sensitive, SI-traceable measure of MW electric field amplitudes, as described above. [58] However, if the AT splitting is less than the linewidth of the EIT sig-

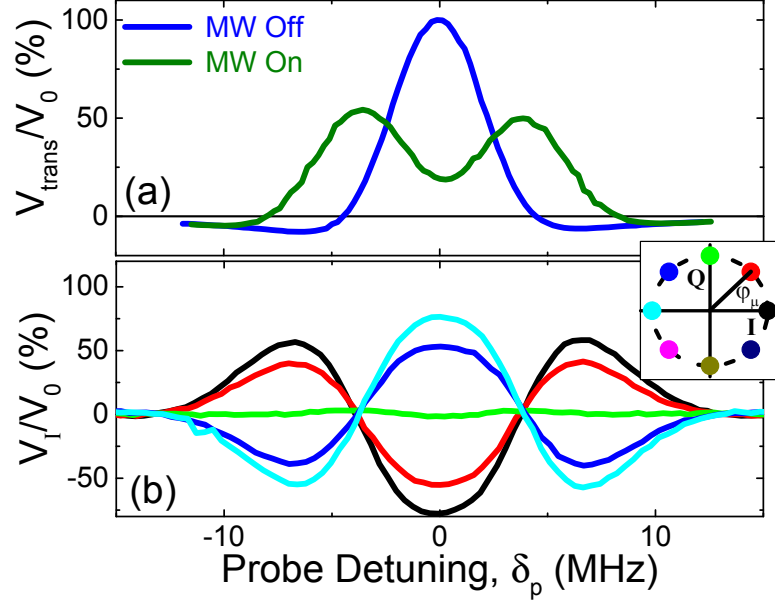


Figure 3.12: (a) The observed Rydberg EIT (blue) and Autler-Townes split Rydberg EIT (green) probe transmissions V_{trans} vs probe detuning δ_p . (b) Example demodulated transmission signals V_I with color corresponding to amplitude modulation phases $\phi_\mu = 0, 45, 90, 135$ and 180 degrees, matching the amplitude modulation phase states shown in the inset.

nal the splitting is unresolved and other, less exact, methods must be used. [54] Furthermore, even when AT splitting is resolvable, if the splitting is not greater than twice the EIT full-width-half-max linewidth, the linear dependence described above is not valid as the atomic system transitions from an AT dominated signal to an EIT dominated signal. [60] As a result, techniques for obtaining linear, precise measures of AT splitting near or less than the EIT linewidth are of particular value to the accurate measure of MW electric field amplitudes. The demodulated signal shown in Fig. 3.12(b) has two primary features with widths that depend on the MW Rabi frequency that are also clearly resolvable well within the EIT linewidth: the outer peaks splitting and the zero crossings splitting. Furthermore, thinking of the demodulated signal as the simple subtraction of the AT signal by the EIT

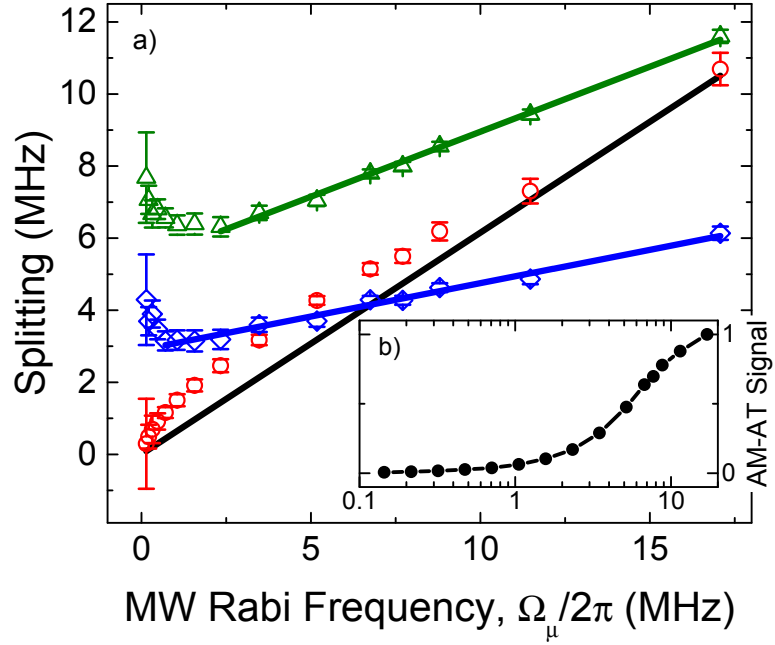


Figure 3.13: (a) Summary of splittings extracted from demodulated signal. The black line is the expected linear AT splitting extrapolated from higher MW field measurements. The red circles are the extracted AT splittings from the Gaussian based model fits. The green triangles show the splitting between the peaks and the blue diamonds show the splitting between zero crossings of the signal. The blue and green lines are linear fits to guide the eye. (b) Amplitude of demodulated signal with the probe resonant, normalized to the maximum measured signal, versus MW Rabi frequency.

background hints at the possibility of a way to model the signal to extract the MW Rabi frequency directly.

Due to residual Doppler-broadening the typical lorentzian peak of EIT becomes approximately gaussian. If I assume the AT peaks to also be gaussian I can write a simple model of three gaussian peaks, one with negative amplitude, to fit the demodulated signals and extract the AT splitting. Figure 3.13(a) shows the result of these fits compared with the linear AT splitting expected for higher MW powers. In agreement with the results of Ref. [60] I obtain non-linear deviations from the linear AT splitting when the splitting is less than twice the EIT linewidth

($2\Gamma_{\text{FWHM}} \sim 8 \text{ MHz}$). This suggests the model is effective at extracting the AT splitting.

Figure 3.13(a) shows the width of the outer peaks splitting and the zero crossings splitting for the same demodulated signals, the green and blue points respectively. While analytic models of this transitional region are difficult to obtain it is interesting to note that the dependence on the MW Rabi frequency is linear, even when the AT splitting is well within the EIT linewidth. As might be expected, the slope and zero crossings of the linear fits to these data depend on experimental parameters other than the MW field. However, their linear regions continue into the well-resolved, AT split regime and therefore could be calibrated precisely using the AT splitting of higher MW fields, effectively extending the regime of linear response to MW fields nearly an order of magnitude lower.

Figure 3.13(b) shows the amplitude scaling of the resonant demodulated signal (shown in Fig. 3.12(b)) versus MW Rabi frequency. As can be expected, the scaling of the signal magnitude changes as the signal transitions through the EIT linewidth. This measured scaling allows me to extrapolate the photon-shot-noise limited sensitivity from the measured SNR of the heterodyne measurement at the relatively high MW field of 395 mV/m . From this I estimate the photon-shot-noise limited sensitivity of the Rydberg receiver to be $0.13 \text{ mV}/(\text{m} \sqrt{\text{Hz}})$. Accounting for the differences in experimental parameters, this value roughly agrees with the measured photon-shot-noise limited sensitivity reported by Kumar *et. al.* [67]

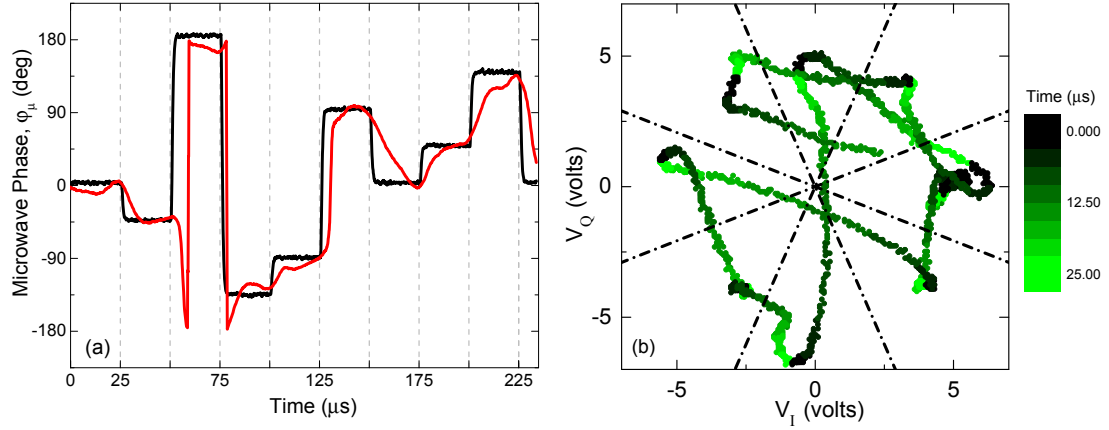


Figure 3.14: (a) PSK sent and received phase (black and red, respectively) with $\Omega_\mu = 2\pi \times 11.4 \text{ MHz}$ at a 40 kHz symbol frequency and an amplitude modulation rate of 1.98 MHz. The vertical dashed lines delineate the individual symbol periods. (b) Phase constellation of the received phase in (a) (red line). The axes V_I and V_Q are in volts measured at the lock-in amplifier. The dashed lines delineate the eight phase states. Marker colors ranging from black to green denote the passage of one 25 μs symbol period.

3.2.3 Phase Shift Keying Demonstration

I can demonstrate a PSK protocol by rapidly changing the phase φ_μ of the amplitude modulation while measuring the lock-in signals at zero detuning. φ_μ is reconstructed from $\varphi_\mu = \arctan(V_Q/V_I)$. Figure 3.14(a) shows example sent and received amplitude-modulation phases (black and red traces respectively) where each symbol representing three bits of data is transmitted for 25 μs . Figure 3.14(b) shows the same recovered signal in the corresponding phase space shown in the inset of Fig. 3.12(b). Effective signal recovery is done when the demodulation phase is optimized (*i.e.* rotation of the phase space) and the clock is properly recovered (*i.e.* sampling the correct set of data points spaced by the symbol send period). The data transmission rate in this experimental configuration is ultimately limited

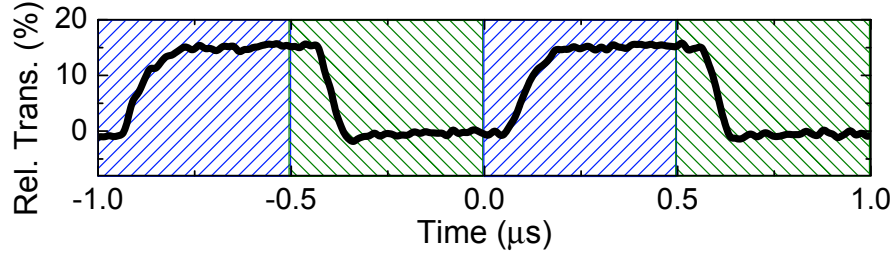


Figure 3.15: An example time-domain trace of the transmitted probe signal as MWs are modulated at 1 MHz. The blue and green regions show when the MWs are off and on, respectively.

to ~ 1 Mbit/s by the speed of the lock-in amplifier. This is due to the lock-in amplifier's minimum output time constant of $1 \mu\text{s}$ which limits the symbol rate. In order to show the potential utility of the Rydberg receiver I next characterize the more fundamental limits.

3.2.4 EIT Detection Bandwidth Limitations

I first theoretically model and experimentally measure the bandwidth of the Rydberg receiver. Figure 3.15 shows a typical time-domain trace of the signal where the MW field is modulated on and off (green and blue regions respectively) at 1 MHz. Exponential time constants are extracted from the signal time traces and plotted against the relevant pumping rates in Fig. 3.15(b) and (c). This type of measure for the system bandwidth is similar to switching time measures in photon-switching [86–88] and cross-phase modulation [46, 89] experiments based on EIT, which allows me to apply theory developed in those contexts to understand the limitations of the system bandwidth.

The $1/e$ fall times τ_f , corresponding to the MWs being turned on, are shown in

Fig. 3.15(b) for five different MW powers and a fixed coupling power $P_c = 48$ mW. The MW and coupling Rabi frequencies combine to form the characteristic Autler-Townes pumping rate, $\Omega_{AT} \equiv \sqrt{\Omega_c^2 + \Omega_\mu^2}$, shown on the horizontal axis. The blue lines in Fig. 3.15(b) and (c) show results obtained from numerically integrating the optical Bloch equations for the 4-level system under the same experimental parameters. I apply a constant multiplicative scale factor to these theory lines, corresponding to systematic under-estimation, due to unaccounted-for Doppler-broadening and magnetic sublevels. The value of this parameter, 1.2, is consistent with similar offset effects described in [90]. The measured data show good agreement with the numerical model over the entire experimental range. In the weak probe/strong EIT regime ($\Omega_p \ll \Gamma$, $\Omega_c^2/\gamma\Gamma \gg 1$, where Γ , γ are the dephasing rates for the intermediate and ground states) a simple analytical model for laser-cooled atoms, which assumes no dephasing in the ground state, predicts that the fastest possible switching time is $2/\Gamma$. [91] This model is readily generalized to include ground-state dephasing (dominated by transit effects, as described in the next section) to give a limit of $2/(\Gamma + 2\gamma) = 1.45/\Gamma$, with $\gamma = 2\pi \times 1.14$ MHz as the estimated ground-state dephasing rate. The black-dashed line of Fig. 3.15(b) shows this limit. This analytical prediction is also confirmed by the data.

I note that the above models are best suited to experimental conditions that result in distinct EIT. Figure 3.16(a) shows the same data and model, but with a coupling power of 11 mW. We see that while the numerical model reproduces the qualitative features of the data, the quantitative fit is poor. In the next section I will discuss some of the limitations of these models. In general I note that the

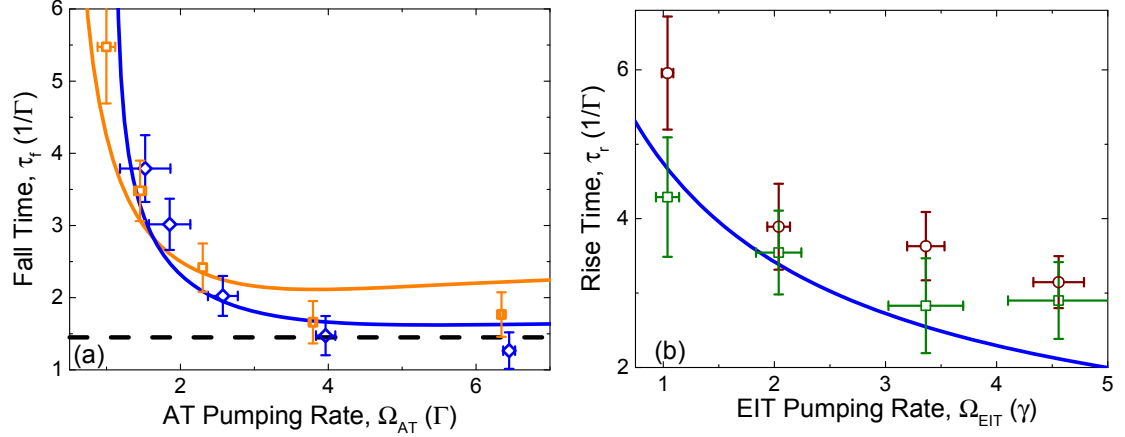


Figure 3.16: (a) Measured fall times τ_f of the time traces versus characteristic pumping rate Ω_{AT} set by the MW and coupling laser powers. A numerical model is shown as a solid line, and the dashed black line shows the asymptotic fall time ($1.45/\Gamma$) for pumping into the dark state. Blue is for $\Omega_c = 2\pi \times 8$ MHz and orange is for $\Omega_c = 2\pi \times 3.8$ MHz, or approximately 1/4 the optical power. (b) Measured rise times τ_r versus the characteristic EIT pumping rate Ω_{EIT} set by the coupling laser power. The green and maroon points show the measured rise times for the lowest and highest MW powers measured ($\Omega_\mu = 2\pi \times 5$ MHz & $2\pi \times 38$ MHz, respectively). The blue line shows the rise times from the numerical model.

dynamics of this system are complicated and can vary wildly depending on experimental parameters. A general model will require more sophisticated methods than those employed here.

Figure 3.15(c) shows the $1/e$ rise times corresponding to the MWs being turned off, τ_r . This situation represents the well-studied EIT pumping rate, $\Omega_{EIT} \equiv \Omega_c^2/2\Gamma$, for a ladder EIT system and translates to the time needed to establish the EIT dark state (*i.e.* resulting in greater probe transmission). [92] I show fitted rise times for the lowest and highest MW powers (green and maroon points, respectively) versus Ω_{EIT} in units of the ground-state dephasing rate γ . In these units, $\Omega_{EIT} \gg 1$ is considered to be in the strong EIT regime. As expected, τ_r scales inversely with Ω_{EIT} . This also shows reasonable quantitative agreement with the numerical model.

In Fig. 3.15 parts (b) and (c), for the current parameters, the best achievable rise time τ_r is slower than the best fall time τ_f , showing the system is limited by the coupling power. However, I note that for a sufficiently strong coupling laser, the fall-time limit would be the bandwidth limit for the EIT probing scheme.

3.2.4.1 Derivation of τ_f Limit for a Transit-Broadened Medium

The analytical model for τ_f described above is generalized from the expression for τ_f presented in the footnotes of [91]. It is derived in the context of laser-cooled atoms, to be

$$\tau_f = \frac{2(\gamma_\mu \Gamma + \Omega_c^2 + \Omega_\mu^2)}{\gamma_\mu \Omega_c^2 + \Gamma \Omega_\mu^2}. \quad (3.13)$$

This assumes a typical N -level configuration with two excited states with natural linewidths Γ , γ_μ (for the probing and MW transitions, respectively) and the two ground states having infinite lifetime. The four levels are coupled together with optical fields with Rabi frequencies Ω_p , Ω_c , and Ω_μ that correspond to the probe, coupling, and MW fields used in the experimental configuration. This result is derived from the optical Bloch equations in the weak probe limit (*i.e.* equations are taken to first order in Ω_p and all population is assumed to be in the lowest ground state.). In the limit of large MW Rabi frequency Ω_μ the fall time τ_f approaches a minimum value of $2/\Gamma$. Assuming sufficiently large Ω_c such that the EIT condition is met, this time sets the basic bandwidth limit for EIT probing of the MW modulation.

For warm atoms, as used in this work, ground-state dephasing due to transit and other effects must also be considered. Transit dephasing is the result of thermal

atoms traversing the probe beam profile. While within the profile, an atom interacts with the light as expected and becomes polarized according to the Hamiltonian of the system. Once the atom leaves the profile, it is replaced by a fresh, unpolarized atom, which dephases any coherent effects established. The transit dephasing is related to the probe beam size and the temperature of the atoms. I estimate the total ground-state dephasing, including non-transit sources, to be $\gamma \approx 2\pi \times 1.14$ MHz for this experimental setup. [52]

Under the weak probe approximation, using the method of [91] explained above, and including transit dephasing with all excited-state natural lifetimes for the experimental system, the optical Bloch equations for the coherences induced by the probe, coupling, and MW fields are

$$\frac{d}{dt}\rho_{21} = -\frac{1}{2}(\Gamma + 2\gamma)\rho_{21} + \frac{i}{2}(\Omega_p + \Omega_c\rho_{31}) \quad (3.14)$$

$$\frac{d}{dt}\rho_{31} = -\frac{1}{2}(\Gamma_D + 2\gamma)\rho_{31} + \frac{i}{2}(\Omega_c\rho_{21} + \Omega_\mu\rho_{41}) \quad (3.15)$$

$$\frac{d}{dt}\rho_{41} = -\frac{1}{2}(\Gamma_P + 2\gamma)\rho_{41} + \frac{i}{2}\Omega_\mu\rho_{31} \quad (3.16)$$

where ρ_{i1} is the density matrix element representing the coherence between the $i = (2, 3, 4) = (|5P_{3/2}\rangle, |5D_{5/2}\rangle, |5P_{3/2}\rangle)$ states and the ground state $|5S_{1/2}\rangle$. $\Gamma_{D,P}$ are the natural lifetimes of the D and P Rydberg states. The probe absorption is proportional to $Im(\rho_{21})$ so solving the above equations to obtain an approximate, first-order differential equation for ρ_{21} allows me to model the expected exponential decay of the absorption as the MW field is turned on.

Taking $\Gamma_{D,P} \ll \gamma$, the resulting differential equation becomes

$$\frac{d}{dt}\rho_{21} = -\frac{1}{\tau_f} \left(\rho_{21} - \rho_{21}^{(SS)} \right) \quad (3.17)$$

where the steady state value (proportional to the observed transmission) with MWs on is

$$\rho_{21}^{(SS)} = \frac{i\Omega_p (4\gamma^2 + \Omega_\mu^2)}{8\gamma^3 + 4\gamma^2\Gamma + 2\gamma\Omega_{AT}^2 + \Gamma\Omega_\mu^2} \quad (3.18)$$

and the $1/e$ fall time is

$$\tau_f = \frac{2(12\gamma^2 + 4\gamma\Gamma + \Omega_{AT}^2)}{8\gamma^3 + 4\gamma^2\Gamma + 2\gamma\Omega_{AT}^2 + \Gamma\Omega_\mu^2}. \quad (3.19)$$

When $\Omega_\mu \gg \Omega_c, \Gamma, \gamma$ this reduces to a minimum fall time of $2/(2\gamma + \Gamma)$, which is approximately 1.45Γ using the experimental parameters of Fig. 3.16(b). This shows that transit dephasing allows for fall times to exceed the cold-atom EIT result ($2/\Gamma$) by providing a second loss mechanism for the atomic coherence established in EIT. In much the same way a parallel resistance can improve the bandwidth of a classical antenna at the expense of signal efficiency, transit decoherence can improve the bandwidth of the EIT probing scheme at a cost of reduced signal by acting as an effective re-pumping mechanism.

Figure 3.17 compares this model to experimental fall time data and the full numerical model versus coupling Rabi frequency Ω_c for a few fixed MW powers. For the higher coupling powers good agreement with the measured data is observed. However, the analytical model predicts that the fall time should decrease with de-

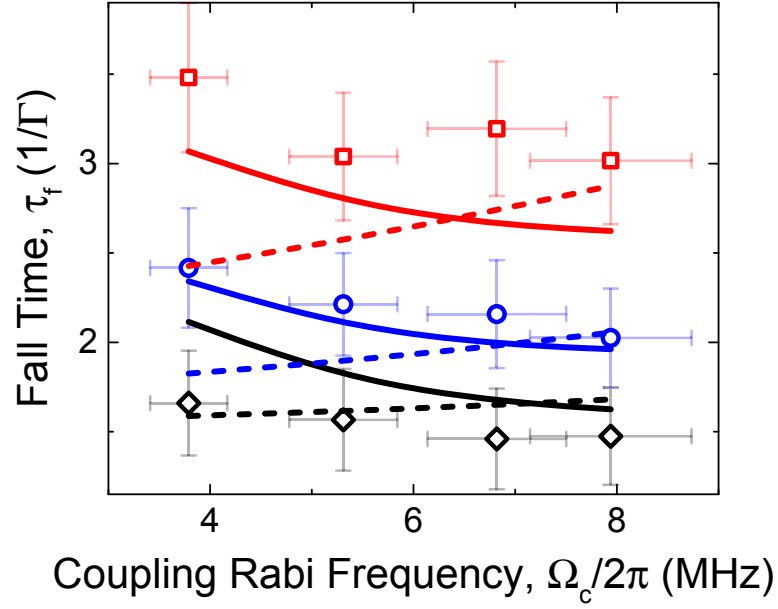


Figure 3.17: Comparison of experimental data to numerical and analytical model predictions for the fall time τ_f . The red squares, blue circles, and black diamonds show the measured τ_f versus coupling Rabi frequency Ω_c for $\Omega_\mu/2\pi = 8.0$, 13.4, and 22.7 MHz. The solid lines show the numerical model fits (scaled by 1.2 as described in the main text) and the dashed lines the analytical model predictions for the same experimental parameters. The data points at $\Omega_c/2\pi = 8$ MHz correspond to the middle data points of Fig. 3.16(b).

creased Ω_c . This expected behavior has been seen in similar EIT-based cross-phase modulation systems where the EIT linewidth, which is inversely proportional to Ω_c , sets the bandwidth of the modulation. [90, 92] However, both the data and the numerical model show the opposite trend. This is due to a breakdown of the analytical model as the weak probe/strong EIT regime assumption becomes less valid. As already mentioned, the EIT regime is when $\Omega_c^2/\Gamma\gamma \gg 1$ which is only approximately true for the data presented. In this weak EIT regime greater Ω_c leads to a stronger EIT signal that effectively has a larger linewidth and therefore bandwidth. Furthermore, due to Doppler-averaging, larger Ω_c relative to the intermediate state lifetime results in AT splitting of velocity classes that average to an even greater Rydberg EIT linewidth and therefore bandwidth.

In short, increased coupling power to fully obtain the EIT regime, or even exceed it, is necessary for greater signal bandwidth. However, increasing the coupling power well beyond the EIT regime will eventually lead to reduced signal bandwidth as other deleterious effects on the signal make themselves known.

3.2.5 Measuring Channel Capacity

To measure the photon-shot-noise-limited channel capacity the measurement scheme is changed to the heterodyne configuration (see Fig. 3.11(d)). In heterodyne, gain from the LO amplifies the signal and increases the photon-shot-noise. For sufficiently high LO powers, the photon-shot-noise becomes the dominant noise source, allowing one to disregard other technical noise sources. The transmission

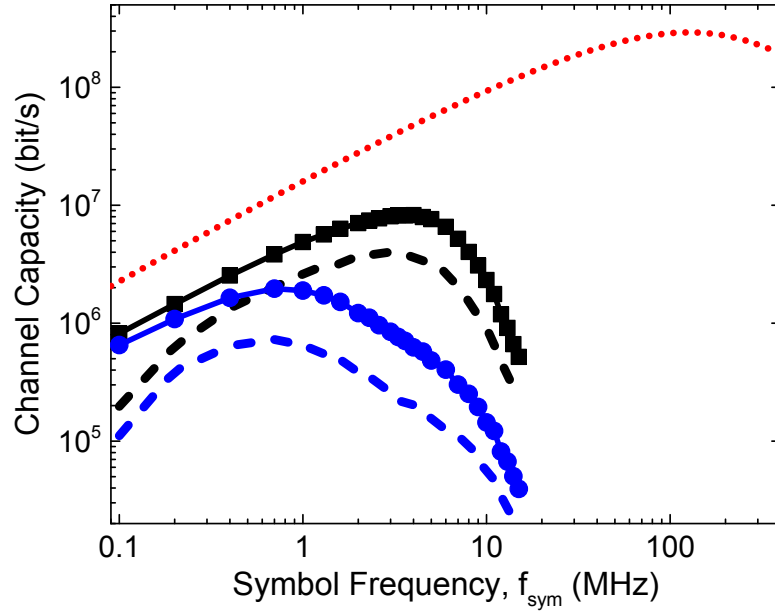


Figure 3.18: Empirical channel capacity versus symbol frequency with an $\Omega_\mu = 2\pi \times 8$ MHz MW Rabi frequency for two coupling powers: $P_c = 48$ mW (black) and $P_c = 11$ mW (blue). The dashed lines represent the channel capacity including all noise sources. The lines with symbols represent the channel capacity with only photon-shot-noise considered. The dotted red line shows the theoretically-predicted atom-shot-noise limited capacity for the same MW power.

signal amplitude $\mathbb{S} = V_{\text{trans}}$ and output voltage noise spectrum \mathbb{N} is recorded using a spectrum analyzer. Measuring these quantities versus the symbol frequency (assuming one symbol per modulation period) allows for calculation of the maximum attainable channel capacity via Eq. 3.11. Figure 3.18(d) shows the empirical channel capacities for the highest (black) and lowest (blue) coupling powers. The dashed lines show the channel capacity including all measured noise sources (*i.e.* detector and laser frequency noise) while the lines with data points show the channel capacity with only photon-shot noise. There are three primary regions of interest. For low symbol frequency the channel capacity is limited by the modulation rate, and shows a linear rise in capacity. The channel capacity then peaks when SNR is reduced to 1 by the increasing photon-shot noise and decrease in signal, due to the limiting bandwidths τ_r and τ_f described above. For higher symbol rates the bandwidth-limited signal reduction dominates and the channel capacity decreases rapidly.

The maximum empirical channel capacity for the $\Omega_\mu = 2\pi \times 8 \text{ MHz}$ MW field (395 mV/m) shown is 8.2 Mbit/s at a 4 MHz symbol rate. As already described, this capacity is significantly limited by the EIT probing scheme and the associated photon shot-noise. Even so, the sensitivity of the photon-shot-noise limited Rydberg receiver detecting a $\sim 13 \text{ mV/m}$ MW field would still allow for a channel capacity of 10 kbit/s which is sufficient for some applications such as audio transmission.

Fundamentally, wave-function collapse limits the SNR when using Rydberg atoms, or any other sensor made of 2-level quantum systems, to the Standard Quantum Limit for measurement of a quantum phase ϕ . I will discuss this limit in more

detail in the next section. For now I show an estimated, quantum-limited, channel capacity as the red dashed line of Fig. 3.18. It assumes the same magnitude RF field and an atom number of $N = 1000$.

3.2.6 Contrast with Classical Receivers

Determining the utility of a Rydberg receiver for classical communication requires a direct comparison to current classical antennas. Unfortunately, such comparisons are often simplistic and potentially even misleading because the Rydberg receiver and a classical antenna fundamentally differ in operation. A classical antenna is a passive device that couples power from a free-space mode of the MW field into a transmission line. It is a sensor that measures RF power. The Rydberg receiver is sensitive to the perturbations caused by the presence of electric fields. On average it does not absorb MW photons but rather performs a non-perturbative measurement. It is a sensor that measures the local RF electric field. Moreover, it does so in a way that is not directly dependent on size of the device, which is very different from the classical analog of measuring the voltage on a wire to determine the electric field applied.

The implications of this fundamental difference for communications reception are widely varied and understanding them can inform where potential applications of the Rydberg receiver may lie. For instance, non-perturbative measurement of wireless signals may be desirable for covert signals interception. This non-perturbative measurement of electric field is also what allows the Rydberg receiver to have good

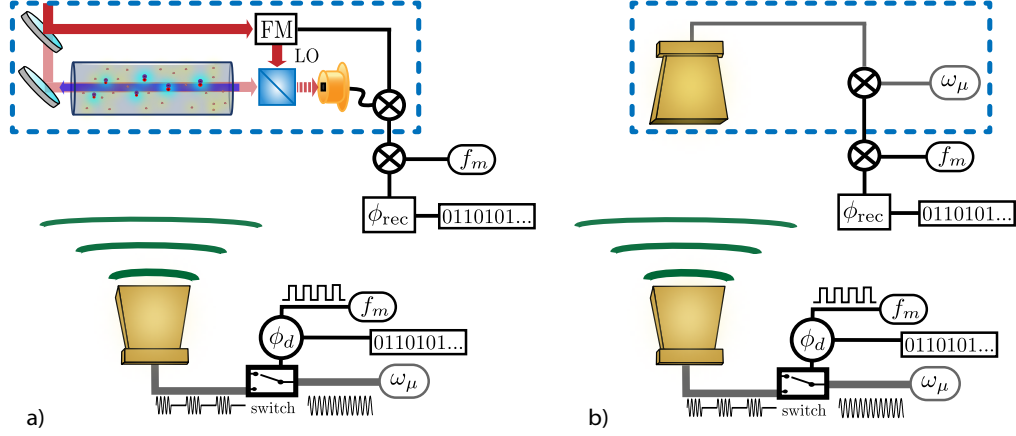


Figure 3.19: Comparison between (a) Rydberg receiver system and (b) classical receiver system. Each system uses the same transmitter where a MW carrier ω_μ modulated at a rate f_m with a switch. The phase of this modulation ϕ_d is varied to encode the information to transmit. The blue outlined regions denote the receiver portions that detect the transmitted field and mixes it down to baseband. The final portion demodulates the baseband signal at frequency f_m . Phase sensitive detection reproduces the sent ϕ_d as ϕ_{rec} which is then interpreted as the transmitted data. The Rydberg receiver in part (a) includes the optional, but typically necessary, optical frequency modulation (FM) to produce of local oscillator (LO) for optical mixing to improve the SNR of optical detection of weak fields.

sensitivity and bandwidth performance in the electrically small regime.

Another important difference between the Rydberg receiver and a classical antenna is their function in a classical communications architecture. Figure 3.19 provides a simplified block diagram of an entire communications system with transmitter and receiver for the case of the Rydberg receiver (a) and a classical antenna receiver system (b). In both systems, there are four operational components: encoding, transmitter, receiver, and decoding. The encoding stage takes input information and encodes it into the phase of some modulation on a MW carrier. This modulated signal is then broadcast into a free-space mode by a classical antenna. The MW field propagates through free-space where the receiver detects the signal and reproduces the modulation from the transmitted field at baseband. The decoding

stage then performs phase sensitive detection of the modulation to recover the transmitted signal. The blue highlighted components show the receiver portion of each system, which points to the hurdle in making fair comparisons between a Rydberg receiver and a classical antenna. The classical antenna alone cannot produce an output at baseband (modulation at DC instead of the carrier frequency), whereas the Rydberg receiver can because demodulation from the carrier is performed internally via the atoms.

Note that the reception mixing stages in both systems require frequency sources that are stable relative to the input frequencies that transmitted the signal. However, only the classical receiver requires a MW frequency source, which can be difficult for high frequencies or when the local interference cannot be tolerated (such as in RADAR where the reception MW source can leak out of the reception antenna and cause interference for other receivers of the same field). The Rydberg receiver instead uses the atoms as the MW reference. While not strictly necessary, detector noise often necessitates some kind of comparable optical mixing to improve the SNR. However this mixing can be done internally to the receiver at a significantly lower frequency than ω_μ , though greater than f_m .

By nature of its design, the Rydberg receiver is a natural interface for transduction of modulation on a MW carrier to modulation on an optical carrier. This makes the system a natural fit for Radio-over-Fiber applications, as suggested in [93]. In effect, the sensitivity of Rydberg atoms allows the Rydberg receiver to be an unusually effective electro-optic modulator with a free-space drive; an unusual, yet interesting device. While the optical carrier is currently in the near-infrared band

which does not have good propagation characteristics, there are more amenable infrared transitions in the spectra of the alkali atoms (rubidium has transitions at 1324 nm and 1367 nm for instance) that can be linked into the EIT detection process through three-photon excitation. [94]

The broad-band nature of the Rydberg sensitivity to MW electric fields is also an important fundamental difference to a classical antenna. The vast number of MW resonant transitions in the Rydberg state manifolds allows for high SNR reception at a broad range of carrier frequencies ranging from approximately 100 MHz to 1 THz. The only change required to detect each field is tuning of optical wavelength within a range of 10 nm, a feat that is possible with speed and accuracy for modern laser light sources. Furthermore, as I demonstrate in the next section, off-resonant detection of MW fields can also be done with high SNR, meaning that effectively the entire frequency spectrum from quasi-DC to 1 THz can be detected. This opens up the possibility of simultaneous reception at wildly disparate carrier frequencies, fast carrier frequency hopping reception, and broad-spectrum characterization of unknown frequency fields all with the same device.

Another curious aspect of the Rydberg receiver is the potential for vector detection, as demonstrated by [65]. It relies on the relative orientation of the MW polarization relative to the laser polarizations. By including configurable polarizations of the light field, one could conceivably distinguish between MW fields with different polarizations or even directions without physical adjustment of the sensor, a feat only possible in more complicated and difficult to manufacture phased-arrays antennas.

Related to vector detection is the potential for sub-wavelength imaging, already demonstrated many times in the context of Rydberg electrometry. [63, 64] In the context of digital communications, sub-wavelength imaging techniques could also be used to implement highly accurate directionality measurements of incoming communications.

In conclusion, Rydberg receivers open up many potential avenues of exciting possibility. I emphasize that these opportunities do not exclusively rely on absolute performance characteristics such as bandwidth or sensitivity, but more on the fundamentally different method of reception that allows for completely new capabilities, some likely yet to be proposed.

3.3 Digital Communication in the Electrically Small Regime

Antennas do not obey Moore’s law. As cutting-edge devices become smaller and smaller, the communication transmitter and receiver antennas present significant size constraints [44, 73]. This is because fundamental principles limit the performance of a traditional antenna that is significantly smaller than the wavelength of the electromagnetic field being detected, λ . Specifically, a lossless, resonant, electrically-small antenna of characteristic radius a is guaranteed to have a quality factor Q greater than the Chu limit, $Q_{\text{Chu}} = \lambda^3/(2\pi a)^3$, that limits the operation bandwidth to $BW_{\text{Chu}} \lesssim f_0/Q_{\text{Chu}}$ for carrier frequency f_0 . Discovery of modest optimizations within the Chu limit constraint is still an active area of research [95, 96], as well as exploration into alternative communications technologies, (e.g. based on acoustics or active circuits) that are not subject to the Chu limit [97, 98]. Here I introduce another alternative path: using a quantum sensor operating at the standard quantum limit (SQL) to receive classical communications.

In this section I describe a modification of the Rydberg receiver system described in the last section such that it can detect RF electric fields ranging from 10 kHz to 30 MHz. The 7 cm vapor cell used has a corresponding electrical size a ranging from $\lambda/800k$ to $\lambda/270$ which places this system well inside the electrically small regime. I will show measurements of the channel capacity of this electrically small system and compare it with the expected channel capacity of a Chu-limited

antenna of the same size as the vapor cell. The Rydberg receiver system outperforms the Chu-limited antenna by over four orders of magnitude over the tested frequency range.

3.3.1 Far Off-Resonant Configuration

The modified system employs far off-resonant electrometry methods using Rydberg atoms. As described above in Section 3.1.3, off-resonant electrometry employs frequency shifts of the EIT resonance due to the presence of electric fields. In much the same way resonant electrometry uses field dependent shifts to measure modulated RF signals, the off-resonant electrometry also measures modulations of low frequency RF fields.

A simplified version of the modified experimental setup and level diagram is shown in Fig. 3.20(a) and (b). Using two parallel plates separated by 60 mm, a transverse low-frequency electric field is driven by a square wave function generator (Rigol DG4162). The 480 nm (blue) beam (tuned to the ^{85}Rb $|5P_{3/2}, F = 4\rangle$ to $|50D_{5/2}\rangle$ transition) and the 780 nm (red) beam (tuned to the $|5S_{1/2}, F = 3\rangle$ to $|5P_{3/2}, F = 4\rangle$ transition), counter-propagate to establish nearly Doppler-free EIT. The vapor cell is heated to approximately 60 °C using metallic heating elements at either end of the cell. While these elements have a perturbative effect on the E-field, it is small due to the long characteristic wavelengths and small plate gap used.

In the regime of low-frequency E-fields, the Stark shift of the Rydberg state, $\delta\omega = \frac{1}{2}\alpha E^2$, where α is the scalar polarizability of the atomic transition, is approxi-

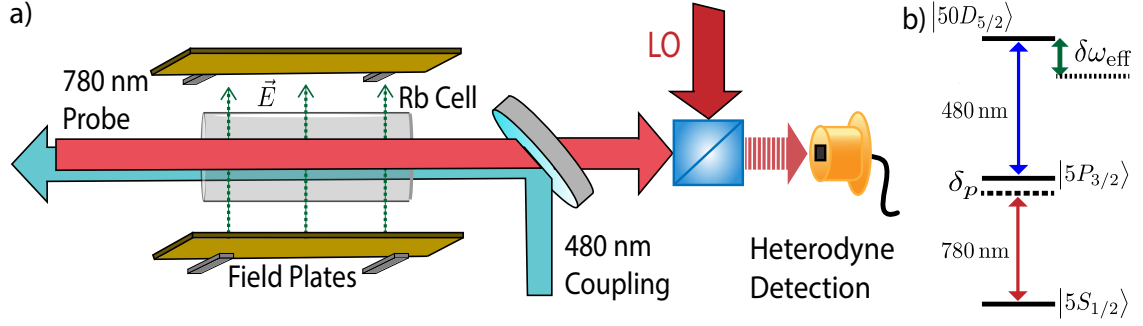


Figure 3.20: (a) Experimental Setup: Configuration is a modification of the resonant configuration in Fig. 3.11. The RF field is applied to the cell by two large plates. Detection is done using the heterodyne technique. (b) Level diagram for the Off-Resonant Configuration. The RF field causes Stark shifts of the Rydberg state that can be detected using Rydberg EIT.

mately constant over the frequency range tested. In the presence of an approximately static electric field, the $|50D_{5/2}, |m_j| = 1/2, 3/2, 5/2\rangle$ Rydberg states split into three distinct levels due to the tensor component of the polarizability. I have calculated the polarizabilities of these states to be $\alpha = 2\pi \times (-36, 42, 212)$ MHz/(V/cm)² respectively using the ARC package (described in detail in Appendix B) [66]. This calculation assumes approximately static fields, which is a fair approximation when the frequency is far from any atomic resonances. The nearest Rydberg-Rydberg transition for $|50D_{5/2}\rangle$ is the 17 GHz transition used above. However, potential resonances were observed at much lower frequencies near 50 MHz likely due to intra-level transitions. The following description avoids these resonances for the sake of theoretical simplicity in the ultimate analysis.

Figure 3.21 shows a plot of the EIT transmission profile with no electric field (red), and with an electric field of 0.4 V/cm applied (blue). Due to the shielding effect of vapor cells (described below) this measurement was performed by square-modulating the electric field at a rate of 1 MHz from 0 to 5 V. The DC component

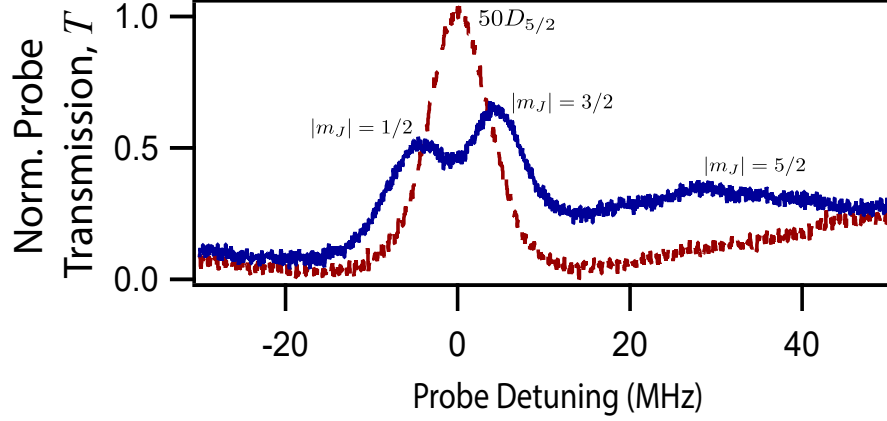


Figure 3.21: When no E-field is applied, a single EIT transmission window is observed (red). Low frequency electric fields cause scalar and tensor Stark shifts, that split the resonance into three peaks (blue).

is shielded resulting in the atoms experiencing, on average, ± 2.5 V. The Stark shift is insensitive to the sign of the field resulting in an effectively constant electric field, producing a “constant” DC Stark shift of the Rydberg state’s three m_j sublevels. To detect electric fields, the change in transmission of the 780 nm probe laser through the cell is measured as the EIT resonance is shifted due to the applied electric field. As before, the 780 nm probe beam is overlapped with a strong heterodyne local oscillator (LO) detuned by 78.5 MHz to obtain high SNR optical readout. In contrast to RF systems, optical heterodyne detection allows readout with zero thermal noise; here the observed quantum shot noise is 6 dB greater than detector noise.

This experimental configuration is highly sensitive to low frequency electric fields. While I do not explicitly demonstrate a modulation protocol like in the last section, the principle remains the same. The RF field modulated the probe transmission through the cell and changes in the phase of that modulation can be detected

as corresponding changes in the phase of the probe transmission modulation.

3.3.2 Measuring Channel Capacity

As before, I use channel capacity as defined in Eq. 3.11 as the figure of merit. This quantity is obtained by measuring the SNR for detecting the RF field as a function of modulation bandwidth. Instead of explicitly operating at many different frequencies, I can apply a step function in the electric field, as is done in Fig. 3.22, and measure the SNR of detecting the step as a function of measurement bandwidth. Specifically, for each applied step in the field, the probe transmission signal is averaged in a time window of length t_d (pink window in Fig. 3.22(b)) placed adjacent to the step. The outcome of this average can be used to determine a sent data symbol.⁵ To change the effective bandwidth, the length of the averaging window $t_d = 1/f_d$ is changed.

As seen in Fig. 3.22(a) the square wave modulation of the electric field going from zero (on EIT resonance) to 0.8 V/cm (Stark shifted out of EIT resonance) is not directly mapped to the probe transmission for long timescales as one might expect. This is due to shielding of DC electric fields in the vapor cell, an effect observed in vapor-cell based systems and is attributed to free charges in the glass cell shielding the electric field. [61, 72] This manifests as the probe transmission relaxing back to the 0 field value over 0.5 ms in the particular cell used (procured from Precision Glass Blowing). Given the slow relaxation time, signals with bandwidths greater

⁵For communication purposes, absolute determination of the electric field strength is not necessary. When necessary, signal recovery techniques can be used as real-time calibrations.

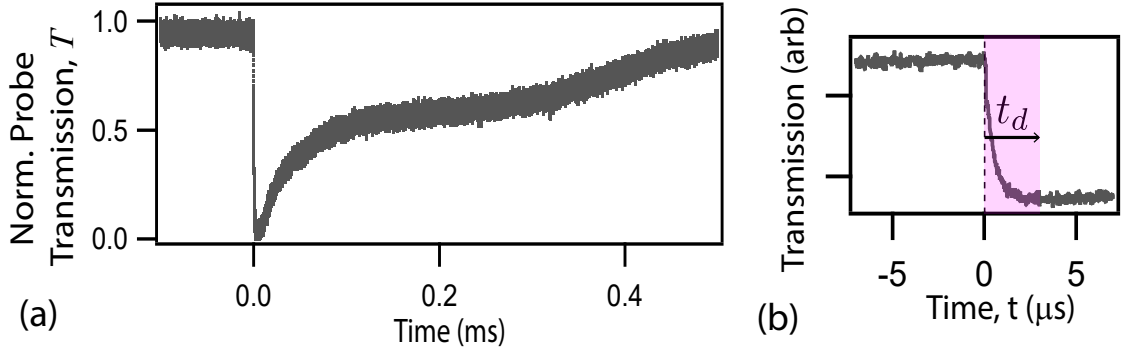
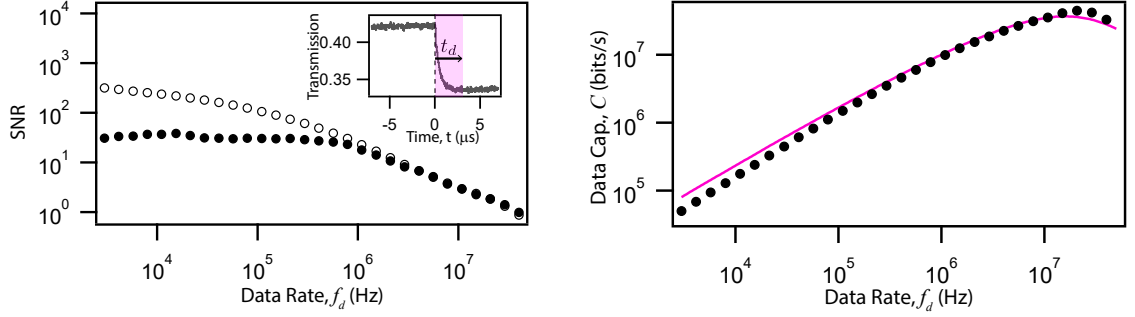


Figure 3.22: (a) At $t = 0$ s, a square pulse is applied to the electric field, changing the electric field from zero (on EIT resonance) to 0.8 V/cm . The probe transmission rapidly follows the applied field, but then slowly relaxes over 0.5 ms due to free charges in the glass cell that shield the electric field. (b) SNR vs f_d measurement. The probe transmission is averaged in the pink window over 100 independent measurements. The average and standard deviation for these 100 measurements gives the SNR.

than $\sim 100 \text{ kHz}$ are largely unaffected. I note that we tested a number of vapor cells from Triad and found that all had different relaxation times for the same applied field, with most being significantly faster than the cell ultimately used. The only obvious difference was noticeable rubidium build-up on the walls of the Precision Glass cell, which is likely the cause of the slower relaxation.

The SNR is determined from the outcome of 100 independent measurements of the electric field, where the average of the window averages is proportional to the signal and the standard deviation gives the noise. The resulting SNR for detecting an electric field as a function of data rate is shown as black solid data points in Fig. 3.23a. By independently calibrating the PSN level, I can measure and subtract out additional $1/f$ laser noise that contributes at low frequencies (plotted as open circles in Fig. 3.23a). For simplicity I have chosen the electric field strength to create Stark shifts on the order of the EIT linewidth. However, using active stabilization of



(a) Directly measured SNR (black points) and SNR with technical noise subtracted (open circles) is plotted versus f_d .

(b) Measured channel capacity for the SNR data shown in (a). The quantum limit, shown as a pink line for the fitted effective atom number and signal size, is described in Section 3.4

Figure 3.23: Measured Channel Capacity of the Electrically-Small Rydberg Receiver. The statistical error bars for both plots are smaller than the data point markers.

the probe laser to the EIT feature, the dynamic range can be made much larger than the linewidth. For strong fields, Rydberg state mixing must be accounted for. [61]

Figure 3.23b shows the data capacity C (black points), with no noise subtractions, inferred from the measured SNR and data rate of Fig. 3.23a using the Shannon-Hartley theorem. At the optimum data rate the achieved $C_{\text{opt}} = 4 \times 10^7$ bit/s. The pink line is the fitted standard quantum limited capacity described in Section 3.4.

3.3.3 Comparison with the Chu Limit

Figure 3.24 presents a basic comparison between the measured channel capacity and the classical data capacity bound arising from the Chu limit. To determine the Chu-limited data capacity, one needs to know both the bandwidth and the SNR of the classical antenna. Here I consider an efficient classical antenna with maxi-

imum Chu-limited data rate $f_d \sim BW_{\text{chu}}$, whose enclosing sphere [77] has the same radius, a , as that required for the Rb vapor cell ($a = 3.75$ cm). I assume the classical antenna to be subjected to $50\ \Omega$ Johnson noise at room temperature, and plot for the experimental electric field, 0.8 V/cm.

The black data points of Fig. 3.24 show the experimentally measured maximum channel capacity from Fig. 3.23b. To obtain the maximum channel capacity, I choose the optimum data rate f_d to maximize the capacity at each carrier frequency f_0 while enforcing $f_d \leq f_0$. At $f_0 = 10^7$ Hz, the optimum data rate $f_d = f_0 = f_d^*$ is reached. Subsequent increases in f_d only reduce the capacity, resulting in a saturated capacity when $f_0 > f_d^*$. The pink line, again, represents the fitted model described in the next section corresponding to the standard quantum limit. I note that the measurements are quantum-limited.

The Rydberg receiver outperforms the efficient electrically-small antenna by a factor of more than 10^4 at 10 MHz, and the advantage is even more extreme at lower frequencies. For the $a = 3.75$ cm antenna considered here, the Chu-limited and projected quantum-limited performance cross at $f_0 \approx 1.5 \times 10^8$ Hz, as the traditional antenna leaves the extreme electrically small regime. To be clear, there are other methods that surpass the nominal Chu-limited data capacity, such as using inefficient designs,⁶ active Non-Foster circuit elements [98, 99], or non-impedance-matched antennas (viable when the field wavelength is long and reflections can be tolerated). Despite these details, I expect that a Rydberg atom based receiver can

⁶Traditional AM radio receiver antennas in cars (meter scale) are a good example, which operate with approximately 5% efficiency to reach audio bandwidths [73].

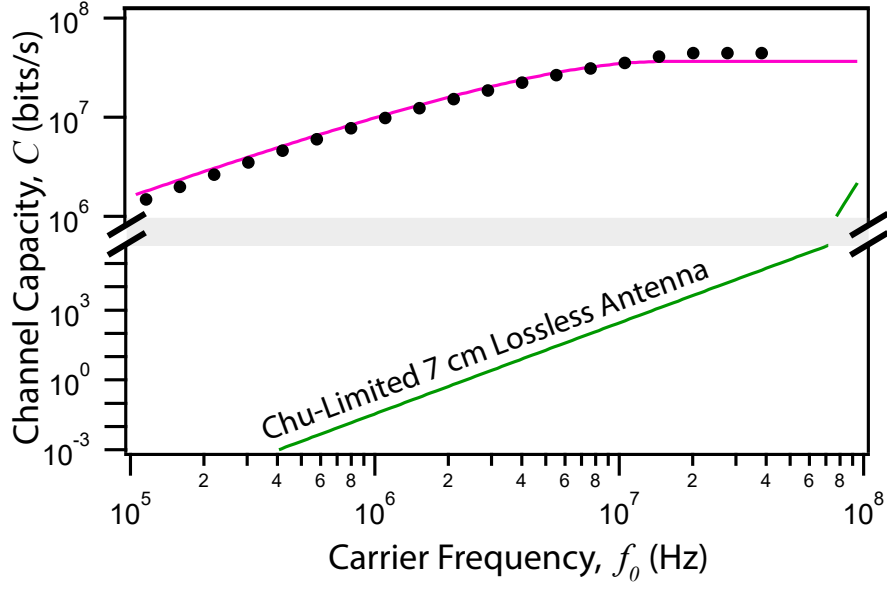


Figure 3.24: The Chu limit to data capacity for an efficient 7 cm classical antenna is shown in green (see text for details). The corresponding maximum measured data capacity of the Rydberg sensor is shown as black points. The maximum standard quantum limit C_{Max} for the experimental parameters is shown in pink (described in the next section).

provide significant benefits in both sensitivity and bandwidth for certain applications requiring electrically small antennas.

3.4 The Standard Quantum Limit for Digital Communication

In the previous two sections I have shown the measured the channel capacity of the Rydberg receiver and made some comparisons to classical analogs. In this section I will delve in to one of the unique aspects of the Rydberg receiver relative to a classical system: the fundamental quantum noise due to finite atom number. I will demonstrate that the current systems have sufficiently low atom number such that the hallmarks of quantum noise are observable. I will also define the standard quantum limit for channel capacity and show that the data represents this limit once quantum efficiency of the EIT detection is accounted for.

3.4.1 The Standard Quantum Limit

Any quantum sensor based on 2-level systems observes an applied electromagnetic field as an evolution of a quantum phase ϕ in the superposition state $|\psi\rangle = \frac{1}{\sqrt{2}}(|g\rangle + e^{i\phi}|e\rangle)$ with ground and excited quantum states $|g\rangle$ and $|e\rangle$. In the case of low frequency sensing, studied in Section 3.3, an applied electric field E changes the atomic transition frequency by an amount $\delta\omega = \frac{1}{2}\alpha E^2/\hbar$, where α is the atomic polarizability. In the case of resonant electrometry studied in Section 3.2, the shift $\delta\omega = \frac{1}{2}\wp|E|/\hbar$, where \wp is the resonant dipole moment of the $|g\rangle \rightarrow |e\rangle$ transition. In a sensing time t_d , $\delta\omega$ accumulates into the evolved quantum phase $\phi = \delta\omega \times t_d$. When operating with N independent atoms, the individual collapse of

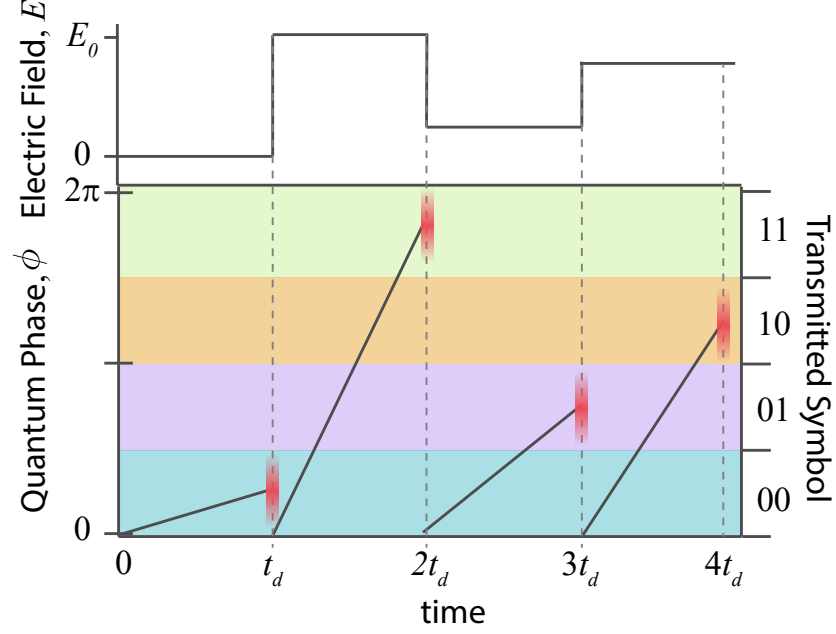


Figure 3.25: The quantum limit for data capacity. Data can be sent, for example, by encoding information in the strength of the electric field. The quantum sensor detects symbols by measuring the evolved phase ϕ at the end of each period, therefore inferring the transmitted symbol (right axis).

atomic wave-functions into either $|e\rangle$ or $|g\rangle$ limits the resolution of a measurement of ϕ to the SQL, $\Delta\phi_{SQL} = 1/\sqrt{N}$, where Δ denotes the standard deviation.

Figure 3.25 shows how noise like that due to the SQL limits digital communication. As described earlier this chapter, the continuous observable ϕ can be broken into a number of discrete binary symbols (for example, 2 bit permutations ranging from 00 to 11 as shown in the figure). The symbols may be transmitted by changing the amplitude of a static or oscillatory electric field with nominal amplitude E_0 . Symbols are received at bandwidth f_d by allowing ϕ to linearly evolve into a specific binary state in time t_d . In the optimum case, readout is much faster than t_d and is considered an instantaneous sample where quantum noise is observed as an instantaneous uncertainty to each readout of ϕ (shown as red distributions at each

sampling point).

3.4.2 The Standard Quantum Limit for Channel Capacity

Combining the Shannon-Hartley theorem and the SQL, I derive the quantum-limited data capacity, for N independent atoms, to be

$$C_{\text{SQL}} = f_d \times \log_2 \left(1 + \frac{\delta\omega^2 \cdot N}{f_d^2} \right). \quad (3.20)$$

C_{SQL} increases with f_d until the argument inside the logarithm becomes approximately 4.92. This occurs at an optimal (denoted by a star) data transmission rate $f_d^* = 0.505 \times \delta\omega\sqrt{N}$. The corresponding optimal quantum-limited data capacity is $C_{\text{SQL}}^* = 1.16 \times \delta\omega\sqrt{N}$. An important aspect of this quantum limitation is that the only way to increase the SNR, and thereby the data capacity, of a Rydberg receiver is to probe a higher Rydberg state (the polarizability increases as n^7 and the dipole moments as n^2) [45], to probe more atoms, or entangle the atoms.

One important caveat to Eq. 3.20 is that, in practice, 100% efficient probing of quantum systems is very difficult to achieve. In the specific case of optical probing as done with the Rydberg receiver, any losses of signal photons or spurious noise photons in the signal reduce what is known as the quantum efficiency, QE, which reduces N to $N_{\text{eff}} = \text{QE} \cdot N$. Optimizing the quantum efficiency for probing the quantum systems is another avenue for increasing the practical performance of the Rydberg receiver.

Finally, for the sake of completeness, I allow $\delta\omega$ to reduce to $\delta\omega_{\text{eff}}$. This

accounts for unknown systematic effects, such as field shielding, that alter the experimental result from the theoretical prediction. In the context of determining the quantum noise limit, the absolute value of $\delta\omega_{\text{eff}}$ is largely irrelevant since these changes can be experimentally calibrated out. This is not true for sensitivity comparisons to classical receiver systems where effective reductions in the received field directly influence the sensitivity.

3.4.3 EIT, Photon Shot Noise, and the Standard Quantum Limit

In the Rydberg receiver, optical detection of atomic systems is performed using Rydberg EIT. I can model this detection at the quantum level, assuming a few approximations, as outlined in Fig. 3.26. Under conditions of EIT, the intermediate state of EIT can be eliminated leaving an effective two-level system analogous to that used to derive the quantum-limited channel capacity, see parts (a-b). This two-level system can be further generalized by changing to the EIT bright/dark state basis (part (c)). In part (d) I show the steps of EIT detection using Bloch spheres in the basis of part (c). Each atom is first optically pumped into the EIT dark state. The atom then accumulates phase from the applied electric field, rotating the Bloch vector towards the equator, or equal super-position between dark and bright states. The atom is then probed and the superposition collapses into the bright or dark state and one of two things occurs: the bright state scatters the probing photon, which is now correlated to an atom in the bright state, into free-space; or the dark state allows the photon to transmit. By measuring how many probe photons are

transmitted relative to EIT without any applied field, one can determine the value of ϕ , the accumulated phase and thereby the electric field amplitude. This type of measurement is considered state selective in that transmitted photons are indicative of an atom being in the dark state.

In many quantum sensors, state selective readout means photon shot noise (PSN) is uncorrelated with atomic shot noise. [100] This is because both collapsed states are typically in some long-lived state that can be probed many times, increasing the signal to noise. In EIT, on the other hand, scattering of a photon has a one-to-one correspondence with atom wave-function collapse. Explicitly, the SNR observed is determined by the number of atoms that collapse into the EIT bright state, absorbing and scattering photons out of the probe beam during the communication time t_d . This leads to a quantum-limited SNR,

$$\text{SNR}_{\text{SQL}} = \delta\omega_{\text{eff}} \cdot t_d \sqrt{N_{\text{eff}}}. \quad (3.21)$$

Here $N_{\text{eff}} = \text{QE} \cdot N$ is the effective atom number for which quantum-limited operation is observed and accounts for imperfect quantum efficiency in the detection due to signal photon losses, detector noise, spurious photons from finite optical depth, *etc.* I also define the effective Stark shift $\delta\omega_{\text{eff}}$ that accounts for reductions in the signal due to additional decoherence, non-optimal probing, and shielding effects (with associated signal efficiency Q_{sig}), $\delta\omega_{\text{eff}} = \delta\omega \times Q_{\text{sig}}$.

If the symbol period t_d is longer than the coherence time of the dark state in the presence of the electric field, an atom is likely to scatter many times during a

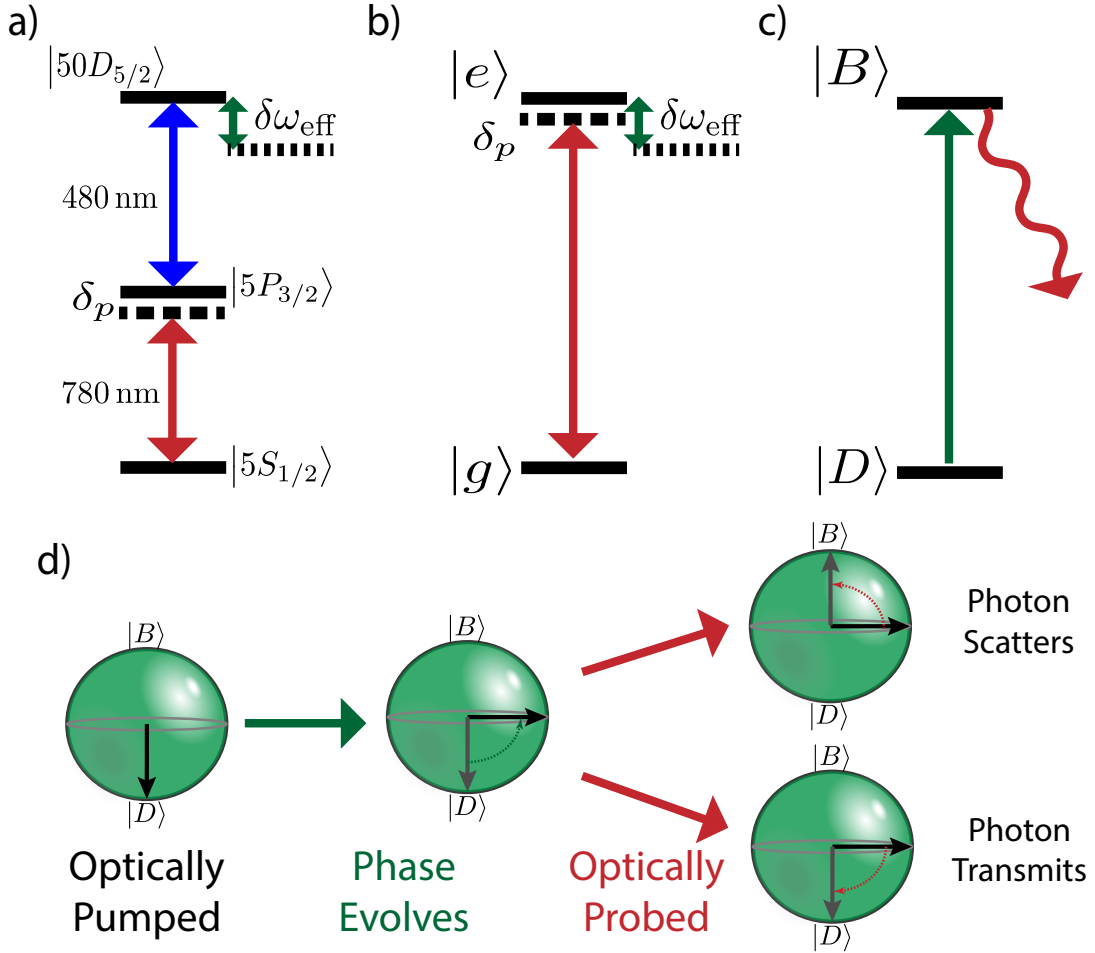
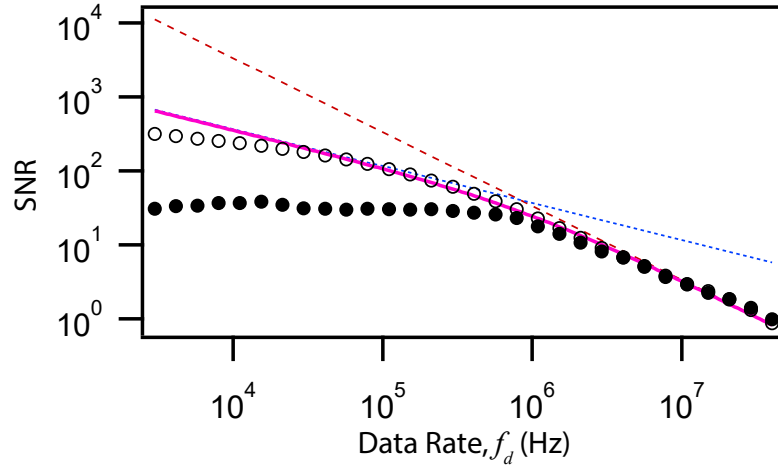
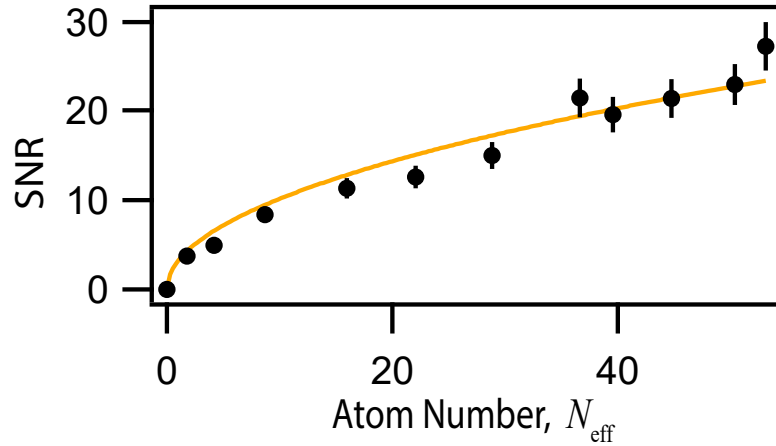


Figure 3.26: (a) The Rydberg EIT system used in Section 3.3. (b) When EIT conditions are satisfied, the system from (a) can be reduced to a two-level system with a ground and excited state. The applied electric field shifts the excited state by $\delta\omega_{\text{eff}}$. (c) Changing basis from (b) to the EIT bright and dark states. An atom is in a super-position of both states and the applied electric field gives a phase shift $\phi = \delta\omega_{\text{eff}} \cdot \tau_d$. (d) Bloch spheres showing the EIT detection process using the model from part (c).



(a) Directly measured SNR (black points) and SNR with technical noise subtracted (open circles) is plotted versus f_d , as shown in Fig. 3.23a above. At high frequencies, there is a standard-quantum-limited SNR $1/f_d$ scaling (red dash). At lower frequencies, there is a steady-state, $1/\sqrt{f_d}$ scaling (blue dots). The data is fit to the complete quantum noise model (pink line). The SNR data (open circles) lie within two standard deviations of the fit over the fitted range of $f_d = 5 \times 10^4$ Hz to $f_d = 10^7$ Hz. The larger deviations at low frequencies are due to the cell shielding effect.



(b) The SNR for receiving symbols in a bandwidth $f_d = 0.5$ MHz as a function of the effective atom number. The data is fit to a square-root scaling.

Figure 3.27: Demonstration of Quantum Limited Performance with the off-resonant Rydberg Receiver. Figure (a) shows the different scaling regimes for quantum noise in digital communication. Figure (b) shows the scaling of the SNR with effective atom number.

single symbol. In this steady-state (SS) regime, the SNR is

$$\text{SNR}_{\text{SS}} = \sqrt{N_{\text{eff}} \cdot t_d / \tau}, \quad (3.22)$$

where τ is the characteristic time for an atom to transition from the dark state to the bright state and scatter a photon. In Fig. 3.27, SNR_{SS} is displayed as a blue dotted line. If $t_d < \tau$, atoms collapse, on average, less than once in the symbol period. In this regime, the SNR can approach the quantum limit. SNR_{SQL} is plotted as a red dashed line in Fig. 3.27.

I fitted the observed SNR in Fig. 3.27 to a model combining the two SNR limits, SNR_{SQL} and SNR_{SS} :

$$\text{SNR}_{\text{tot}}(f_d) = \sqrt{\left(\frac{1}{\text{SNR}_{\text{SQL}}^2} + \frac{1}{\text{SNR}_{\text{SS}}^2} \right)^{-1}} = \sqrt{\frac{\left(\frac{\delta\omega_{\text{eff}}^2 N_{\text{eff}}}{f_d^2} \right) \cdot \left(\frac{N_{\text{eff}}}{\tau f_d} \right)}{\left(\frac{\delta\omega_{\text{eff}}^2 N_{\text{eff}}}{f_d^2} \right) + \left(\frac{N_{\text{eff}}}{\tau f_d} \right)}} \quad (3.23)$$

Since the applied Stark shift is larger than the rubidium $D2$ excited state lifetime ($\Gamma = 2\pi \times 6$ MHz), I can set the scattering rate $1/\tau$ in the model to be the upper bound, $\Gamma/2$, described in Section 3.2. I allow $\delta\omega_{\text{eff}}$ and N_{eff} to be fit parameters. The fit is plotted as a pink line in Fig. 3.27(a). The fit returns $\delta\omega_{\text{eff}} = 680(60)$ kHz and $N_{\text{eff}} = 63(7)$. From this I deduce $Q_{\text{sig}} \approx 3\%$. Further, the measured optical depth and EIT contrast allows me to approximate the total number of atoms participating in EIT to be of order 10^4 , which gives the total quantum efficiency QE of approximately 0.5%. These returned values are in rough agreement with what I expect from known inefficiencies. There is also a distinct transition from the steady state

PSN regime to the SQL regime at 800 kHz, a frequency governed by τ . Previous Rydberg electrometry experiments have focused on lower bandwidth sensing, and have not explicitly reached the regime of SQL scaling. [67] However, I emphasize that atomic wavefunction collapse, resulting in quantum noise in the transmitted light, limits the SNR at all bandwidths, even in the steady-state regime.

Figure 3.27(b) shows the SNR for detecting a symbol in a bandwidth $f_d = 0.5$ MHz as a function of the effective atom number N_{eff} . N_{eff} is adjusted by taking the SNR at different effective static electric fields which moves the EIT two-photon transition off of resonance by different amounts. Figure 3.27(b) shows that the SNR, limited by atomic wavefunction collapse manifesting as PSN, indeed scales as $\sqrt{N_{\text{eff}}}$ (fit displayed as solid orange line). This scaling is observed in both the steady state and SQL-scaling regimes and can be equivalently viewed as either a consequence of atomic wavefunction collapse or photon shot noise.

More broadly, Figs. 3.23b & 3.27 associates the performance of the atomic sensor used for classical data reception to the foundational quantum principles governing the system. This is important, for one, because it sets a fundamental bound—much like the Chu limit for traditional antennas—on the system’s capabilities based on the basic resources used. Second, the ability to relate the receiver’s performance to the underlying quantum dynamics also alludes to the potential for Rydberg atomic sensors to extend communication into the quantum regime. Current work in this area is ongoing [84, 101–105]; I hope that these results further inspire quantum communication tools based on Rydberg vapor cell platforms.

3.4.4 Quantum Limits for Resonant Electrometry

I can also apply a similar analysis to the SNR measurements from the resonant Rydberg receiver of Section 3.2. Figure 3.28 shows these measurements, with (filled circles) and without (open circles) technical noise, along with the SNR_{SS} scaling, again as a blue line. However, unlike the off-resonant data shown above, the high bandwidth region has $1/f_d^2$ scaling. It is not immediately obvious why this scaling does not follow the expected $1/f_d$ scaling from the SQL. To get an accurate fit of these two regions, I generalize the model from Eq. 3.23 to include this unknown scaling:

$$\text{SNR}_{\text{res}} = \sqrt{\frac{1}{\frac{f_d \tau}{N_{\text{eff}}} + \frac{f_d^4}{b^4}}}, \quad (3.24)$$

where b and N_{eff} are fit parameters and $\tau = 2/\Gamma$ is fixed. The fit gives $N_{\text{eff}} = 1.5$ and the free parameter $b = 2\pi \times 0.94 \text{ MHz}$.

Please note that this data was taken before we arrived at the more complete understanding of how quantum noise limits the Rydberg receiver described above. As a result, the differences shown here were not immediately apparent and as such were not explored in more detail. Ultimately, the two systems are different at a basic level and the quantum model used to derive the above quantum limits in the off-resonant configuration does not accurately capture the dynamics of the resonant case. Further investigation is needed to determine how the SQL effects the resonant Rydberg electrometer.

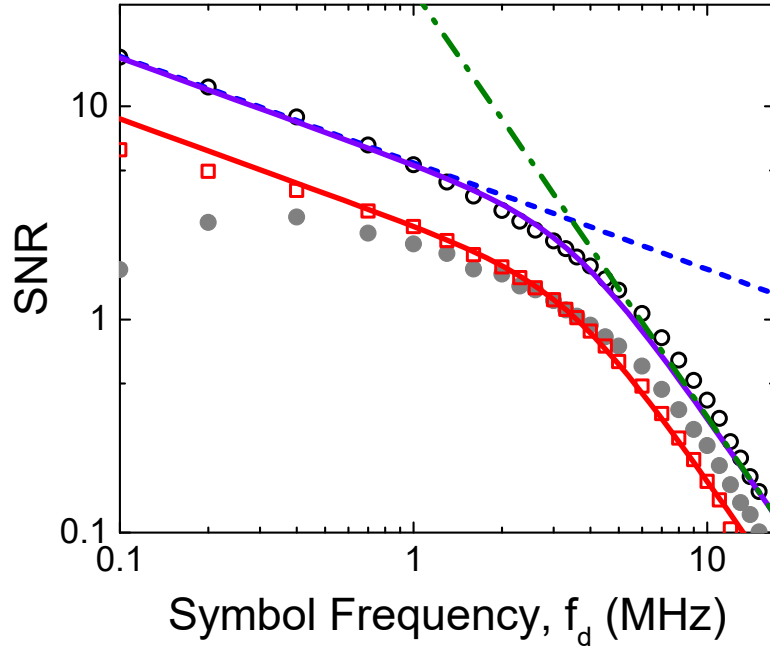


Figure 3.28: Directly measured SNR from the resonant receiver of Section 3.2. The filled circles show the measured SNR with $\Omega_\mu = 2\pi \times 8$ MHz, with the open circles showing the SNR with technical noise (predominantly detector noise) subtracted off. Similar limiting behaviors are observed as in the off-resonant case: the same steady-state region (blue short dashed line) as shown in Fig. 3.27 as well as a region with $1/f_d^2$ scaling (green dash-dot line). The purple line shows a fit combining both regions to the data. The red open squares show the SNR with technical noise subtracted for $\Omega_\mu = 2\pi \times 4.5$ MHz. The solid red line shows the combined SNR regions fit for this lower power data.

3.5 Sensitivity of the Rydberg Receiver

In much of the above discussions as well as other recent works studying Rydberg atoms as receivers, [93,106–108] the absolute sensitivity to the free-space carrier field has taken a back seat to the detection bandwidth. While we specify the electric field applied, the absolute value is often an arbitrarily chosen value and is naturally calibrated out when measuring the bandwidth. When considering digital communication applications, both the bandwidth and the sensitivity matter, which is why I have used the channel capacity as a figure of merit. As described above, this figure of merit emphasizes bandwidth at the expense of sensitivity, which can conceal the fact that the sensitivity of the Rydberg receiver is not very competitive with classical antennas unless the carrier frequency is above ~ 40 GHz. As discussed in Section 3.2.6, sensitivity comparisons between antennas and the Rydberg receiver can be tricky since antennas detect RF power in a free-space mode and Rydberg atoms detect the local electric field amplitude. In this section I will show how to convert between local field strength and mode power in order to have a direct, quantitative comparison of field sensitivity. I will then discuss how to significantly improve the sensitivity of the Rydberg electrometer.

3.5.1 Resonant Rydberg Electrometer/Receiver Sensitivity & SNR

The current record for sensitivity with a resonant Rydberg electrometer is found in Ref. [67] and is $3\,\mu\text{V}/(\text{cm}\sqrt{\text{Hz}})$. This measurement was taken well into

the low-bandwidth, steady-state regime with an integration time of approximately 1 s, so it represents an optimistic bound on the sensitivity for a Rydberg receiver operating at higher bandwidths. This sensitivity can also be calculated from system parameters using:

$$\frac{|E_{min}|}{\sqrt{Hz}} = \frac{h}{\wp_{\mu}\sqrt{N_{\text{eff}}T_2}}, \quad (3.25)$$

where \wp_{μ} is the resonant dipole moment, N_{eff} is the effective number of atoms probed at the SQL, and $T_2 = 1/\Gamma_{\text{EIT}}$ is the Rydberg state decoherence time (inverse of the Rydberg EIT linewidth). Using the measured sensitivity, linewidth, and calculated dipole moment from [67], their $N_{\text{eff}} \approx 0.8$.

The sensitivity defined in Eq. 3.25 is analogous to the quantum noise used in SNR_{SS} defined above in Eq. 3.22. Comparing that result with Eq. 3.25 shows how one can relate experimentally quantifiable SNRs in the low bandwidth limit to electric field sensitivity.

$$\text{SNR}_{\text{Low-BW}} = \frac{|E|\wp_{\mu}\sqrt{N_{\text{eff}}T_2} \cdot T}{\hbar} = \Omega\sqrt{N_{\text{eff}}T_2T} = \sqrt{N_{\text{eff}}T/\tau}, \quad (3.26)$$

where T represents the averaging or evolution time for an RF field with amplitude $|E|$ and is assumed to be much longer than the coherence time T_2 . I have also defined a new parameter $\tau = 1/(T_2\Omega^2)$. The physical interpretation of τ is the average time for an atom initially in the dark state to evolve towards the bright state until it scatters a probe photon. For the resonant Rydberg electrometer, the Rabi frequency is defined as $\Omega = \wp_{\mu}|E|/\hbar$. Here I have implicitly assumed that the

Rabi frequency is equivalent with the phase accumulation rate ω_{eff} defined in the quantum model of Section 3.4.2. Given the data in Section 3.4.4 this is likely not a great assumption for resonant electrometry, but I will use it as a best case scenario in order to have quantitative numbers to compare.

In the high bandwidth limit, I assume that $T \ll T_2$, and can therefore replace the coherence time with the averaging time T leading to the high-bandwidth SNR:

$$\text{SNR}_{\text{High-BW}} = \Omega T \sqrt{N_{\text{eff}}}. \quad (3.27)$$

Note that the SNR and therefore the realizable electric field sensitivity can, in principle, be predicted for the entire BW range as long as two of the three experimental parameters (Ω , T_2 or τ , N_{eff}) are known. In the experimental systems described above the realized quantum efficiencies for detection make accurate, absolute determination of these parameters difficult. In the following I will describe experimental techniques that should improve them, making the Rydberg electrometer more sensitive, and will use my best judgment when making quantitative estimates for the expected sensitivity of the proposed, optimized system.

3.5.2 Converting to Power Sensitivity

Converting the sensitivity in Eq. 3.25 to a power unit more typical of a receiver specification requires an assumption about the area over which the electric field is measured. Since the Rydberg receiver measures the local electric field amplitude, its size is only important in dictating how many atoms are involved in the measurement,

not the magnitude of the electric field measured. In contrast, the power of an electric field that can be coupled into a classical antenna depends strongly on the size of the device. Therefore, a fair comparison between electric field sensitivity and RF power sensitivity requires an assumption about the effective size of the antenna to which one compares. Since this size can vary wildly depending on application, carrier frequency, and desired bandwidth, general comparisons are difficult. In the interest of being fair, but also competitive, I will compare with an ideal dipole antenna and an antenna the size of the sensing volume of the Rydberg Receiver.

The specific area required to convert electric field to power is the effective aperture, A . This is determined empirically for most real antenna systems, but theoretically-idealized systems can be used to determine the effective aperture. For an ideal dipole with length $\ll \lambda$ that is impedance matched to the radiation resistance the maximum effective aperture is [73]

$$A_{\text{dip}} = \frac{3}{8\pi} \lambda^2. \quad (3.28)$$

Again note that for electrically small antennas (size $< \lambda/10$), this maximum is difficult to achieve due to the impedance matching assumption. By the Chu limit, a properly impedance matched electrically small antenna must be resonant and therefore have reduced bandwidth in order to reach this maximum effective aperture.

One can use the effective aperture of the comparison antenna to convert the Rydberg electrometer sensitivity to an equivalent power sensitivity. The noise in-

tensity in bandwidth, BW, of the low-bandwidth Rydberg electrometer is

$$I_{\text{noise}} = \frac{|E_{\text{min}}|^2 \text{BW}}{2\eta} = \frac{h^2 \text{BW}}{2\eta \epsilon_\mu^2 N_{\text{eff}} T_2}, \quad (3.29)$$

where $\eta \approx 377 \Omega$ is the impedance of free space. The associated noise power over the effective aperture is

$$P_{\text{noise}} = I_{\text{noise}} \cdot A_{\text{eff}}. \quad (3.30)$$

Conversion to the high bandwidth limit only requires letting $T_2 \rightarrow 1/\text{BW}$.

Conversion in the opposite direction is also readily available. One only needs to determine the external and internal noise temperature of the receiver in question, combine with the effective aperture, and the noise floor in electric field units compatible with the Rydberg receiver is easily found. As an example, if I assume a noise temperature of 298 K and an effective aperture of an ideal dipole for a 17 GHz carrier, the noise floor is

$$E_{\text{dip}} = \sqrt{2k_B T \eta / A_{\text{dip}}} \approx 3 \text{ nV}/(\text{cm } \sqrt{\text{Hz}}). \quad (3.31)$$

This value is three orders of magnitude lower than the current record for resonant Rydberg electrometer sensitivity. Given that the Rydberg receiver sensitivity is at best the low bandwidth electrometer sensitivity, significant improvements are necessary for the Rydberg receiver to have comparable sensitivity to classical dipole antenna.

3.5.3 Improving the Sensitivity of the Rydberg Receiver

In this section I will outline methods for approximating both N_{eff} and T_2 , which dictate the sensitivity, and suggest an experimental configuration that can increase both parameters. The python code used to calculate the following estimates can be found in Appendix [B](#).

Since the sensitivity is limited by quantum noise at all bandwidths, the only improvements to be had are to either probe more atoms, probe with higher quantum efficiency, increase the coherence time, or take advantage of entangled or squeezed states. Entanglement and squeezing is beyond the scope of this current work since there are a number of immediate, easier improvements to be made. But first I must describe how to estimate N_{eff} and T_2 .

I will start with T_2 , the Rydberg state coherence time, since fewer elements factor in to its determination. More importantly, it is also easy to experimentally measure. In the Rydberg electrometer, the Rydberg coherence time is simply the inverse of the Rydberg EIT FWHM linewidth, Γ_{EIT} . There are four primary influences to this linewidth in the configurations described above in Section [3.1.1](#): the natural lifetime of the Rydberg state, black-body induced dephasing, transit broadening, and finally Doppler-broadening. If higher density vapors or higher n Rydberg levels are used, Rydberg-Rydberg and Rydberg-Ground collisional broadening must also be considered. [\[2, 56\]](#) Typical linewidths for Rydberg EIT range from 2 to 20 MHz. This gives a typical range for T_2 of between 80 and 8 ns. Note that the Rydberg natural lifetime, which is the fundamental limit to T_2 can be orders of magnitude

higher, leaving significant room for improvement.

I next address N_{eff} , which necessitates estimating the number of atoms excited to the Rydberg state inside the sensing volume (probe and coupling beam intersection volume) as well as the quantum efficiency of probing those Rydberg atoms.

The density of rubidium atoms in a thermal vapor can be easily found by the use of the empirical formulas from [109]. When using a thermal vapor, the light fields do not interact with all of the present ground state atoms within the volume. If the vapor cell has natural abundance rubidium, only 72.172% are ^{85}Rb . Further, the fine structure splitting of the ground state is large enough that only atoms in one ground state can be interacted with at a time. The sublevels of these ground states are populated equally and the above experiments use the higher $F = 3$ state, so the density is further reduced by a factor of $7/(7 + 5)$. Finally, the vapor is in thermal equilibrium, meaning the atoms are distributed in velocity according to the Maxwell-Boltzmann distribution. Under conditions of EIT, only a small portion of those velocity classes can participate in the resonance. An effective way to empirically estimate how many atoms are excluded due to this is to take the ratio of the EIT linewidth and the probing transition Doppler-broadened linewidth, which is approximately 500 MHz in rubidium. Finally, when EIT is un-ideal and has contrast sub-100%, the EIT contrast gives the number of potential atoms interacted with that are actually excited to the Rydberg state. Care needs to be taken when applying the contrast in this calculation since other effects beyond the efficiency of Rydberg excitation influence it. The resulting density can then be used with the

sensing volume to estimate the number of Rydberg atoms excited.

The number of Rydberg atoms excited is only half of the equation. Assuming technical noise has been sufficiently reduced such that noise is predominantly quantum, I must also determine the quantum efficiency with which I can probe these atoms. The quantum efficiency of detection can be limited via two mechanisms: loss of signal photons and the presence of non-signal photons. This can be seen by considering the SNR for photon shot noise, which is proportional to $N_{\text{sig}}/\sqrt{N_{\text{det}}}$, where N_{sig} is the number of detected signal photons and N_{det} is the number of total detected photons. I can define a quantum efficiency $q = N_{\text{sig}}/N_{\text{det}}$ representing the addition of extra noise photons. Defining a second quantum efficiency $Q = N_{\text{trans}}/N_{\text{tot}}$ that accounts for photon losses leaves $\text{SNR} = \sqrt{QqN}$ where N is the total number of signal photons that interacted with a Rydberg atom.

The efficiency Q includes losses due to absorption in windows and mirrors, fiber coupling losses, 50/50 beamsplitter losses from heterodyne and homodyne detection, and detector efficiency.

The efficiency q accounts for the extra photons from finite optical depth and improper beam overlap. Efficiency loss due to finite optical depth is due to photons that would not be absorbed even in the absence of EIT are also detected and cannot be distinguished from signal photons. This is estimated by comparing the EIT contrast to the overall absorption contrast. Imperfect overlap of the probe and coupling beams also effects q in the same way since transmitted probe photons from spatial regions of the probe beam profile that do not overlap the coupling beam cannot participate in EIT. Assuming gaussian profiles for both beams, the ratio of

probe power inside the $1/e^2$ waist of the coupling is $\text{erf}(\sqrt{2}R)$, where R is the ratio of the waist of the smaller coupling beam to that of the larger probe.

Accounting for known elements in the configuration from Section 3.3 I expect a $Q \sim 3\%$ and $q \sim 20\%$. Methods from improving these efficiencies are included in the next few sections.

3.5.3.1 *Increasing Sensing Volume*

The most important thing anyone can do to increase N_{eff} is to simply increase the number of Rydberg atoms in the sensing volume. There are two ways to do this: increase the density of atoms or increase the volume being probed. Increasing the density relies on heating the vapor cell, which comes with a number of complications: increased dephasing due to black-body radiation, transit effects, and eventually collisional effects between Rydberg states. The collisional effects are of particular importance since Rydberg-Rydberg interactions in the form of Rydberg blockade will limit the possible density of Rydberg atoms. Heating the cell with elements that are transparent to RF fields is also non-trivial. As a result, it seems better to increase the sensing volume.

In the two-photon configurations described above, I can roughly estimate the sensing volume by taking the cross section of the smaller of the two overlapped beams and multiplying by the length, L , of the cell:

$$V_{2\text{-photon}} = \pi w_0^2 L. \quad (3.32)$$

Assuming the Raleigh range of the focused beams is larger than the cell, this is a reasonable approximation.

Since meter-long vapor cells would be impractical, the way to significantly increase the sensing volume is to use larger beams. The current hurdle for large beam sizes is the EIT requirement of strong coupling Rabi frequency with simultaneous small dipole moments on the coupling transition, making significant focusing necessary. One potential workaround is to use a build-up cavity on the coupling light. A simple Fabry-Pérot cavity around a vapor cell can somewhat easily have a Finesse in excess of 100, meaning light in the cavity, on average, will pass through the system 100 times. [110] This would give an effective enhancement of the intra-cavity intensity by the same factor. Significant increases in coupling intensity would allow for a much larger beam. Sufficient probe power to match that beam size is easily obtained to maintain the same Rabi frequency ratios for EIT. Using a 1 mm waist beam in the above experiments would increase the sensing volume by a factor of 400.

Large beams also give the advantage of reducing the observed transit broadening. Again comparing with the above experiments, using a beam with a $1/e^2$ waist of 1 mm would reduce the transit broadening to $2\pi \times 40$ kHz; which is significantly closer to Rydberg natural lifetime and represents a reduction of two orders of magnitude.

3.5.3.2 *High QE Probing*

Above I describe using optical heterodyne detection in order to overcome technical noise sources. Heterodyne, and the related homodyne, detection is very effective at making photon shot noise limited optical measurements with small probing powers. This detection scheme requires overlapping the probe field with a local oscillator field, resulting in a 50% loss in probe photons. To improve the overlap a fiber beam splitter was used which necessitated fiber coupling the probe light, which leads to even lower quantum efficiency.

Frequency Modulation spectroscopy implemented in [67] presents a promising alternative. It requires neither fiber coupling the signal beam nor beamsplitter mixing while still allowing one to improve on technical noise. Effectively this is because the modulation sidebands on the probing light act as the reference which is already mode-matched to the signal beam. Direct detection with a fast photo-detector gives high SNR readout. In [67], this probing method allowed them to achieve the current sensitivity record for Rydberg electrometry and they were ultimately limited by poor probe beam overlap reducing their quantum efficiency.

Another aspect of improving the probing quantum efficiency is to reduce the number of noise photons. This means proper overlap of the coupling and probe beams and attaining high EIT contrast. One can also increase the optical depth, either by heating or using a longer sample. Assuming size is a constraining factor, some heating to increase optical depth at the expense of increased dephasing mechanisms described above may be recommended. In the context of a Rydberg receiver,

heating will always help since the dephasing mechanisms primarily hurt T_2 , which is irrelevant for high bandwidth detection, assuming the method of heating does not shield the incoming RF field.

3.5.3.3 *Doppler-Broadening*

Finally, elimination of Doppler-broadening would be beneficial for low bandwidth sensing as it allows one to increase the T_2 coherence time. In warm vapor this is possible by using excitation schemes with more than two transitions and using non-orthogonal geometries to cancel Doppler shifts. This type of cancellation was attempted in [111]. They were able to observe coherent signals, but they were transit broadened significantly due to low available power in the coupling beam necessitating tight focusing. As a result, they were unable to observe the expected narrowed EIT linewidth. If one were to combine a three photon configuration with the build-up cavity discussed above to maintain large beams, I would expect significantly longer T_2 times, though they would likely still be transit limited to some extent.

A three-photon system would affect other aspects as well. The Doppler-free configuration will limit signals to approximately the zero velocity class only, reducing the atom number. Beams also do not counter-propagate resulting in comparatively smaller sensing volumes. Assuming sufficient power in the intermediate transition beam such that it can be large enough to illuminate the entire intersection of the

probe and coupling beams, the sensing volume is defined as

$$V_{3\text{-photon}} = \frac{16}{3 \sin \theta / 2w^3}, \quad (3.33)$$

where w is the waist of the probe and coupling beam and θ the angle between their center axes.

3.5.3.4 *Estimated Improvement to Rydberg Electrometer Sensitivity*

In Appendix B I include a python notebook that accounts for these various consideration and calculates estimated sensitivities for a low bandwidth Rydberg electrometer. Using experimental parameters from Section 3.2 I estimate a sensitivity of $300 \text{ nV}/(\text{cm} \sqrt{\text{Hz}})$, in rough agreement with the measured sensitivity estimate described in Section 3.2.2.1 of $1.3 \text{ } \mu\text{V}/(\text{cm} \sqrt{\text{Hz}})$.

I also include a calculation for a hypothetical three-photon system that takes advantage of a build-up cavity on the coupling beam to increase the beam sizes. It uses a $|5S_{1/2}\rangle \rightarrow |5P_{1/2}\rangle \rightarrow |6S_{1/2}\rangle \rightarrow |48P_{3/2}\rangle$ excitation scheme. The required wavelengths are 795 nm, 1324 nm, and 740 nm, which are readily available with significant power. Overall I expect a smaller overall atom number with higher detection efficiency and a much longer T_2 time to give a sensitivity of approximately $70 \text{ nV}/(\text{cm} \sqrt{\text{Hz}})$. This sensitivity would represent nearly two orders of magnitude improvement over the current record in [67].

I note that this sensitivity is still an order of magnitude higher than the classical antenna external, room temperature noise floor calculated above. While further

technical improvements to the Rydberg electrometer setup are possible, I stress that this system will likely only be on par with classical receiver systems in most cases. In order to determine potential application spaces relative to classical systems, it will likely be more fruitful to rely on the Rydberg sensor's fundamentally different properties.

3.6 Conclusions

In this chapter I have outlined two experimental configurations of the Rydberg electrometer and applied them to digital communication. I have characterized their operation bandwidth and found them to be limited by the EIT probing system to the order of 10 MHz. I have also explored using this sensor in the extreme electrically small regime and shown that it outperforms Chu-limited classical systems. I have shown that Rydberg EIT systems exhibit scalings consistent with the standard quantum limit due to the underlying quantum noise from detecting wavefunction collapse. This implies that improving sensor performance will rely on increasing atom numbers and quantum efficiencies. Finally, I have included a discussion of the sensitivity of the Rydberg electrometer and a future path for dramatically increasing its sensitivity.

The Rydberg receiver is a fundamentally different system for performing digital communication reception. In this work I have explored some of the potential avenues where this type of system could have real-world benefit. Applications that require a sensor with broad operating range, electrically small footprint, perturbation-free detection, direct RF-to-optical conversion, and/or RF oscillator-free reception seem particularly appealing. Further basic research into the capabilities and limitations of this sensor are necessary to determine what may be possible. I expect that communications with Rydberg atoms will be a field of particular interest in the future and may even provide another practical device platform that relies on the

principles of atomic physics.

Appendix A: `labscript` Experimental Control

When transitioning from the NMOR experiment of Chapter 2 to the experiment of Chapter 3 I desired to also transition away from the legacy LabVIEW control system that was written in-house. Like many one-off experimental control systems written by physicists, it suffered from severe spaghetti code syndrome making the system very difficult to maintain and augment. I was also determined to move away from LabVIEW itself to avoid the cost and the various idiosyncrasies of programming large, complicated projects.

I performed a broad search of Open-Source experimental control systems released by other experimental groups. The desire was to select something written in a friendlier language, undergoing active development, and with reasonable adoption to provide an active user base that can furnish bug reports and development support. I ultimately settled on `labscript` developed at Monash University for a couple of BEC experiments there. [85] `labscript` is a python-based experimental control system with a modular design. This system was chosen over others largely to take advantage of the simplicity of a scripted language like python, because one

of the primary developers had recently taken a post-doctoral position nearby at the JQI, and the base hardware support included most of the devices we already owned (Spincore Pulseblaster Digital Output Boards, Novatech DDS, National Instruments DAQs).

`labscript` is primarily made up of three separate programs with their corresponding graphical user interfaces: `runmanager`, `BLACS`, and `lyse`. These programs interface by passing around paths to experiment files that contain instructions, run variables, return data, and analysis results. A typical run of the experiment begins by first using `runmanager` to take a master script written in python that employs device class drivers to compile the various instructions, timings, and variables into instrument level instructions. The file is then passed to `BLACS` which interprets the instructions, programs the various devices, executes the experiment, then takes any measured values and saves them to the experiment file. Finally, `BLACS` sends the completed experiment file to `lyse` which runs user-defined analysis scripts, saving the results back to the experimental file. At the end of each shot a complete record of the run, its results, and the analysis is created. Complete, arbitrary sequences of experimental parameters can be configured using `runmanager` to provide complete data sets for `lyse` analysis. We have found this system to be powerful enough for our needs while remaining relatively user friendly to the average atomic physicist who is familiar with python programming.

A.1 Adoption

I have since configured three separate experiments to use the `labscript` experimental control system. Each experiment uses varying, yet similar, hardware. Overall, adoption has gone fairly smoothly. We use the Anaconda Python distribution in order to have simple installation and package control on our Windows systems. While highly configurable, it is important to choose the correct bit-ness for the Python distribution in order to properly interface with the many driver packages necessary to control the experiment. Fortunately, 64-bit appears to be a safe, common choice that generally works.

Most issues with installation and use are due to a lack of complete documentation. In particular, the minutia of hardware triggering all of the devices correctly proved difficult. The developers proved to be extremely helpful in answering my questions and helping me get things up and running. Ultimately the solutions revolved around putting together appropriate hardware solutions to properly interface the various hardware triggers. I will discuss these hardware solutions next.

A.2 Hardware Augmentation

I put together two simple hardware solutions for properly interfacing hardware triggers. The first is a box for properly triggering the controlling master clock off the 60 Hz main line frequency. The second is for doing synchronous triggering of the Novatech 409B-AC DDS.

A.2.1 AC-Line Trigger Box

For many experiments, triggering sensitive portions of the experiment off the 60 Hz main line frequency is crucial to eliminate noise sources due to the line currents of the room. This is particularly important for experiments involving small magnetic fields that are easily swamped by the magnetic fields induced from the surrounding line currents. The Spincore Pulseblaster boards we use allow the use of a hardware trigger to restart pre-programmed execution after a wait command. By synchronizing the resumption of the program execution with the AC line frequency, AC frequency-dependent systematics can be effectively controlled.

In practice, this can be quite difficult. The Pulseblaster hardware trigger line is held high internally through a 10 k Ω resistor and triggers when shorted to ground. In order to ensure a trigger on a falling edge, one must ensure that one trigger pulse is sent to the Pulseblaster *after* the Pulseblaster is already waiting for the trigger. The circuit shown in Fig. [A.1](#) performs this function. It uses an MID400 integrated circuit to optically isolate the AC-line voltage from the triggering circuit, providing a 5VTTL compatible trigger signal. I use that signal as the clock line of a standard flip-flop that is connected to an arm line from the Pulseblaster that is set to go high just before the wait command and low immediately after it. This high arm line is passed through to the flip-flop output synchronous with the AC line frequency. The rising edge is detected with a simple differentiator and a diode to reject falling edges. The output of the differentiator then feeds the base of a transistor connected to the hardware trigger line and ground.

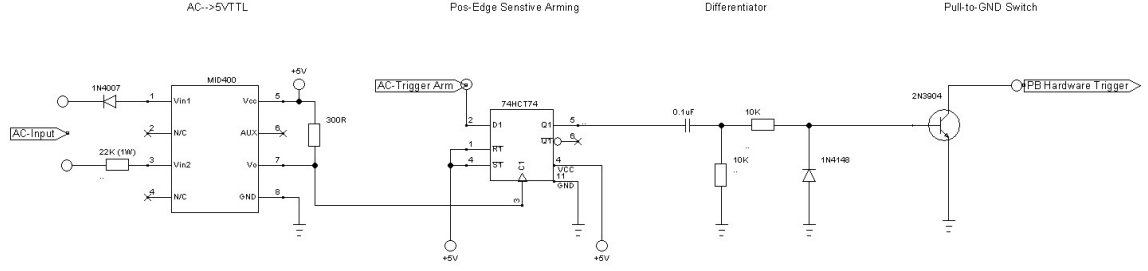


Figure A.1: AC-Trigger Wiring Diagram. This system uses the MID400 integrated circuit to give optically isolated trigger edges from the AC-Main Line frequency. It then converts the TTL output into a compatible CMOS level short to ground that Pulseblaster hardware trigger expects.

This circuit can be further modified to allow for a second TTL input that can also cause a hardware trigger. This is accomplished by using an OR gate with the flip-flop output. Having a secondary trigger that can override the AC-Trigger allows for more arbitrary feedback mechanisms in the experiment. For example. re-triggering the experiment with a heralding photon detected with a single photon counter would be easily accomplished.

A.2.2 Novatech Synchronous Trigger Conversion

Hardware triggering the table mode updates of a Novatech 409B-AC (based on the Novatech DDS 9m board) has two modes: asynchronous and synchronous. The 409B-AC table mode is pre-programmed with output frequencies, amplitudes, and phases that are transferred from an internal memory to a loading register and finally to the outputs. The update can be hardware triggered precisely.

Asynchronous mode only requires a single falling edge on pin 10 (the TS input of the 409B-AC). This mode triggers a hardware update of the output registers from the table and then an automatic update to the output with a timing jitter of 100 μ s

due to the Novatech’s internal clock.

Synchronous mode uses a rising edge on pin 14 (IOUD of the 409B-AC) in conjunction with the falling edge of pin 10. The rising edge triggers an update of the registers from the table and the falling edge updates the outputs from the registers. Updating the outputs in this way has a timing jitter of only 10 ns. `labscript` is already configured to provide the correct triggers for either mode using a single Pulseblaster digital output.

Unfortunately, the IOUD input is also an output for synchronizing updates of the outputs when not in table mode. If the Pulseblaster trigger line is directly connected to both pins, the output function is interfered with and static updates cannot be performed. This limitation is simple to workaround by connecting both lines internally through a standard SN7407N open-collector type buffer. This chip can be run off the 5 V supply of the Novatech itself, meaning the entire thing can be worked seamlessly into to device case.

A.3 Software Augmentation

While most of the hardware we use is supported by the main `labscript` distribution, there are a number other unsupported devices that we need: oscilloscopes, signal generators, cameras, *etc.* In the hope that my code might be useful to others looking to use `labscript`, easing their adoption, I have made my code available online through a few repositories. The primary repository is the `naqslab_devices` repository found at https://bitbucket.org/dihm/naqslab_devices.

In order to use these devices, the above repository should be put in a folder inside the `labscript` directory and a modification of the `labscript_devices'__init__.py` file to look for devices in the directory must be made. An example of how to do this is provided at the above link.

In the next sections I describe the basics of how to use these device files in an experiment.

A.3.1 VISA Devices–`VISA.py`

Many lab instruments use one of a small collection of standardized communication protocols and interfaces. These protocols and interfaces have been generalized into a single programming interface known as VISA; a freely available component of LabVIEW that has an open-source python wrapper, PyVISA. The power of VISA is that it generalizes the communication interface for sending instrument specific commands in the form of strings to many interfaces; including GPIB, USB, and ethernet.

In order to facilitate communication with these devices I created a parent VISA instrument class that the various device classes inherit from. This class specifies the standardized components of VISA communication: open and closing the communication handle, reading instrument status bytes, and prototyping `labscript` integration.

*A.3.1.1 Tektronix Oscilloscopes–**TekScope.py***

While the National Instrument DAQs we use for analog voltage outputs also have analog inputs for data acquisition, the devices tend to be severely limited in their acquisition rate, particularly when multiple input channels are needed. As a result, I found it necessary to incorporate digital storage oscilloscopes into the **labscript** environment. Compared with traditional DAQs, oscilloscopes have significantly higher acquisition rates at the expense of limited total number of data points, which is often an acceptable trade-off.

The first child VISA class is for Tektronix digital storage oscilloscopes from the TDS 200, 1000, and 2000 series. These scopes share a common code base, making a generalized driver possible. The scope is instantiated with an external trigger line to facilitate hardware timed acquisitions within the experiment:

```
TekScope(labscript_name, VISA_name, trigger_device, trigger_connection)
```

The **VISA_name** can be either the default VISA connection string, unique to every device connection or it can be a user specified name configured in NI-MAX.

Which scope channels to acquire on is configured using the **ScopeChannel** class from the same file:

```
ScopeChannel(labscript_name, parent_device, connection)

labscript_name.acquire()
```

Here the **parent_device** is the **labscript_name** of the scope and **connection** is the internal connection name for the desired channel. For Tektronix oscilloscopes this

takes the form of '`Channel X`', where `X` is the desired channel number. The second line tells `labscript` to acquire the specified channel and should be placed after the `labscript start` command. This allows one to disable channels for acquisition without needing to recompile the connection table.

As an oscilloscope, all channels must be triggered at the same time by default, so calling an acquisition within the experiment is done at the scope level with

```
labscript_name.acquire(start\_time)
```

For simplicity of programming most configuration parameters for the scope acquisition (*i.e.* horizontal & vertical scales, trigger configuration, AC/DC coupling ...) are assumed to be manually set at the scope before the experiment. This is often preferable since oscilloscope data can often be previewed live to ascertain the correct settings before running a triggered shot to acquire data for later analysis.

A.3.1.2 Keysight Oscilloscopes—`KeysightXXXXScope.py`

Over time we found the memory limitations of our basic Tektronix oscilloscopes to be a problem and obtained some newer oscilloscopes from Keysight to enable more powerful acquisitions. We ended up with two Infinivision series oscilloscopes: an MSO-X3000 series and a DSO-X1000 series. These scopes, much like the Tektronix scopes described above, share a common code base, allowing for significant code re-use. However, when using the 1000 series scope, I found a few minor differences in the implementation that necessitated a full sub-class of the 3000 series instead of a common class for both.

Instantiation is similar to the above TekScope class, though there are a few more options to account for different numbers of analog input channels and the presence of digital inputs.

```
KeysightMSOX3000Scope(labscript_name, VISA_name, trigger_device,  
                        trigger_connection, num_AI=4, DI=True, trigger_duration=1e-3)
```

Here some default arguments are specified. The digital inputs are of particular interest. This scope was purchased with the idea of using it as a mid-range pulse counter for use with single photon counters. These digital lines allow for significant data accumulation without required large file storage sizes. Furthermore, direct counting operations on each of the digital lines can be configured if only the total count is necessary. These count operations are specified using a specific version of the ScopeChannel class above.

```
CounterScopeChannel(labscript_name, parent_device, connection)  
  
labscript_name.count(type, polarity)
```

The first line instantiates a counter-enabled scope channel. The second command tells `labscript` to use a counter with type pulse or edge and polarity positive or negative. These scope channels can also use the same acquire command detailed above with the base ScopeChannel class.

A.3.1.3 Signal Generators

One need we have found in the lab is configuration and use of high frequency signal generators. This type of frequency source typically does not have the abil-

ity do hardware triggered changes mid-experiment. However, incorporating these sources into `labscript` allows for their settings to be part of the experiment record, automated configuration on a shot-to-shot basis, and allows for static instrument control using `BLACS`.

These signal generators have extremely similar operation and typically only differ in the exact command strings. I wrote a parent Signal Generator class that inherits from the `VISA` class. This parent class can then be sub-classed for specific devices to configure instrument-specific parameters.

These classes use a `StaticFreqAmp` class for the frequency output configuration.

```
StaticFreqAmp(labscript_name, parent_device, connection,  
              freq_limits, amp_limits)
```

It allows for static frequency and amplitude control, similar to the `StaticDDS` classes used by the Novatechs. It is important to set the frequency and amplitude limits tuples to ensure invalid parameters are not accidentally set. The limits can be determined by the signal generator itself or by whatever the generator is connected to.

Sub-classing to specific devices involves configuring default limits, scale factors to convert between absolute units and instrument programming units, return value parsing functions, and status byte labels. Examples for how to do this are in the repository in the form of device classes written for signal generators we have used at various times. Models include: HP 8642A, Rhode & Schwarz SMF100A, and Rhode

& Schwarz SMHU.

A.3.1.4 Stanford Research SR865 Lock-In Amplifier–SR865.py

The final VISA-based device is a Lock-In amplifier. This is a relatively simple control that does not allow for return data (though the Lock-In is capable). This class allows one to set the phase, sensitivity, and time constant of the amplifier. Again, this allows for a record of set parameters for each experiment and remote control through **BLACS**.

Getting data from the Lock-In amplifier is much trickier. While it can return data, it is not hardware timed. In order to get hardware timed data, we connect the outputs of the amplifier to an oscilloscope or a DAQ analog input.

A.3.2 Novatech 409B Series Boards

During adoption we found that the Novatech devices used by the upstream developers did not quite match the Novatech devices we had. They use the 9m development board that the 409B devices we use are based on. The differences are ultimately minor, but they were significant enough to necessitate making our own classes. Ultimately I made a master class for the 409B-AC that is sub-classed for the 409B that only has static channels. The master class has a number of improvements over the 9m class it is based on. It only programs channels being used in the shot and it can handle arbitrary baud rates at instantiation.

The usage is identical to the DDS 9m class available in the main release.

A.3.3 Camera Servers

One major limitation of `labscript` at the moment is a lack of integrated camera support. The initial release used a LabVIEW based implementation called `BIAS`. This program acted as an independent camera server that interacted with `BLACS` to handle communication and image acquisition with the cameras. This implementation had limitations, the most significant being a core dependency on LabVIEW. Eventually a python-based solution will be implemented. In the meantime simple text-based servers for use with particular models of cameras have been made. The following three servers I have written are based on an implementation by Chris Billington and Dan Barker for PointGrey cameras.

The camera servers themselves are very similar in their operation, the largest difference being the underlying SDK that they use to interact with the physical cameras. Since these servers run entirely separate from `labscript`, I use separate conda environments for each server. This is particularly helpful since the various camera SDKs often require very specific versions of various packages for compatibility.

Below I describe the individual quirks of the servers and their associated SDKs. Environment configuration can be particularly tricky due to compilation needs when using cython wrappers of the manufacturer provided driver libraries.

A.3.3.1 Basler Pylon SDK

Basler makes a large line of affordable area scan cameras that all use the same SDK and share very similar configuration code. The Pylon SDK is freely available

from Basler and an open-source python wrapper is available on github. This wrapper is not officially supported and has not had continuous development. My fork has some improvements and is the specific fork used by the server. Others continue to develop the wrapper however. After my initial work, Basler restarted work on their own python wrapper. It appears the functionality is similar, though the exact implementation is different enough to necessitate re-working the server.

For my cython-based wrapper, you must install the same C/C++ compiler as that used to compile the version of python you intend to use. You can then use pip to install the git repository directly via

```
pip install -U https://github.com/dihm/PyPylon.git#egg=PyPylon
```

The specifics of interacting with a Basler camera depends on the exact communication interface used. For example USB3 cameras set the exposure time using the 'ExposureTime' parameter. In contrast, GigE cameras instead use the parameter name 'ExposureTimeRaw'. Both interfaces require specific hardware with compatible firmware to enable the fastest acquisition rates, described in the camera documentation. Also, GigE cameras require configuring the ethernet adapter for Jumbo frames to operate properly and matching the SDK packet size parameter, as outlined in the Pylon installation manual. At present, my server is tested for use with USB3 and GigE cameras only.

A.3.3.2 Princeton Instruments PIcam SDK

We have an older Princeton Instruments PIXIS 1024BR camera that I desired to use. The SDK is freely available from Princeton Instruments in the form of the PIcam library. The python wrapper I use is part of a larger hardware interface package available on github (<https://github.com/ddietze/Py-Hardware-Support>). This wrapper is based on the ctypes python module and therefore does not require the compilation resources needed for cython-based wrappers. This wrapper is not configured to be pip installable. In order for the server to find the wrapper code, the full path to the wrapper directory (cloned from github) must be provided and appended to the system path before import within the server script.

This server works reasonably well, but has some remaining issues. The camera itself is very slow on readout due to being a CCD read out over a USB 2.0 interface. There were further issues with random timeouts during successive shots that I did not chase down, likely residing in the wrapper class itself, since I moved on to a faster Andor camera with similar noise specifications.

A.3.3.3 Andor 3 SDK

Andor makes a number of high performance scientific cameras. Unfortunately, Andor is currently transitioning from SDK2 to SDK3 which are very different. We have a newer Andor Zyla 5.5 which uses SDK3. I did not find much in the way of python wrappers so I took the best I could find, forked it, and made major modifications to improve functionality, speed, and reliability. This wrapper can be

found at <https://bitbucket.org/dihm/pyandorsdk3>. Installation requires cython and the same C/C++ compiler as that used to compile the version of python you intend to use. Again, you can install the wrapper using git and pip with the following command

```
pip install -U https://bitbucket.org/dihm/pyandorsdk3.git#egg=PyAndorSDK3
```

The SDK is available from Andor if you own a camera. To ensure proper operation, the SDK library path must be added to the system path, which is not done by default.

Appendix B: Computational Packages & Example Source Code

In this appendix I provide some example source code for select computations presented in the main work. This code is provided in the hope that explicit examples will aid others who want to implement similar analyses.

B.1 Atomic Density Matrix Package

Code samples in this section rely on functionality provided by the Atomic Density Matrix package written by Simon Rochester, [23] available at <http://rochesterscientific.com/ADM/>. This package is written for Mathematica and allows for a high degree of configuration when modeling different experimental systems. It relies on specification of atomic levels based on quantum numbers and is specifically optimized for hyperfine transitions in alkali atoms.

The code base is not especially well documented, but the worked-through examples in the package documentation are very detailed and informative.

B.1.1 NMOR Numerical Simulations

The following code overlays the numerical model, derived from a density matrix representation of the atomic system and the Optical Bloch equations, with experiment data for different probe powers, shown in Figure [2.26\(a\)](#).

NMOR with ADM Package

This notebook makes use of the Atomic Density Matrix *Mathematica* Package developed by Simon Rochester in conjunction with Dimitri Budker. It is available for free at <http://budker.berkeley.edu/ADM/>.

Please see the ADM package documentation examples for examples and some documentation.

```
Needs["AtomicDensityMatrix"]
ParallelNeeds["AtomicDensityMatrix"]
SetOptions[DensityMatrix, TimeDependence -> False];
$Assumptions = {wp | ue | y | r | GR | DB | DBx | DBy | Delta | t | phi | e} < Reals;
SetOptions[Plot, AspectRatio -> 0.77, BaseStyle -> Large, Frame -> True, FrameStyle -> Directive[Thick, Black, FontSize -> 36, FontFamily -> "Arial"], ImageSize -> 1000];
SetOptions[ListPlot, AspectRatio -> 0.77, BaseStyle -> Large, Frame -> True, FrameStyle -> Directive[Thick, Black, FontSize -> 36, FontFamily -> "Arial"], PlotRange -> 0.5];
SetOptions[SphericalPlot3D, Axes -> False, Boxed -> False, PlotRange -> 0.5];

ParallelEvaluate[SetOptions[DensityMatrix, TimeDependence -> False];
$Assumptions = {wp | ue | y | r | GR | DB | DBx | DBy | Delta | t | phi | e} < Reals;
];

If[$VersionNumber < 10.,,
SetOptions[Plot, PlotTheme -> None];
SetOptions[ListPlot, PlotTheme -> None];]

(* put helper functions here *)
nf = NumberForm[#, {4, 1}, NumberPadding -> {"", "0"}] &;

SetDirectory[NotebookDirectory[]]

{Null, Null}
```

C:\Users\David\Google Drive\NMOR Thesis Chapter\NMOR Draft Figures

Let's import the data we want to compare with.

```
214
importerSwept[filename_String] := Block[{times, D1, D2, fields, Rot, Trans, RotOffset},
{times, D1, D2, fields, Rot, Trans, RotOffset} = Transpose[Drop[Import[filename], 1]]
]
importerStepped[filename_String] := Block[{fields, Rot},
{fields, Rot} = Transpose[Drop[Import[filename], 1]]
]

(*sweptNames=FileNames[FileNameJoin[{NotebookDirectory[], "Swept", "*.csv"}]]*)
steppedNames = FileNames[FileNameJoin[{NotebookDirectory[], "sY278Z+.csv"}]]

{L\Cold Atom Optics\Projects\Atom chip 1\Figures\NMOR Draft Figures\2015-12-01 Initial Better Data Runs\Power Scan\V025Y278Z450.csv,
L\Cold Atom Optics\Projects\Atom chip 1\Figures\NMOR Draft Figures\2015-12-01 Initial Better Data Runs\Power Scan\V05Y278Z450.csv,
L\Cold Atom Optics\Projects\Atom chip 1\Figures\NMOR Draft Figures\2015-12-01 Initial Better Data Runs\Power Scan\V075Y278Z450.csv,
L\Cold Atom Optics\Projects\Atom chip 1\Figures\NMOR Draft Figures\2015-12-01 Initial Better Data Runs\Power Scan\V10Y278Z450.csv}

importAllSwept[filename_String] := Block[{file},
file = FileBaseName[filename];
Evaluate[ToExpression[file]] = importerSwept[filename];
]
importAllStepped[filename_String] := Block[{file},
file = FileBaseName[filename];
Evaluate[ToExpression[file]] = importerStepped[filename];
]

(*Map[Clear, FileBaseName[#]] & /@ sweptNames - Join - steppedNames
importAllSwept[#] & /@ sweptNames*)
Map[Clear, FileBaseName[#]] & /@ steppedNames
importAllStepped[#] & /@ steppedNames

{V025Y278Z450, V05Y278Z450, V075Y278Z450, V10Y278Z450}

{Null, Null, Null, Null}
```

Defining the Hamiltonian

Define the atomic system. Assumptions made here: Lower state cannot decay. Excited State has a Branching Ratio of 1.

```
sys = Sublevels[{AtomicState[1, J -> 1/2, F -> 2, L -> 0, S -> 1/2, Energy -> 0, NaturalWidth -> 0, NuclearSpin -> 3/2, HyperfineA -> 0],
AtomicState[2, J -> 3/2, F -> 3, L -> 1, S -> 1/2, Energy -> ue, NaturalWidth -> r, NuclearSpin -> 3/2, BranchingRatio[1] -> 1,
HyperfineA -> 0, HyperfineB -> 0]}]

{AtomicState[1, J -> 1/2, F -> 2, L -> 0, S -> 1/2, Energy -> 0, NaturalWidth -> 0, NuclearSpin -> 3/2, HyperfineA -> 0, M -> 2],
AtomicState[1, J -> 1/2, F -> 2, L -> 0, S -> 1/2, Energy -> 0, NaturalWidth -> 0, NuclearSpin -> 3/2, HyperfineA -> 0, M -> 1],
AtomicState[1, J -> 1/2, F -> 2, L -> 0, S -> 1/2, Energy -> 0, NaturalWidth -> 0, NuclearSpin -> 3/2, HyperfineA -> 0, M -> 0],
AtomicState[1, J -> 1/2, F -> 2, L -> 0, S -> 1/2, Energy -> 0, NaturalWidth -> 0, NuclearSpin -> 3/2, HyperfineA -> 0, M -> -1],
AtomicState[1, J -> 1/2, F -> 2, L -> 0, S -> 1/2, Energy -> 0, NaturalWidth -> 0, NuclearSpin -> 3/2, HyperfineA -> 0, M -> -2],
AtomicState[2, J -> 3/2, F -> 3, L -> 1, S -> 1/2, Energy -> ue, NaturalWidth -> r, NuclearSpin -> 3/2, BranchingRatio[1] -> 1,
HyperfineA -> 0, HyperfineB -> 0, M -> 3], AtomicState[2, J -> 3/2, F -> 3, L -> 1, S -> 1/2, Energy -> ue, NaturalWidth -> r, NuclearSpin -> 3/2,
BranchingRatio[1] -> 1, HyperfineA -> 0, HyperfineB -> 0, M -> 2], AtomicState[2, J -> 3/2, F -> 3, L -> 1, S -> 1/2, Energy -> ue,
NaturalWidth -> r, NuclearSpin -> 3/2, BranchingRatio[1] -> 1, HyperfineA -> 0, HyperfineB -> 0, M -> 1], AtomicState[2, J -> 3/2, F -> 3,
L -> 1, S -> 1/2, Energy -> ue, NaturalWidth -> r, NuclearSpin -> 3/2, BranchingRatio[1] -> 1, HyperfineA -> 0, HyperfineB -> 0, M -> 0],
AtomicState[2, J -> 3/2, F -> 3, L -> 1, S -> 1/2, Energy -> ue, NaturalWidth -> r, NuclearSpin -> 3/2, BranchingRatio[1] -> 1,
HyperfineA -> 0, HyperfineB -> 0, M -> -1], AtomicState[2, J -> 3/2, F -> 3, L -> 1, S -> 1/2, Energy -> ue, NaturalWidth -> r,
NuclearSpin -> 3/2, BranchingRatio[1] -> 1, HyperfineA -> 0, HyperfineB -> 0, M -> -2], AtomicState[2, J -> 3/2, F -> 3, L -> 1,
S -> 1/2, Energy -> ue, NaturalWidth -> r, NuclearSpin -> 3/2, BranchingRatio[1] -> 1, HyperfineA -> 0, HyperfineB -> 0, M -> -3]]
```

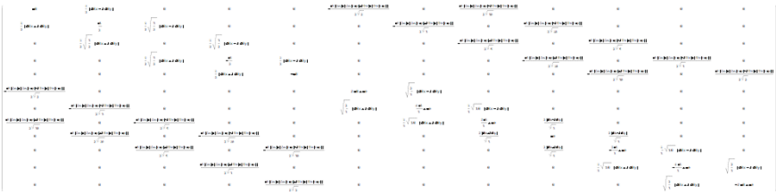
Define the Electric Field and Magnetic Field. The probe field is taken to propagate in the direction of the swept axial B-field.

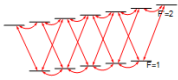
```
polvector = {1, 0, 0};
propvector = {0, 0, 1};
Etot = OpticalField[up, GR / ReducedME[1, {Dipole, 1}, 2], {0, e}, PolarizationVector -> polvector, PropagationVector -> propvector]
Mtot = {0, 0, DB / BohrMagneton};
Mptot = {DBx / BohrMagneton, DBy / BohrMagneton, 0};
```

$$\left(\frac{e^{-i t \omega} GR \cos[e]}{\text{ReducedME}[1, \{\text{Dipole}, 1\}, 2]}, \frac{i e^{-i t \omega} GR \sin[e]}{\text{ReducedME}[1, \{\text{Dipole}, 1\}, 2]}, 0 \right)$$

H_L

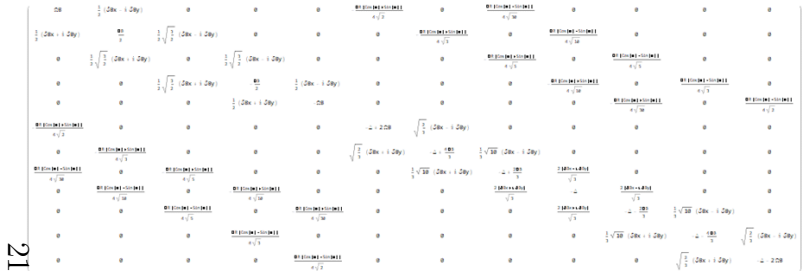
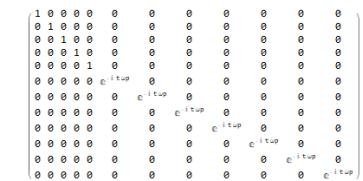
```
Rasterize[MatrixForm[HL = Hamiltonian[sys, MagneticField -> Mtot + Mptot, ElectricField -> Etot // Simplify], ImageSize -> 1000]
LevelDiagram[sys, HL /. {ue -> 2, DB -> 0.2, up -> 2, GR -> 1, HyperfineA[1] -> 0, HyperfineA[2] -> 0, HyperfineB[2] -> 0}, Epilog -> {Text["F=1", {2.5, 0}], Text[
```





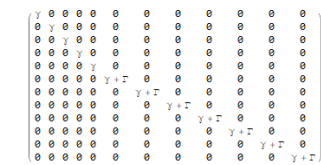
Apply Rotating Wave Approximation

```
MatrixForm[U = RotatingWaveTransformMatrix[sys, {up, 1 -> 2, Δ}]]
Rasterize[MatrixForm[Hrwa = RotatingWaveApproximation[sys, HL, {up, 1 -> 2, Δ}] // Simplify], ImageSize -> 1000]
```



Define Relaxation and Repopulation Matrices

```
MatrixForm[relaxations = Normal[TransitRelaxation[sys, γ] + IntrinsicRelaxation[sys]]]
```



```
Rasterize[MatrixForm[repopulations = 8/5 TransitRepopulation[sys, γ] + OpticalRepopulation[sys]], ImageSize -> 1000]
```



Generating Optical Bloch Equations

This generates the steady-state equations of the system.

0 == -i [H, ρ] - 1/2*{Γ, ρ} + Λ

```
start = SessionTime[];
eqs = LiouvilleEquation[sys, Hrwa, relaxations, repopulations]
end = SessionTime[];
end - start
```

$$\left\{ \begin{aligned} 0 &= \frac{\gamma}{5} - \gamma \rho_{(1,2,2),(1,2,2)} + \frac{\Delta}{25} \Gamma \rho_{(2,1,1),(2,1,1)} + \frac{1}{5} \Gamma \rho_{(2,2,2),(2,2,2)} - \\ &\frac{i}{2} \left(\frac{1}{2} (\mathcal{GB}x - i \mathcal{GB}y) \rho_{(1,2,2),(1,2,2)} - \frac{1}{2} (\mathcal{GB}x + i \mathcal{GB}y) \rho_{(1,2,2),(1,2,2)} - \frac{\mathcal{GB} \cos[\theta] \sin[\theta]}{4 \sqrt{30}} \rho_{(1,2,2),(2,2,2)} - \frac{\mathcal{GB} \cos[\theta] \sin[\theta]}{4 \sqrt{2}} \rho_{(1,2,2),(2,2,2)} + \right. \\ &\left. \frac{\mathcal{GB} \cos[\theta] \sin[\theta]}{4 \sqrt{30}} \rho_{(2,2,2),(1,2,2)} - \frac{\mathcal{GB} \cos[\theta] \sin[\theta]}{4 \sqrt{2}} \rho_{(2,2,2),(1,2,2)} \right) + \Gamma \rho_{(2,2,2),(2,2,2)} \times \frac{105}{4}, 0 = \\ &- (\gamma + \Gamma) \rho_{(2,2,2),(2,2,2)} - i \left(\frac{\mathcal{GB} \cos[\theta] \sin[\theta]}{4 \sqrt{2}} \rho_{(1,2,2),(2,2,2)} - \frac{\mathcal{GB} \cos[\theta] \sin[\theta]}{4 \sqrt{2}} \rho_{(2,2,2),(1,2,2)} - \sqrt{\frac{2}{5}} (\mathcal{GB}x - i \mathcal{GB}y) \rho_{(2,2,2),(2,2,2)} + \sqrt{\frac{2}{5}} (\mathcal{GB}x + i \mathcal{GB}y) \rho_{(2,2,2),(2,2,2)} \right) \end{aligned} \right\}$$

0.0624855

Look at the results

The differential changes in an incident probe beam are given by Observables[]. We care about the probe absorption and the polarization angle rotation.

abs[] & FR[] use Mathematica's NSolve[] method with the precision set with the p variable.

Finally, we define the absorption length as given in the Zeeman Structure Tutorial of the ADM Package documentation. Namely:

$$l_0 = - \left(\frac{1}{r} \frac{dr}{d\epsilon} \right)^{-1} = \left(\frac{2}{\epsilon_0} \frac{d\epsilon_0}{d\epsilon} \right)^{-1} \text{ with } \Delta = \Omega_B = 0 \text{ and } \Omega_R, \gamma \rightarrow 0.$$

Observables and Absorption Length Calculation

Need to numerically find the absorption length for anything larger than F=1,F'=1. We can assume it has the form of C*oe^3/(π*op).

```
(* Does the absorption length need to be calculated with pure linear light? *)
absleq =
Observables[sys, up, GR / ReducedME[1, {Dipole, 1}, 2], {0, 0}, PolarizationVector -> polvector, PropagationVector -> propvector,
TransformMatrix -> U][[1, 1]] // Simplify
absseq =
Observables[sys, up, GR / ReducedME[1, {Dipole, 1}, 2], {0, e}, PolarizationVector -> polvector, PropagationVector -> propvector,
TransformMatrix -> U][[1, 1]] // Simplify;
FReq =
Observables[sys, up, GR / ReducedME[1, {Dipole, 1}, 2], {0, e}, PolarizationVector -> polvector, PropagationVector -> propvector,
TransformMatrix -> U][[2, 1]] // Simplify;

(*abslength=Limit[2abseq/.Solve[eqs/.{Δ=0,GB=0,GB=0},DMVariables[sys]][[1]],GR=0]^-1/(γ+0)*)

p = 30;
liouvilleEqs[GR, ε, Δ, Γ, γ, ΔB, ΔBx, ΔBy] = N[eqs, p];
abslength = Module[{sol, abslen, Rabif = 2 Pi 0.000001, Gam = QuantityMagnitude[Rb87Naturallinewidth], gamma = 2 Pi 0.0000001,
sol = NSolve[liouvilleEqs[N[Rabif, p], N[0, p], N[0, p], N[Gam, p], N[gamma, p], N[0, p], N[0, p], N[0, p], DMVariables[sys]][[1]];
abslen = -(2*abseq)^(-1) /. sol;
abslen /. {GR -> Rabif, ε -> 0, Γ -> Gam}

1

absNorm = -abseq*abslength
FRNorm = FReq*abslength
```

$$= \frac{1}{5 \omega^3 \mathcal{GB}} \sqrt{3} \pi \Gamma \omega p \left\{ 5 \sqrt{6} \operatorname{Im}[\rho_{(1,2,2),(2,2,2)}] - \sqrt{10} \operatorname{Im}[\rho_{(1,2,2),(2,2,2)}] + 10 \operatorname{Im}[\rho_{(1,2,2),(2,2,2)}] - \sqrt{30} \operatorname{Im}[\rho_{(1,2,2),(2,2,2)}] + 2 \sqrt{15} \operatorname{Im}[\rho_{(1,2,2),(2,2,2)}] - \right.$$

$$\left. 2 \sqrt{15} \operatorname{Im}[\rho_{(1,2,2),(2,2,2)}] + \sqrt{30} \operatorname{Im}[\rho_{(1,2,2),(2,2,2)}] - 10 \operatorname{Im}[\rho_{(1,2,2),(2,2,2)}] + \sqrt{10} \operatorname{Im}[\rho_{(1,2,2),(2,2,2)}] - 5 \sqrt{6} \operatorname{Im}[\rho_{(1,2,2),(2,2,2)}] \right\}$$

$$\frac{0.113682 \omega^3}{\omega p}$$

```

- 1
ΩR 0.123718 ⌈ -10 Cos[ϵ] Im[ρ(1,2,1),(2,2,2)] + √30 Cos[ϵ] Im[ρ(1,2,1),(2,3,0)] -
2 √15 Cos[ϵ] Im[ρ(1,2,0),(2,3,1)] + 2 √15 Cos[ϵ] Im[ρ(1,2,0),(2,3,1)] - √30 Cos[ϵ] Im[ρ(1,2,1),(2,3,0)] + 10 Cos[ϵ] Im[ρ(1,2,1),(2,3,2)] -
√10 Cos[ϵ] Im[ρ(1,2,2),(2,3,1)] + 5 √6 Cos[ϵ] Im[ρ(1,2,2),(2,3,1)] - 5 √6 Im[ρ(1,2,2),(2,3,1)] (Cos[ϵ] - Sin[ϵ]) + 10 Im[ρ(1,2,1),(2,3,2)] Sin[ϵ] +
√30 Im[ρ(1,2,1),(2,3,0)] Sin[ϵ] + 2 √15 Im[ρ(1,2,0),(2,3,1)] Sin[ϵ] + 2 √15 Im[ρ(1,2,0),(2,3,1)] Sin[ϵ] + √30 Im[ρ(1,2,1),(2,3,0)] Sin[ϵ] +
10 Im[ρ(1,2,1),(2,3,2)] Sin[ϵ] + √10 Im[ρ(1,2,2),(2,3,1)] Sin[ϵ] + 5 √6 Im[ρ(1,2,2),(2,3,1)] Sin[ϵ] + √10 Im[ρ(1,2,2),(2,3,1)] (Cos[ϵ] + Sin[ϵ]) ⌋

- 1
ΩR 0.123718 ⌈ Sec[2 ϵ] ⌈ 10 Cos[ϵ] Re[ρ(1,2,1),(2,3,2)] + √30 Cos[ϵ] Re[ρ(1,2,1),(2,3,0)] +
2 √15 Cos[ϵ] Re[ρ(1,2,0),(2,3,1)] + 2 √15 Cos[ϵ] Re[ρ(1,2,0),(2,3,1)] + √30 Cos[ϵ] Re[ρ(1,2,1),(2,3,0)] + 10 Cos[ϵ] Re[ρ(1,2,1),(2,3,2)] +
√10 Cos[ϵ] Re[ρ(1,2,2),(2,3,1)] + 5 √6 Cos[ϵ] Re[ρ(1,2,2),(2,3,1)] + √10 Re[ρ(1,2,2),(2,3,1)] (Cos[ϵ] - Sin[ϵ]) + 10 Re[ρ(1,2,1),(2,3,2)] Sin[ϵ] -
√30 Re[ρ(1,2,1),(2,3,0)] Sin[ϵ] + 2 √15 Re[ρ(1,2,0),(2,3,1)] Sin[ϵ] - 2 √15 Re[ρ(1,2,0),(2,3,1)] Sin[ϵ] + √30 Re[ρ(1,2,1),(2,3,0)] Sin[ϵ] -
10 Re[ρ(1,2,1),(2,3,2)] Sin[ϵ] + √10 Re[ρ(1,2,2),(2,3,1)] Sin[ϵ] - 5 √6 Re[ρ(1,2,2),(2,3,1)] Sin[ϵ] + 5 √6 Re[ρ(1,2,2),(2,3,1)] (Cos[ϵ] + Sin[ϵ]) ⌋

```

Numeric Solvers

```

p = 30;
liouvilleEqs[aR_, c_, d_, f_, γ_, dB_, dBx_, dBz_] := N[eqs, p];
solVars = DMVariables[sys];
solveDM[OmegaR_, epsilon_, Delta_, gamma_, gammaO, deltaBx_, deltaBy_] :=
NSolve[liouvilleEqs[N[OmegaR, p], N[epsilon, p], N[Delta, p], N[gamma, p], N[gammaO, p], N[deltaBx, p], N[deltaBy, p]], solVars][[1]]

abs[dm_, OmegaR_, epsilon_, gamma_] := absNorm /. dm /. {aR -> OmegaR, e -> epsilon, f -> gamma}
FR[dm_, OmegaR_, epsilon_, gamma_] := FRNorm /. dm /. {aR -> OmegaR, e -> epsilon, f -> gamma}
dm[dm_] := DensityMatrix[sys] /. dm
groundDM[dm_] := DensityMatrix[SelectStates[sys, 1]] /. dm
pops[dm_] := Chop[Diagonal[DensityMatrix[sys]] /. dm]
coherences[dm_] :=
{Abs[ρ(1,2,-2),(1,2,-1) / Sqrt[ρ(1,2,-2),(1,2,-2) * ρ(1,2,-1),(1,2,-1)]], Abs[ρ(1,2,-1),(1,2,0) / Sqrt[ρ(1,2,-1),(1,2,-1) * ρ(1,2,0),(1,2,0)]], Abs[ρ(1,2,0),(1,2,1) / Sqrt[ρ(1,2,0),(1,2,0) * ρ(1,2,1),(1,2,1)]],
Abs[ρ(1,2,1),(1,2,2) / Sqrt[ρ(1,2,1),(1,2,1) * ρ(1,2,2),(1,2,2)]], Abs[ρ(1,2,-2),(1,2,0) / Sqrt[ρ(1,2,-2),(1,2,-2) * ρ(1,2,0),(1,2,0)]], Abs[ρ(1,2,-1),(1,2,1) / Sqrt[ρ(1,2,-1),(1,2,-1) * ρ(1,2,1),(1,2,1)]]
} /. dm
(* (-2,-1), (-1,0), (0,1), (1,2), (-2,0), (-1,1), (0,2)
*)

```

Note about Units

Units in the ADM package are theory units. Converting to the real world takes a bit of work.

First note that ħ=c=1, so energies are given in units of rad/s. Linewidths are also specified in units of rad/s. B-fields are given in units of μ_B/ħ. All terms are in Mega-radians/second.

Note: To better highlight the ratio of Γ to γ, γ is defined in terms of Γ for all plots. In line with our experimental parameters, γ = Γ/6066.6 = 2π 0.999988 kHz.

```

ħ = Quantity[1, "ReducedPlanckConstant"];
μB = Quantity[1, "BohrMagneton"];
hfs = {HyperfineA[1] -> 21471.8, HyperfineA[2] -> 532.302, HyperfineB[2] -> 78.5178};
Rb87NaturalLineWidth = Quantity[38.11711*6, "Seconds"^-1] * 10^-6
hfShifts = Quantity[5/4 * (HyperfineB[2] - HyperfineA[1]) /. hfs, "Seconds"^-1]
Rb87D2TransitionEnergy = (Quantity[2.41419*15, "Seconds"^-1]) * 10^-6 + hfShifts
BfieldUnits = UnitConvert[μB/ħ * Quantity[1, "Gausses"]] * 10^-6

```

38.1171 per second

-28737.7 per second

2.41416×10⁶ per second

8.794100 per second

In order to convert power meter Watts to Rabi Frequency used in this calculation we need to do a bit more work. Namely:

$\Omega_F = d_F \langle J=1 || e^{-iJ} || J=3/2 \rangle \tilde{E} / \hbar$, where $|\tilde{E}| = \sqrt{\frac{2I}{c \epsilon_0}}$, $I = \frac{W}{\pi(d/2)^2}$ is assumed, and d_F is a polarization-dependent coefficient that scales the reduced matrix element to the effective dipole moment.

```

RabiFreq[microwatts_, diameter_] := Module[{Watts, Efield, Intensity, e0 = Quantity[1, "ElectricConstant"], c = Quantity[1, "SpeedOfLight"], ħ = Quantit
Watts = Quantity[microwatts, "Microwatts"];
Intensity = Watts / (Quantity[diameter, "Millimeters"] / 2)^2 / Pi;
Int = UnitConvert[Intensity // N, "Milliwatts" * "Centimeters"^-2];
Efield = Sqrt[2 * Intensity / c / e0];
RabiF = UnitConvert[2 * D2DipoleME * Efield / ħ / 2 / Pi, "Megahertz"];
Print["Intensity is: ", Int];
Print["Rabi Frequency is: ", RabiF];
QuantityMagnitude[RabiF]
]
RabiFreq[#, 1] & /@ {5.17, 7.7, 10.23, 13.9, 15.34, 20.45}

```

Intensity is: 0.658265 mW/cm²

Rabi Frequency is: 7.01485 MHz

Intensity is: 0.908394 mW/cm²

Rabi Frequency is: 8.56888 MHz

Intensity is: 1.30252 mW/cm²

Rabi Frequency is: 9.86759 MHz

Intensity is: 1.7698 mW/cm²

Rabi Frequency is: 11.5022 MHz

Intensity is: 1.95315 mW/cm²

Rabi Frequency is: 12.0833 MHz

Intensity is: 2.68377 mW/cm²

Rabi Frequency is: 13.9515 MHz

{7.01485, 8.56888, 9.86759, 11.5022, 12.0833, 13.9515}

NSolve Transverse Field Plots - Ω_R = 7 MHz, Δ=4.0Γ, δB=55mG, θ=0°

Simulation Parameters & DM Solve

Set the power, detuning, and γ here.

```

rabiFreq = 2 Pi 9.26;
detuning = 4.43 * QuantityMagnitude[Rb87NaturalLineWidth];
transitRate = 2 Pi (2.0/1000);

```

```

gamma = QuantityMagnitude[Rb87NaturalLineWidth];
Bscaling = QuantityMagnitude[BfieldUnits];

```

Bmax = 0.17;

```

Btrns = 0.055;
o = 0 Degree;
ellipticity = 0 Degree;
Bx = Btrns * Cos[o]; (* By on the setup *)
By = Btrns * Sin[o]; (* Bz on the setup *)
AbsoluteTiming[solDMs = ParallelTable[solveDM[rabiFreq, ellipticity, detuning, gamma, transitRate, B * Bscaling, Bx * Bscaling, By * Bscaling], {B, -Bmax,

```

{7.08076, Null}]

```

BaxialRange = Range[-Bmax, Bmax, Bmax * 2 / 200];
Baxial[Bx_] := Nearest[BaxialRange -> Automatic, Bx, 1][[1]];
(* returns the nearest element to that specified *)
Print["Baxial resolution is ", Bmax * 2 / 200, " G"];

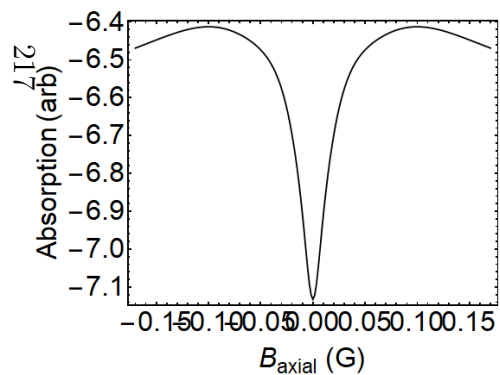
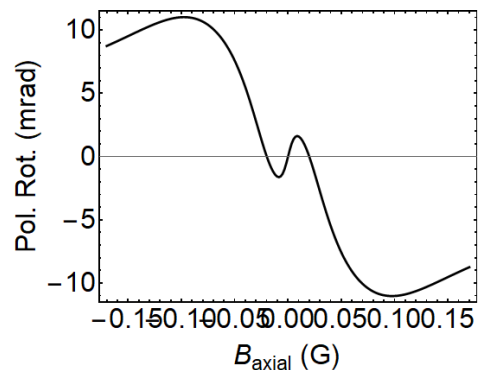
```

Baxial resolution is 0.0017 G

Pol. Rot. and Abs. -- Baxial \pm Bmax

```
color = Black;

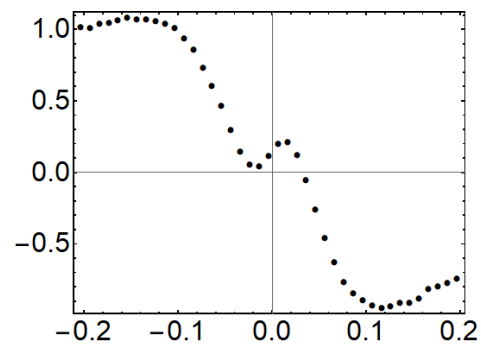
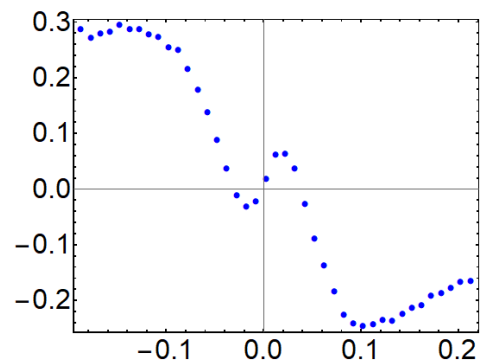
ampFactor = -1000;
FRPlot0deg = ListPlot[Map[ampFactor*FR[#, rabiFreq, ellipticity, gamma] &, solDMs], DataRange -> {-Bmax, Bmax}, PlotRange -> Full, Axes -> {True, True}, A
  FrameLabel -> {"Baxial (G)", "Pol. Rot. (mrad)"}]
AbsPlot0deg = ListPlot[Map[ampFactor*abs[#, rabiFreq, ellipticity, gamma] &, solDMs], DataRange -> {-Bmax, Bmax}, PlotRange -> Full, Axes -> {True, True},
  FrameLabel -> {"Baxial (G)", "Absorption (arb)"}]
```

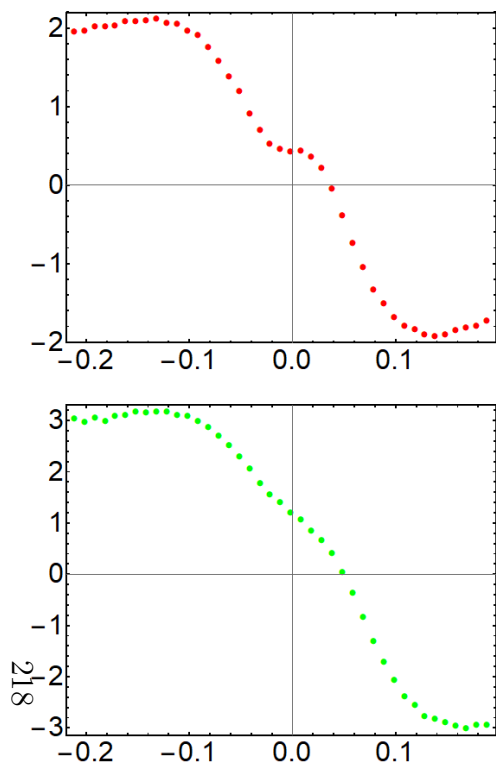


Data Import

```
Clear[dataPlotter];
dataPlotter[data_List, color_:= Black] := ListPlot[Transpose[{data[[1]] + BxOffset, data[[2]] + rotOffset}, PlotStyle -> {color}]
```

```
BxOffset = 0.033;
rotOffset = -0.005;
V025Y278p1ot = dataPlotter[V025Y278Z450, Blue]
BxOffset = 0.017;
rotOffset = 0.0;
V05Y278p1ot = dataPlotter[V05Y278Z450]
BxOffset = 0.009;
rotOffset = 0.0;
V075Y278p1ot = dataPlotter[V075Y278Z450, Red]
rotOffset = -0.05;
V10Y278p1ot = dataPlotter[V10Y278Z450, Green]
```





Simulation Overlays

```

detuning = 4.43 * QuantityMagnitude[Rb87NaturalLineWidth];
transitRate = 2 Pi (1/1.5) / 1000;
Btrns = (2.78 - 2.08) * 0.099;
gamma = QuantityMagnitude[Rb87NaturalLineWidth];
Bscaling = QuantityMagnitude[BfieldUnits];

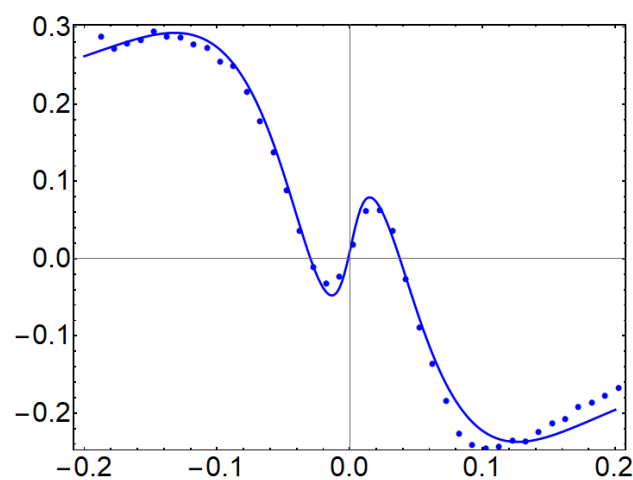
ampFactor = -50;

Bmax = 0.2;

phi = 0 Degree;
ellipticity = -0.75 Degree;
Bstatic = -0.008;
rabiFreq = 2 Pi 8.75;
OO = 0.43;
Bx = Btrns * Cos[phi]; (* By on the setup *)
By = Btrns * Sin[phi] + Bstatic; (* Bz on the setup *)
AbsoluteTiming[V025 = ParallelTable[{B, ampFactor * OO * FR[solveDM[rabiFreq, ellipticity, detuning, gamma, transitRate, B * Bscaling, Bx * Bscaling, By * B:
Show[ListLinePlot[V025, PlotStyle -> {AbsoluteThickness[3], Blue}], V025V278plot]

{1.076407, Null}

```



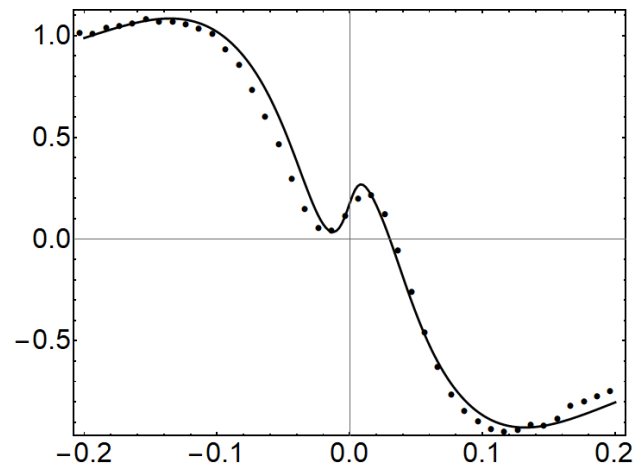
```

rabiFreq = 2 Pi 10.25;
OO = 1.2;

AbsoluteTiming[V05 = ParallelTable[{B, ampFactor * OO * FR[solveDM[rabiFreq, ellipticity, detuning, gamma, transitRate, B * Bscaling, Bx * Bscaling, By * B:
Show[ListLinePlot[V05, PlotStyle -> {AbsoluteThickness[3], Black}], V05V278plot]

{0.717605, Null}

```

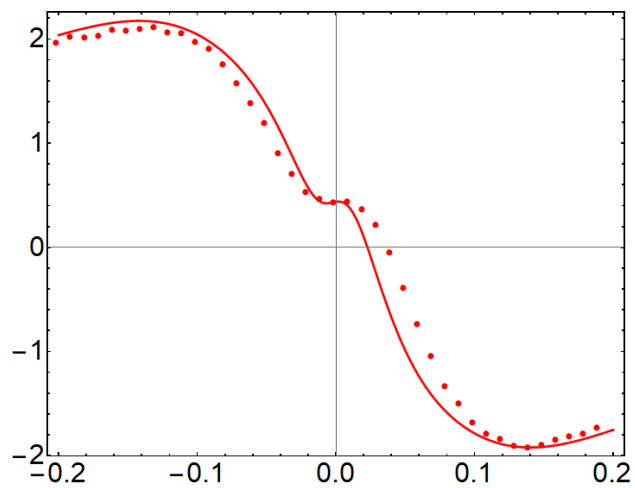


```

rabiFreq = 2 Pi 11.8;
OO = 1.95;
AbsoluteTiming[V075 = ParallelTable[{B, ampFactor * OO * FR[solveDM[rabiFreq, ellipticity, detuning, gamma, transitRate, B * Bscaling, Bx * Bscaling, By * B:
Show[ListLinePlot[V075, PlotStyle -> {AbsoluteThickness[3], Red}], V075V278plot]

{0.733205, Null}

```



```
Export["V025Y278-Sim.csv", V025]  
Export["V05Y278-Sim.csv", V05]  
Export["V075Y278-Sim.csv", V075]
```

V025Y278-Sim.csv

V05Y278-Sim.csv

V075Y278-Sim.csv

B.1.2 Perturbation Model Calculation

This code implements the 5-Step Perturbative model from Section [2.3.2](#). It relies on some ADM package functionality to perform frame rotations, conversions between tensor and cartesian forms, and the spherical tensor product.

```
<< AtomicDensityMatrix`
SetOptions[DensityMatrix, TimeDependence -> False];
SetOptions[AMPSPlot, Boxed -> False, Axes -> False, ViewPoint -> {1/3, 1, 1/3}, ViewVertical -> {1, 0, 0}, ImageSize -> 600];
SetOptions[Axes3D, BaseStyle -> Directive[Black, Opacity[0.7]], AutoLengthScale -> 2, LabelStyle -> Directive[Thick, Black, FontSize -> 36, FontFamily -> 'ParallelNeeds["AtomicDensityMatrix`"]];
SetDirectory[NotebookDirectory[]]
ParallelEvaluate[
SetOptions[DensityMatrix, TimeDependence -> False];
SetOptions[AMPSPlot, Boxed -> False, Axes -> False, ViewPoint -> {1/3, 1, 1/3}, ViewVertical -> {1, 0, 0}, ImageSize -> 600];
SetOptions[Axes3D, BaseStyle -> Directive[Black, Opacity[0.7]], AutoLengthScale -> 2, LabelStyle -> Directive[Thick, Black, FontSize -> 36, FontFamily -> '
]
```

```
C:\Users\David\Google Drive\WJOR Thesis Chapter\5-Stage Theory
```

```
{Null, Null}
```

```
gstate = Sublevels[AtomicState[1, J -> 1, Energy -> 0, NaturalWidth -> 0]]
```

```
[AtomicState[1, J -> 1, Energy -> 0, NaturalWidth -> 0, M -> 1],
AtomicState[1, J -> 1, Energy -> 0, NaturalWidth -> 0, M -> 0], AtomicState[1, J -> 1, Energy -> 0, NaturalWidth -> 0, M -> -1]]
```

```
TensorForm[pmgstate = DensityMatrix[gstate, Representation -> PolarizationMoments]]
```

$$\left(\left\{\left(\begin{array}{c} \rho_{(1,1),(0,0)} \end{array}\right), \left(\begin{array}{c} \rho_{(1,1),(1,1)} \\ \rho_{(1,1),(1,0)} \\ \rho_{(1,1),(1,-1)} \end{array}\right), \left(\begin{array}{c} \rho_{(1,1),(2,2)} \\ \rho_{(1,1),(2,1)} \\ \rho_{(1,1),(2,0)} \\ \rho_{(1,1),(2,-1)} \\ \rho_{(1,1),(2,-2)} \end{array}\right)\right\}\right)$$

```
rotateToLab[tensor_] := Block[{btotTok},
btotTok = WignerRotate[tensor, {0, Pi/2 - α, 0}];
WignerRotate[btotTok, {0, 0, -β}]
]
```

5-Stage Modeling of Alignment-to-Orientation Conversion

Stage 1

In stage 1 the light creates alignment along the z-axis (ie E-field direction for EIT).

We then rotate to the Btot direction frame

```
Component[pmgstate[[1, 1]], 2]
% /. ρ<sub>(1,1)</sub>,(2,0)</sub> -> 1;
labAlignStage1 = % /. ρ__ -> 0
```

```
{{ρ<sub>(1,1)</sub>,(2,2)</sub>}, {ρ<sub>(1,1)</sub>,(2,1)</sub>}, {ρ<sub>(1,1)</sub>,(2,0)</sub>}, {ρ<sub>(1,1)</sub>,(2,-1)</sub>}, {ρ<sub>(1,1)</sub>,(2,-2)</sub>}}
```

```
{{0}, {0}, {1}, {0}, {0}}
```

In order for angles to cleanly represent Btrans and Baxial, need to start with alignment in x-direction.

Then Tan[β]=By/Bx & Tan[α]=Bz/Bt. Bt=±√ Bx²+By²

Note that α defined this way results in a rotation of -(Pi/2-α) in the Euler angles.

```
WignerRotate[ToCovariant@labAlignStage1, {0, Pi/2, 0}] // Simplify
btotAlignStage1 = WignerRotate[%, {0, α - Pi/2, β}] // FullSimplify
```

$$\left\{\left\{-\frac{\sqrt{\frac{3}{2}}}{2}, 0, -\frac{1}{2}, 0, \frac{\sqrt{\frac{3}{2}}}{2}\right\}\right\}$$

$$\left\{\left\{-\frac{1}{2}\sqrt{\frac{3}{2}}\left(\cos\left[\beta\right]\sin\left[\alpha\right]+i\sin\left[\beta\right]\right)^2,-\sqrt{\frac{3}{2}}\cos\left[\alpha\right]\cos\left[\beta\right]\left(\cos\left[\beta\right]\sin\left[\alpha\right]+i\sin\left[\beta\right]\right),\right.\right.$$

$$\left.\frac{1}{8}\left(-1+3\cos\left[2\alpha\right]+6\cos\left[\alpha\right]^2\cos\left[2\beta\right]\right),\sqrt{\frac{3}{2}}\cos\left[\alpha\right]\cos\left[\beta\right]\left(\cos\left[\beta\right]\sin\left[\alpha\right]-i\sin\left[\beta\right]\right),-\frac{1}{2}\sqrt{\frac{3}{2}}\left(\cos\left[\beta\right]\sin\left[\alpha\right]-i\sin\left[\beta\right]\right)^2\right\}\right\}$$

```
btotAlignStage1 /. {β -> 0} // Simplify
```

$$\left\{\left\{-\frac{1}{2}\sqrt{\frac{3}{2}}\sin\left[\alpha\right]^2,-\sqrt{\frac{3}{2}}\cos\left[\alpha\right]\sin\left[\alpha\right],-\frac{1}{4}\left(1+3\cos\left[2\alpha\right]\right),\sqrt{\frac{3}{2}}\cos\left[\alpha\right]\sin\left[\alpha\right],\frac{1}{2}\sqrt{\frac{3}{2}}\sin\left[\alpha\right]^2\right\}\right\}$$

Stage 2

Stage 2 includes precession from the total magnetic field

```
precFactor[q_]=
YIntegrate[Exp[-γ (t - tp)] Exp[I q αL (t - tp)], {tp, -Infinity, t}, Assumptions -> {q ∈ Reals, γ > 0, αL ∈ Reals}] /. γ -> ξ + αL // Simplify
```

$$\frac{i \xi}{q + i \xi}$$

```
btotAlignStage1[[1]] + Evaluate[precFactor[#] & /@ Range[2, -2, -1]];
btotAlignStage2 = Normal@{Series[%, {ξ, 0, 1}]} // FullSimplify
btotAlignzpzStage2 = btotAlignStage2 * {(0, 0, 1, 0, 0)};
btotAlignNonzpzStage2 = btotAlignStage2 * {(1, 1, 0, 1, 1)};
```

$$\left\{\left\{\frac{1}{4}\left(1-\sqrt{\frac{3}{2}}\xi\left(\cos\left[\beta\right]\sin\left[\alpha\right]+i\sin\left[\beta\right]\right)^2,\sqrt{\frac{3}{2}}\xi\cos\left[\alpha\right]\cos\left[\beta\right]\left(-i\cos\left[\beta\right]\sin\left[\alpha\right]+\sin\left[\beta\right]\right),\right.\right.$$

$$\left.\frac{1}{8}\left(-1+3\cos\left[2\alpha\right]+6\cos\left[\alpha\right]^2\cos\left[2\beta\right]\right),\sqrt{\frac{3}{2}}\xi\cos\left[\alpha\right]\cos\left[\beta\right]\left(-i\cos\left[\beta\right]\sin\left[\alpha\right]-\sin\left[\beta\right]\right),-\frac{1}{4}\sqrt{\frac{3}{2}}\xi\left(\cos\left[\beta\right]\sin\left[\alpha\right]-i\sin\left[\beta\right]\right)^2\right\}\right\}$$

```
btotAlignStage2 /. {β -> 0} // Simplify
```

$$\left\{\left\{\frac{1}{4}\left(1-\sqrt{\frac{3}{2}}\xi\sin\left[\alpha\right]^2,-i\sqrt{\frac{3}{2}}\xi\cos\left[\alpha\right]\sin\left[\alpha\right],-\frac{1}{4}\left(1+3\cos\left[2\alpha\right]\right),-i\sqrt{\frac{3}{2}}\xi\cos\left[\alpha\right]\sin\left[\alpha\right],\frac{1}{4}\sqrt{\frac{3}{2}}\xi\sin\left[\alpha\right]^2\right\}\right\}\right.$$

```
baseIsotropic = {1/Sqrt[3]} // ToContravariant;
baseOrient = {{0, 0, 0}} // ToContravariant;
```

Full Alignment PMs

Just z' oriented alignment

```
btotPMszpzStage2 = {baseIsotropic, baseOrient, ToContravariant@btotAlignzpzStage2};
labPMszpzStage2 = rotateToLab[btotPMszpzStage2];
```

```
Btotal[α_] := Graphics3D[{Blue, Arrowheads[0.08], Arrow[Tube[{{0, 0, 0}, {Cos[α], 0, Sin[α]}], 0.011]}];
labAlongBtot = ParallelTable[Show[Axes3D[AMPSPlot[labPMszpzStage2 /. {ξ -> 1, β -> 0, α -> α}], Btotal[α]], {α, -3.14/2, 3.14/2, Pi/50}];
```

```
angles = Range[-3.14/2, 3.14/2, Pi/50];
angles[[1]] / Pi
```

```
0.300253
```

```
Manipulate[labAlongBtot[[i]], {i, 1, Length[labAlongBtot], 1}]
```

```
Export["labAlongBtot-1.png", labAlongBtot[[1]]]
Export["labAlongBtot-4.png", labAlongBtot[[4]]]
Export["labAlongBtot-11.png", labAlongBtot[[11]]]
Export["labAlongBtot-18.png", labAlongBtot[[18]]]
Export["labAlongBtot-26.png", labAlongBtot[[26]]]
```

labAlongBtot-1.png

labAlongBtot-4.png

labAlongBtot-11.png

labAlongBtot-18.png

labAlongBtot-26.png

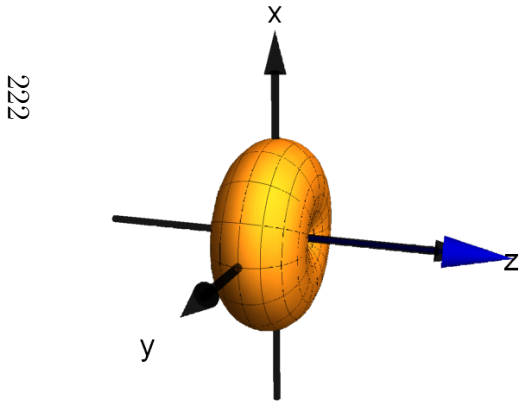
```
Export["labAlongBtot-34.png", labAlongBtot[[34]]]
Export["labAlongBtot-41.png", labAlongBtot[[41]]]
Export["labAlongBtot-48.png", labAlongBtot[[48]]]
```

labAlongBtot-34.png

labAlongBtot-41.png

labAlongBtot-48.png

```
labAlongBtotAxis = Show[Axes3D[AMPSPlot[labPMszpStage2 /. {ξ → 1, β → 0, α → Pi / 2.0001}], Btotal[Pi / 2.0001]]
```



```
Export["labAlongBtot-50.png", labAlongBtotAxis]
```

labAlongBtot-50.png

```
Export["labAlongBtot2.avi", labAlongBtot, "FrameRate" → 2]
```

test.avi

Just Non-z' oriented alignment

```
btotPMsNonzpStage2 = {baseIsotropic, baseOrient, ToContravariant@btotAlignNonzpStage2};
labPMsNonzpStage2 = rotateToLab[btotPMsNonzpStage2];
```

```
Btotal[α_] := Graphics3D[{Blue, Arrowheads[0.08], Arrow[Tube[{{0, 0, 0}, {Cos[α], 0, Sin[α]}], 0.011]]];
labNotAlongBtot = ParallelTable[Show[Axes3D[AMPSPlot[labPMsNonzpStage2 /. {ξ → 1, β → 0, α → a}], Btotal[a]], {a, -3.14 / 2, 3.14 / 2, Pi / 50}];
```

```
Manipulate[labNotAlongBtot[[i]], {i, 1, Length[labNotAlongBtot], 1}]
```

```
Export["labNotAlongBtot2.avi", labNotAlongBtot, "FrameRate" → 2]
```

labNotAlongBtot2.avi

```
Export["labNotAlongBtot-1.png", labNotAlongBtot[[1]]]
Export["labNotAlongBtot-4.png", labNotAlongBtot[[4]]]
Export["labNotAlongBtot-11.png", labNotAlongBtot[[11]]]
Export["labNotAlongBtot-18.png", labNotAlongBtot[[18]]]
Export["labNotAlongBtot-26.png", labNotAlongBtot[[26]]]
```

labNotAlongBtot-1.png

labNotAlongBtot-4.png

labNotAlongBtot-11.png

labNotAlongBtot-18.png

labNotAlongBtot-26.png

```
Export["labNotAlongBtot-34.png", labNotAlongBtot[[34]]]
Export["labNotAlongBtot-41.png", labNotAlongBtot[[41]]]
Export["labNotAlongBtot-48.png", labNotAlongBtot[[48]]]
```

labNotAlongBtot-34.png

labNotAlongBtot-41.png

labNotAlongBtot-48.png

```
Range[-3.14 / 2, 3.14 / 2, Pi / 50][[34]] / Pi
```

0.160253

Stage 3

Stage 3 we include the effect of the AC-Stark shifts that generate AOC.
The E-field needs the same frame transformation as above.

```
Elab = {1, 0, 0};
ToCovariant[Elab];
Ebtot = WignerRotate[%, {0, α - Pi / 2, β}] // FullSimplify
Ebtot /. β → 0
```

$$\left\{ \left\{ -\frac{\cos[\beta] \sin[\alpha] + i \sin[\beta]}{\sqrt{2}}, \cos[\alpha] \cos[\beta], \frac{\cos[\beta] \sin[\alpha] - i \sin[\beta]}{\sqrt{2}} \right\} \right\}$$

$$\left\{ \left\{ -\frac{\sin[\alpha]}{\sqrt{2}}, \cos[\alpha], \frac{\sin[\alpha]}{\sqrt{2}} \right\} \right\}$$


```
SphericalTensorProduct[btotAlignStage2, Ebtot, {1}];
btotOrientStage3 = I * SphericalTensorProduct[%, Ebtot, {1}] // Simplify;
btotOrientStage3Cart = ToCartesian[btotOrientStage3] // Simplify
```

$$\left\{ \frac{3 \cos[\alpha] \cos[\beta] (2 \xi \cos[\beta]^2 \sin[\alpha]^3 + \cos[\alpha]^2 (8 \xi \cos[\beta]^2 \sin[\alpha] - 6 \cos[2\beta] \sin[\beta]) + \sin[\beta] (1 - 3 \cos[2\alpha] + \xi \sin[\alpha] \sin[2\beta]))}{16 \sqrt{5}}, \right.$$

$$\frac{3 \cos[\alpha] \cos[\beta] (\cos[\beta] (-1 + 3 \cos[2\alpha] + 6 \cos[\alpha]^2 \cos[2\beta]) \sin[\alpha] + \xi (5 + 3 \cos[2\alpha]) \cos[\beta]^2 \sin[\beta] + 2 \xi \sin[\beta]^2)}{16 \sqrt{5}},$$

$$\left. - \frac{3 \xi (\cos[\beta] \sin[\alpha] - i \sin[\beta]) (\cos[\beta] \sin[\alpha] + i \sin[\beta]) (4 \cos[\alpha]^2 \cos[\beta]^2 + \cos[\beta]^2 \sin[\alpha]^2 + \sin[\beta]^2)}{8 \sqrt{5}} \right\}$$

```
btotOrientStage3Cart /. {β → 0} // Simplify
```

$$\left\{ \frac{3 \xi \cos[\alpha] (7 \sin[\alpha] + 3 \sin[3\alpha])}{32 \sqrt{5}}, \frac{3 (1 + 3 \cos[2\alpha]) \sin[2\alpha]}{16 \sqrt{5}}, - \frac{3 \xi (5 + 3 \cos[2\alpha]) \sin[\alpha]^2}{16 \sqrt{5}} \right\}$$

Just Orientation from z' Alignment

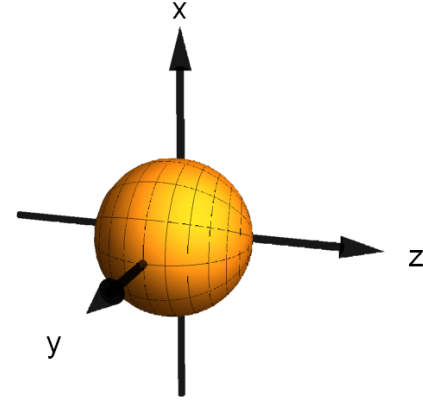
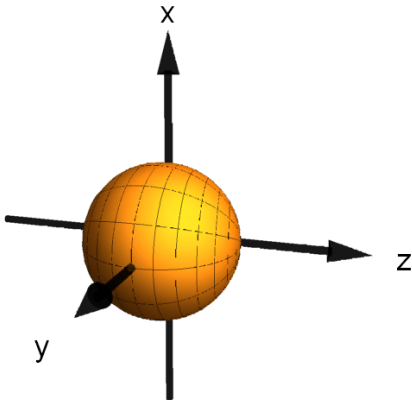
```
SphericalTensorProduct[btotAlignzpStage2, Ebtot, {1}];
btotOrientzpStage3 = I * SphericalTensorProduct[%, Ebtot, {1}] // Simplify;
ToCartesian[btotOrientzpStage3] // Simplify
% /. β → 0
```

$$\left\{ - \frac{3 \cos[\alpha] \cos[\beta] (-1 + 3 \cos[2\alpha] + 6 \cos[\alpha]^2 \cos[2\beta]) \sin[\beta]}{16 \sqrt{5}}, \frac{3 \cos[\alpha] \cos[\beta]^2 (-1 + 3 \cos[2\alpha] + 6 \cos[\alpha]^2 \cos[2\beta]) \sin[\alpha]}{16 \sqrt{5}}, 0 \right\}$$

$$\left\{ 0, \frac{3 \cos[\alpha] (-1 + 6 \cos[\alpha]^2 + 3 \cos[2\alpha]) \sin[\alpha]}{16 \sqrt{5}}, 0 \right\}$$

```
btotPMszpStage3 = {baseIsotropic, ToContravariant@btotOrientzpStage3};
labPMszpStage3 = rotateToLab[btotPMszpStage3];
Axes3D[AMPSPlot[btotPMszpStage3 /. {ξ → 1, β → 0, α → 0.5}]]
Axes3D[AMPSPlot[labPMszpStage3 /. {ξ → 1, β → 0, α → 0.5}]]
```

23



```
Btotal[α_] := Graphics3D[{Blue, Arrowheads[0.08], Arrow[Tube[{0, 0, 0}, {Cos[α], 0, Sin[α]}], 0.01]}];
labAlongBtot3 = ParallelTable[Show[Axes3D[AMPSPlot[labPMszpStage3 /. {ξ → 1, β → 0, α → a}]], Btotal[a]], {a, -3.14/2, 3.14/2, Pi/100}];
```

```
Manipulate[labAlongBtot3[[i]], {i, 1, Length[labAlongBtot3], 1}]
```

Just Orientation from non-z' Alignment

```
SphericalTensorProduct[btotAlignNonzpStage2, Ebtot, {1}];
btotOrientNonzpStage3 = I * SphericalTensorProduct[%, Ebtot, {1}] // Simplify;
ToCartesian[btotOrientNonzpStage3] // Simplify
% /. β → 0
```

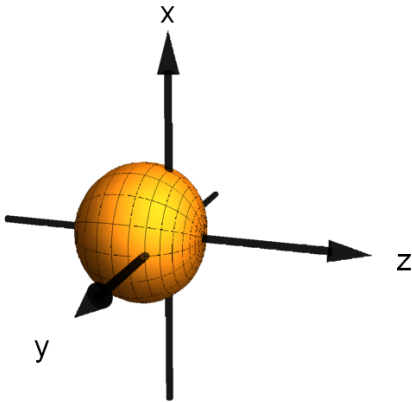
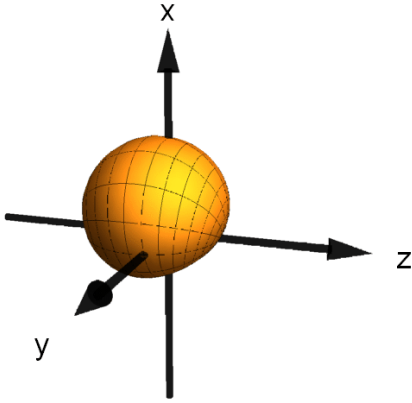
$$\left\{ \frac{3 \xi \cos[\alpha] \cos[\beta]^2 \sin[\alpha] (4 \cos[\alpha]^2 \cos[\beta]^2 + \cos[\beta]^2 \sin[\alpha]^2 + \sin[\beta]^2)}{8 \sqrt{5}}, \right.$$

$$\frac{3 \xi \cos[\alpha] \cos[\beta] \sin[\beta] (4 \cos[\alpha]^2 \cos[\beta]^2 + \cos[\beta]^2 \sin[\alpha]^2 + \sin[\beta]^2)}{8 \sqrt{5}},$$

$$\left. - \frac{3 \xi (\cos[\beta] \sin[\alpha] - i \sin[\beta]) (\cos[\beta] \sin[\alpha] + i \sin[\beta]) (4 \cos[\alpha]^2 \cos[\beta]^2 + \cos[\beta]^2 \sin[\alpha]^2 + \sin[\beta]^2)}{8 \sqrt{5}} \right\}$$

$$\left\{ \frac{3 \xi \cos[\alpha] \sin[\alpha] (4 \cos[\alpha]^2 + \sin[\alpha]^2)}{8 \sqrt{5}}, 0, - \frac{3 \xi \sin[\alpha]^2 (4 \cos[\alpha]^2 + \sin[\alpha]^2)}{8 \sqrt{5}} \right\}$$

```
btotPMsNonzpStage3 = {baseIsotropic, ToContravariant@btotOrientNonzpStage3};
labPMsNonzpStage3 = rotateToLab[btotPMsNonzpStage3];
Axes3D[AMPSPlot[btotPMsNonzpStage3 /. {ξ → 1, β → 0, α → 0.5}]]
Axes3D[AMPSPlot[labPMsNonzpStage3 /. {ξ → 1, β → 0, α → 0.5}]]
```



224

Stage 4

Stage 4 we again apply the precession of the atomic polarization by the magnetic field, this time only the orientation.

```
btotOrientStage3 = Evaluate[precFactor[#] & /@ {Range[1, -1, -1]}];
btotOrientStage4 = Normal@Series[%, {ε, 0, 1}] // Simplify
btotOrientStage4Cart = ToCartesian[btotOrientStage4]
```

$$\left\{ \left\{ \frac{3 \varepsilon \cos[\alpha] \cos[\beta] (-1 + 3 \cos[2\alpha] + 6 \cos[\alpha]^2 \cos[2\beta]) (\cos[\beta] \sin[\alpha] + i \sin[\beta])}{16 \sqrt{10}}, \right. \right. \\ \left. - \frac{3 \varepsilon (\cos[\beta] \sin[\alpha] - i \sin[\beta]) (\cos[\beta] \sin[\alpha] + i \sin[\beta]) (4 \cos[\alpha]^2 \cos[\beta]^2 + \cos[\beta]^2 \sin[\alpha]^2 + \sin[\beta]^2)}{8 \sqrt{5}}, \right. \\ \left. - \frac{3 \varepsilon \cos[\alpha] \cos[\beta] (-1 + 3 \cos[2\alpha] + 6 \cos[\alpha]^2 \cos[2\beta]) (\cos[\beta] \sin[\alpha] - i \sin[\beta])}{16 \sqrt{10}} \right\} \right\}$$

btotOrientStage4Cart /. {β → 0} // Simplify

$$\left\{ -\frac{3 \varepsilon (1 + 3 \cos[2\alpha]) \sin[2\alpha]}{16 \sqrt{5}}, 0, -\frac{3 \varepsilon (5 + 3 \cos[2\alpha]) \sin[\alpha]^2}{16 \sqrt{5}} \right\}$$

```
btotOrientzStage3 = Evaluate[precFactor[#] & /@ {Range[1, -1, -1]}];
btotOrientzStage4 = Normal@Series[%, {ε, 0, 1}] // Simplify
btotOrientzStage4Cart = ToCartesian[btotOrientzStage4]
% /. β → 0
```

$$\left\{ \left\{ \frac{3 \varepsilon \cos[\alpha] \cos[\beta] (-1 + 3 \cos[2\alpha] + 6 \cos[\alpha]^2 \cos[2\beta]) (\cos[\beta] \sin[\alpha] + i \sin[\beta])}{16 \sqrt{10}}, \right. \right. \\ \left. 0, -\frac{3 \varepsilon \cos[\alpha] \cos[\beta] (-1 + 3 \cos[2\alpha] + 6 \cos[\alpha]^2 \cos[2\beta]) (\cos[\beta] \sin[\alpha] - i \sin[\beta])}{16 \sqrt{10}} \right\} \right\}$$

$$\left\{ -\frac{3 \varepsilon \cos[\alpha] \cos[\beta] (-1 + 3 \cos[2\alpha] + 6 \cos[\alpha]^2 \cos[2\beta]) (\cos[\beta] \sin[\alpha] - i \sin[\beta])}{32 \sqrt{5}}, \right. \\ \left. -\frac{3 \varepsilon \cos[\alpha] \cos[\beta] (-1 + 3 \cos[2\alpha] + 6 \cos[\alpha]^2 \cos[2\beta]) (\cos[\beta] \sin[\alpha] + i \sin[\beta])}{32 \sqrt{5}}, \right. \\ \left. -\frac{3 i \varepsilon \cos[\alpha] \cos[\beta] (-1 + 3 \cos[2\alpha] + 6 \cos[\alpha]^2 \cos[2\beta]) (\cos[\beta] \sin[\alpha] - i \sin[\beta])}{32 \sqrt{5}}, \right. \\ \left. -\frac{3 i \varepsilon \cos[\alpha] \cos[\beta] (-1 + 3 \cos[2\alpha] + 6 \cos[\alpha]^2 \cos[2\beta]) (\cos[\beta] \sin[\alpha] + i \sin[\beta])}{32 \sqrt{5}}, 0 \right\}$$

$$\left\{ -\frac{3 \varepsilon \cos[\alpha] (-1 + 6 \cos[\alpha]^2 + 3 \cos[2\alpha]) \sin[\alpha]}{16 \sqrt{5}}, 0, 0 \right\}$$

```
btotOrientNonzpStage3 = Evaluate[precFactor[#] & /@ {Range[1, -1, -1]}];
btotOrientNonzpStage4 = Normal@Series[%, {ε, 0, 1}] // Simplify
btotOrientNonzpStage4Cart = ToCartesian[btotOrientNonzpStage4]
% /. β → 0
```

$$\left\{ \left\{ 0, -\frac{3 \varepsilon (\cos[\beta] \sin[\alpha] - i \sin[\beta]) (\cos[\beta] \sin[\alpha] + i \sin[\beta]) (4 \cos[\alpha]^2 \cos[\beta]^2 + \cos[\beta]^2 \sin[\alpha]^2 + \sin[\beta]^2)}{8 \sqrt{5}}, 0 \right\} \right\}$$

$$\left\{ 0, 0, -\frac{3 \varepsilon (\cos[\beta] \sin[\alpha] - i \sin[\beta]) (\cos[\beta] \sin[\alpha] + i \sin[\beta]) (4 \cos[\alpha]^2 \cos[\beta]^2 + \cos[\beta]^2 \sin[\alpha]^2 + \sin[\beta]^2)}{8 \sqrt{5}} \right\}$$

$$\left\{0, 0, -\frac{3 \xi \sin(\alpha)^2 (4 \cos(\alpha)^2 + \sin(\alpha)^2)}{8 \sqrt{5}}\right\}$$

Stage 5

Finally, we find the polarization rotation from the generated orientation along the light propagation direction. To do this we need to change frames such that the z-axis is aligned with the propagation direction. This is effectively the reverse of the Stage 1 rotations.

```
cartOrient = {p1,x,p1,y,p1,z};
btotToLab = Thread[cartOrient -> btotOrientStage4Cart];
RotationMatrix[-beta, {0, 0, 1}].RotationMatrix[Pi/2 - alpha, {0, 1, 0}];
labOrient = % . cartOrient;
labOrientStage4 = labOrient /. btotToLab // Simplify;
```

```
WignerRotate[btotOrientStage4, {0, Pi/2 - alpha, 0}];
WignerRotate[%, {0, 0, -beta}];
labOrientStage4 = ToCartesian[%] // ExpToTrig // Simplify
```

$$\left\{-\frac{1}{1024 \sqrt{5}} 3 \xi \cos(\alpha) \cos(\beta) (-30 - 104 \cos(2\alpha) + 54 \cos(4\alpha) + 36 \cos(2\alpha - 4\beta) + 9 \cos(4\alpha - 4\beta) - 16 \cos(2\alpha - 2\beta) + 36 \cos(4\alpha - 2\beta) - 104 \cos(2\beta) + 54 \cos(4\beta) - 16 \cos(2(\alpha + \beta)) + 9 \cos(4(\alpha + \beta)) + 36 \cos(4\alpha + 2\beta) + 36 \cos(2\alpha + 4\beta)), \right. \\ \left. -\frac{1}{1024 \sqrt{5}} 3 \xi \cos(\alpha) (-94 + 88 \cos(2\alpha) + 54 \cos(4\alpha) + 36 \cos(2\alpha - 4\beta) + 9 \cos(4\alpha - 4\beta) + 80 \cos(2\alpha - 2\beta) + 36 \cos(4\alpha - 2\beta) + 88 \cos(2\beta) + 54 \cos(4\beta) + 80 \cos(2(\alpha + \beta)) + 9 \cos(4(\alpha + \beta)) + 36 \cos(4\alpha + 2\beta) + 36 \cos(2\alpha + 4\beta)) \sin(\beta), \right. \\ \left. \frac{1}{1024 \sqrt{5}} 3 \xi (-94 + 88 \cos(2\alpha) + 54 \cos(4\alpha) + 36 \cos(2\alpha - 4\beta) + 9 \cos(4\alpha - 4\beta) + 80 \cos(2\alpha - 2\beta) + 36 \cos(4\alpha - 2\beta) + 88 \cos(2\beta) + 54 \cos(4\beta) + 80 \cos(2(\alpha + \beta)) + 9 \cos(4(\alpha + \beta)) + 36 \cos(4\alpha + 2\beta) + 36 \cos(2\alpha + 4\beta)) \sin(\alpha)\right\}$$

```
labOrientStage4 /. {beta -> 0} // Simplify
```

$$\left\{-\frac{3 \xi \cos(\alpha) (7 + 9 \cos(2\alpha)) \sin(\alpha)^2}{16 \sqrt{5}}, 0, \frac{3 \xi (3 + 20 \cos(2\alpha) + 9 \cos(4\alpha)) \sin(\alpha)}{64 \sqrt{5}}\right\}$$

```
WignerRotate[btotOrientzpzStage4, {0, Pi/2 - alpha, 0}];
WignerRotate[%, {0, 0, -beta}];
labOrientzpzStage4 = ToCartesian[%] // ExpToTrig // Simplify
labOrientzpzStage4 /. {beta -> 0} // Simplify
```

$$\left\{-\frac{1}{256 \sqrt{5}} 3 \xi \cos(\alpha) \cos(\beta) (-6 + 2 \cos(2\alpha) + \cos(2(\alpha - \beta)) + 2 \cos(2\beta) + \cos(2(\alpha + \beta))) \right. \\ \left. (-2 + 6 \cos(2\alpha) + 3 \cos(2(\alpha - \beta)) + 6 \cos(2\beta) + 3 \cos(2(\alpha + \beta))), \right. \\ \left. \frac{3 \xi \cos(\alpha)^3 \cos(\beta)^2 (-2 + 6 \cos(2\alpha) + 3 \cos(2(\alpha - \beta)) + 6 \cos(2\beta) + 3 \cos(2(\alpha + \beta))) \sin(\beta)}{32 \sqrt{5}}, \right. \\ \left. \frac{3 \xi \cos(\alpha)^2 \cos(\beta)^2 (-2 + 6 \cos(2\alpha) + 3 \cos(2(\alpha - \beta)) + 6 \cos(2\beta) + 3 \cos(2(\alpha + \beta))) \sin(\alpha)}{32 \sqrt{5}}\right\}$$

$$\left\{-\frac{3 \xi \cos(\alpha) (1 + 3 \cos(2\alpha)) \sin(\alpha)^2}{8 \sqrt{5}}, 0, \frac{3 \xi \cos(\alpha)^2 (1 + 3 \cos(2\alpha)) \sin(\alpha)}{8 \sqrt{5}}\right\}$$

```
WignerRotate[btotOrientNonzpzStage4, {0, Pi/2 - alpha, 0}];
WignerRotate[%, {0, 0, -beta}];
labOrientNonzpzStage4 = ToCartesian[%] // ExpToTrig // Simplify
labOrientNonzpzStage4 /. {beta -> 0} // Simplify
```

$$\left\{-\frac{3 \xi \cot(\alpha) \csc(\alpha) \csc(\beta)^3 \sin(2\beta) (4 \sin(\beta)^4 + \sin(\alpha)^2 \sin(2\beta)^2) (4 \sin(\alpha)^2 \sin(\beta)^4 + \sin(\alpha)^4 \sin(2\beta)^2 + \sin(2\alpha)^2 \sin(2\beta)^2)}{256 \sqrt{5}}, \right. \\ \left. \frac{3 \xi \cot(\alpha) \csc(\alpha) \csc(\beta)^3 (4 \sin(\beta)^4 + \sin(\alpha)^2 \sin(2\beta)^2) (4 \sin(\alpha)^2 \sin(\beta)^4 + \sin(\alpha)^4 \sin(2\beta)^2 + \sin(2\alpha)^2 \sin(2\beta)^2)}{128 \sqrt{5}}, \right. \\ \left. -\frac{3 \xi (14 + 6 \cos(2\alpha) + 3 \cos(2(\alpha - \beta)) + 6 \cos(2\beta) + 3 \cos(2(\alpha + \beta))) \sin(\alpha) (\cos(\beta) \sin(\alpha) - i \sin(\beta)) (\cos(\beta) \sin(\alpha) + i \sin(\beta))}{64 \sqrt{5}}\right\}$$

$$\text{Infinity: Indeterminate expression } \frac{0 \xi \cot(\alpha) \csc(\alpha) \text{ComplexInfinity}}{\sqrt{5}} \text{ encountered.}$$

$$\text{Infinity: Indeterminate expression } \frac{0 \xi \cot(\alpha) \csc(\alpha) \text{ComplexInfinity}}{\sqrt{5}} \text{ encountered.}$$

$$\left\{\text{Indeterminate, Indeterminate, } -\frac{3 \xi (5 + 3 \cos(2\alpha)) \sin(\alpha)^3}{16 \sqrt{5}}\right\}$$

```
labOrientzpzStage4 + labOrientNonzpzStage4;
%[{3}] /. {beta -> 0} // Simplify
```

$$\frac{3 \xi (-14 \sin(\alpha) + 11 \sin(3\alpha) + 9 \sin(5\alpha))}{128 \sqrt{5}}$$

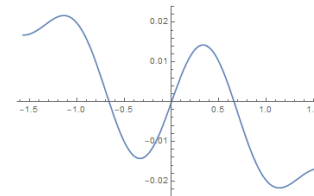
Which is identical to the above, so these components do add correctly.

Test Plots

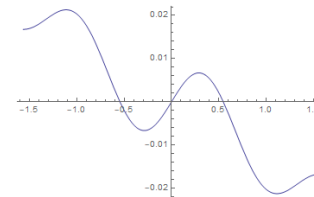
We check to make sure the changes in frame have not changed the base result for when By=0

```
labOrientStage4 /. {beta -> 0} // FullSimplify
Plot[%[{3}] /. {xi -> 0.1}, {alpha, -Pi/2, Pi/2}]
```

$$\left\{-\frac{3 \xi \cos(\alpha) (7 + 9 \cos(2\alpha)) \sin(\alpha)^2}{16 \sqrt{5}}, 0, \frac{3 \xi (3 + 20 \cos(2\alpha) + 9 \cos(4\alpha)) \sin(\alpha)}{64 \sqrt{5}}\right\}$$



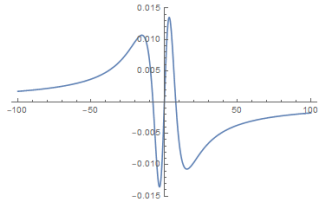
```
Plot[labOrientStage4[{3}] /. {xi -> 0.1, beta -> Pi/8}, {alpha, -Pi/2, Pi/2}]
```



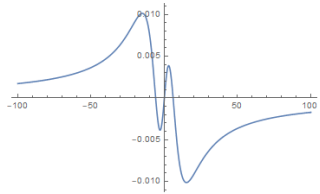
```
Tan[Pi/8] * 10 // N
```

```
4.14214
```

```
labOrientStage4[{3}] /. {xi -> y/Sqrt[Bx^2 + By^2 + Bz^2], alpha -> ArcTan[Bz/Sqrt[Bx^2 + By^2]], beta -> ArcTan[By/Bx]};
Plot[% /. {y -> 1, By -> 0 * Tan[Pi/8], Bx -> 10}, {Bz, -100, 100}]
```



```
labOrientStage4[{3}] /. {ξ → γ / Sqrt[Bx^2 + By^2 + Bz^2], α → ArcTan[Bz / Sqrt[Bx^2 + By^2]], β → ArcTan[By / Bx]};
Plot[% /. {γ → 1, By → 5, Bx → 10}, {Bz, -100, 100}]
```



```
cartLabOrient = With[{γ = 1.0, Bx = 10, By = 5},
  Table[{Bz, labOrientStage4[{3}] /. {ξ → γ / Sqrt[Bx^2 + By^2 + Bz^2], α → ArcTan[Bz / Sqrt[Bx^2 + By^2]], β → ArcTan[By / Bx]}],
    {Bz, -100, 100, 0.1}]];
```

```
Export["cartLabOrient4-By.csv", cartLabOrient]
```

cartLabOrient4-By.csv

26 Alignment

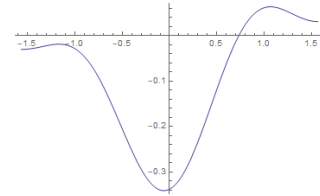
```
WignerRotate[btotAlignStage2, {0, Pi / 2 - α, 0}];
WignerRotate[%, {0, 0, -β}];
labAlignStage4 = %[[1, 1]] // ExpToTrig // Simplify
Im@labAlignStage4 // Simplify
Plot[% /. {β → Pi / 8, ξ → 0.1}, {α, -Pi / 2, Pi / 2}]
```

$$\frac{1}{128} \sqrt{\frac{3}{2}} (\cos(2\beta) - i \sin(2\beta))$$

$$(2 + 8 \cos(2\alpha) + 6 \cos(4\alpha) - 22 \xi \cos(\alpha - 2\beta) - 6 \xi \cos(3\alpha - 2\beta) + 3 \cos(4\alpha - 2\beta) + 12 \cos(2(\alpha - \beta)) + 18 \cos(2\beta) + 12 \cos(2(\alpha + \beta)) + 3 \cos(2(2\alpha + \beta)) + 22 \xi \cos(\alpha + 2\beta) + 6 \xi \cos(3\alpha + 2\beta) + 12 i \xi \sin(\alpha) + 12 i \xi \sin(3\alpha) + 22 i \xi \sin(\alpha - 2\beta) + 6 i \xi \sin(3\alpha - 2\beta) + 22 i \xi \sin(\alpha + 2\beta) + 6 i \xi \sin(3\alpha + 2\beta))$$

$$\frac{1}{128} \sqrt{\frac{3}{2}}$$

$$\text{Im}[(\cos(2\beta) - i \sin(2\beta)) (2 + 8 \cos(2\alpha) + 6 \cos(4\alpha) - 22 \xi \cos(\alpha - 2\beta) - 6 \xi \cos(3\alpha - 2\beta) + 3 \cos(4\alpha - 2\beta) + 12 \cos(2(\alpha - \beta)) + 18 \cos(2\beta) + 12 \cos(2(\alpha + \beta)) + 3 \cos(2(2\alpha + \beta)) + 22 \xi \cos(\alpha + 2\beta) + 6 \xi \cos(3\alpha + 2\beta) + 12 i \xi \sin(\alpha) + 12 i \xi \sin(3\alpha) + 22 i \xi \sin(\alpha - 2\beta) + 6 i \xi \sin(3\alpha - 2\beta) + 22 i \xi \sin(\alpha + 2\beta) + 6 i \xi \sin(3\alpha + 2\beta))]$$



Splitting Orientation Components

```
WignerRotate[btotOrientzpStage4, {0, Pi / 2 - α, 0}];
WignerRotate[%, {0, 0, -β}];
labOrientzpStage4 = ToCartesian[%] // ExpToTrig // Simplify
% /. β → 0
```

$$\left\{ \frac{1}{256 \sqrt{5}} \frac{3 \xi \cos(\alpha) \cos(\beta) (-6 + 2 \cos(2\alpha) + \cos(2(\alpha - \beta)) + 2 \cos(2\beta) + \cos(2(\alpha + \beta)))}{(-2 + 6 \cos(2\alpha) + 3 \cos(2(\alpha - \beta)) + 6 \cos(2\beta) + 3 \cos(2(\alpha + \beta)))}, \right.$$

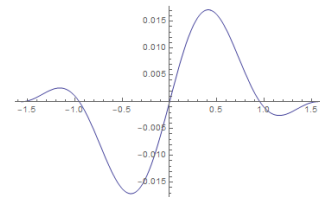
$$\left. \frac{3 \xi \cos(\alpha)^3 \cos(\beta)^2 (-2 + 6 \cos(2\alpha) + 3 \cos(2(\alpha - \beta)) + 6 \cos(2\beta) + 3 \cos(2(\alpha + \beta))) \sin(\beta)}{32 \sqrt{5}}, \right.$$

$$\left. \frac{3 \xi \cos(\alpha)^2 \cos(\beta)^2 (-2 + 6 \cos(2\alpha) + 3 \cos(2(\alpha - \beta)) + 6 \cos(2\beta) + 3 \cos(2(\alpha + \beta))) \sin(\alpha)}{32 \sqrt{5}} \right\}$$

$$\left\{ \frac{3 \xi \cos(\alpha) (-4 + 4 \cos(2\alpha)) (4 + 12 \cos(2\alpha))}{256 \sqrt{5}}, 0, \frac{3 \xi \cos(\alpha)^2 (4 + 12 \cos(2\alpha)) \sin(\alpha)}{32 \sqrt{5}} \right\}$$

```
labOrientzpStage4[{3}] /. {β → 0} // FullSimplify
Plot[% /. {ξ → 0.1}, {α, -Pi / 2, Pi / 2}]
```

$$\frac{3 \xi \cos(\alpha)^2 (1 + 3 \cos(2\alpha)) \sin(\alpha)}{8 \sqrt{5}}$$



```
Export["labOrientAlongBtot4.csv", Table[{a, labOrientzpStage4[{3}] /. {β → 0.0, ξ → 1.0, α → a}, {a, -Pi / 2, Pi / 2, Pi / 100.0}]]
```

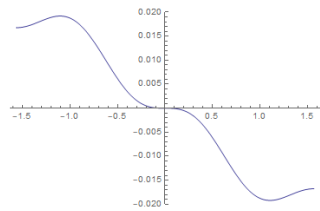
labOrientAlongBtot4.csv

```
WignerRotate[btotOrientNonzpStage4, {0, Pi / 2 - α, 0}];
WignerRotate[%, {0, 0, -β}];
labOrientNonzpStage4 = ToCartesian[%] // ExpToTrig // Simplify
Limit[%, β → 0]
```

$$\left\{ -\frac{1}{256\sqrt{5}} \frac{3\xi \cot(\alpha) \csc(\alpha) \csc(\beta)^5 \sin(2\beta) (4\sin(\beta)^4 + \sin(\alpha)^2 \sin(2\beta)^2) (4\sin(\alpha)^2 \sin(\beta)^4 + \sin(\alpha)^4 \sin(2\beta)^2 + \sin(2\alpha)^2 \sin(2\beta)^2)}{3\xi \cot(\alpha) \csc(\alpha) \csc(\beta)^3 (4\sin(\beta)^4 + \sin(\alpha)^2 \sin(2\beta)^2) (4\sin(\alpha)^2 \sin(\beta)^4 + \sin(\alpha)^4 \sin(2\beta)^2 + \sin(2\alpha)^2 \sin(2\beta)^2)}, \right. \\ \left. -\frac{1}{64\sqrt{5}} \frac{3\xi (14 + 6\cos(2\alpha) + 3\cos(2(\alpha - \beta)) + 6\cos(2\beta) + 3\cos(2(\alpha + \beta))) \sin(\alpha) (\cos(\beta) \sin(\alpha) - i \sin(\beta)) (\cos(\beta) \sin(\alpha) + i \sin(\beta))}{3\xi (13\cos(\alpha) + 3\cos(3\alpha)) \sin(\alpha)^2}, 0, -\frac{3\xi (5 + 3\cos(2\alpha)) \sin(\alpha)^3}{16\sqrt{5}} \right\}$$

```
labOrientNonzpStage4[{3}] /. {β → 0} // FullSimplify
Plot[% /. {ξ → 0.1}, {α, -Pi/2, Pi/2}]
```

$$-\frac{3\xi (5 + 3\cos(2\alpha)) \sin(\alpha)^3}{16\sqrt{5}}$$

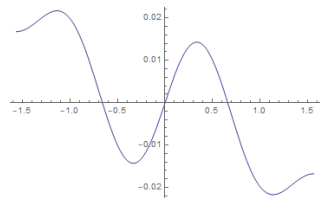


```
Export["labOrientNotAlongBtot4.csv", Table[{a, Re[labOrientNonzpStage4[{3}]]} /. {β → 0.0, ξ → 1.0, α → a}, {a, -Pi/2, Pi/2, Pi/100.0}]]
```

```
labOrientNotAlongBtot4.csv
```

```
labOrientNonzpStage4[{3}] + labOrientzpStage4[{3}] /. {β → 0} // FullSimplify
Plot[% /. {ξ → 0.1}, {α, -Pi/2, Pi/2}]
```

$$\frac{3\xi (-14\sin(\alpha) + 11\sin(3\alpha) + 9\sin(5\alpha))}{128\sqrt{5}}$$

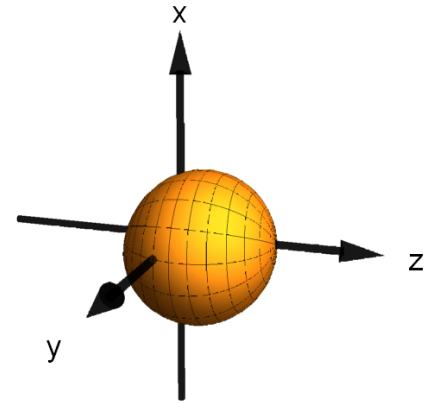


```
Export["labOrientBtot4.csv", Table[{a, labOrientStage4[{3}]]} /. {β → 0.0, ξ → 1.0, α → a}, {a, -Pi/2, Pi/2, Pi/100.0}]]
```

```
labOrientBtot4.csv
```

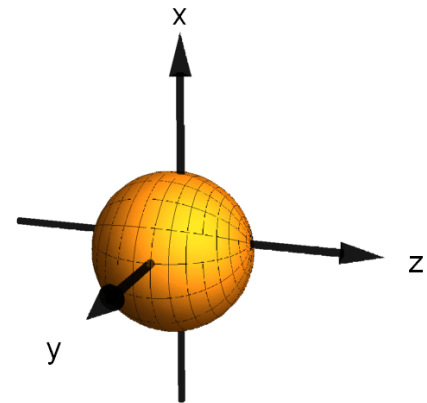
Just Orientation from z' Alignment

```
labPMszpStage4 = {baseIsotropic, ToContravariant@labOrientzpStage4};
Axes3D[AMPSPlot[labPMszpStage4 /. {ξ → 1, β → 0, α → 0.5}]]
```



Just Orientation from non-z' Alignment

```
labPMsNonzpStage4 = {baseIsotropic, ToContravariant@labOrientNonzpStage4};
Axes3D[AMPSPlot[labPMsNonzpStage4 /. {ξ → 1, β → 0.00001, α → 0.5}]]
```



Solving for peak widths

\$Assumptions = { (α | Bx | By | Bz) ∈ Reals, γ > 0, Bx > 0, Bz > 0};

labOrientStage4[{3}] /. {β → 0} // Simplify
Solve[% == 0, α, Reals]
% /. {C[1] → 0} // N

$$\frac{3 \sqrt[2]{3 + 20 \cos(2 \alpha)} + 9 \cos(4 \alpha)}{64 \sqrt{5}} \sin(\alpha)$$

$$\left\{ \left\{ \alpha \rightarrow \text{ConditionalExpression}\left[2 \pi C(1), C(1) \in \mathbb{Z}\right], \left\{ \alpha \rightarrow \text{ConditionalExpression}\left[\pi + 2 \pi C(1), C(1) \in \mathbb{Z}\right], \right. \right. \\ \left. \left\{ \alpha \rightarrow \text{ConditionalExpression}\left[\frac{1}{2} \left(-2 \operatorname{ArcTan}\left[\sqrt{-3 + \sqrt{13}}\right] + 2 \pi C(1)\right], C(1) \in \mathbb{Z}\right], \right. \right. \\ \left. \left. \left\{ \alpha \rightarrow \text{ConditionalExpression}\left[\frac{1}{2} \left(2 \operatorname{ArcTan}\left[\sqrt{-3 + \sqrt{13}}\right] + 2 \pi C(1)\right], C(1) \in \mathbb{Z}\right] \right\} \right\} \right\}$$

$$\left\{ \left\{ \alpha \rightarrow 0. \right\}, \left\{ \alpha \rightarrow 3.14159 \right\}, \left\{ \alpha \rightarrow -0.661289 \right\}, \left\{ \alpha \rightarrow 0.661289 \right\} \right\}$$

labOrientStage4[{3}] /. {β → 0, α → ArcTan[Bz/Bx], ξ → γ/Sqrt[Bz^2 + Bx^2]} // FullSimplify
Solve[% == 0, Bz, Reals] // FullSimplify // N

$$-\frac{3 Bz \left(-4 Bx^4 + 6 Bx^2 Bz^2 + Bz^4\right) \gamma}{8 \sqrt{5} \left(Bx^2 + Bz^2\right)^3 \operatorname{Sign}(Bx)}$$

$$\left\{ \left\{ Bz \rightarrow 0. \right\}, \left\{ Bz \rightarrow -0.778172 \operatorname{Abs}(Bx) \right\}, \left\{ Bz \rightarrow 0.778172 \operatorname{Abs}(Bx) \right\} \right\}$$

labOrientStage4[{3}] /. {β → 0, α → ArcTan[Bz/Bx], ξ → γ/Sqrt[Bz^2 + Bx^2]} // Simplify;
D[%, Bz] // FullSimplify
sol = Solve[% == 0, Bz, Reals] // FullSimplify
sol // ToRadicals // N // Chop

$$\frac{3 \left(4 Bx^6 - 38 Bx^4 Bz^2 + 13 Bx^2 Bz^4 + Bz^6\right) \gamma}{8 \sqrt{5} \left(Bx^2 + Bz^2\right)^4}$$

$$\left\{ \left\{ Bz \rightarrow -\sqrt{\operatorname{Root}\left[4 Bx^6 - 38 Bx^4 \operatorname{I}1 + 13 Bx^2 \operatorname{I}1^2 + \operatorname{I}1^3 \&, 2\right]}, \left\{ Bz \rightarrow \sqrt{\operatorname{Root}\left[4 Bx^6 - 38 Bx^4 \operatorname{I}1 + 13 Bx^2 \operatorname{I}1^2 + \operatorname{I}1^3 \&, 2\right]}, \right. \right. \\ \left. \left\{ Bz \rightarrow -\sqrt{\operatorname{Root}\left[4 Bx^6 - 38 Bx^4 \operatorname{I}1 + 13 Bx^2 \operatorname{I}1^2 + \operatorname{I}1^3 \&, 3\right]}, \left\{ Bz \rightarrow \sqrt{\operatorname{Root}\left[4 Bx^6 - 38 Bx^4 \operatorname{I}1 + 13 Bx^2 \operatorname{I}1^2 + \operatorname{I}1^3 \&, 3\right]} \right\} \right\}$$

$$\left\{ \left\{ Bz \rightarrow -3.93353 \sqrt{-Bx^2} \right\}, \left\{ Bz \rightarrow 3.93353 \sqrt{-Bx^2} \right\}, \left\{ Bz \rightarrow -0.330744 \sqrt{Bx^2} \right\}, \left\{ Bz \rightarrow 0.330744 \sqrt{Bx^2} \right\} \right\}$$

$$0.330744 * 2$$

$$0.661488$$

labOrientzpStage4[{3}] /. {β → 0} // Simplify
Solve[% == 0, α, Reals] /. C[1] → 0
% // N

$$\frac{3 \sqrt[2]{\cos(\alpha)^2 \left(1 + 3 \cos(2 \alpha)\right)} \sin(\alpha)}{8 \sqrt{5}}$$

$$\left\{ \left\{ \alpha \rightarrow 0 \right\}, \left\{ \alpha \rightarrow -\frac{\pi}{2} \right\}, \left\{ \alpha \rightarrow \frac{\pi}{2} \right\}, \left\{ \alpha \rightarrow \pi \right\}, \left\{ \alpha \rightarrow -\frac{1}{2} \operatorname{ArcCos}\left[-\frac{1}{3}\right] \right\}, \left\{ \alpha \rightarrow \frac{1}{2} \operatorname{ArcCos}\left[-\frac{1}{3}\right] \right\} \right\}$$

$$\left\{ \left\{ \alpha \rightarrow 0. \right\}, \left\{ \alpha \rightarrow -1.5708 \right\}, \left\{ \alpha \rightarrow 1.5708 \right\}, \left\{ \alpha \rightarrow 3.14159 \right\}, \left\{ \alpha \rightarrow -0.955317 \right\}, \left\{ \alpha \rightarrow 0.955317 \right\} \right\}$$

ArcCos[-1/3]/2 // N
ArcCos[1/Sqrt[3]] // N

$$0.955317$$

$$0.955317$$

labOrientzpsStage4[{3}] /. {β → 0, α → ArcTan[Bz/Bx], ξ → γ/Sqrt[Bz^2 + Bx^2]} // Simplify
Solve[% == 0, Bz, Reals] // N

$$\frac{3 Bx Bz \gamma \left(1 + 3 \cos\left[2 \operatorname{ArcTan}\left[\frac{Bz}{Bx}\right]\right]\right)}{8 \left(Bx^2 + Bz^2\right)^{3/2} \sqrt{5 + \frac{5 Bz^2}{Bx^2}}}$$

$$\left\{ \left\{ Bz \rightarrow 0. \right\}, \left\{ Bz \rightarrow -1.41421 Bx \right\}, \left\{ Bz \rightarrow 1.41421 Bx \right\} \right\}$$

labOrientzpsStage4[{3}] /. {β → 0, α → ArcTan[Bz/Bx], ξ → γ/Sqrt[Bz^2 + Bx^2]} // Simplify;
D[%, Bz] // FullSimplify
sol = Solve[% == 0, Bz, Reals] // Simplify[#, Assumptions → Bx ∈ Reals] &
% // N

$$\frac{3 Bx^2 \left(2 Bx^4 - 13 Bx^2 Bz^2 + 3 Bz^4\right) \gamma}{4 \sqrt{5} \left(Bx^2 + Bz^2\right)^4}$$

$$\left\{ \left\{ Bz \rightarrow -\sqrt{\frac{1}{6} \left(13 - \sqrt{145}\right)} \operatorname{Abs}(Bx) \right\}, \left\{ Bz \rightarrow \sqrt{\frac{1}{6} \left(13 - \sqrt{145}\right)} \operatorname{Abs}(Bx) \right\}, \left\{ Bz \rightarrow -\sqrt{\frac{1}{6} \left(13 + \sqrt{145}\right)} \operatorname{Abs}(Bx) \right\}, \left\{ Bz \rightarrow \sqrt{\frac{1}{6} \left(13 + \sqrt{145}\right)} \operatorname{Abs}(Bx) \right\} \right\}$$

$$\left\{ \left\{ Bz \rightarrow -0.399668 \operatorname{Abs}(Bx) \right\}, \left\{ Bz \rightarrow 0.399668 \operatorname{Abs}(Bx) \right\}, \left\{ Bz \rightarrow -2.04294 \operatorname{Abs}(Bx) \right\}, \left\{ Bz \rightarrow 2.04294 \operatorname{Abs}(Bx) \right\} \right\}$$

$$0.399668 * 2$$

$$0.799336$$

B.2 Alkali Rydberg Calculator

The code in this section relies on functionality provided by the Alkali-Rydberg-Calculator python package written by Nikola Šibalić, [66] and is available through `pip` as `ARC-Alkali-Rydberg-Calculator`. It is well documented and encapsulates many common computational tasks when modeling Rydberg atoms. In particular it can perform fast numerical integrations of wavefunction overlaps, which is the slowest part of many Rydberg atom calculations. It also has intelligent caching of results for later lookup which further improves subsequent computation times.

The following code was used to inform the discussions of Section 3.5 and to generate some of the general Rydberg properties plots for Section 3.1.1. It relies on ARC for calculation of various Rydberg properties as well as the standard `numpy`, `scipy` and `matplotlib` python packages.

3 Photon Sensitivity Estimate

September 14, 2018

```
In [116]: # import other libraries
import numpy as np
import matplotlib.pyplot as plt
from scipy.constants import c
from scipy.constants import Boltzmann as kB
from scipy.constants import e
from scipy.constants import h
from scipy.constants import epsilon_0 as e0
from scipy.constants import physical_constants
from scipy.special import erf
a0 = physical_constants['Bohr radius'][0]
relec = physical_constants['classical electron radius'][0]
eta = 1/e0/c
```

```
from arc import *
```

```
In [16]: %matplotlib inline
plt.style.reload_library()
plt.style.use(['base'])
```

```
In [42]: atom = Rubidium85(cpp_numerov=True)
mRb85 = 1.4099931997e-25
```

```
In [43]: angMomentum = {0:'S',1:'P',2:'D',3:'F'}
```

0.0.1 Transit Dephasing

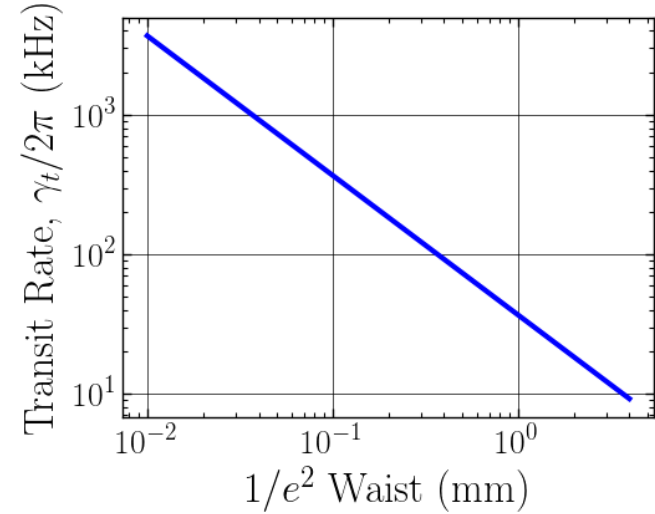
```
In [5]: w = 1000e-6 #1/e^2 waist
T = 273.15 + 24
vRMS = np.sqrt(2*kB*T/mRb85)
transitRate = 1.13*vRMS/(np.sqrt(2*np.log(2))*w)
print('Transit Rate is 2pi {:.2f} kHz'.format(transitRate/2/np.pi*1e-3))
print('Transit Lifetime is {:.2f} us'.format(1/transitRate*1e6))
```

Transit Rate is 2pi 36.85 kHz
Transit Lifetime is 4.32 us

```
In [37]: def TransRate(w,T=273.15+24):
vRMS = np.sqrt(2*kB*T/mRb85)
return 1.13*vRMS/(np.sqrt(2*np.log(2))*w)

waists = np.geomspace(10e-3,4,10)
transits = TransRate(waists*1e-3)*1e-3/2/np.pi

fig, ax = plt.subplots(1)
ax.loglog(waists,transits,'b-')
ax.set_xlabel(r'$1/e^2$ Waist (mm)')
ax.set_ylabel(r'$\gamma_t/2\pi$ (kHz)')
ax.grid(color='k',linestyle='-',linewidth=0.5)
plt.savefig('TransitRateVsWaist.pdf',format='pdf',dpi=600)
```



```
In [30]: print(TransRate(10e-6)*1e-3/2/np.pi)
print(TransRate(100e-6)*1e-3/2/np.pi)
print(TransRate(1e-3)*1e-3/2/np.pi)
```

3684.7393195722416
368.4739319572241
36.84739319572241

0.0.2 Rydberg state Lifetimes

```
In [47]: T = 273.15 + 24
nr = 48
lr = 1
jr = 1.5
```

```
In [48]: natLifetime = atom.getStateLifetime(nr,lr,jr,temperature=0.0)
withBBRLifetime = atom.getStateLifetime(nr,lr,jr,temperature=T,includeLevelsUpTo=nr+10)
print('Natural lifetime of {}_{}_{} is {:.2f} us'.format(nr,angMomentum[lr],jr,natLifetime*1e6))
print('Lifetime with BBR is {:.2f} us'.format(nr,angMomentum[lr],jr,withBBRLifetime*1e6))
```

Natural lifetime of 48P_1.5 is 253.95 us
Lifetime with BBR is 48.00 us

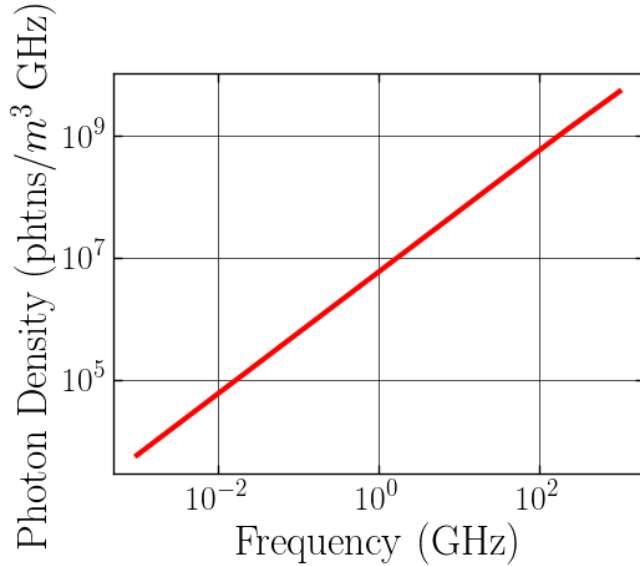

```
In [49]: natRate = 1/natLifetime
withBBRRate = 1/withBBRLifetime
BBRinducedRate = withBBRRate-natRate
print('Depopulation rates: Natural {:.3f} kHz, BBR induced {:.3f} kHz, Natural + BBR
{:.3f}
kHz'.format(natRate/2/np.pi*1e-3,BBRinducedRate/2/np.pi*1e-3,withBBRRate/2/np.pi*1e-3))
```

Depopulation rates: Natural 0.627 kHz, BBR induced 1.285 kHz, Natural + BBR 1.912 kHz

```
In [41]: # make a BBR plot
def BBRphotons(f,T=273.15+24):
    return 6*np.pi*f**2/c**3/(np.exp(h*f/kB/T)-1)

freqs = np.geomspace(1e-3,1e3,10)
specRad = BBRphotons(freqs*1e9)*1e9

fig, ax = plt.subplots(1)
ax.plot(freqs,specRad,'r-')
ax.grid(color='k',linestyle='-',linewidth=0.5)
ax.set_xlabel(r'Frequency (GHz)')
ax.set_ylabel(r'Photon Density (phtns/$m^3$ GHz)')
ax.set_xscale('log')
ax.set_yscale('log')
plt.savefig('BBPhotonDensity.pdf',format='pdf',dpi=600)
```



0.03 Atom Number

```
In [50]: # get the ground state atom number density
T = 273.15 + 24
dens=atom.getNumberDensity(T)
print('Number density at {:.1f} C is {:.2e} cm^(-3)'.format(T-273.15,dens*1e-6))
```

Number density at 24.0 C is 1.16e+10 cm⁻³

```
In [51]: # now scale down based on Doppler velocity class, ground state populations, and natural
abundance
abundance = 0.72172
gstate = 7.0/(7+5)
velocityClass2 = 3.0/515
velocityClass3 = 0.04/515
partDens2 = dens*abundance*gstate*velocityClass2
partDens3 = dens*abundance*gstate*velocityClass3
print('Scaling factor is {}'.format(abundance*gstate*velocityClass2))
print('Participating Ground state 2 Photon Number density at {:.1f} C is {:.2e}
cm^(-3)'.format(T-273.15,partDens2*1e-6))
print('Participating Ground state 3 Photon Number density at {:.1f} C is {:.2e}
cm^(-3)'.format(T-273.15,partDens3*1e-6))
```

Scaling factor is 0.002452446601941748

Participating Ground state 2 Photon Number density at 24.0 C is 2.85e+07 cm⁻³

Participating Ground state 3 Photon Number density at 24.0 C is 3.80e+05 cm⁻³

```
In [52]: # now scale by the EIT transparency window depth to get participating ground state atoms
in EIT
eit2 = 0.2
partDensEIT2 = partDens2*eit2
print('Participating EIT 2 Photon Number density at {:.1f} C is {:.2e}
cm^(-3)'.format(T-273.15,partDensEIT2*1e-6))
eit3 = 0.5
partDensEIT3 = partDens3*eit3
print('Participating EIT 3 Photon Number density at {:.1f} C is {:.2e}
cm^(-3)'.format(T-273.15,partDensEIT3*1e-6))
```

Participating EIT 2 Photon Number density at 24.0 C is 5.70e+06 cm⁻³

Participating EIT 3 Photon Number density at 24.0 C is 1.90e+05 cm⁻³

```
In [53]: # now estimate the sensing volume
v = 50e-6
L = 75e-3
Vol2Photon = np.pi*v**2*L
# for 3 photon geometry
theta = 33.4226*np.pi/180
r = 1e-3
Vol3Photon = 16/3*np.sin(theta)*r**3
print('Vol 2 Photon {} mm^3 \nVol 3 Photon {}
mm^3'.format(Vol2Photon*1e9,Vol3Photon*1e9))
```

Vol 2 Photon 0.5890486225480861 mm³

Vol 3 Photon 9.682709735730551 mm³

```
In [54]: # for later use, the cross sectional area to the MWs on the perpendicular axis is
Area2Photon = L*w*2
Area3Photon = 2/np.sin(theta/2)*r*2
print('Cross Section 2 Photon {} mm^2 \nCross Section 3 Photon {}
mm^2'.format(Area2Photon*1e6,Area3Photon*1e6))
```

Cross Section 2 Photon 7.5 mm²
 Cross Section 3 Photon 13910.65238833251 mm²

```
In [55]: # the resulting atom number participating in EIT is then
N2 = partDensEIT2*Vol2Photon
N3 = partDensEIT3*Vol3Photon
print('N2: {}, N3: {}, N3/N2: {}'.format(N2,N3,N3/N2))
```

N2: 3356.3688270396224, N3: 1839.0527750605224, N3/N2: 0.5479292860321909

Doppler Scaling of atom number

```
In [8]: T = 273.15+24
vRMS = np.sqrt(kB*T/mRb85)
print('1D rms velocity at {} C: {} m/s'.format(vRMS,T-273.15))
lprobe = 780.241e-9
lcouple = 480.125e-9
dopplLineWidth = 2 * np.sqrt(2*np.log(2)) * vRMS / lprobe
print('Full Doppler linewidth for probe is: {} MHz'.format(dopplLineWidth*1e-6))
print('Fraction of ground state atoms excitable to Rydberg is:
{}'.format(6.0666/dopplLineWidth*1e6))
```

1D rms velocity at 24.0 C: 170.577177552 m/s
 Full Doppler linewidth for probe is: 514.813444723 MHz
 Fraction of ground state atoms excitable to Rydberg is: 0.0117840745268

```
In [9]: # Now the doppler linewidth for the mismatched 2 Photon system
l2photon = -(1/lprobe-1/lcouple)**(-1)
print('Uncancelled wavelength: {} nm'.format(l2photon*1e9))
resDopplLineWidth = 2 * np.sqrt(2*np.log(2)) * vRMS / l2photon
print('Residual Doppler Linewidth for 2 photons scheme is: {}
MHz'.format(resDopplLineWidth*1e-6))
print('Fraction of ground state atoms excitable to Rydberg is:
{}'.format(6.0666/resDopplLineWidth*1e6))
```

Uncancelled wavelength: 1248.22805224 nm
 Residual Doppler Linewidth for 2 photons scheme is: 321.799014374 MHz
 Fraction of ground state atoms excitable to Rydberg is: 0.0188521397798

```
In [25]: # given limited Rabi frequency, only can detune coupling so far before EIT condition is
not satisfied
# this probably is not accurate
coupleRabi = 7e6
Gamma = 6.0666e6
vLimit = coupleRabi*lcouple*np.sqrt((coupleRabi**2/Gamma)**2-1)
print('Limiting velocity class for EIT condition: +/- {} m/s'.format(vLimit))
eitDopplLineWidth = 2 * vLimit / l2photon
print('Resulting Doppler Width is: {} MHz'.format(eitDopplLineWidth*1e-6))
```

Limiting velocity class for EIT condition: +/-6.98994200078 m/s
 Resulting Doppler Width is: 11.1997835464 MHz

```
In [ ]: # try using some numerical guesses
# FWHM of doppler broadened EIT is basically the AT splitting of the probing state due
to the coupling
# less the FWHM of the probing state
```

0.04 Transition Properties and Rabi Frequency Estimates

In [44]: # define the levels we want to work with

```
ng = 5
lg = 0
jg = 0.5
mjg = 0.5
ne = 5
le = 1
je = 0.5
mje = -0.5

nc = 6
lc = 0
jc = 0.5
mjc = 0.5

nr = 48
lr = 1
jr = 1.5
mjr = 0.5

nr2 = nr-1
lr2 = 2
jr2 = 2.5
mjr2 = 0.5

q = 0 # specify linearly polarized light
```

```
In [5]: proberadialME = atom.getRadialMatrixElement(ng,lg,jg,ne,le,je)
probedipoleME = atom.getDipoleMatrixElement(ng,lg,jg,mjg,ne,le,je,mje,q)
probeangularME = probedipoleME/proberadialME
probewavelength = atom.getTransitionWavelength(ng,lg,jg,ne,le,je)
probefrequency = atom.getTransitionFrequency(ng,lg,jg,ne,le,je)

print("Angular ME {0}, Radial ME: {1} ea_0, Total Dipole ME: {2}
ea_0".format(probeangularME,proberadialME,probedipoleME))
print("Transition Wavelength: {0} nm, Transition Frequency: {1}
THz".format(probewavelength*1e9,probefrequency/1e12))
```

Angular ME -0.0, Radial ME: -5.169648102143898 ea_0, Total Dipole ME: 0.0 ea_0
 Transition Wavelength: 794.9789232972437 nm, Transition Frequency: 377.1074291587316 THz

```
In [6]: coupleradialME = atom.getRadialMatrixElement(ne,le,je,nc,lc,jc)
coupledipoleME = atom.getDipoleMatrixElement(ne,le,je,mje,nc,lc,jc,mjc,q)
coupleangularME = coupledipoleME/coupleradialME
couplewavelength = atom.getTransitionWavelength(ne,le,je,nc,lc,jc)
couplefrequency = atom.getTransitionFrequency(ne,le,je,nc,lc,jc)
```

```
hfs = 717.541e6
ADM = 80e6
upperShiftRatio = 1.264888516325/3.035732439060
lowerShiftRatio = 1.770843922835/3.035732439060
shift = 210.92399e6+hfs*upperShiftRatio+ADM

print("Angular ME {0}, Radial ME: {1} ea_0, Total Dipole ME: {2}
ea_0".format(coupleangularME,coupleradialME,coupledipoleME))
print("Transition Wavelength: {0} nm, Transition Frequency: {1}
THz".format(couplewavelength*1e9,couplefrequency/1e12))
print("HFS adjusted Frequency: {0} THz".format((couplefrequency+shift)/1e12))
```

Angular ME -0.0, Radial ME: -5.044724125261956 ea_0, Total Dipole ME: 0.0 ea_0
 Transition Wavelength: 1323.8791763184124 nm, Transition Frequency: 226.45001399122808 THz

HFS adjusted Frequency: 226.45060389063474 THz

```
In [7]: rydradialME = atom.getRadialMatrixElement(nc,lc,jc,nr,lr,jr)
ryddipoleME = atom.getDipoleMatrixElement(nc,lc,jc,mjc,nr,lr,jr,mjr,q)
rydangularME = ryddipoleME/rydradialME
rydwavelength = atom.getTransitionWavelength(nc,lc,jc,nr,lr,jr)
rydfrequency = atom.getTransitionFrequency(nc,lc,jc,nr,lr,jr)

hfs = 717.541e6
AOM = 80e6
upperShiftRatio = 1.264888516325/3.035732439060
lowerShiftRatio = 1.770843922835/3.035732439060
shift = -hfs*upperShiftRatio
```

```
print("Angular ME {0}, Radial ME: {1} ea_0, Total Dipole ME: {2}
ea_0".format(rydangularME,rydradialME,ryddipoleME))
print("Transition Wavelength: {0} nm, Transition Frequency: {1}
THz".format(rydwavelength*1e9,rydfrequency/1e12))
print("HFS adjusted Frequency: wavelength {1} nm, {0}
THz".format((rydfrequency*shift)/1e12,c/(rydfrequency*shift)*1e9))
```

Angular ME 0.4714045207910316, Radial ME: 0.009618513370174676 ea_0, Total Dipole ME:
0.004534210685989324 ea_0
Transition Wavelength: 740.4692439165431 nm, Transition Frequency: 404.86821088518974
THz
HFS adjusted Frequency: wavelength 740.4697907173496 nm, 404.86791190977306 THz

```
In [45]: MWradiialME = atom.getRadialMatrixElement(nr,lr,jr,nr2,lr2,jr2)
MWdipoleME = atom.getDipoleMatrixElement(nr,lr,jr,mjr,nr2,lr2,jr2,mjr2,q)
MWangularME = MWdipoleME/MWradiialME
MWwavelength = atom.getTransitionWavelength(nr,lr,jr,nr2,lr2,jr2)
MWfrequency = atom.getTransitionFrequency(nr,lr,jr,nr2,lr2,jr2)

print("Angular ME {0}, Radial ME: {1} ea_0, Total Dipole ME: {2}
ea_0".format(MWangularME,MWradiialME,MWdipoleME))
print("Transition Wavelength: {0} cm, Transition Frequency: {1}
GHz".format(MWwavelength*1e2,MWfrequency/1e9))
```

Angular ME 0.48989794855663543, Radial ME: 2830.840802591352 ea_0, Total Dipole ME:
1386.8231018799227 ea_0
Transition Wavelength: 1.4522991610435063 cm, Transition Frequency: 20.642610423639784
GHz

```
In [44]: # Define the beam parameters
Pp = 30e-6 # in Watts
wp = 1000e-6 # 1/e**2 beam radius

Pc = 10e-3
wc = 3500e-6

Pr = 2000e-3
wr = 1000e-6

eField = 1e-6/1e-2 #V/m
```

```
In [46]: # get the Rabi frequency for probe and coupling transitions, in rad/s
probeRabiFreq = atom.getRabiFrequency(ng,lg,jg,mjg,ne,le,je,mje,Pp,wp)
print("Probe Rabi Frequency: {0:.3f} MHz".format(probeRabiFreq/2/np.pi/1e6))

coupleRabiFreq = atom.getRabiFrequency(ne,le,je,mje,nc,lc,jc,mjc,Pc,wc)
print("Coupling Rabi Frequency: {0:.3f} MHz".format(coupleRabiFreq/2/np.pi/1e6))
```

```
rydRabiFreq = atom.getRabiFrequency(nc,lc,jc,mjc,nr,lr,jr,mjr,Pr,wr)
print("Rydberg Laser Rabi Frequency: {0:.3f} MHz".format(rydRabiFreq/2/np.pi/1e6))

rfRabiFreq = atom.getRabiFrequency2(nr,lr,jr,mjr,nr2,lr2,jr2,q,eField)
print("RF Rabi Frequency for {:.2f} uV/cm Efield: {:.3f}
kHz".format(eField*1e4,rfRabiFreq/2/np.pi*1e-3))
```

Probe Rabi Frequency: 3.741 MHz
Coupling Rabi Frequency: 13.464 MHz
Rydberg Laser Rabi Frequency: 1.797 MHz
RF Rabi Frequency for 1.00 uV/cm Efield: 1.775 kHz

0.1 2 Photon Sensitivity

Use estimates from above to get the low and high bandwidth sensitivity estimates for the Rydberg electrometer.

Compare with a classical ideal dipole antenna and something the size of the Rydberg system

```
In [ ]: # define parameters for two photon system
n2 = 50
l2 = 2
j2 = 2.5
mj2 = 0.5
q = 0
T=273.15+24
```

```
In [88]: # get Rydberg state parameters
mu = atom.getDipoleMatrixElement(n2,l2,j2,mj2,n2+1,l2-1,j2-1,mj2,0)
BBRRate = 1/atom.getStateLifetime(n2,l2,j2,temperature=T,includeLevelsUpTo=n2+10)
wavelength = -atom.getTransitionWavelength(n2,l2,j2,n2+1,l2-1,j2-1)
print('Dipole matrix element between {}-{} and {}-{} is {}
ea_0'.format(n2,angMomentum[l2],j2,n2+1,angMomentum[l2-1],j2-1,mu))
print('Resonant RF wavelength {:.2f} cm'.format(wavelength*1e2))
print('Rydberg Lifetime {:.2f} kHz'.format(BBRRate*1e-3))
```

Dipole matrix element between 50D2.5 and 51P1.5 is 1574.8539565193548 ea_0
Resonant RF wavelength 1.76 cm
Rydberg Lifetime 14.40 kHz

We can check our rough estimate by accounting for our known losses and inefficiencies.

```
In [123]: window = 0.96**2
dichroic = 0.99
responsivity = 0.425
BS = 0.5**2
fiberCouple = 0.6
buttCouple = 0.5
# likely more losses in fiber system as well
Q = window*dichroic*responsivity*BS*fiberCouple*buttCouple
print(Q)
OD = 1
EITcontrast = 0.2
contrast = (1-np.exp(-OD))*EITcontrast/np.exp(-OD)
overlap = erf(np.sqrt(2)*(50.0/100))
q = contrast*overlap
print(q)
print('Total quantum efficiency is: {:.2} %'.format(q*Q*100))
```

0.029082239999999995
0.23461058976381774
Total quantum efficiency is: 0.68 %

```
In [80]: QE = 0.005
         N = QE*N2
         print('Estimated total Rydberg atoms number in sensing volume is: {:.1f}'.format(N2))
         print('Estimated effective atom number is: {:.1f}'.format(N))
```

Estimated total Rydberg atoms number in sensing volume is: 3356.4
Estimated effective atom number is: 16.8

```
In [91]: w0 = 50e-6
         T2 = 1/(TransRate(w0) + 1/BRRRate)
         print('Estimated Rydberg state lifetime: {:.2f} us, 2pi {:.2f} kHz'.format(T2*1e6, (TransRate(w0)+withBRRRate)/2/np.pi*1e-3))
```

Estimated Rydberg state lifetime: 0.22 us, 2pi 738.86 kHz

```
In [92]: sens = h/(mu*e*a0*np.sqrt(N*T2))
         print('Estimated sensitivity is {:.2f} nV/cm*Hz1/2'.format(sens*1e7))
         sensHighBW = h/(mu*e*a0*np.sqrt(N))
         print('Estimated sensitivity is {:.2f} nV/cm*Hz'.format(sensHighBW*1e7))
```

Estimated sensitivity is 260.67 nV/cm*Hz^{1/2}
Estimated sensitivity is 0.12 nV/cm*Hz

Low BW Power sensitivity (1 Hz BW)

```
In [93]: BW = 1 #hertz
         Elim = sens*np.sqrt(BW)
         Inten = 1.0/2*(1.0/377)*Elim**2
         Pow = Inten*Area2Photon
         dBm = 10*np.log10(Pow/0.001)
         print('Efield in {0:.0f} Hz BW: {1:.2e} V/m,\nMW intensity: {2:.2e} W/m2,\nMW Power over sensing volume: {3:.2e} W,\nMW power sensitivity in {0:.0f} Hz BW: {4:.1f} dBm'.format(BW, Elim, Inten, Pow, dBm))
```

Efield in 1 Hz BW: 2.61e-05 V/m,
MW intensity: 9.01e-13 W/m²,
MW Power over sensing volume: 6.76e-18 W,
MW power sensitivity in 1 Hz BW: -141.7 dBm

High BW Power sensitivity (10 MHz BW)

```
In [94]: BW = 10e6
         Elim = sensHighBW*BW
         Inten = 1.0/2*(1.0/377)*Elim**2
         Pow = Inten*Area2Photon
         dBm = 10*np.log10(Pow/0.001)
         print('Efield in {0:.0f} Hz BW: {1:.2e} V/m,\nMW intensity: {2:.2e} W/m2,\nMW Power over sensing volume: {3:.2e} W,\nMW power sensitivity in {0:.0f} Hz BW: {4:.1f} dBm'.format(BW, Elim, Inten, Pow, dBm))
```

Efield in 10000000 Hz BW: 1.21e-01 V/m,
MW intensity: 1.95e-05 W/m²,
MW Power over sensing volume: 1.46e-10 W,
MW power sensitivity in 10000000 Hz BW: -68.4 dBm

Compare with classical antennas: 1) an ideal dipole 2) antenna with effective area size of Rydberg sensing cross section

```
In [98]: noisePow = kB*298
         idealDipole = 3.0/8/np.pi*wavelength**2
         noiseEfield = np.sqrt(noisePow*2*eta/idealDipole)
         print('Noise floor for 298 K noise temperature {:.2f} nV/cm Hz1/2'.format(noiseEfield*1e7))
         print('Estimated Reciever internal noise floor/external noise floor: {:.2f}'.format(sens/noiseEfield))
```

Noise floor for 298 K noise temperature 2.90 nV/cm Hz^{1/2}
Estimated Reciever internal noise floor/external noise floor: 89.98

```
In [97]: noisePow = kB*298
         idealDipole = 3.0/8/np.pi*wavelength**2
         noiseEfield = np.sqrt(noisePow*2*eta/Area2Photon)
         print('Noise floor for 298 K noise temperature {:.2f} nV/cm Hz1/2'.format(noiseEfield*1e7))
         print('Estimated Reciever internal noise floor/external noise floor: {:.2f}'.format(sens/noiseEfield))
```

Noise floor for 298 K noise temperature 6.43 nV/cm Hz^{1/2}
Estimated Reciever internal noise floor/external noise floor: 40.55

0.2 Our expected 3 Photon Sensitivity

From some of the above, we can expect a few things from this.

First: is that we are almost certainly going to be transit limited still, so big beams are going to be critical.

Second: the atom number we use will only be comparable (potentially slightly less) without doppler averaging. Big beams are critical here to keep the sensing volume up. Also critical is QE of detection, which FM spectroscopy and not being stupid should help considerably.

```
In [101]: mu = MWdipoleME
          print('Dipole matrix element between {} and {} is {}
          ea_0'.format(nr,angMomentum[1r],jr,nr2,angMomentum[1r2],jr2,mu))
```

Dipole matrix element between 48P1.5 and 47D2.5 is 1386.8231018799227 ea_0

Previous works we observe a Quantum Efficiency of 0.5% using heterodyne and with known inefficiencies (extra beam splitters etc). A 1% efficiency is a very conservative estimate.

```
In [102]: QE = 0.01
          N = QE*N3
          print('Estimated total Rydberg atoms number in sensing volume is: {:.1f}'.format(N3))
          print('Estimated effective atom number is: {:.1f}'.format(N))
```

Estimated total Rydberg atoms number in sensing volume is: 1839.1
Estimated effective atom number is: 18.4

Rydberg lifetime will still be transit limited

```
In [103]: T2 = 1/(transitRate + 1/withBRRRate)
          print('Estimated Rydberg state lifetime: {:.2f} us, 2pi {:.2f} kHz'.format(T2*1e6, (transitRate+withBRRRate)/2/np.pi*1e-3))
```

Estimated Rydberg state lifetime: 4.32 us, 2pi 38.76 kHz

```
In [104]: sens = h/(mu*e*a0*np.sqrt(N*T2))
print('Estimated sensitivity is {:.2f} nV/cm*Hz1/2'.format(sens*1e7))
sensHighBW = h/(mu*e*a0*np.sqrt(N))
print('Estimated sensitivity is {:.2f} nV/cm*Hz'.format(sensHighBW*1e7))
```


Estimated sensitivity is 63.23 nV/cm*Hz^{1/2}
Estimated sensitivity is 0.13 nV/cm*Hz

Convert this expected sensitivity to dBm

Assume MW field is a plane wave (i.e. we are in far field)

```
In [114]: BW = 1 #hertz
Elim = sens*np.sqrt(BW)
Inten = 1.0/2*(1.0/377)*Elim**2
Pow = Inten*Area3Photon
dBm = 10*np.log10(Pow/0.001)
print('Efield in {0:.0f} Hz BW: {1:.2e} V/m,\nMW intensity: {2:.2e} W/m2,\nMW Power
over sensing volume: {3:.2e} W,\nMW power sensitivity in {0:.0f} Hz BW: {4:.1f}
dBm'.format(
    BW,Elim,Inten,Pow,dBm))
```

Efield in 1 Hz BW: 6.32e-06 V/m,
MW intensity: 5.30e-14 W/m²,
MW Power over sensing volume: 7.38e-16 W,
MW power sensitivity in 1 Hz BW: -121.3 dBm

 Sensitivity assuming a semi-reasonable BW of 10 MHz

```
In [106]: BW = 10e6
Elim = sensHighBW*BW
Inten = 1.0/2*(1.0/377)*Elim**2
Pow = Inten*Area3Photon
dBm = 10*np.log10(Pow/0.001)
print('Efield in {0:.0f} Hz BW: {1:.2e} V/m,\nMW intensity: {2:.2e} W/m2,\nMW Power
over sensing volume: {3:.2e} W,\nMW power sensitivity in {0:.0f} Hz BW: {4:.1f}
dBm'.format(
    BW,Elim,Inten,Pow,dBm))
```

Efield in 10000000 Hz BW: 1.31e-01 V/m,
MW intensity: 2.29e-05 W/m²,
MW Power over sensing volume: 3.19e-07 W,
MW power sensitivity in 10000000 Hz BW: -35.0 dBm

Compare our sensitivity with the noise temperature of 298 K (ie the room temp. ground)

To convert from antenna powers to Rydberg E-fields, need an area. Let's use the maximum effective aperture of an ideal dipole.

```
In [109]: noisePow = kB*298
idealDipole = 3.0/8*np.pi*MWwavelength**2
noiseEfield = np.sqrt(noisePow*2*eta/idealDipole)
print('Noise floor for 298 K noise temperature {:.2f} nV/cm
Hz1/2'.format(noiseEfield*1e7))
print('Estimated Reciever internal noise floor/external antenna noise floor:
{:.2f}'.format(sens/noiseEfield))
```

Noise floor for 298 K noise temperature 3.51 nV/cm Hz^{1/2}

Estimated Reciever internal noise floor/external antenna noise floor: 18.02

Now the using the sensing volume of the Rydberg Electrometer

```
In [108]: noisePow = kB*298
noiseEfield = np.sqrt(noisePow*2*eta/Area3Photon)
print('Noise floor for 298 K noise temperature {:.2f} nV/cm
Hz1/2'.format(noiseEfield*1e7))
print('Estimated Reciever internal noise floor/external antenna noise floor:
{:.2f}'.format(sens/noiseEfield))
```

Noise floor for 298 K noise temperature 0.15 nV/cm Hz^{1/2}

Estimated Reciever internal noise floor/external antenna noise floor: 423.56

0.3 Compare Expected Sensivity with Single Photon Field

```
In [94]: # this assumes a photon focused to the diffraction limit, which is a bit unreasonable
Ephoton = np.sqrt((h*MWfrequency)/(4/3*np.pi*MWwavelength**3*e0))
print('Electric field of a single photon: {} mV/m'.format(Ephoton*1e3))
```

Electric field of a single photon: 0.4006608317 mV/m

B.3 Rydberg EIT with *Mathematica*

The following code snippet was used to generate the plots in Figure 3.4. Its implementation is based on code from [112] and follows the Lindblad/Density Matrix approach for a simplified three-level system. *Mathematica* 11.2 was used to perform the calculations. Using the built-in parallel functionality with a dual core laptop, data for each set of parameters required a couple minutes of run time.

```
SetDirectory[NotebookDirectory[]]
```

```
C:\Users\David\Google Drive\3Photon\Calcs
```

```
SetOptions[Plot, AspectRatio -> 0.77, BaseStyle -> Large, Frame -> True, FrameStyle -> Directive[Thick, Black, FontSize -> 36, FontFamily -> "Arial"], PlotRan
SetOptions[ListPlot, AspectRatio -> 0.77, BaseStyle -> Large, Frame -> True, FrameStyle -> Directive[Thick, Black, FontSize -> 36, FontFamily -> "Arial"], Plo
SetOptions[ListLinePlot, AspectRatio -> 0.77, BaseStyle -> Large, Frame -> True, Axes -> False, FrameStyle -> Directive[Thick, Black, FontSize -> 36, FontFam
SetOptions[ListContourPlot, AspectRatio -> 0.77, BaseStyle -> Large, Frame -> True, Axes -> False, FrameStyle -> Directive[Thick, Black, FontSize -> 36, FontF
PlotLegends -> Placed[BarLegend[Automatic, None, "Ticks" -> {0, 0.05, 0.1}, LegendLabel -> None, LabelStyle -> Directive[Thick, Black, FontSize -> 36, For
```

Follows basic construction from code in Arne Schwettmann's University of Oklahoma Thesis

Total number of levels

$n = 3$;

The Hamiltonian, Rabi Frequency is $\mu E_0/\hbar$

$$H = \hbar/2 \begin{pmatrix} 0 & \Delta\rho & 0 \\ \Delta\rho & -2\Delta\rho & \Delta C \\ 0 & \Delta C & -2(\Delta\rho + \Delta C) \end{pmatrix};$$

Define density matrix $\rho\rho$ in terms of $p[i,j]$

```
MatrixForm[ $\rho\rho = \text{Table}[p[i, j], \{i, 1, n\}, \{j, 1, n\}]$ ]
```

$$\begin{pmatrix} \rho[1, 1] & \rho[1, 2] & \rho[1, 3] \\ \rho[2, 1] & \rho[2, 2] & \rho[2, 3] \\ \rho[3, 1] & \rho[3, 2] & \rho[3, 3] \end{pmatrix}$$

Unit vectors for constructing projection matrices

```
e[i_] = Table[{KroneckerDelta[i, j]}, {j, 1, n}];
```

Define the projectors

```
 $\sigma[i_, j_] = e[i].\text{Transpose}[e[j]]$ ;  
 $\sigma[2, 2] // \text{MatrixForm}$ 
```

$$\begin{pmatrix} 0 & 0 & 0 \\ 0 & 1 & 0 \\ 0 & 0 & 0 \end{pmatrix}$$

Construct decay operators

```
Clear[r, L]
```

```
r[i_, j_] = \gamma[i];  
MatrixForm[r[3, 2] + \Gamma[2, 1] + \Gamma[3, 1]]  
L[i_, j_] = \Gamma[i, j]/2 + (2 * \sigma[j, i] . \rho\rho . \sigma[i, j] - \sigma[i, i] . \rho\rho - \rho\rho . \sigma[i, i]);  
MatrixForm[L[3, 2] + L[2, 1] + L[3, 1]]
```

```
\Gamma[2, 1] + \Gamma[3, 1] + \Gamma[3, 2]
```

$$\begin{pmatrix} \Gamma[2, 1] \rho[2, 2] + \Gamma[3, 1] \rho[3, 3] & -\frac{1}{2} \Gamma[2, 1] \rho[1, 2] & -\frac{1}{2} \Gamma[3, 1] \rho[1, 3] & -\frac{1}{2} \Gamma[3, 2] \rho[1, 3] \\ -\frac{1}{2} \Gamma[2, 1] \rho[2, 1] & -\Gamma[2, 1] \rho[2, 2] + \Gamma[3, 2] \rho[3, 3] & -\frac{1}{2} \Gamma[2, 1] \rho[2, 3] - \frac{1}{2} \Gamma[3, 1] \rho[2, 3] - \frac{1}{2} \Gamma[3, 2] \rho[2, 3] \\ -\frac{1}{2} \Gamma[3, 1] \rho[3, 1] - \frac{1}{2} \Gamma[3, 2] \rho[3, 1] & -\frac{1}{2} \Gamma[2, 1] \rho[3, 2] - \frac{1}{2} \Gamma[3, 1] \rho[3, 2] - \frac{1}{2} \Gamma[3, 2] \rho[3, 2] & -\Gamma[3, 1] \rho[3, 3] - \Gamma[3, 2] \rho[3, 3] \end{pmatrix}$$

Define the OBEs

```
dephasings = {\gamma -> 2 Pi 0.120, \Gammap -> 2 Pi 6.0666, \Gammaryd -> 2 Pi 0.001};  
simpledephasings = {\Gamma[2, 1] -> \Gammap + \gamma,  
 \Gamma[3, 2] -> \Gammaryd, \Gamma[3, 1] -> \gamma};  
pdot = -1/\hbar * (H . \rho\rho - \rho\rho . H) + L[3, 2] + L[2, 1] + L[3, 1] // Simplify;
```

```
Thread[0 = Flatten[pdot]];  
TableForm[eqs = Append[%, 1 = Plus @@ Table[\rho[i, i], {i, 1, n}]]]  
solVars = Flatten[\rho\rho]
```

$$\begin{aligned} 0 &= -i \Delta\rho[\rho[1, 2] - \rho[2, 1]] + \Gamma[2, 1] \rho[2, 2] + \Gamma[3, 1] \rho[3, 3] \\ 0 &= -i (-2\Delta\rho[1, 2] + i \Gamma[2, 1] \rho[1, 2] + \Delta C \rho[1, 3] + \Delta\rho[\rho[1, 1] - \rho[2, 2]]) \\ 0 &= -i (\Delta C \rho[1, 2] - 2\Delta C \rho[1, 3] - 2\Delta\rho[1, 3] + i \Gamma[3, 1] \rho[1, 3] + i \Gamma[3, 2] \rho[1, 3] - \Delta\rho[2, 3]) \\ 0 &= -i (2\Delta\rho[2, 1] + i \Gamma[2, 1] \rho[2, 1] + \Delta\rho[-\rho[3, 1] + \rho[2, 2]]) - \Delta C \rho[3, 1] \\ 0 &= -i (\Delta\rho[-\rho[1, 2] + \rho[2, 1]] + 2i \Gamma[2, 1] \rho[2, 2] + \Delta C \rho[2, 3] - \Delta C \rho[3, 2] - 2i \Gamma[3, 2] \rho[3, 3]) \\ 0 &= -i (\Delta\rho[1, 3] + (2\Delta C - i (\Gamma[2, 1] + \Gamma[3, 1] + \Gamma[3, 2])) \rho[2, 3] + \Delta C (-\rho[2, 2] + \rho[3, 3])) \\ 0 &= -i (-\Delta C \rho[2, 1] + 2\Delta C \rho[3, 1] + 2\Delta\rho[3, 1] + i \Gamma[3, 1] \rho[3, 1] + i \Gamma[3, 2] \rho[3, 1] + \Delta\rho[3, 2]) \\ 0 &= -i (\Delta\rho[3, 1] + (2\Delta C + i (\Gamma[2, 1] + \Gamma[3, 1] + \Gamma[3, 2])) \rho[3, 2] + \Delta C (-\rho[2, 2] + \rho[3, 3])) \\ 0 &= -i \Delta C (\rho[2, 3] - \rho[3, 2]) - (\Gamma[3, 1] + \Gamma[3, 2]) \rho[3, 3] \\ 1 &= p[1, 1] + p[2, 2] + p[3, 3] \end{aligned}$$

$\{\rho[1, 1], \rho[1, 2], \rho[1, 3], \rho[2, 1], \rho[2, 2], \rho[2, 3], \rho[3, 1], \rho[3, 2], \rho[3, 3]\}$

```
Clear[nEqs, fullNSolve];  
nEqs[ $\Delta\rho_-, \Delta C_-, \Delta\rho_-, \Delta C_-, \gamma_-, \Gammaryd_-, \Gammap_-]$  = eqs /. simpledephasings  
fullNSolve[ $\Delta\rho_-, \Delta C_-, \Delta\rho_-, \Delta C_-, \gamma_-, \Gammaryd_-$ : 2 Pi 0.002,  $\Gammap_-$ : 2 Pi 6.0666] := Block[{sol},  
 sol = Solve[nEqs[ $\Delta\rho_-, \Delta C_-, \Delta\rho_-, \Delta C_-, \gamma_-, \Gammaryd_-, \Gammap_-$ ], solVars][[1]];  
 Im[\rho[2, 1]] /. sol  

```

$$\begin{aligned} 0 &= -i \Delta\rho[\rho[1, 2] - \rho[2, 1]] + (\gamma + \Gammap) \rho[2, 2] + \gamma \rho[3, 3], \\ 0 &= -i (i (\gamma + \Gammap) \rho[1, 2] - 2\Delta\rho[1, 2] + \Delta C \rho[1, 3] + \Delta\rho[\rho[1, 1] - \rho[2, 2]]), \\ 0 &= -i (\Delta C \rho[1, 2] + i \gamma \rho[1, 3] + i \Gammaryd \rho[1, 3] - 2\Delta C \rho[1, 3] - 2\Delta\rho[1, 3] - \Delta\rho[2, 3]), \\ 0 &= -i (i (\gamma + \Gammap) \rho[2, 1] + 2\Delta\rho[2, 1] + \Delta\rho[-\rho[1, 1] + \rho[2, 2]]) - \Delta C \rho[3, 1], \\ 0 &= -i (\Delta\rho[-\rho[1, 2] + \rho[2, 1]] + 2i (\gamma + \Gammap) \rho[2, 2] + \Delta C \rho[2, 3] - \Delta C \rho[3, 2] - 2i \Gammaryd \rho[3, 3]), \\ 0 &= -i (\Delta\rho[1, 3] + (-i (2\gamma + \Gammap + \Gammaryd) + 2\Delta C) \rho[2, 3] + \Delta C (-\rho[2, 2] + \rho[3, 3])), \\ 0 &= -i (-\Delta C \rho[2, 1] + i \gamma \rho[3, 1] + i \Gammaryd \rho[3, 1] + 2\Delta C \rho[3, 1] + 2\Delta\rho[3, 1] + \Delta\rho[3, 2]), \\ 0 &= -i (\Delta\rho[3, 1] + (i (2\gamma + \Gammap + \Gammaryd) + 2\Delta C) \rho[3, 2] + \Delta C (-\rho[2, 2] + \rho[3, 3])), \\ 0 &= -i \Delta C (\rho[2, 3] - \rho[3, 2]) - (\gamma + \Gammaryd) \rho[3, 3], 1 = \rho[1, 1] + \rho[2, 2] + \rho[3, 3] \end{aligned}$$

fullNSolve[0.1, 0, 1, 5, 2 Pi 0.120]

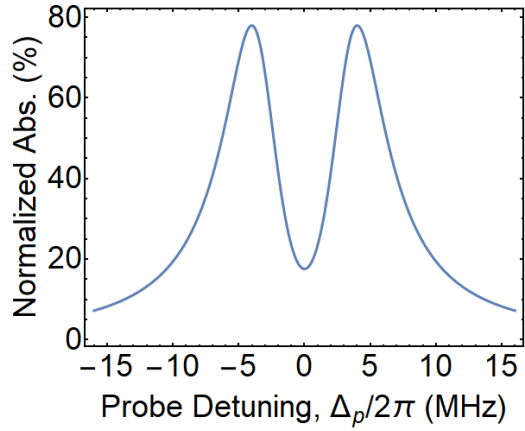
-0.0142154

```
zeroNorm = Block[{ $\Delta\rho = 2 \text{ Pi } 3.0, \Delta C = 2 \text{ Pi } 7.5, \Delta C = 0, \gamma = 2 \text{ Pi } 1.18$ },  
 fullNSolve[0,  $\Delta C, \Delta\rho, 0, \gamma$ ]]
```

-0.308308

Test solve without any Doppler effects.

```
zero = Block[{ $\Delta\rho = 2 \text{ Pi } 3.0, \Delta C = 2 \text{ Pi } 7.5, \Delta C = 0, \gamma = 2 \text{ Pi } 1.18$ , range = 16, step = 0.05, norm},  
 norm = fullNSolve[0,  $\Delta C, \Delta\rho, 0, \gamma$ ];  
 ParallelTable[{ $\Delta\rho, \text{fullNSolve}[2 \text{ Pi } \Delta\rho, \Delta C, \Delta\rho, \Delta C, \gamma] * 100 / \text{norm}$ }, { $\Delta\rho, \text{range-range, range, step}$ }}];  
ListLinePlot[zero, PlotRange -> Full, FrameLabel -> {"Probe Detuning,  $\Delta\rho/2\pi$  (MHz)", "Normalized Abs. (%)"}, PlotRange -> {0, 100}]
```



Define parameters necessary for doing Doppler averaging.

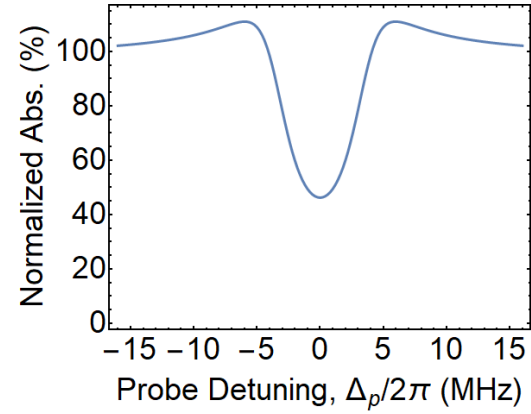
```
m = 1.40999319970*^-25 ; (*kg*)
kB = 1.380650424*^-23; (*J/K*)
T = 273.15 + 24; (*K*)
kp = 2 Pi / (780.241*^-3); (*1/μm*)
kc = 2 Pi / (480.125*^-3); (*1/μm*)
```

```
dopScale = Sqrt[m / (2 Pi kB T)];
expScale = m / (2 kB T);
```

Test solve with Doppler averaging.

```
testData = Block[{vMax = 50, vStep = 0.2, ΔpMax = 2 Pi 16.0, ΔpStep = 2 Pi 0.2,
  Δp = 2 Pi 3.0, Δc = 2 Pi 7.5, γ = 2 Pi 1.18, norm},
  norm = 1/100 * ParallelSum[dopScale * vStep * Exp[-expScale v^2] * fullNSolve[0 + kp * v, kc * v, Δp, 0, γ], {v, -vMax, vMax, vStep}];
  ParallelTable[
    {Δp / 2 / Pi, dopScale / norm * vStep * Sum[Exp[-expScale v^2] * fullNSolve[Δp + kp * v, -kc * v, Δp, Δc, γ], {v, -vMax, vMax, vStep}]}
    , {Δp, -ΔpMax, ΔpMax, ΔpStep}]];
```

```
averagedPlot = ListLinePlot[testData, PlotRange -> Full, FrameLabel -> {"Probe Detuning, Δp/2π (MHz)", "Normalized Abs. (%)"}]
```



Test solves for normalized absorption versus velocity class and probe detuning. The above averaged trace is essentially the sum of vertical columns in this plot.

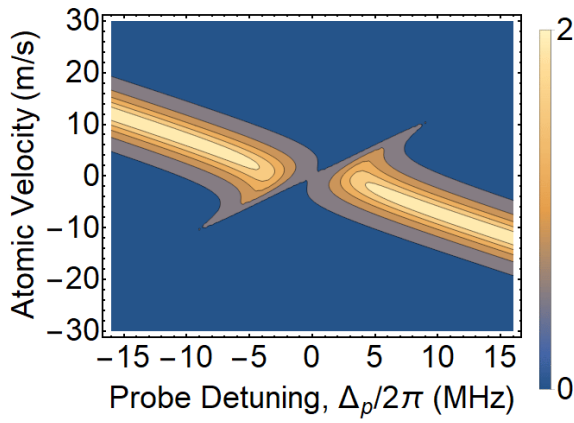
```
pvData = Block[{vMax = 50, vStep = 0.5, ΔpMax = 2 Pi 16.0, ΔpStep = 2 Pi 0.25,
  Δp = 2 Pi 3.0, Δc = 2 Pi 7.5, Δc = 0, γ = 2 Pi 1.18, norm},
  norm = 100 / ParallelSum[dopScale * vStep * Exp[-expScale v^2] * fullNSolve[kp * v, kc * v, Δp, 0, γ], {v, -vMax, vMax, vStep}];
  Print[norm];
  ParallelTable[{Δp / 2 / Pi, v, norm * dopScale * vStep * Exp[-expScale v^2] * fullNSolve[Δp + kp * v, Δc - kc * v, Δp, Δc, γ]},
    {v, -vMax, vMax, vStep}, {Δp, -ΔpMax, ΔpMax, ΔpStep}]];
```

```
-14.0817
```

```
pvData = Block[{vMax = 30, vStep = 0.1, ΔpMax = 2 Pi 16.0, ΔpStep = 2 Pi 0.5,
  Δp = 2 Pi 3.0, Δc = 2 Pi 7.5, Δc = 0, γ = 2 Pi 1.18, norm},
  norm = 100 / ParallelSum[vStep * Exp[-expScale v^2] * fullNSolve[kp * v, 0, Δp, 0, γ], {v, -vMax, vMax, vStep}];
  Print[norm];
  ParallelTable[{Δp / 2 / Pi, v, norm * vStep * Exp[-expScale v^2] * fullNSolve[Δp + kp * v, Δc - kc * v, Δp, Δc, γ]},
    {v, -vMax, vMax, vStep}, {Δp, -ΔpMax, ΔpMax, ΔpStep}]];
```

```
-33.8893
```

```
max = Ceiling[Max[pvData][[All, All, 3]]];
contourPlot = ListContourPlot[Flatten[pvData, 1], FrameLabel -> {"Probe Detuning, Δp/2π (MHz)", "Atomic Velocity (m/s)"}, Contours -> 10, PlotRange ->
  PlotLegends -> Placed[BarLegend[{Automatic, {0, max}}, None, "Ticks" -> {0, max}], LegendLabel -> None, LabelStyle -> Directive[Thick, Black, FontSize ->
```

Export["Averaged-3MHz-7.5MHz-1.18MHz.pdf", averagedPlot]
Export["Contour-3MHz-7.5MHz-1.18MHz.pdf", contourPlot]

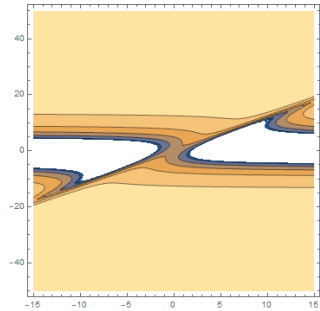
Averaged-3MHz-7.5MHz-1.18MHz.pdf

Contour-3MHz-7.5MHz-1.18MHz.pdf

An example of the same absorption versus velocity class and coupling detuning. Note that a fixed probe frequency effectively rotates the avoided crossing and helps isolate some of the Doppler averaging effects experimentally.

```
cvData = With[{vMax = 50, vStep = 0.5, ΔpMax = 2 Pi 15.0, ΔpStep = 2 Pi 0.5,
  Δp = 2 Pi 3.0, Δc = 2 Pi 7.5, Δp = 2 Pi 0.0, γ = 2 Pi 1.18},
  ParallelTable[{Δc / 2 / Pi, v, dopScale * vStep * Exp[-expScale v^2] * fullNSolve[Δp + kp * v, Δc - kc * v, Δp, Δc, γ],
    {v, -vMax, vMax, vStep}}, {Δc, -ΔpMax, ΔpMax, ΔpStep}]];
```

ListContourPlot[Flatten[cvData, 1]]



This code wraps together all of the above into a single solve to same on computation time.

```
Clear[genDataP, showPlotsP, genDataC, showPlotsC];
genDataP[Op_, Oc_, g_] := Block[{vMax = 30, vStep = 0.25, ΔpMax = 2 Pi 16.0, ΔpStep = 2 Pi 0.25,
  Δp = 2 Pi Op, Δc = 2 Pi Oc, Δc = 0, γ = 2 Pi g,
  norm, normFree, detunings, freeData, data, flat, aveData, zeroData},
  detunings = Range[-ΔpMax, ΔpMax, ΔpStep] / 2 / Pi;
  norm = 1 / 100 * ParallelSum[dopScale * vStep * Exp[-expScale v^2] * fullNSolve[kp * v, Δc - kc * v, Op, 0, γ], {v, -vMax, vMax, vStep}];
  normFree = 1 / 100 * fullNSolve[0, Δc, Op, 0, γ];
  freeData = ParallelTable[{Δp / 2 / Pi, v, dopScale / norm * Exp[-expScale v^2] * fullNSolve[Δp + kp * v, Δc - kc * v, Op, Δc, γ]}, {v, -vMax, vMax, vStep}, {Δp,
  flat = Flatten[data, 1];
  aveData = Transpose[{detunings, Total[data] / {All, 3}] * vStep}];
  zeroData = Transpose[{detunings, Select[flat, Chop[Re[[2]]] == 0 &] / {All, 3}] * 5}];
  {freeData, flat, aveData, zeroData}
];
showPlotsP[list_] := Block[{data, aveData, zeroData},
  Print[ListLinePlot[list[[1]], PlotRange -> Full, FrameLabel -> {"Probe Detuning, Δp/2π (MHz)", "Normalized Abs. (%)", PlotRange -> {0, 100}}];
  Print[ListContourPlot[list[[2]], FrameLabel -> {"Probe Detuning (MHz)", "Velocity Class (m/s)", PlotRange -> Full}];
  Print[ListLinePlot[list[[3 ;; 4]], FrameLabel -> {"Probe Detuning (MHz)", "Absorption (%)", PlotLegends -> {"Doppler Averaged Absorption", "Zero V
  }
];
genPlotsP[list_] := Block[{freePlot, contPlot, dopPlot},
  freePlot = ListLinePlot[list[[1]], PlotRange -> Full, FrameLabel -> {"Probe Detuning, Δp/2π (MHz)", "Normalized Abs. (%)", PlotRange -> {0, 100}}] *
  contPlot = ListContourPlot[list[[2]], FrameLabel -> {"Probe Detuning (MHz)", "Velocity Class (m/s)", PlotRange -> Full}];
  dopPlot = ListLinePlot[list[[3 ;; 4]], FrameLabel -> {"Probe Detuning (MHz)", "Absorption (%)", PlotLegends -> {"Doppler Averaged Absorption", "Zero V
  }
];
genDataC[Op_, Oc_, g_] := Block[{vMax = 50, vStep = 0.25, ΔpMax = 2 Pi 15.0, ΔpStep = 2 Pi 0.25,
  Δp = 2 Pi Op, Δc = 2 Pi Oc, Δp = 0, γ = 2 Pi g,
  norm, detunings, data, flat, aveData, zeroData},
  detunings = Range[-ΔpMax, ΔpMax, ΔpStep] / 2 / Pi;
  norm = ParallelSum[dopScale * vStep * Exp[-expScale v^2] * fullNSolve[Δp + kp * v, Δc - kc * v, Op, 0, γ], {v, -vMax, vMax, vStep}];
  Print[norm];
  data = ParallelTable[{Δc / 2 / Pi, v, dopScale * vStep * Exp[-expScale v^2] * fullNSolve[Δp + kp * v, Δc - kc * v, Op, Δc, γ]}, {v, -vMax, vMax, vStep}, {Δc,
  flat = Flatten[data, 1];
  aveData = Transpose[{detunings, Total[data] / {All, 3}] / norm}];
  zeroData = Transpose[{detunings, Select[flat, Chop[Re[[2]]] == 0 &] / {All, 3}] * 10 / norm}];
  {flat, aveData, zeroData}
];
showPlotsC[list_] := Block[{data, aveData, zeroData},
  Print[ListContourPlot[list[[1]], FrameLabel -> {"Coupling Detuning (MHz)", "Velocity Class (m/s)", PlotRange -> Full}];
  Print[ListLinePlot[list[[2 ;; 3]], FrameLabel -> {"Coupling Detuning (MHz)", "Absorption (%)", PlotLegends -> {"Doppler Averaged Absorption", "Zero V
  }
];

2^2 / 6 / 0.2

3.33333

probe = 3.0;
couple = 7.5;
gamma = 1.2;
couple^2 / 6.0666 / gamma
2 * couple / 6.0666
6.0666 / gamma

7.72673

2.47255

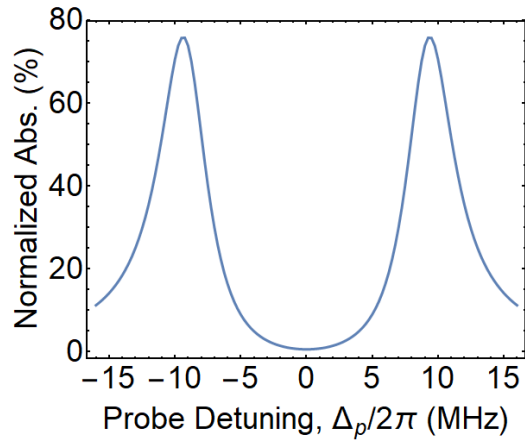
5.0555

Generate the data for plotting, plot each data set individually.

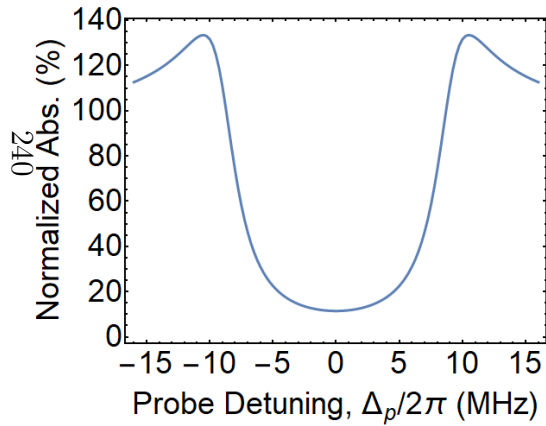
Output structure is {Doppler-free, flattend Doppler grid, Doppler-averaged trace, zero velocity class Doppler-data}

d = genDataP[3.0, 18.5, 0.2];

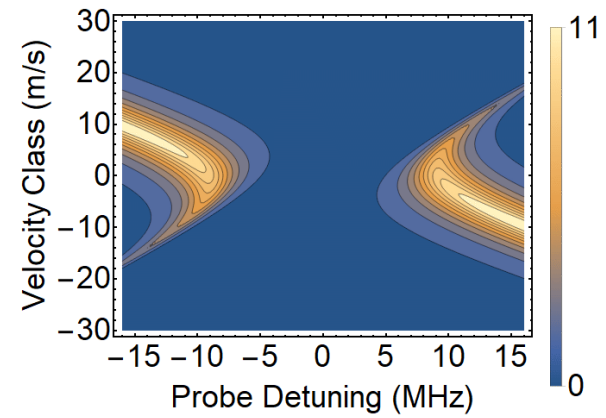
freePlot = ListLinePlot[d[[1]], PlotRange -> Full, FrameLabel -> {"Probe Detuning, Δp/2π (MHz)", "Normalized Abs. (%)",
  PlotRange -> {0, 100}}];
```



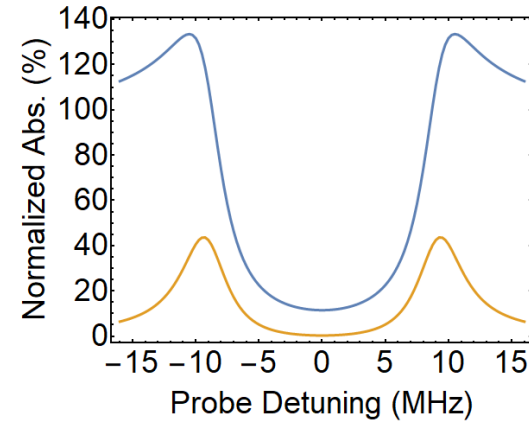
```
dopPlot = ListLinePlot[d[[3]], PlotRange -> Full, FrameLabel -> {"Probe Detuning, Δp/2π (MHz)", "Normalized Abs. (%)"},
PlotRange -> {0, 100}]
```



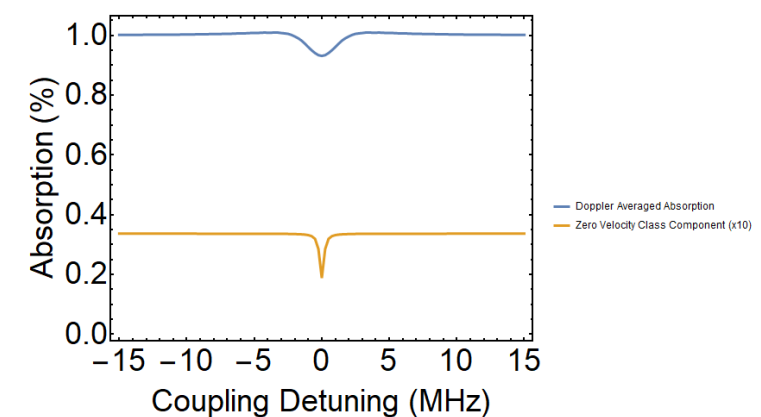
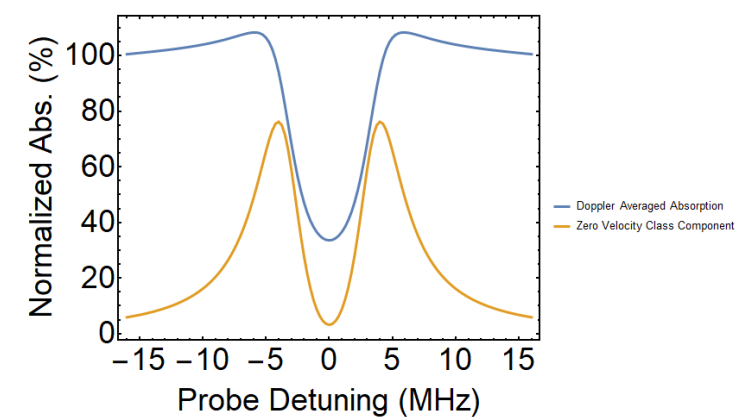
```
max = Ceiling[Max[d[[2, All, 3]]];
contPlot = ListContourPlot[d[[2]], FrameLabel -> {"Probe Detuning (MHz)", "Velocity Class (m/s)"}, Contours -> 10, PlotRange -> {0, max},
PlotLegends -> Placed[BarLegend[Automatic, {0, max}], None, "Ticks" -> {0, max}, LegendLabel -> None, LabelStyle -> Directive[Thick, Black, FontSize ->
```



```
dopPlot = ListLinePlot[d[[3 ;; 4]], FrameLabel -> {"Probe Detuning (MHz)", "Normalized Abs. (%)"},
(* second plot is zero velocity class component x5 for scale*)
```



```
compPlot = ListLinePlot[d[[3, 1]], FrameLabel -> {"Probe Detuning (MHz)", "Normalized Abs. (%)"},
PlotLegends -> {"Doppler Averaged Absorption", "Zero Velocity Class Component"}]
```



Export plots for Thesis

```
paramString = "-0.1MHz-2.0MHz-0.2MHz.pdf";
Export["Averaged"<>paramString,dopPlot]
Export["Contour"<>paramString,contPlot]
```

Averaged-0.1MHz-2.0MHz-0.2MHz.pdf

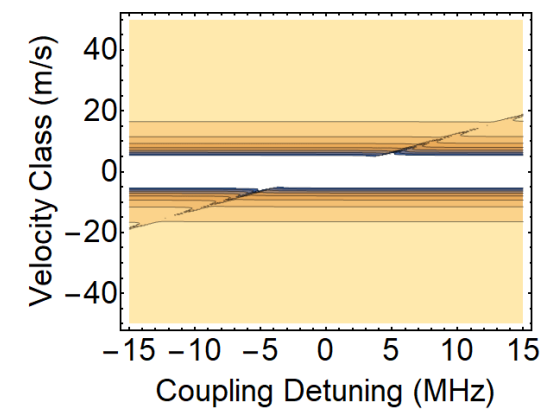
Contour-0.1MHz-2.0MHz-0.2MHz.pdf

Similar to above, but with coupling detuning instead.

```
d = genDataC[0.1, 1.0, 0.2];
```

-0.000277321

```
showPlotsC[d]
```



Bibliography

- [1] Paul D. Kunz, David H. Meyer, and Fredrik K. Fatemi. Twists in nonlinear magneto-optic rotation with cold atoms. *Optics Express*, 25(14):16392–16399, July 2017.
- [2] David H. Meyer, Kevin C. Cox, Fredrik K. Fatemi, and Paul D. Kunz. Digital communication with Rydberg atoms and amplitude-modulated microwave fields. *Applied Physics Letters*, 112(21):211108, May 2018.
- [3] Kevin C. Cox, David H. Meyer, Fredrik K. Fatemi, and Paul D. Kunz. Quantum-Limited Atomic Receiver in the Electrically Small Regime. *Physical Review Letters*, 121(11):110502, September 2018.
- [4] Daniel T. Stack, Paul D. Kunz, David H. Meyer, and Neal Solmeyer. Microwave electric field sensing with Rydberg atoms. In *Proceedings of SPIE*, volume 9873, pages 987306–987306–8, 2016.
- [5] David H. Meyer, Paul D. Kunz, and Neal Solmeyer. Nonlinear polarization spectroscopy of a Rydberg state for laser stabilization. *Applied Optics*, 56(3):B92–B96, January 2017.
- [6] D. Budker, W. Gawlik, D. F. Kimball, S. M. Rochester, V. V. Yashchuk, and A. Weis. Resonant nonlinear magneto-optical effects in atoms. *Reviews of Modern Physics*, 74(4):1153–1201, November 2002.
- [7] Dmitry Budker and Derek F. Jackson Kimball. *Optical Magnetometry*. Cambridge University, 2013.
- [8] Dmitry Budker, Valeriy Yashchuk, and Max Zolotarev. Nonlinear Magneto-optic Effects with Ultranarrow Widths. *Physical Review Letters*, 81(26):5788–5791, December 1998.
- [9] Gianni Di Domenico, Georg Bison, Stephan Groeger, Paul Knowles, Anatoly S. Pazgalev, Martin Rebetez, Hervé Saudan, and Antoine Weis. Experimental study of laser-detected magnetic resonance based on atomic alignment. *Physical Review A*, 74(6):063415, December 2006.

- [10] Antoine Weis, Georg Bison, and Anatoly S. Pazgalev. Theory of double resonance magnetometers based on atomic alignment. *Physical Review A*, 74(3):033401, September 2006.
- [11] T. Zigdon, A. D. Wilson-Gordon, S. Guttikonda, E. J. Bahr, O. Neitzke, S. M. Rochester, and D. Budker. Nonlinear magneto-optical rotation in the presence of a radio-frequency field. *Optics Express*, 18(25):25494–25508, December 2010.
- [12] Marcis Auzinsh, Dmitry Budker, and Simon Rochester. *Optically Polarized Atoms: Understanding Light-Atom Interactions*. Oxford University Press, Oxford, 2010.
- [13] D. Budker, D. F. Kimball, S. M. Rochester, and V. V. Yashchuk. Nonlinear Magneto-optical Rotation via Alignment-to-Orientation Conversion. *Physical Review Letters*, 85(10):2088–2091, September 2000.
- [14] D. V. Brazhnikov, A. M. Tumaikin, V. I. Yudin, and A. V. Taichenachev. Electromagnetically induced absorption and transparency in magneto-optical resonances in an elliptically polarized field. *Journal of the Optical Society of America B*, 22(1):57–64, January 2005.
- [15] A. V. Taichenachev, A. M. Tumaikin, and V. I. Yudin. Electromagnetically induced absorption in a four-state system. *Physical Review A*, 61(1):011802, December 1999.
- [16] C. Goren, A. D. Wilson-Gordon, M. Rosenbluh, and H. Friedmann. Electromagnetically induced absorption due to transfer of coherence and to transfer of population. *Physical Review A*, 67(3):033807, March 2003.
- [17] Robert W. Boyd. *Nonlinear Optics*. Academic Press, 3rd edition, 2008.
- [18] Yu. Malakyan, S. Rochester, D. Budker, D. Kimball, and V. Yashchuk. Nonlinear magneto-optical rotation of frequency-modulated light resonant with a low-J transition. *Physical Review A*, 69(1):013817, January 2004.
- [19] Dmitry Budker, Derek F. Kimball, and David P. DeMille. *Atomic Physics: An Exploration through Problems and Solutions*. Oxford University Press, Oxford ; New York, 2nd ed edition, 2008.
- [20] Simon Michael Rochester. *Modeling Nonlinear Magneto-Optical Effects in Atomic Vapors*. PhD thesis, University of California, Berkeley, 2010.
- [21] Peter E. Powers. *Fundamentals of Nonlinear Optics*. CRC Press, 2nd edition, 2011.
- [22] Karl Blum. *Density Matrix Theory and Applications*. Springer, 3rd edition, 2012.

- [23] Simon Rochester. AtomicDensityMatrix Mathematica Package, <http://rochesterscientific.com/ADM/>.
- [24] Irina Novikova, Andrey B. Matsko, and George R. Welch. Influence of a buffer gas on nonlinear magneto-optical polarization rotation. *JOSA B*, 22(1):44–56, January 2005.
- [25] Z. D. Grujić, M. M. Lekić, M. Radonjić, D. Arsenović, and B. M. Jelenković. Ramsey effects in coherent resonances at closed transition $F_g = 2 \rightarrow F_e = 3$ of ^{87}Rb . *Journal of Physics B: Atomic, Molecular and Optical Physics*, 45(24):245502, December 2012.
- [26] M. V. Balabas, K. Jensen, W. Wasilewski, H. Krauter, L. S. Madsen, J. H. Müller, T. Fernholz, and E. S. Polzik. High quality anti-relaxation coating material for alkali atom vapor cells. *Optics Express*, 18(6):5825–5830, March 2010.
- [27] S. M. Rochester and D. Budker. Atomic polarization visualized. *American Journal of Physics*, 69(4):450–454, April 2001.
- [28] S. I. Kanorsky, A. Weis, J. Wurster, and T. W. Hänsch. Quantitative investigation of the resonant nonlinear Faraday effect under conditions of optical hyperfine pumping. *Physical Review A*, 47(2):1220–1226, February 1993.
- [29] Robert C. Hilborn, Larry R. Hunter, Kent Johnson, Stephen K. Peck, Alison Spencer, and John Watson. Atomic barium and cesium alignment-to-orientation conversion in external electric and magnetic fields. *Physical Review A*, 50(3):2467–2474, September 1994.
- [30] Robert C. Hilborn. Atoms in orthogonal electric and magnetic fields: A comparison of quantum and classical models. *American Journal of Physics*, 63(4):330–338, April 1995.
- [31] D. A. Varshalovich, A. N. Moskalev, and V. K. Khersonskii. *Quantum Theory of Angular Momentum*. World Scientific Publishing Company, 1988.
- [32] Dmitry Budker, Valeriy Yashchult, and Max Zolotarev. Resonant Magneto-Optical Rotation: New Twists in an Old Plot. *Lawrence Berkeley National Laboratory Preprint*, (LBNL-41149), December 1997.
- [33] E. A. Donley, T. P. Heavner, F. Levi, M. O. Tataw, and S. R. Jefferts. Double-pass acousto-optic modulator system. *Review of Scientific Instruments*, 76(6):063112, June 2005.
- [34] Matthew L. Terraciano, Mark Bashkansky, and Fredrik K. Fatemi. Faraday spectroscopy of atoms confined in a dark optical trap. *Physical Review A*, 77(6):063417, June 2008.

- [35] N. Behbood, F. Martin Ciurana, G. Colangelo, M. Napolitano, M. W. Mitchell, and R. J. Sewell. Real-time vector field tracking with a cold-atom magnetometer. *Applied Physics Letters*, 102(17):173504, April 2013.
- [36] E. Breschi, Z. Grujić, and A. Weis. In situ calibration of magnetic field coils using free-induction decay of atomic alignment. *Applied Physics B*, 115(1):85–91, July 2013.
- [37] B. S. Mathur, H. Tang, and W. Happer. Light Shifts in the Alkali Atoms. *Physical Review*, 171(1):11–19, July 1968.
- [38] Fang Fang, Ryan Olf, Shun Wu, Holger Kadau, and Dan M. Stamper-Kurn. Condensing Magnons in a Degenerate Ferromagnetic Spinor Bose Gas. *Physical Review Letters*, 116(9):095301, March 2016.
- [39] D. L. Campbell, R. M. Price, A. Putra, A. Valdés-Curiel, D. Trypogeorgos, and I. B. Spielman. Magnetic phases of spin-1 spin–orbit-coupled Bose gases. *Nature Communications*, 7:10897, March 2016.
- [40] A. Smith, B. E. Anderson, H. Sosa-Martinez, C. A. Riofrío, Ivan H. Deutsch, and Poul S. Jessen. Quantum Control in the Cs $|S_{-1/2}\rangle$ Ground Manifold Using Radio-Frequency and Microwave Magnetic Fields. *Physical Review Letters*, 111(17):170502, October 2013.
- [41] Y. O. Dudin, L. Li, and A. Kuzmich. Light storage on the time scale of a minute. *Physical Review A*, 87(3):031801, March 2013.
- [42] M. Ebert, M. Kwon, T. G. Walker, and M. Saffman. Coherence and Rydberg Blockade of Atomic Ensemble Qubits. *Physical Review Letters*, 115(9):093601, August 2015.
- [43] Lajos S. Hanzo and William Webb. *Single- and Multi-Carrier Quadrature Amplitude Modulation*. John Wiley & Sons, Ltd., 2000.
- [44] John L. Volakis. *Antenna Engineering Handbook*. McGraw-Hill Education, New York, 4 edition edition, June 2007.
- [45] Thomas Gallagher. *Rydberg Atoms*. Number 3 in Cambridge Monographs on Atomic, Molecular and Chemical Physics. Cambridge University Press, Cambridge, 1st edition, November 2005.
- [46] Michael Fleischhauer, Atac Imamoglu, and Jonathan P. Marangos. Electromagnetically induced transparency: Optics in coherent media. *Reviews of Modern Physics*, 77(2):633–673, July 2005.
- [47] Claude Cohen-Tannoudji, Jacques Dupont-Roc, and Gilbert Grynberg. *Atom-Photon Interactions: Basic Processes and Applications*. John Wiley & Sons, Inc., New York, 1992.

- [48] Tony Y. Abi-Salloum. Electromagnetically induced transparency and Autler-Townes splitting: Two similar but distinct phenomena in two categories of three-level atomic systems. *Physical Review A*, 81(5):053836, May 2010.
- [49] Petr M. Anisimov, Jonathan P. Dowling, and Barry C. Sanders. Objectively Discerning Autler-Townes Splitting from Electromagnetically Induced Transparency. *Physical Review Letters*, 107(16):163604, October 2011.
- [50] L. Giner, L. Veissier, B. Sparkes, A. S. Sheremet, A. Nicolas, O. S. Mishina, M. Scherman, S. Burks, I. Shomroni, D. V. Kupriyanov, P. K. Lam, E. Giacobino, and J. Laurat. Experimental investigation of the transition between Autler-Townes splitting and electromagnetically-induced-transparency models. *Physical Review A*, 87(1):013823, January 2013.
- [51] A. K. Mohapatra, T. R. Jackson, and C. S. Adams. Coherent Optical Detection of Highly Excited Rydberg States Using Electromagnetically Induced Transparency. *Physical Review Letters*, 98(11):113003, March 2007.
- [52] J. Sagle, R. K. Namiotka, and J. Huennekens. Measurement and modelling of intensity dependent absorption and transit relaxation on the cesium D1 line. *Journal of Physics B: Atomic, Molecular and Optical Physics*, 29(12):2629, 1996.
- [53] A. Osterwalder and F. Merkt. Using High Rydberg States as Electric Field Sensors. *Physical Review Letters*, 82(9):1831–1834, March 1999.
- [54] Jonathon A. Sedlacek, Arne Schwettmann, Harald Kübler, Robert Löw, Tilman Pfau, and James P. Shaffer. Microwave electrometry with Rydberg atoms in a vapour cell using bright atomic resonances. *Nature Physics*, 8(11):819–824, November 2012.
- [55] D. J. Wineland, J. J. Bollinger, W. M. Itano, and D. J. Heinzen. Squeezed atomic states and projection noise in spectroscopy. *Physical Review A*, 50(1):67–88, July 1994.
- [56] Haoquan Fan, Santosh Kumar, Jonathon Sedlacek, Harald Kübler, Shaya Karimkashi, and James P. Shaffer. Atom based RF electric field sensing. *Journal of Physics B: Atomic, Molecular and Optical Physics*, 48(20):202001, September 2015.
- [57] D. A. Anderson, S. A. Miller, G. Raithel, J. A. Gordon, M. L. Butler, and C. L. Holloway. Optical Measurements of Strong Microwave Fields with Rydberg Atoms in a Vapor Cell. *Physical Review Applied*, 5(3):034003, March 2016.
- [58] C.L. Holloway, J.A. Gordon, S. Jefferts, A. Schwarzkopf, D.A. Anderson, S.A. Miller, N. Thaicharoen, and G. Raithel. Broadband Rydberg Atom-Based Electric-Field Probe for SI-Traceable, Self-Calibrated Measurements. *IEEE Transactions on Antennas and Propagation*, 62(12):6169–6182, December 2014.

- [59] Matt T. Simons, Joshua A. Gordon, and Christopher L. Holloway. Simultaneous use of Cs and Rb Rydberg atoms for dipole moment assessment and RF electric field measurements via electromagnetically induced transparency. *Journal of Applied Physics*, 120(12):123103, September 2016.
- [60] Christopher L. Holloway, Matt T. Simons, Joshua A. Gordon, Andrew Dientstfrey, David A. Anderson, and Georg Raithel. Electric field metrology for SI traceability: Systematic measurement uncertainties in electromagnetically induced transparency in atomic vapor. *Journal of Applied Physics*, 121(23):233106, June 2017.
- [61] S. A. Miller, D. A. Anderson, and G. Raithel. Radio-frequency-modulated Rydberg states in a vapor cell. *New Journal of Physics*, 18(5):053017, 2016.
- [62] C. G. Wade, N. Šibalić, N. R. de Melo, J. M. Kondo, C. S. Adams, and K. J. Weatherill. Real-time near-field terahertz imaging with atomic optical fluorescence. *Nature Photonics*, 11(1):40–43, January 2017.
- [63] Christopher L. Holloway, Joshua A. Gordon, Andrew Schwarzkopf, David A. Anderson, Stephanie A. Miller, Nithiwadee Thaicharoen, and Georg Raithel. Sub-wavelength imaging and field mapping via electromagnetically induced transparency and Autler-Townes splitting in Rydberg atoms. *Applied Physics Letters*, 104(24):244102, June 2014.
- [64] H. Q. Fan, S. Kumar, R. Daschner, H. Kübler, and J. P. Shaffer. Subwavelength microwave electric-field imaging using Rydberg atoms inside atomic vapor cells. *Optics Letters*, 39(10):3030–3033, May 2014.
- [65] J. A. Sedlacek, A. Schwettmann, H. Kübler, and J. P. Shaffer. Atom-Based Vector Microwave Electrometry Using Rubidium Rydberg Atoms in a Vapor Cell. *Physical Review Letters*, 111(6):063001, August 2013.
- [66] N. Šibalić, J. D. Pritchard, C. S. Adams, and K. J. Weatherill. ARC: An open-source library for calculating properties of alkali Rydberg atoms. *Computer Physics Communications*, 220:319–331, November 2017.
- [67] Santosh Kumar, Haoquan Fan, Harald Kübler, Akbar J. Jahangiri, and James P. Shaffer. Rydberg-atom based radio-frequency electrometry using frequency modulation spectroscopy in room temperature vapor cells. *Optics Express*, 25(8):8625–8637, April 2017.
- [68] A. Sargsyan, M. G. Bason, D. Sarkisyan, A. K. Mohapatra, and C. S. Adams. Electromagnetically induced transparency and two-photon absorption in the ladder system in thin columns of atomic vapors. *Optics and Spectroscopy*, 109(4):529–537, October 2010.
- [69] Markus Mack, Florian Karlewski, Helge Hattermann, Simone Höckh, Florian Jessen, Daniel Cano, and József Fortágh. Measurement of absolute transition

frequencies of $^{87}\mathrm{Rb}$ to nS and nD Rydberg states by means of electromagnetically induced transparency. *Physical Review A*, 83(5):052515, May 2011.

- [70] Stephanie A Miller. *Optical Measurements of Strong Radio-Frequency Fields Using Rydberg Atoms*. PhD thesis, University of Michigan, Ann Arbor, MI, 2017.
- [71] Matt T. Simons, Joshua A. Gordon, Christopher L. Holloway, David A. Anderson, Stephanie A. Miller, and Georg Raithel. Using frequency detuning to improve the sensitivity of electric field measurements via electromagnetically induced transparency and Autler-Townes splitting in Rydberg atoms. *Applied Physics Letters*, 108(17):174101, April 2016.
- [72] M. G. Bason, M. Tanasittikosol, A. Sargsyan, A. K. Mohapatra, D. Sarkisyan, R. M. Potvliege, and C. S. Adams. Enhanced electric field sensitivity of rf-dressed Rydberg dark states. *New Journal of Physics*, 12(6):065015, June 2010.
- [73] Warren L. Stutzman and Gary A. Thiele. *Antenna Theory and Design*. Wiley, Hoboken, NJ, 3 edition edition, May 2012.
- [74] Robert C. Hansen. *Electrically Small, Superdirective, and Superconducting Antennas*. John Wiley & Sons, Inc., Hoboken, NJ, 2006.
- [75] C. E. Shannon. Communication in the Presence of Noise. *Proceedings of the IRE*, 37(1):10–21, January 1949.
- [76] Michael S. Eggleston, Kevin Messer, Liming Zhang, Eli Yablonovitch, and Ming C. Wu. Optical antenna enhanced spontaneous emission. *Proceedings of the National Academy of Sciences*, 112(6):1704–1709, February 2015.
- [77] L. J. Chu. Physical Limitations of Omni-Directional Antennas. *Journal of Applied Physics*, 19(12):1163–1175, December 1948.
- [78] H. A. Wheeler. Fundamental Limitations of Small Antennas. *Proceedings of the IRE*, 35(12):1479–1484, December 1947.
- [79] Roger F. Harrington. Effect of antenna size on gain, bandwidth, and efficiency. *J. Res. Nat. Bur. Stand*, 64(1):1–12, 1960.
- [80] J. S. McLean. A re-examination of the fundamental limits on the radiation Q of electrically small antennas. *IEEE Transactions on Antennas and Propagation*, 44(5):672–, May 1996.
- [81] Philip Morrison. The Search for Extraterrestrial Intelligence (SETI). Technical report, January 1977.

- [82] Robert A. Bernheim. *Optical Pumping: An Introduction*. Frontiers in Chemistry. W. A. Benjamin, Inc., New York, 1965.
- [83] Martin Kiffner, Amir Feizpour, Krzysztof T. Kaczmarek, Dieter Jaksch, and Joshua Nunn. Two-way interconversion of millimeter-wave and optical fields in Rydberg gases. *New Journal of Physics*, 18(9):093030, 2016.
- [84] Jingshan Han, Thibault Vogt, Christian Gross, Dieter Jaksch, Martin Kiffner, and Wenhui Li. Coherent Microwave-to-Optical Conversion via Six-Wave Mixing in Rydberg Atoms. *Physical Review Letters*, 120(9):093201, March 2018.
- [85] P. T. Starkey, C. J. Billington, S. P. Johnstone, M. Jasperse, K. Helmersen, L. D. Turner, and R. P. Anderson. A scripted control system for autonomous hardware-timed experiments. *Review of Scientific Instruments*, 84(8):085111, August 2013.
- [86] S. E. Harris and Y. Yamamoto. Photon Switching by Quantum Interference. *Physical Review Letters*, 81(17):3611–3614, October 1998.
- [87] Min Yan, Edward G. Rickey, and Yifu Zhu. Observation of absorptive photon switching by quantum interference. *Physical Review A*, 64(4):041801, September 2001.
- [88] Danielle A. Braje, Vlatko Balić, G. Y. Yin, and S. E. Harris. Low-light-level nonlinear optics with slow light. *Physical Review A*, 68(4):041801, October 2003.
- [89] H. Schmidt and A. Imamoglu. Giant Kerr nonlinearities obtained by electromagnetically induced transparency. *Optics Letters*, 21(23):1936–1938, December 1996.
- [90] Greg Dmochowski, Amir Feizpour, Matin Hallaji, Chao Zhuang, Alex Hayat, and Aephraim M. Steinberg. Experimental Demonstration of the Effectiveness of Electromagnetically Induced Transparency for Enhancing Cross-Phase Modulation in the Short-Pulse Regime. *Physical Review Letters*, 116(17):173002, April 2016.
- [91] Yong-Fan Chen, Guan-Chi Pan, and Ite A. Yu. Transient behaviors of photon switching by quantum interference. *Physical Review A*, 69(6):063801, June 2004.
- [92] Amir Feizpour, Greg Dmochowski, and Aephraim M. Steinberg. Short-pulse cross-phase modulation in an electromagnetically-induced-transparency medium. *Physical Review A*, 93(1):013834, January 2016.
- [93] A. B. Deb and N. Kjærgaard. Radio-over-fiber using an optical antenna based on Rydberg states of atoms. *Applied Physics Letters*, 112(21):211106, May 2018.

- [94] Christopher Carr, Monsit Tanasittikosol, Armen Sargsyan, David Sarkisyan, Charles S. Adams, and Kevin J. Weatherill. Three-photon electromagnetically induced transparency using Rydberg states. *Optics Letters*, 37(18):3858, September 2012.
- [95] C. Pfeiffer. Fundamental Efficiency Limits for Small Metallic Antennas. *IEEE Transactions on Antennas and Propagation*, 65(4):1642–1650, April 2017.
- [96] S. R. Best. Electrically Small Resonant Planar Antennas: Optimizing the quality factor and bandwidth. *IEEE Antennas and Propagation Magazine*, 57(3):38–47, June 2015.
- [97] Tianxiang Nan, Hwaider Lin, Yuan Gao, Alexei Matyushov, Guoliang Yu, Huaihao Chen, Neville Sun, Shengjun Wei, Zhiguang Wang, Menghui Li, Xinjun Wang, Amine Belkessam, Rongdi Guo, Brian Chen, James Zhou, Zhenyun Qian, Yu Hui, Matteo Rinaldi, Michael E. McConney, Brandon M. Howe, Zhongqiang Hu, John G. Jones, Gail J. Brown, and Nian Xiang Sun. Acoustically actuated ultra-compact NEMS magnetoelectric antennas. *Nature Communications*, 8(1):296, August 2017.
- [98] S. E. Sussman-Fort and R. M. Rudish. Non-Foster Impedance Matching of Electrically-Small Antennas. *IEEE Transactions on Antennas and Propagation*, 57(8):2230–2241, August 2009.
- [99] N. Zhu and R. W. Ziolkowski. Broad-Bandwidth, Electrically Small Antenna Augmented With an Internal Non-Foster Element. *IEEE Antennas and Wireless Propagation Letters*, 11:1116–1120, 2012.
- [100] C. L. Degen, F. Reinhard, and P. Cappellaro. Quantum sensing. *Reviews of Modern Physics*, 89(3):035002, July 2017.
- [101] Bryan T. Gard, Kurt Jacobs, R. McDermott, and M. Saffman. Microwave-to-optical frequency conversion using a cesium atom coupled to a superconducting resonator. *Physical Review A*, 96(1):013833, July 2017.
- [102] H. Hattermann, D. Bothner, L. Y. Ley, B. Ferdinand, D. Wiedmaier, L. Sárkány, R. Kleiner, D. Koelle, and J. Fortágh. Coupling ultracold atoms to a superconducting coplanar waveguide resonator. *Nature Communications*, 8(1):2254, December 2017.
- [103] Wenlan Chen, Kristin M. Beck, Robert Bücker, Michael Gullans, Mikhail D. Lukin, Haruka Tanji-Suzuki, and Vladan Vuletić. All-Optical Switch and Transistor Gated by One Stored Photon. *Science*, 341(6147):768–770, August 2013.
- [104] Y.-Y. Jau, A. M. Hankin, T. Keating, I. H. Deutsch, and G. W. Biedermann. Entangling atomic spins with a Rydberg-dressed spin-flip blockade. *Nature Physics*, 12(1):71–74, January 2016.

- [105] Lin Li and A. Kuzmich. Quantum memory with strong and controllable Rydberg-level interactions. *Nature Communications*, 7:13618, November 2016.
- [106] Yuechun Jiao, Xiaoxuan Han, Jiabei Fan, Georg Raithel, Jianming Zhao, and Suotang Jia. Atom-based quantum receiver for amplitude- and frequency-modulated baseband signals in high-frequency radio communication. *arXiv:1804.07044 [quant-ph]*, April 2018.
- [107] David A. Anderson, Rachel E. Sapiro, and Georg Raithel. An atomic receiver for AM and FM radio communication. *arXiv:1808.08589 [physics, physics:quant-ph]*, August 2018.
- [108] Zhenfei Song, Wanfeng Zhang, Hongping Liu, Xiachi Liu, Haiyang Zou, Jie Zhang, and Jifeng Qu. The credibility of Rydberg atom based digital communication over a continuously tunable radio-frequency carrier. *arXiv:1808.10839 [physics]*, August 2018.
- [109] C. B. Alcock, V. P. Itkin, and M. K. Horrigan. Vapour Pressure Equations for the Metallic Elements: 298–2500K. *Canadian Metallurgical Quarterly*, 23(3):309–313, July 1984.
- [110] Arijit Sharma, Tridib Ray, Rahul V. Sawant, G. Sheikholeslami, S. A. Rangwala, and D. Budker. Optical control of resonant light transmission for an atom-cavity system. *Physical Review A*, 91(4):043824, April 2015.
- [111] N. Šibalić, J. M. Kondo, C. S. Adams, and K. J. Weatherill. Dressed-state electromagnetically induced transparency for light storage in uniform-phase spin waves. *Physical Review A*, 94(3):033840, September 2016.
- [112] Arne Schwettmann. *Atom Chip Setup for Cold Rydberg Atom Experiments*. Ph.D., University of Oklahoma, 2012.